Theoretical and Experimental Investigations About the AFM Tip-Based Nanomachining Process

Thesis submitted in fulfilment of the requirement for the degree of

Doctor of Philosophy

By

Raheem Sadoon Jamel Al-Musawi

Mechanical and Manufacturing Engineering

Cardiff School of Engineering

Cardiff University

United Kingdom

December 2016

PAPERS PRODUCED FROM THIS THESIS

1- Al-Musawi, R.S.J., Brousseau, E.B., Geng, Y. and Borodich, F.M., 2016. “Insight into mechanics of AFM tip-based nanomachining: bending of cantilevers and machined grooves”. *Nanotechnology*, *27*(38), p.385302.

2- Al-Musawi, R.S.J., Brousseau, E.B., 2016. “Influence of the mechanical behaviour of cantilevers on the topography of nano-scale grooves during AFM tip-based machining". *Proceedings of the 16th International Conference of the European Society for Precision Engineering and Nanotechnology*, pp. 383–384, Nottingham, UK, May 2016

3- Al-Musawi, R.S.J., Brousseau, E.B., 2016. “Assessing the applied normal load during contact mode AFM: an issue with the conventional approach” *The International Conference for Students on Applied Engineering*, Newcastle, United Kingdom, October 2016.

DECLARATION

This work has not been submitted in substance for any other degree or award at this or any other university or place of learning, nor is being submitted concurrently in candidature for any degree or other award.

Signed …………………………………… (candidate) Date …………………………

STATEMENT 1

This thesis is being submitted in partial fulfilment of the requirements for the degree of PhD

Signed …………………………………… (candidate) Date …………………………

STATEMENT 2

This thesis is the result of my own independent work/investigation, except where otherwise, and the thesis has not been edited by third party beyond what is permitted by Cardiff University's policy on the Use of Third Party Editors by Research Degree Students. Other sources are acknowledged by explicit references. The views expressed are my own.

Signed …………………………………… (candidate) Date …………………………

STATEMENT 3

I hereby give consent for my thesis, if accepted, to be available for photocopying and for inter-library loan, and for the title and summary to be made available to outside organisations.

Signed ……………………………………(candidate) Date …………………………

Abstract

In the last two decades, technological progress towards the miniaturisation of products and components has increased significantly. This trend has also been driven by demands for the manufacture of devices with functional features on the nanoscale. One of the nanofabrication processes, which has been proposed by researchers to meet such needs, relies on the mechanical machining of the surface of a workpiece with the tip of an atomic force microscope (AFM) probe. In this case, the AFM probe is utilised as a cutting tool as it enables the direct contact between its sharp tip, which is fixed on a flexible micro cantilever, and the workpiece surface. A relatively large numbers of studies have been reported in the field of AFM tip-based nanomachining since the invention of the AFM instrument itself just over thirty years ago. However, such studies have typically neglected the fact that AFM probes should be considered as flexible tools when investigating this process. Thus, this shortcoming constitutes the main motivation behind this PhD research.

Following a review of the literature, the work reported in this Thesis starts by a study of the bending orientation of cantilevers during AFM tip-based nanomachining operations along different processing directions. To achieve this, an advanced experimental set-up is developed first in order to monitor a number of output signals, which characterise the motions of both the fixed and the free ends of the cantilever together with the displacements of the AFM stage. A refined theoretical analysis is also presented to express the bending orientation of an AFM probe cantilever at its free end as a function of the forces acting on the tip when machining in a direction pointing away from the probe. This refined model shows that the bending orientation depends on both geometric parameters of the cantilever and on the cutting forces. Complementary experiments, which are designed to determine the quasi-static bending behaviour of cantilevers in practice, show that, contrary to assumed knowledge, both concave and convex bending orientations could take place when machining along this direction. The occurrence of a change of the cantilever deflected shape from convex to concave bending during machining can principally change the depth and width of grooves produced. For instance, the depth of grooves machined on a single crystal copper specimen may increase up to 70% following this phenomenon.

Following this, another refined model is also developed to measure the normal force acting on the tip when the AFM stage is static by taking in account the cantilever geometry and its inclination angle with respect to the sample surface. This work leads to the introduction of a correction factor that should be applied when using the conventional equation for determining the normal load in this configuration. Results obtained when implementing this model based on the dimensions of typical commercial AFM probes show that the conventional approach always leads to an underestimation of the normal applied force. In addition, it is demonstrated, both theoretically and experimentally, that the conventional method for determining the applied normal load during AFM tip-based nanomachining, i.e. when the stage is not static, is wrong.

Based on this shortcoming, a novel procedure is proposed to estimate all three force components (i.e. thrust, axial, and lateral forces) acting on the tip during AFM tip-based nanomachining. To achieve this, two novel methods are also developed to assess the actual value of normal force during machining, which in this case is referred to as the thrust force. Based on experimental data, a good agreement is found between both methods for different physical quantities evaluated. Another refined theoretical model, based on the classical beam theory, is also employed in this procedure to determine the axial force acting on the tip and subsequently, the lateral force. Using this novel procedure to estimate the cutting forces, it is also shown that even if the deflection angle at free end of probe is constant, this does not mean that the associated cantilever vertical deflection is constant between the configurations when the AFM stage is static (i.e. for nanoindentation) and when it is moving (i.e. during an actual cutting operation).

Finally, in order to gain further insights into the material removal mechanisms that influence the process, a series of post-machining investigations on the topography of produced grooves is reported for different applied loads and processing directions. This particular experimental study takes advantage of the prior knowledge established in this Thesis. Indeed, the understanding of the cantilever deflected shape and the accurate assessment of cutting forces provide key inputs when the groove formation process is analysed.

ACKNOWLEDGEMENTS

First, I would like to give thanks to Allah the almighty, the all great without whom I could not have completed this educational endeavour.

I am deeply indebted to the Iraqi army and People's Mobilization (*Al-Hashd Al-Sha'abi)* for defencing the homeland against the savage militants (ISIS). Without them, this work would not be possible. That is why, I dedicate this thesis to them with all my love and gratitude.

The dissertation would not have been possible without the many people who took part in my life as a graduate student. They made this time special and memorable for me.

I would like to express sincere gratitude to Dr. Emmanuel Brousseau, Prof. Feodor M Borodich my immediate supervisor, for introducing me into this fantastic research area. They are generous and patient, guiding me in the research from the beginning to the end. “Actions speak louder than words”. Words cannot express my heartfelt gratitude for their efforts towards my development as a good researcher and a future academic. I consider myself ever so lucky to have been mentored by them. Their strong understanding and passion for academic quality resonates with me in every single way and has shaped my future goals as a researcher. They offered unquestionable support through the inevitable ups and downs of this research and kept me focused, giving me sound advice in all aspects of my studentship.

During my time in Cardiff University, I had the privilege of knowing and working with many great people. Extra special thanks goes to my colleagues, Ali AL Khafaji, Ali Al-Zughaibi, Adnan ALAmili, Zaynab Alraziqi, Zinah Ahmed and Nur Farah Hafizah. I am deeply grateful to them for their consistent encouragement, invaluable guidance and strong support during the course of this study.

I would also like to thank Dr. Yanquan Geng for his guidance in the lab and for allowing me to call upon his expertise whenever I needed. I wish to express my sincere thanks to Cardiff University, especially the Manufacturing Engineering Centre (MEC) for the use of the facilities to pursue this research.

I will also take this opportunity to thank my Ministry of higher education and scientific research sponsors at Baghdad, Kufa University at Najaf city, Iraq and Iraqi Cultural Attaché in London- not only for their financial support but also for allowing me to gain an industrial perspective for my work.

Finally, this research would not have been possible without the never-ending support of my family. I hope to make them proud, especially to the memory of my beloved father and my mother who has been a welcome distraction and ray of sunshine throughout. Many thanks for my brothers and sisters for their support and for being truly brothers when needed. My most sincere gratitude and appreciation go to my love wife Thickra for her patience, continuous encouragement and support over the past difficult years. Thanks as well to Allah for his gift; my beloved daughter Mariam and my son Ahmed.

List of Acronyms

AFM	Atomic Force Microscope
ANSI	American National Standards Institute
DAQ	Data Acquisition System
DLC	Diamond-Like Carbon
ISO	International Organization for Standardization
LFM	Lateral Force Monitor
NC	Non-Contact
NEMS	Nano Electro Mechanical System
NI	National Instrument
PE	Polyethylene
PMMA	Poly(methyl methacrylate)
PSPD:	Position Sensitive Photodiode Detector
SAM	Signal Access Module
SEM	Scanning Electron Microscopy
SPL	Scanning Probe Lithography
SPM	Scanning Probe Microscopy
STM	Scanning Tunnelling Microscope
Y DET	Y-detector (V)
Z DET	Z-detector (V)

Nomenclature

γ	Angle between the resultant force and longitudinal axial of cantilever
F_a	Axial force (μN)
M_{axial}	Axial moment (N.m)
α_2	Backward rake angle
t	Cantilever thickness (μm)
ψ	Clearance angle
μ_{flat}	Coefficient of friction on the flat surface of wedge sample
β_c	Conversion coefficient (PSPD)
h	Depth of groove (nm)
F_{in}	Force applied by the user in the lithography window (indentation)
α_1	Forward rake angle
P_A^y	Horizontal reaction force at fix end of cantilever (N)
δ_L	Lateral bending of cantilever (μm)
α	Lateral calibration constant (μN/V)
F_L	Lateral force (μN)
S_L	Lateral sensitivity of the optical level system (μm/V)
K_L	Lateral spring constant (N/m)
L	Length of cantilever (μm)
F_n	Normal force applied on the tip (μN)
C	Normal force correction factors (-)
M_{normal}	Normal moment (N.m)
δ_n:	Normal sensitivity of optical system (μm/V)
σ	Optical lever detection sensitivity of AFM (V/ μm)
V_{C-D}	PSPD voltage corresponding to lateral bending of cantilever
V_{A-B}	PSPD voltage corresponding to vertical deflection of cantilever
R_e	Radius of tip (nm)
M_A	Reaction moment (N.m)
f_o	Resonant frequency of a cantilever (Hz)
Δf_o	Resonant frequency shift
F_R	Resultant forces (μN)

m	Slope of PSPD voltage-distance curve (V/µm)
D	Spatial distance between the PSPD and the cantilever free
K_1	Spring constant of cantilever (AFM) (N/m)
K	Spring constant of cantilever (N/m)
K_2	Spring constant of holder (traditional machining) (N/m)
K_s	Spring constant of sample fixture (traditional machining) (N/m)
A	The adhesive force (µN)
θ	The angle of the wedge sample sloped surface (degree)
EI	The flexural rigidity of cantilever
W	The half width of friction loop (V)
d	The linear deflection (shift of the laser spot) on the array of PSPD
Δ	The offset from the friction loop (V)
G	The shear modulus (GPa)
F_{th}	Thrust force (µN)
h_{tip}	Tip height (µm)
δ_{in}	Vertical deflection of free end of indentation stage (µm)
δ_{sc}	Vertical deflection of free end of scratching stage
P_A^z	Vertical reaction force at fix end of cantilever (N)
w	Width of cantilever (µm)
E	Young modulus of cantilever (Gpa)

Table of Contents

Chapter 1 Introduction 1

1.1 Background and Motivation 2

1.2 Research objectives, scope, and tasks 5

1.3 Thesis Outline 6

Chapter 2 Literature Review 9

2.1 Introduction 9

2.2 Atomic Force Microscopy 9

2.2.1 Instrumentation 10

2.2.2 Modes of operations 14

2.3 AFM-tip-based nano mechanical machining 19

2.3.1 First challenge: Control of the groove depth 20

2.3.2 Second challenge: Understanding of scratching mechanisms 28

2.3.3 Third challenge: Influence of the curvature of the deflected shape of the cantilever 33

2.3.4 Fourth challenge: Understanding of the tip cutting angles 36

2.4 Force measurements during AFM probe-based machining 37

2.4.1 Determination of the normal force, F_n 40

2.4.2 Calibration of the normal sensitivity of the PSPD, S_n 40

2.4.3 Determination of the lateral force, F_L 43

2.4.4 Determination of the axial force, F_a 47

2.5 Summary and identified knowledge gaps 51

Chapter 3 Experimental Setup 54

3.1 Introduction 55

3.2 Experimental platform 55

3.2.1 Atomic Force Microscope 55

3.2.2 Data Acquisition System 57

3.3 Operating conditions 61

3.3.1 Workpiece materials....61
3.3.2 AFM probes 61
3.3.3 Experimental cutting conditions and parameter settings 65
3.4 Microscopy techniques....69

Chapter 4 New insight into the quasi-static behaviour of cantilevers during AFM tip-based nanomachining....71

4.1 Introduction 72
4.2 Theoretical analysis of the deformed shape of the cantilever 73
4.3 Illustration and analysis of the Z-detector output signal 78
4.4 Experimental studies of nanomachining with different process directions 83
4.4.1 Nanomachining with backward and inclined backward directions.....83
4.4.2 Shape of the deflected cantilever during nanomachining in the forward direction 89
4.4.2.1 The deflection of the cantilever at low loads 89
4.4.2.2 The deflection of the cantilever at medium loads 94
4.4.2.3 The deflection of the cantilever at high loads 98
4.5 Verification experiment 104
4.5.1 Inclined forward direction....104
4.5.2 Measurements of the machining distance 108
4.6 Summary 110

Chapter 5 Assessment of the applied normal force during the nanoindentation and the tip-based nanomachining processes....112

5.1 Introduction 113
5.2 Assessment of the applied normal force during nanoindentation. 114
5.2.1 Theoretical analysis....114
5.2.2 Assessment of the applied normal load using the refined model......122
5.3 Assessment of the applied normal force during tip-based nanomachining 128
5.3.1 Influence of the axial force: experimental analysis....128

5.3.2 Influence of the axial force: theoretical analysis 132

5.4 Determination of the quasi-static normal sensitivity during tip-based nanomachining 135

5.4.1 Pure and inclined forward direction 135

5.4.2 Pure backward and inclined backward direction 140

5.5 Summary 142

Chapter 6 Measurements of cutting forces during AFM tip-based nanomachining 144

6.1 Introduction 145

6.2 Proposed procedure for calibrating and measuring AFM tip-based nano machining forces 146

6.2.1 Step one: deflection angle for the indentation and scratching stages 148

6.2.2 Step two: thrust force measurement 150

6.2.2.1 Method one: fitting method 151

6.2.2.2 Method two: percentage method 158

6.2.3 Step three: axial force and lateral force measurements 160

6.2.3.1 Pure forward and inclined forward 160

6.2.3.2 Pure backward and inclined backward analysis 162

6.2.3.3 Pure lateral direction 162

6.3 Results and discussion 166

6.3.1 Backward direction 166

6.3.1.1 Normal force and thrust force 166

6.3.1.2 Axial force and resultant force 170

6.3.1.3 Quasi-static normal sensitivity and resultant angle 172

6.3.2 Pure and inclined forward 174

6.3.2.1 Normal force and thrust force 174

6.3.2.2 Axial force, lateral force and resultant force 178

6.3.2.3 Normal sensitivity, lateral force calibration factor and resultant angle 183

6.3.3 Comparison between the fitting method and percentage method 184

6.4 Summary 187

Chapter 7 Advanced investigations of groove formation mechanisms and machining outcomes 189

7.1 Introduction 191

7.2 Investigation of material deformation regimes 192

7.3 Investigation of achieved groove depth and width 198

7.4 Groove geometry and pile-up formation 203

7.4.1 Backward machining 203

7.4.2 Forward machining 204

7.4.3 Inclined forward machining 206

7.5 Influence of tool angles and cutting direction during scratching 211

7.6 Chip morphology 216

7.7 Summary 219

Chapter 8 Contributions, Conclusions and Future Work 220

8.1 Contributions 221

8.2 Conclusions 223

8.3 Future work and recommendations 226

Reference 228

Appendix A 240

List of Figures

Figure 1.1 Classification of SPL-based fabrication methods according to the dominant tip–surface interaction used for nanoscale patterning, namely electrical, thermal, mechanical and diffusive processes (Garcia *et al.* 2014) 4

Figure 2.1 Key components of an AFM instrument 11

Figure 2.2 Force sensor components a) AFM probe and b) illustration of the optical lever method for detecting the vertical and horizontal bending of the cantilever.................... 13

Figure 2.3 Schematic depicting the working principle of the feedback loop for controlling the vertical deflection of the probe.. 14

Figure 2.4 Interatomic force vs. distance curve 15

Figure 2.5 Different implementations of the contact mode: (a) constant-height mode and (b) constant-force mode 17

Figure 2.6 Schematic illustration of the tapping mode (Bruker nano system 2012)....... 18

Figure 2.7 a) Scratching depths with variation in the nromal force and feed rate; (b) scratch depths with pile-up heights for different loads (Mostofa *et al.* 2013) 21

Figure 2.8 The relationship between the depth groove and normal force for (a) PMMA/Silicon (b) PMMA/glass and (c) PE (Hassani and Aghabozorg 2011) 23

Figure 2.9 The relation between the groove dimensions and applied load for Si substrate (Tseng *et al.* 2009a).. 24

Figure 2.10 Depth of grooves at various applied load on the InP crystal (Huang *et al.* 2013) 24

Figure 2.11 (a) influence of applied load on depth of groove and surface roughness (b) the effect of the cycles number of both depth and roughness of groove (Fang *et al.* 2000). 26

Figure 2.12 The influence of cutting speed on the depth of groove. The square, circle, triangle, hexagon and star symbols show the applied force at 30.5, 26.7, 19.1 and 15.2 μN respectively (Fonseca Filho *et al.* 2004) 27

Figure 2.13 The influence of applied force on the depth of groove. The square, circle, triangle, hexagon and star symbols show the cutting speed force at 1, 2.5, 5 and 7.5 μm/s respectively(Fonseca Filho *et al.* 2004) 27

Figure 2.14 Schematic of the effect of the minimum chip thickness (Mostofa *et al.* 2013) 29

Figure 2.15 Schematic of the cantilever axes and direction motion (a) Main axis of..... 31

Figure 2.16 Effects of tip geometry on materials removal states along the scratching direction (Yan *et al.* 2009). 32

Figure 2.17 a) schematic of the AFM tip-based nano mechanical machining system b) schematic of the conventional cutting system (Yan *et al.* 2015) 34

Figure 2.18 (a) Illustration of the backward and forward AFM tip-based machining directions using a top view perspective and (b) side view of the commonly assumed concave cantilever deflection when processing in the forward direction 35

Figure 2.19 Constant load cutting mechanism with control loop. 37

Figure 2.20 Schematic of the different planes and axes based on the geometry of an AFM probe along (a) the forward direction and (b) the lateral direction of the probe movement 39

Figure 2.21 Illustration of the evolution of $V_{A\text{-}B}$ as a function of the displacement of the Z scanner during the calibration of the PSPD normal sensitivity...................................... 42

Figure 2.22 a) wedge sample and b) friction loop 45

Figure 2.23 Schematic showing the cantilever deflected shape due to the axial force (a) during backward scanning and (b) forward scanning (adapted from (Bhushan and Marti 2010)). 49

Figure 2.24 Schematic illustration the Z-scanner movement in both forward and backward scanning direction (from (Bhushan and Marti 2010)) 50

Figure 3.1 Park XE-100 AFM instrument 56

Figure 3.2 Configuration of the X-Y and the Z scanners (Park-systems).......................57

Figure 3.3 Signal Access Module from Park Systems..59

Figure 3.4 Actual experimental set-up..59

Figure 3.5 Schematic description of the AFM probe-based nano-machining 60

Figure 3.6 SEM micrographs of the utilised DNISP probes (a) top view of cantilever (b) side view of the tip apex (c) top view of tip apex 63

Figure 3.7 TESPD type from Bruker (a) top view of cantilever (b) side view of the tip apex 64

Figure 3.8 LabVIEW block diagram of get voltages 67

Figure 3.9 Considered cutting directions with respect to the cantilever orientation and tip geometry...68

Figure 3.10 The Scanning Electron Microscope utilised...70

Figure 4.1 (a) Schematic representation of the AFM probe during nanomachining in the forward direction and (b) corresponding free body diagram. 74

Figure 4.2 The shape of cantilever deflection and slope angle a) convex bending and b) concave bending...77

Figure 4.3 Example of Z-detector signal during nanomachining in the backward direction 80

Figure 4.4 Illustration of the probe and the PSPD status following a) the approach process and b) the initial tip penetration into the specimen..80

Figure 4.5 The evolution of the Z-detector output as a function of the Z-scanner movement..81

Figure 4.6 Illustration of the probe and the PSPD status during the machining stage.... 82

Figure 4.7 Illustration of the probe and the PSPD status following the retraction stage 82

Figure 4.8 Z-detector output signals when processing the PC sample along the backward direction for a set normal load of 3.1 μN 84

Figure 4.9 Z-detector output signals when processing the PC sample along the backward direction for a set normal load of 4.4 μN 85

Figure 4.10 Z-detector output signals when processing the Cu sample along the backward direction for a set normal load of 13 μN 85

Figure 4.11 detector output signals when processing the Cu sample along the backward direction for a set normal load of 34 μN 86

Figure 4.12 Typical A-B and Y stage signals representative of processing in the backward and inclined backward directions. The inset plot shows the change in the A-B voltage as soon as the lateral motion of the stage starts. 87

Figure 4.13 Illustration of the probe being raised as a result of the moment M_a being .. 88

Figure 4.14 Z-detector output signals when processing the Cu sample along the backward direction for a set normal load of 13 μN 90

Figure 4.15 Z-detector output signal when processing the Cu sample along the backward direction for a set normal load of 27 μN 91

Figure 4.16 Z-detector and Y stage output signals when processing the Cu sample along the forward direction for a set normal load of 20 μN. Note that for the inset higher magnification image, the Y stage signal was deliberately shifted up for illustration purpose. 92

Figure 4.17 Illustration of the probe sliding up the face of the initial indent and the subsequent series of events with respect to the V_{A-B} voltage variation on the PSPD and the associated response of the Z-scanner via the force-controlled feedback loop 93

Figure 4.18 Z-detector and Y stage output signals when processing the Cu sample along the forward direction for a set normal load of 24 μN. 95

Figure 4.19 Illustration of the probe being lowered upon the start of the lateral motion of the stage as a result of the effect of the moment M_a dominating over the sliding of the tip. 96

Figure 4.20 Z-detector and Y stage output signals when processing the Cu sample along the forward direction for a set normal load of 27 μN. 97

Figure 4.21 Z-detector and Y-stage voltage output signals when processing the Cu sample along the forward direction for a set normal load of 31 μN. 99

Figure 4.22 (A-B) PSPD voltage output signals when processing the Cu sample along the forward direction for a set normal load of 31 μN. 99

Figure 4.23 Illustration of the cantilever shape changing from convex to concave during the machining of a groove and the associated Z-scanner response........100

Figure 4.24 Z-detector recorded when using a set applied load of 39 μN........102

Figure 4.25 A-B signals recorded when using a set applied load of 39 μN........102

Figure 4.26 SEM micrographs of the grooves obtained when machining with the higher range of normal loads considered along the forward direction. Scale bar: 2 μm........103

Figure 4.27 Z-detector signals obtained when machining the PC specimen along the inclined forward direction for a set normal applied load of 3.1 μN........105

Figure 4.28 Z-detector signals obtained when machining the PC specimen along the inclined forward direction for a set normal applied load of 4.4 μN........105

Figure 4.29 Z-detector signal recorded when machining the Cu specimen along the inclined forward direction for a set applied load of 33 μN........106

Figure 4.30 SEM micrographs of the grooves obtained when machining the Cu specimen with a normal load of 33 μN. 107

Figure 4.31 (a) AFM scan and (b) SEM micrographs of the groove and (c) recorded Z-detector signal when machining the Cu sample for a set normal load of 31 μN in the forward direction. 109

Figure 5.1 Schematic representation of the AFM probe during nanoindentation, (b) corresponding free body diagram and (c) free body diagram of cantilever portion. 115

Figure 5.2 Illustration of the vertical shift of the laser spot on the PSPD.................... 120

Figure 5.3 Curve of loading and unloading for PC sample.. 126

Figure 5.4 SEM micrographs of the probe ND-DYIRS utilised (a) overall view of the cantilever (b) tip geometry (c) cantilever thickness (d) tip heigh 127

Figure 5.5 (a) AFM image of a groove machined with a normal force of 29 μN along the backward direction and (b) comparison of cross-section profiles obtained during the indentation and the scratching steps for this groove. 130

Figure 5.6 V_{A-B} signal measured when processing in the backward direction 131

Figure 5.7 Schematic representation of the AFM probe being subject to an axial load only 133

Figure 5.8 Schematic representation of the AFM probe during nanomachining in the backward direction 134

Figure 5.9 (a) Schematic representation of the AFM probe during forward nano machining (b) corresponding free body diagram and (c) free body diagram of cantilever portion. 138

Figure 5.10 (a) Schematic representation of the AFM probe during backward nano machining (b) corresponding free body diagram and (c) free body diagram of cantilever portion. 141

Figure 6.1 Flow chart developed for determining all cutting forces components during AFM tip-based nanomachining. 147

Figure 6.2 AFM tip-based nanomachining in the forward direction; (a) plot showing that the (A-B) voltage of the PSPD stays constant during scratching process and (b) corresponding schematic representation of the probe moving in the vertical direction to keep the voltage constant as a result of the feedback loop mechanism 149

Figure 6.3 Schematic representation of a) the indentation stage and b) forward machining 150

Figure 6.4 Z-detector output signal during the nanoindentation test 154

Figure 6.5 V_{A-B} output voltage during the nanoindentation test.................................. 154

Figure 6.6 Z-detector output voltage between the selected T_1 and T_2.......................... 155

Figure 6.7 Applied normal force between T_1 and T_2... 155

Figure 6.8 Extracted relationship between the Z-detector signal and the applied normal force between T_1 to T_2.. 156

Figure 6.9 Illustration of employing the Z-detector output voltage to determine the actual normal load during machining 159

Figure 6.10 Forces analysis in the lateral AFM scratching... 164

Figure 6.11 F_n, (i.e. during indentation) and F_{th} (i.e. during scratching in the backward direction) for a pre-set load of (a) 21.5 µN. (b) 29.5 µN and (c) 37 µN...................... 168

Figure 6.12 Percentage difference between the pre-set applied load value and F_{th} in the backward direction during scratching stage 169

Figure 6.13 Resultant force , F_R, and axial force, F_a, during scratching in the backward direction for an applied force of (a) 21.5µN (b) 29.5µN and (c) 37µN........................ 171

Figure 6.14 (a) Resultant force angle, β, and (b) quasi-static normal sensitivity, S_{th}, for different set normal applied loads during backward machining 173

Figure 6.15 F_n, and F_{th} for a pre-set load of (a) 21.5 µN pure forward. (b) 29.5 µN pure forward and (c) 21.5 inclined forward direction µN.. 175

Figure 6.16 F_n, and F_{th} for a pre-set load of (a) 33.5 μN pure forward. (b) 33.5 μN inclined forward direction 177

Figure 6.17 Forces during scratching for a pre-set applied load of 21.5 μN along the a) forward and b) inclined forward direction 180

Figure 6.18 a) Axial force and b) resultant force during scratching in the forward direction for a pre-set applied load of 33.5μN 181

Figure 6.19 (a) Axial, (b) resultant and (c) lateral forces during scratching along the inclined forward direction at a pre-set normal load of 33.4 μN........ 182

Figure 6.20 Comparison between thrust force values for different pre-set applied loads and machining directions 185

Figure 6.21 Comparison between resultant force values for different pre-set applied loads and machining directions 185

Figure 6.22 Comparison between resultant angle values for different pre-set applied loads and machining directions 186

Figure 6.23 Comparison between normal sensitivity values for different pre-set applied loads and machining directions........ 186

Figure 7.1 SEM micrograph of grooves machined in the backward direction for a pre-defined normal force of a) 21.5 μN and b) 36.0 μN 194

Figure 7.2 Illustration of the flow of material ahead of the tip for (a) the backward direction and (b) the forward direction 195

Figure 7.3 SEM micrographs of grooves machined in the forward direction for a pre-defined normal force of (a) 39 μN and (b) 36 μN........ 196

Figure 7.4 SEM micrograph of the groove processed in the inclined forward direction for a pre-defined applied force of 21.5 μN........ 197

Figure 7.5 SEM micrograph of the groove processed in the inclined forward direction for a pre-defined applied force of 33.5 μN 198

Figure 7.6 Width of scratched grooves as a function of the pre-defined applied normal force in the forward direction..200

Figure 7.7 Depth of scratched grooves as a function of the pre-defined applied normal force in the forward direction..200

Figure 7.8 Width of scratched grooves as a function of the pre-defined applied normal force in the inclined forward direction..201

Figure 7.9 Depth of scratched grooves as a function of the pre-defined applied normal force in the inclined forward direction..201

Figure 7.10 Width of scratched grooves as a function of the pre-defined applied normal force in the backward direction...202

Figure 7.11 Depth of scratched grooves as a function of the pre-defined applied normal force in the backward direction...202

Figure 7.12 Cross-sectional profiles of produced groves for different pre-set applied loads in the backward direction..204

Figure 7.13 Cross-sectional profiles of produced grooves for different pre-set applied loads in the forward direction 205

Figure 7.14 AFM image of scratched grooves for pre-set applied forces of (a) 21.5 μN and (b) 33.5 μN in the forward direction 205

Figure 7.15 AFM image of scratched grooves for pre-set applied forces of (a) 21.5 μN and (b) 33.5 μN in the inclined forward direction 207

Figure 7.16 Cross-sectional profiles for different pre-set applied loads in the inclined forward direction...208

Figure 7.17 Illustration of material flow in inclined forward direction for (a) convex cantilever deflected shape and b) concave cantilever deflected shape 209

Figure 7.18 Tip planes and angles: (a) top view of the tip; (b) clearance angle; (c) forward rake angle and (d) backward rake angle...210

Figure 7.19 Side view of the tip showing the influence of the inclination angle on the cutting tool angles 213

Figure 7.20 A schematic of material flow around a tip in forward direction 214

Figure 7.21 A schematic of material flow ahead of the tip in the backward direction . 214

Figure 7.22 Comparison between the groove cross section in the forward and backward directions for an identical pre-set applied load 21.5 μN 215

Figure 7.23 Chip formation for the inclined forward direction for two applied loads, namely 217

Figure 7.24 Chip formation for the backward direction at the pre-set applied load of (a) 21.6 μN and (b) 27.0 μN 218

List of Tables

Table 3.1 Probe specifications..65

Table 3.2 Cutting conditions for the Cu sample..68

Table 3.3 Cutting conditions for the PC sample 69

Table 5.1 Correction factor calculated for a range of commercial probes 125

Table 5.2 Measured dimensions for the ND-DYIRS probe 126

Table 6.1 Experimental normal force values obtained using the fitting method 157

Table 6.2 Thrust force, F_{th}, estimated by both the fitting and the percentage methods 160

Chapter 1

Introduction

1.1 Background and Motivation

In the last two decades, the demand for the fabrication of functional components with nanoscale features has significantly increased (Hassani *et al.* 2010, Iwanaga *et al.* 2005, Martín *et al.* 2005, Massiot *et al.* 2016, Schulte *et al.* 2016). These components are generally used for high-value application products, which benefit from specific nanoscale mechanical, thermal, and optical properties (Cumings and Zettl 2000, El-Sayed. and Mostafa 2001, Gillibert *et al.* 2016, Klinke *et al.* 2006, Link and Mostafa 1999, Lucas *et al.* 2009, Milekhin *et al.* 2016, Mostofa 2014, Zhou and Kim 2016). Some of these applications include semi-conductors integrated circuits (Hiroyuki and Nobuyuki 1997), memory devices, display units, biochips, biosensors (Xie *et al.* 2006), nano fluidic chips (Wu *et al.* 2001), heat transfer components (Perry and Kandlikar 2005), organic electronic devices (Facchetti 2010), nano-wires (Ee *et al.* 2010, Versen *et al.* 2000b), nano dots (Jung *et al.* 2010) and single electron transistors (Schumacher *et al.* 2000). Thus, the accurate and reliable manufacturing of nanoscale features with high surface finish and accuracy is critical and faces many challenges.

Conventional nanoscale fabrication techniques include mask-based photolithography processes (Sun *et al.* 2010, Thian *et al.* 2006), electron beam lithography (Fujita *et al.* 1996, Robinson *et al.* 1998) and focused ion beam (Bach *et al.* 2001, Rennon *et al.* 2000). Although these techniques constitute today's industrial standard for nanoscale manufacturing in the field of semi-conductor development and nano electro mechanical system (NEMS) components, they still have a number of limitations associated with them. In particular, the common drawbacks of such current technologies are as follows:

- They rely on vacuum-based capital intensive equipment (Engstrom *et al.* 2014);
- They can only process a restricted set of materials while also being generally limited to the fabrication of planar (i.e. two-dimensional) features (Dimov *et al.* 2012);
- These are increased concerns over their environmental friendliness as they are energy intensive and generate significant waste (Krishnan *et al.* 2008).

As a result, several alternative techniques have been developed in the last two decades, which employ, as fabrication tools, the sharp tip of probes used in scanning probe microscopy (SPM). These include dip-pen lithography (Piner 1999), local anodic

oxidation (Avouris *et al.* 1997, Keyser *et al.* 2000, Snow and Campbell 1995), electron emission current (Wilder *et al.* 1998), thermal mechanical patterning (Mamin 1996, Vettiger *et al.* 2000), electrochemical machining (Lee *et al.* 2010, Park *et al.* 2007) and direct mechanical machining (Li *et al.* 2005, Magno and Bennett 1997, Sumomogi *et al.* 1994, Wendel *et al.* 1995, Yan *et al.* 2010, Yan *et al.* 2007, Yun and Lieber. 1992). These scanning probe lithography (SPL) techniques have the ability to induce selective surface modification with high resolution, relative simplicity of operations and low cost, while being generally applicable to a wide range of materials. Figure 1.1 shows a summary of the different SPL-based fabrication methods.

Among these methods, direct mechanical machining, which is realised on an Atomic Force Microscope (AFM) is the focus of this research. Since, the invention of the AFM by Binnig and co-workers in 1986 (Binning *et al* 1986), it has been widely utilised not only as a tool to obtain surface topographic data down to atomic resolution and to measure surface interaction forces, but also to fabricate nanoscale structures (Xie *et al.* 2006).

The mechanical modification of a sample surface with the tip of an AFM probe has attracted special interest as a one of the techniques for fabricating nanoscale structures. When implementing this process, the sample surface can be modified in two different ways, i.e. either by using a continuous contact mode approach or a dynamic approach for which the tip contacts the surface intermittently. It was reported by Kunze (2002) that performing nanomachining using the dynamic AFM mode results in a lower force applied by the tip on the sample in comparison with the contact mode implementation. Thus, this can restrict the depth of machined features to a few nanometers, even when processing soft materials. In addition, the amplitude and frequency of the tip oscillations also influence the topography of machined cavities, which make the control of the process more difficult (Hyon *et al.* 1999).

These is a relatively large number of studies in the literature that reported the implementation of the AFM tip-based nanomachining technology, also referred to as scratching or scribing. In spite of that, little attention has been paid to investigate the quasi-static behaviour of the cantilever on which the tip of an AFM probe is mounted and

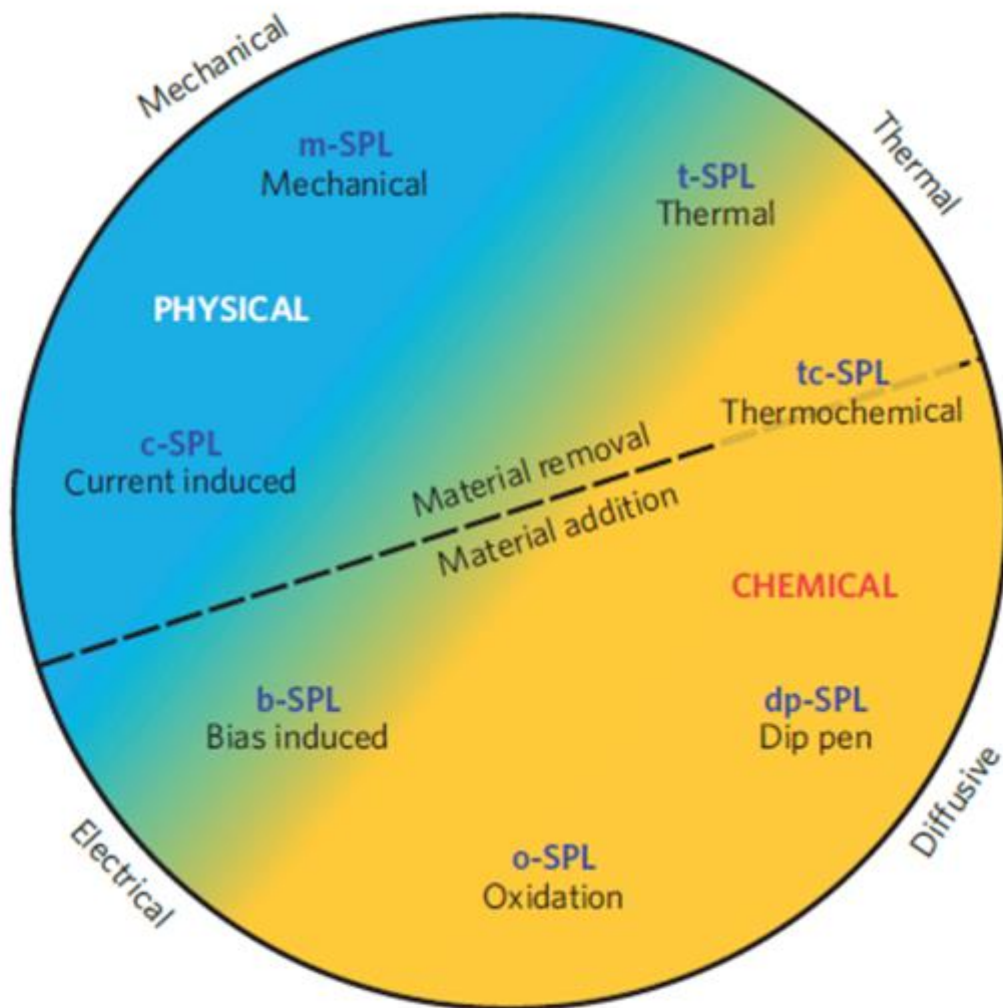

Figure 1.1 Classification of SPL-based fabrication methods according to the dominant tip–surface interaction used for nanoscale patterning, namely electrical, thermal, mechanical and diffusive processes (Garcia *et al.* 2014)

the influence of this behavior on the cutting forces and ultimately, on the resulting process mechanics and the achieved depth of machined grooves. Such investigations are important because AFM probe cantilevers are flexible bodies. Thus, despite the fact that tips can be considered as rigid, the system "tip" and "cantilever" as a whole cannot. In addition, the orientations of the tip cutting angles, i.e, rake and flank face angles, influence the process mechanics which is determined not only by the geometry of a given tip but also by the bending, torsional and lateral stiffness of a given cantilever and the direction of machining. For this reason, the process cannot be considered anisotropic as the

direction of the relative displacement between the tip and the sample surface also influences the machining outcomes, such as the depth of produced grooves. In this context, research investigations are required to understand, model and monitor the behaviour of AFM probes during tip-based nanomachining. It is anticipated that such investigations should contribute to improve and control the machining outcome of this process

1.2 Research objectives, scope, and tasks

The ultimate goal of the research presented in this thesis is to contribute towards the better understanding and prediction of the AFM tip-based nanomachining technology by considering the system “cantilever-tip” as a flexible cutting tool in contact mode.

In particular, to achieve this objective, it is necessary to predict and to monitor the shape of the AFM cantilever deflection during the cutting process. In addition, knowledge of the manner in which the cantilever behaviour affects the surface modification of a processed specimen should shed further light on the groove formation process. Following the better understanding of the mechanical behaviour of the cantilever, a new online technique to measure the cutting forces during the process is required as current approaches show limitations as will be presented in the next chapter. Lastly, it is also necessary to investigate the influence of the tip orientation, the applied forces on the tip and the shape of the cantilever deflection on the actual groove formation and the obtained groove geometry.

To achieve this overall objective, the following research tasks have been identified.

Task 1: Investigation into the quasi-static behaviour of cantilevers during AFM tip-based machining

To achieve this, a new approach is proposed and validated for monitoring the mechanical behaviour of AFM probe cantilevers during tip-based nanomachining.

Task 2: Measurement and calibration of cutting forces

While the determination of the cantilever deflected shape can provide useful insight for understanding the mechanism of the AFM tip-based nanomachining process, it is also

required to monitor accurately the cutting forces acting on the tip. Therefore, the second task of this research is to propose a novel method for the online monitoring of such forces throughout the different steps required to complete such nanomachining operations.

Task 3: Investigation of the groove geometry and machining regime

In order to complete this research, the final task aims to provide further insight into the cutting mechanisms at play during the groove formation process based on the knowledge established from the above tasks. To achieve this, the examination of machined grooves is required using a range of microscope techniques. In this way, it possible to relate processing conditions to machining outcomes, such as cutting regimes and dimensions of grooves.

1.3 Thesis Outline

Figure 1.2 shows the flow chart which is described the organised of thesis and presented as follows:

Chapter 2 starts by introducing background knowledge about the operating principle of the AFM technology and the associated basic hardware elements. Then, a review of the current trends and investigations in the field of AFM tip-based nano mechanical machining is presented. Special attention is given to the current knowledge gaps, which affect the reliability and predictability of the process. Finally, current methods that enable the determination of the cutting forces are presented and their limitations in context of AFM tip-based machining are described.

Chapter 3, presents the experimental setup utilised to monitor signals, which can be used to study the mechanical behaviour of cantilevers during the process.

Chapter 4, presents a theoretical analysis first to predict the shape of the probe during nanomachining determining the sign of the slope of the deflected cantilever at its free end. Then, a novel analysis of the signals recorded via set-up described in chapter 3 is presented. Then, the experimental results are discussed for different machining directions and applied loads. Finally, an experimental validation is reported to demonstrate the applicability of the approach for observing the cantilever deflected shape.

Chapter 5 focusses on the determination of the force applied on the tip in a direction perpendicular to the sample surface, namely the normal force, when the AFM stage is static (i.e. during indentation only). In particular, a refined theoretical analysis is first presented, that extends the conventional approach in the literature, for assessing this applied normal force by taking into account the influence of the cantilever geometry and of its inclination angle with respect to the sample surface. Following that, experimental work is reported to discuss the implications of this refined formula. Next, theoretical and experimental studies are conducted, which show that the conventional method for determining the applied normal load during AFM tip-based nanomachining, i.e. when the AFM stage is moving, is not correct.

In **Chapter 6**, a novel procedure is proposed to estimate the different cutting force components during AFM tip-based nanomachining. To achieve this, two original and alternative methods are described and compared to calibrate and measure the actual value of the normal force as the tip of the AFM probe is engaged into the material and moved horizontally relative to the sample surface. Based on this, a method is also presented to determine the axial force acting on the tip, i.e. the force component parallel to the sample surface and lying on the same plane as that of the cantilever axis. In addition, a method to assess the third force component, namely the lateral force, which is oriented perpendicular to the long axis of the cantilever and that is parallel to the sample surface, is also derived in this chapter.

Chapter 7 presents a series of post-machining investigations of produced grooves to gain further insight into the machining mechanisms that take place for different cutting conditions. In particular, these investigations build on the knowledge established in previous chapters with respect to the understanding of the deflected shape of the cantilever and in regard to the accurate determination of the cutting forces.

Chapter 8 provides a brief summary of the research work completed in this Thesis. The main findings and the original scientific contributions of this thesis are also highlighted. Finally, recommended areas for future work are outlined.

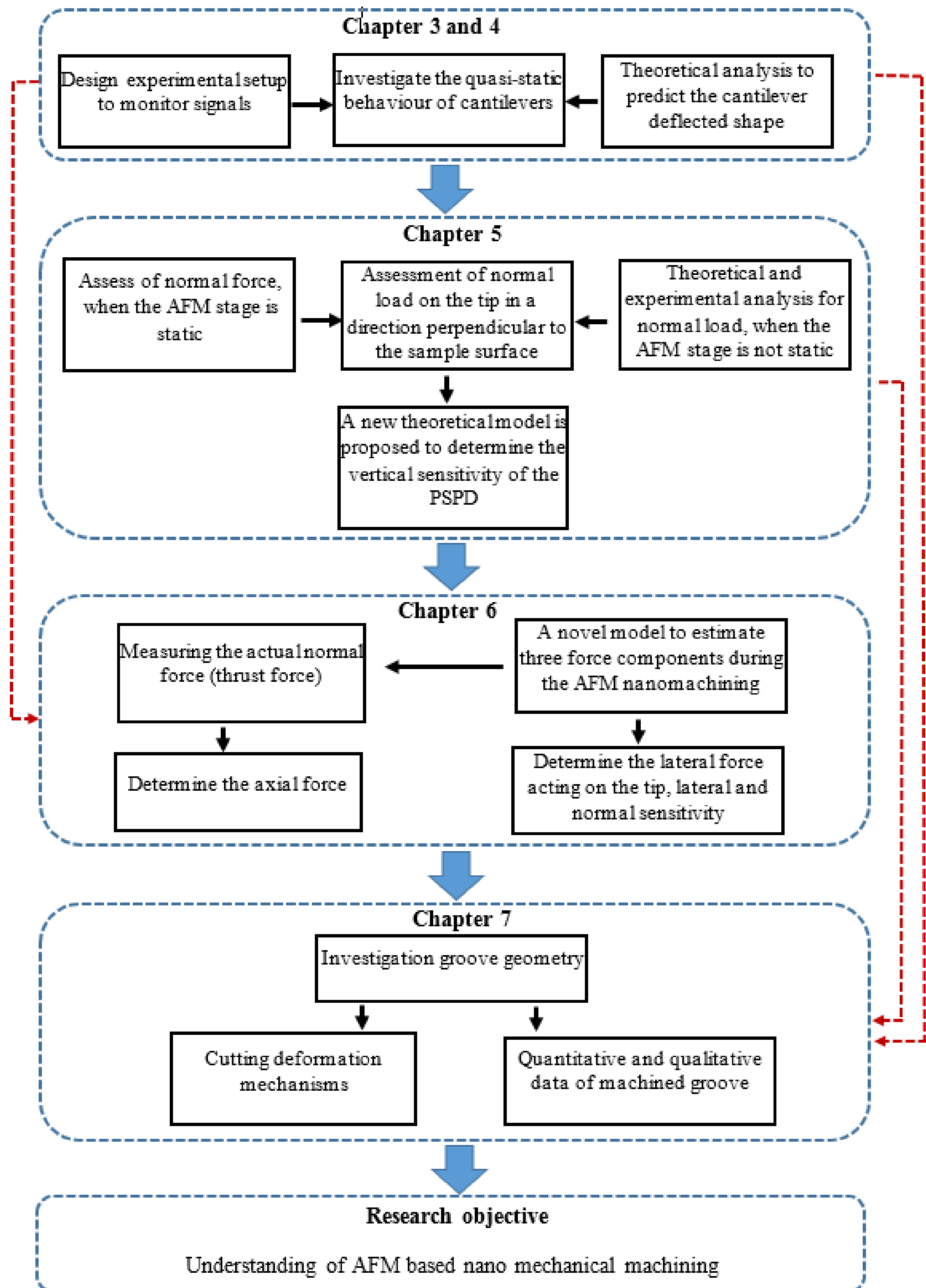

Figure 1.2 Flow chart shows the outline of thesis

Chapter 2

Literature Review

2.1 Introduction

The previous chapter outlined the advantages of AFM tip–based nano mechanical machining over traditional nano lithography processes. Additionally, it was stated that a number of research challenges remained to be addressed in order to achieve a better understanding of this particular AFM-based fabrication technique. These challenges are further elaborated upon here based on the analysis of the state-of-the art knowledge in this field. Prior to presenting the identified challenges, the chapter starts by providing a brief introduction to the basic operating principle and key hardware components of AFM instruments. Next, the main part of this chapter is concerned with the analysis of previous studies which investigated the AFM tip-based nano mechanical machining process. In particular, this is achieved in the context of four specific current engineering research challenges, which could be extracted from the relevant body of literature. Following this, specific issues related to the accurate measurements of the machining forces during the process are reported. Finally, a summary of the identified knowledge gaps is given in the last section of this chapter.

2.2 Atomic Force Microscopy

The invention of the scanning tunnelling microscope (STM) in 1981 by Binnig and his colleagues for obtaining three-dimensional images of specimen surfaces with the atomic resolution was the precursor to the development of the Atomic Force Microscope instrument (Binnig *et al.* 1982). Indeed, a few years following the invention of the STM, Binnig and co-workers introduced the Atomic Force Microscope to overcome the limitation of the STM as a technique applicable to conductive samples only (Binnig *et al.* 1986a). As stated by these authors, the AFM is "*a combination of the principles of the scanning tunneling microscope and the stylus profilometer*" (Binnig *et al.* 1986a). Given that the AFM relies on measuring the deflection of an extremely light cantilever beam, very smaller interaction forces (less than 1 nN) between the AFM tip and the specimen surface can be routinely detected in practice. In the last 30 years, AFM has become a widespread research tool, which has enabled numerous studies relying on the dimensional characterisation of surfaces with high-resolution. In addition, AFM-based techniques have been developed successfully for different applications such as material characterisation, nano-tribology and nanoscale manufacturing. Moreover, AFM has also

been employed on a wide range of materials and under the varied environmental condition, i.e. in air (Binnig *et al.* 1987), liquid solutions (Hansma *et al.* 1988) and vacuum (Meyer and Amer 1990).

2.2.1 Instrumentation

A schematic of the key components presenting in an AFM instrument is provided in Figure 1.2. An AFM operates by using a mechanical probe to "feel" or "touch" the surface of samples to gather the required information. As the probe tip is brought very close to the sample surface, the attractive force between the surface and the tip causes the cantilever to deflect towards the surface. However, as the tip makes contact with the specimen surface, increasingly the repulsive force takes over and causes the cantilever to deflect away from the surface.

The instrumentation required in an AFM instrument can be grouped into three main parts as follows:

- **Piezoelectric actuators**: These are referred to as "Z-scanner" and "XY scanner" in Fig 2.1. AFM scanners are made from piezoelectric materials. This type of materials can change the dimensions in response to an applied voltage. Thus, the Z-scanner expands or contracts proportionally to the applied voltage to move the probe vertically. The XY scanner, commonly made of a stack of two piezoelectric actuators, generates the relative horizontal displacement between the probe and the sample.

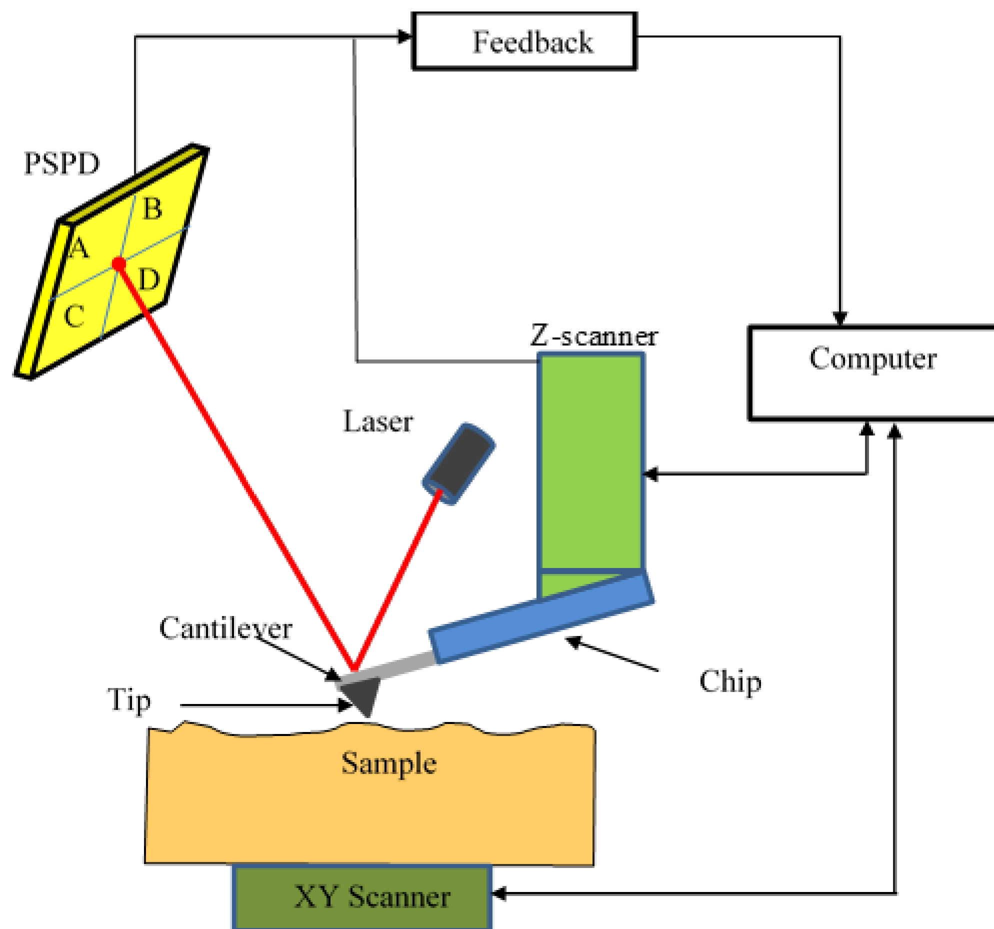

Figure 2.1 Key components of an AFM instrument

- **Force sensor**: The force sensor consists of the AFM probe and the instrumentation required for monitoring the deflection of the probe at its free end. In the majority of AFM implementations, the deflection is detected via the optical lever method. In this case, a position sensitive photodiode (PSPD) is employed to sense the intensity of a laser beam reflected from the back of the cantilever probe, as illustrated with Figure 2.1, and to convert this intensity into a voltage output. An AFM PSPD typically consists of four sections, allowing the normal and torsional deflections of the cantilever to be detected (Morris *et al.* 1999). As shown with Figure 2.2, a typical probe consists of three main parts, namely a chip, a cantilever and a tip. The chip is a relatively large piece of the probe, which provides a base to mount the probe to the AFM head. The cantilever is a thin beam, which extends out from the chip and has a rectangular or a triangular shape. The backside of cantilevers is usually coated with

a thin layer of gold or aluminium to enhance the laser reflectivity. In particular, the vertical deflection of the probe is proportional to the difference in signal between the top two and bottom two segments, i.e. (A+B) -(C-D) while the lateral deflection is proportional to the difference between the rightmost two segments and the leftmost two segments, i.e. (B+D)-(A+C).

- **Feedback control:** A feedback loop is utilised to ensure a constant interaction force between the tip and the sample as the probe scans the surface horizontally. The working principle of the feedback loop used to implement the optical lever method is illustrated with Figure 2.3. Following the vertical deflection of the cantilever, the control electronic receives the (A+B)-(C-D) voltage signal from the PSPD. Based on the difference between this signal and a reference value, the Z-scanner is extended, or contracted, to maintain a constant interaction force between the tip and the sample. For instance, when this voltage is above the target value set by the user, the feedback loop aims to reduce the vertical deflection by contracting the Z-scanner, thereby moving the fixed end of the probe a little further away from the sample surface. Conversely, when the cantilever deflection is less than the given set point, the Z-scanner is expanded to move the fixed end of the probe closer to the specimen. The surface topography of a sample can be assumed to be linearly dependent on the input signal supplied to the Z-scanner during the operation of the feedback loop. However, when measuring an increasing height range, it is possible to exceed the linear operation range of the Z-scanner (Gozen and Ozdoganlar 2014). This can lead to errors in the obtained surface topography data. However, when the applied voltage to Z-scanner used to represent the sample topography, hysteresis and creep in piezoelectric actuator prevent the AFM from providing accuracy topography of the sample. Therefore, an independent position sensor, such as a strain gauge or an interferometric device, can be directly used to measure the actual motions of the Z-scanner. Figure 2.3 illustrates the working principle of the feedback loop. In this figure, the independent motion sensor (referred to as “Z-detector”) is represented as a strain gauge mounted directly on the Z-scanner.

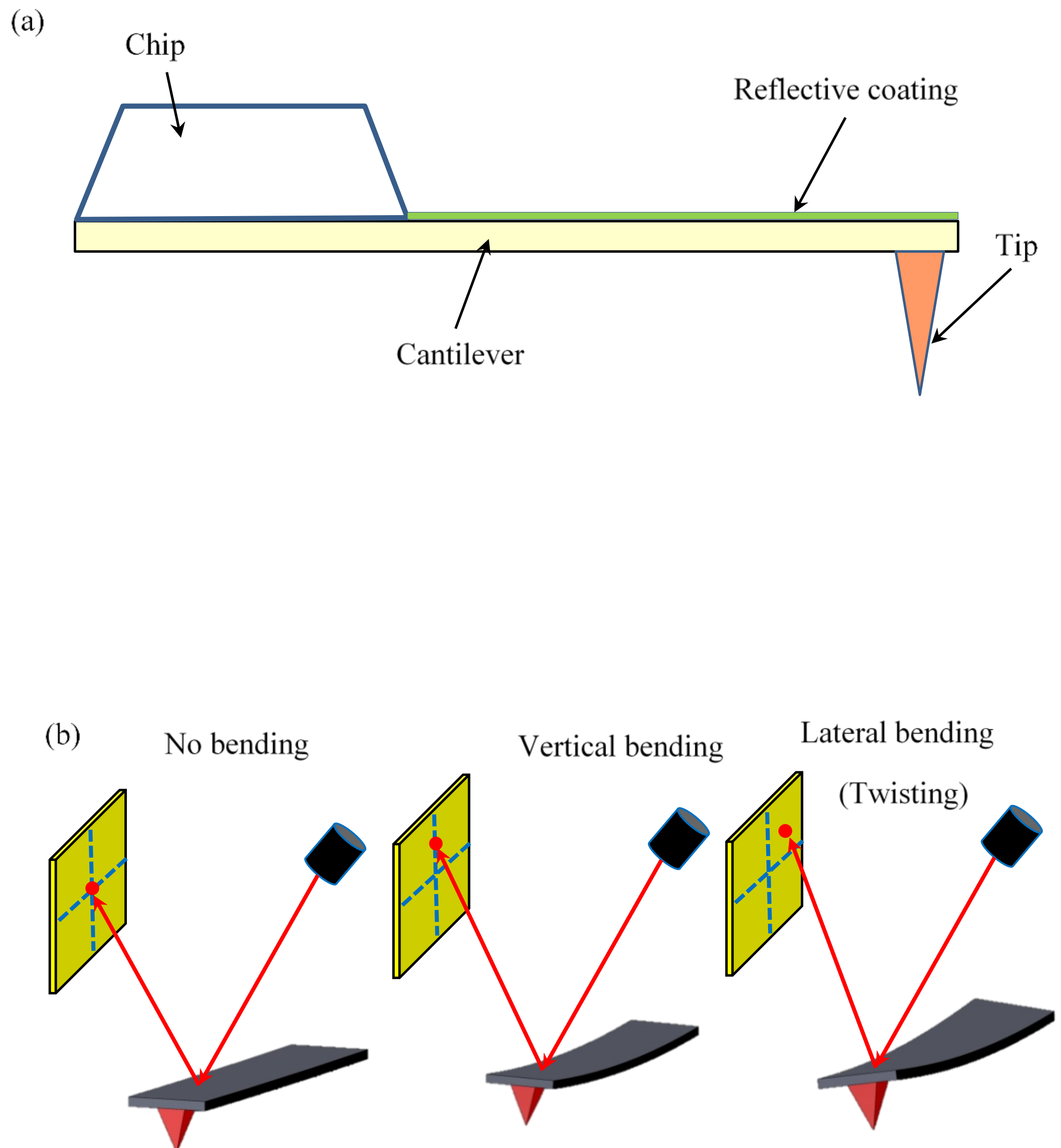

Figure 2.2 Force sensor components a) AFM probe and b) illustration of the optical lever method for detecting the vertical and horizontal bending of the cantilever

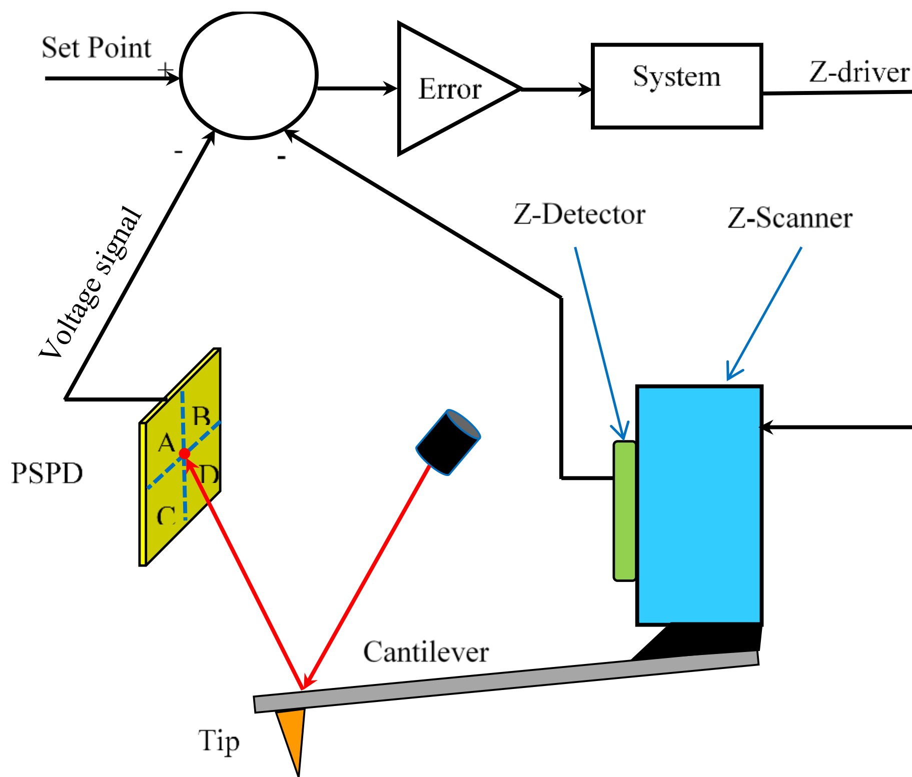

Figure 2.3 Schematic depicting the working principle of the feedback loop for controlling the vertical deflection of the probe

2.2.2 Modes of operations

Three basic modes can be implemented when employing an AFM instrument to image the surface of a sample. Prior to describing each of them, the interaction forces between an AFM tip and a sample, as a function of the tip-surface distance, are briefly introduced here. As shown with Figure 2.4, two kinds of force regimes can be observed as the AFM tip is brought closer to the sample surface. In the attractive regime, the tip is pulled towards the surface as a result of interaction force (i.e.Van der Waals. electrostatic). In spite of the fact that the pure force is attractive, the contact between the sample and tip may be occurring. In the second, repulsive, regime, there is actual contact between the sample surface and the tip. This causes the cantilever to bend upward.

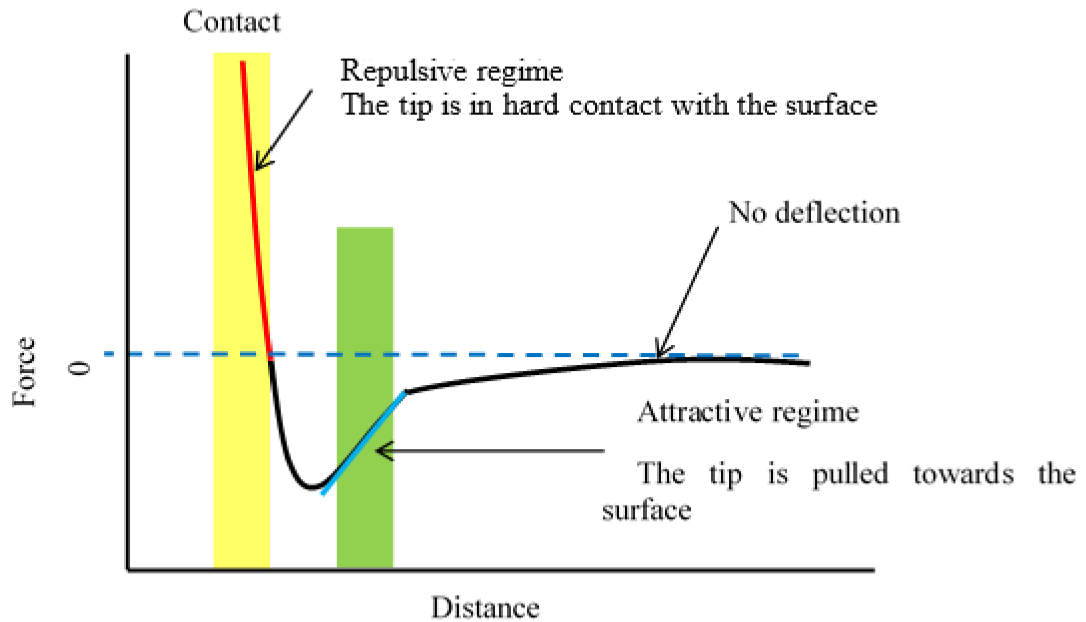

Figure 2.4 Interatomic force vs. distance curve

The three basic modes of operations mentioned earlier are only briefly presented below. The in-depth description of each of them is outside the scope of this work. More advanced information can be found in many sources such as in (Baró and Reifenberger 2012, Bhushan 2011, Haugstad 2012, Hongshun 2014)

1- **Contact mode:** The first mode of operation invented for the AFM was contact mode. In this case, the tip scans the sample in close contact with the specimen surface. The contact mode can be implemented based on two different types of operation: constant-height mode or constant-force mode as shown in Figure 2.5 and as explained below:

- **Constant-height mode**: In this mode, the feedback loop is turned off and thus, the height of the Z-scanner is fixed. Only the deflection of the AFM cantilever is changed during scanning. In this case, surface topography data is generated only by measuring the variation of the laser beam reflected from the cantilever onto the PSPD. This mode is useful for small, high-speed atomic resolution scans. However, the risk of

damage to the tip is large because the interaction force between the tip and sample is not constant.

- **Constant-force mode**: This was the first and original mode of operation. In this case, the deflection of the cantilever is used as input to a feedback loop system that moves the Z-scanner up or down to control the height of the probe relative to sample surface. Keeping the vertical deflection signal constant allow higher resolution. However, the scanning or machining speed is limited by the response time of the feedback loop system. The variation in scanner input voltage (or Z-detector output signal) is accurately converted into changes in the height of the sample surface.

2-**Non-contact mode**: This mode was invented in 1987 (Martin *et al.* 1987) and offer unique advantages over the other AFM mode and STM. The soft sample can be scanned using this mode because of the repulsive force absent. However, in contact mode, very strong repulsive forces appear between the tip and the sample atoms. Moreover, it does not require conducting material like STM. The amplitude modulation is the principle of the AFM NC mode operation, where, the attractive inter-atomic force between the tip and the sample is ultizied for measuring the surface topography. The cantilever is oscillated at the resonant frequency in the attractive regime (refer to Figure 2.4). As the tip approaches toward the sample surface and hovers 30-150 Angstrom (Martin *et al.* 1987), the Van der Waals interactive force causes changes in both the amplitude and the phase of the AFM probe vibration. Thus, the feedback control loop monitors such variations in amplitude and induces corresponding motions of the Z-scanner to keep the amplitude constant.

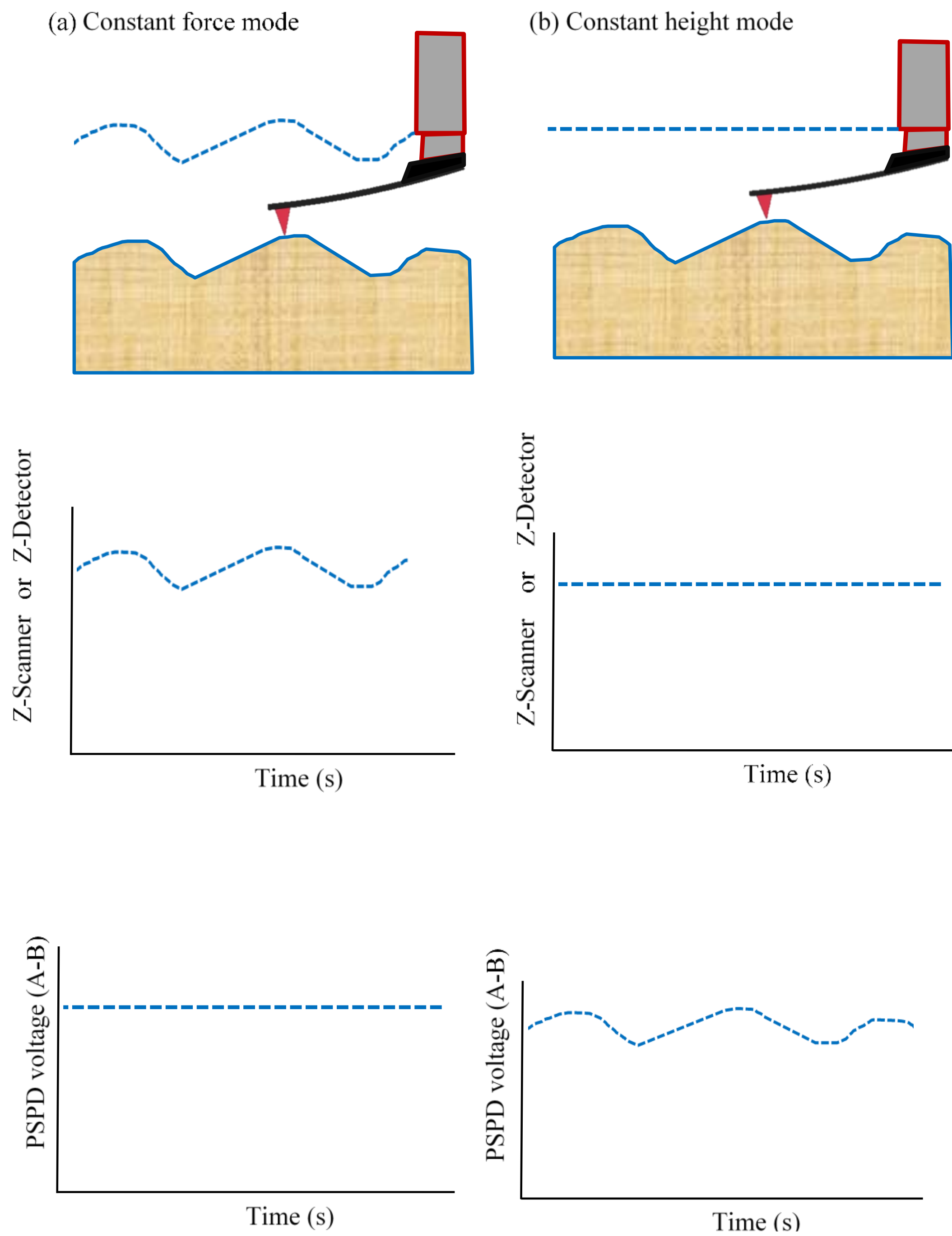

Figure 2.5 Different implementations of the contact mode: (a) constant-force mode and (b) constant-height mode

3-Tapping mode: In some contact and non-contact mode cases, the tip sticks to the sample surface because the z-scanner performance is not sufficiently high. Thus, the feedback loop moves the tip quickly away from the sample surface to increase the distance; as a result, the lateral resolution is significantly reduced. To overcome this issue as well as problems associated with friction, adhesion and electrostatic forces, Zhong proposes “tapping mode” in order to avoid tip sticking on the sample surface by making a large vibration amplitude of the cantilever oscillation (Zhong *et al.* 1993). The tip oscillation is then moved toward the sample until the AFM tip lightly touches or taps the surface as shown in Figure 2.6. Because of energy loss due to the tip contacting, the AFM tip oscillation must be decreased. The reduction in cycle oscillation amplitude is used to characterize and measure surface features.

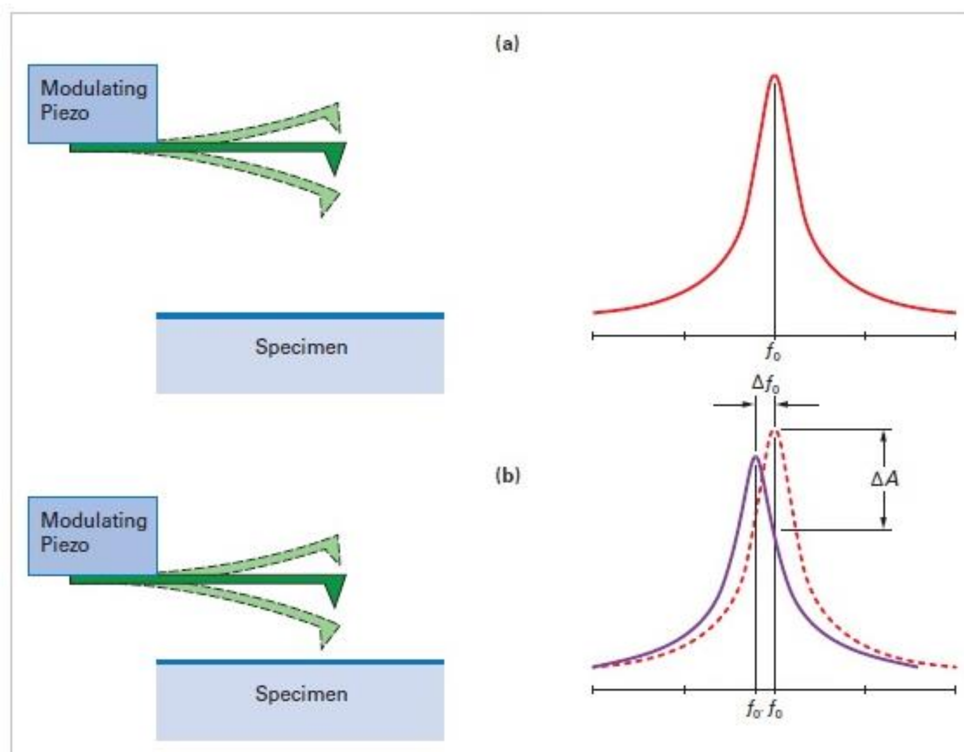

Figure 2.6 Schematic illustration of the tapping mode (Bruker nano system 2012)

2.3 AFM-tip-based nano mechanical machining

A few years after the invention of the AFM, researchers attempted the surface modification of substrates by increasing on purpose the interaction force between the tip and the work piece surface. When a certain threshold is reached, this force is sufficient to scratch the material. As a result, a part of the material is removed or displaced from the specimen surface following a pre-defined path, leaving behind a groove. In the literature, this process is also called scribing, scratching or machining. Initial reports of research studies implementing AFM tip-based nanomachining operations date back from the early 1990s (Jin and Unertl 1992, Jung *et al.* 1992, Kim and LIEBER 1992). Since these early attempts, many studies have been published where implementations of the process have been reported. A variety of specimen materials have been successfully scratched using AFM tip-based nano machining. These include polymers (Gozen and Ozdoganlar 2010, Li *et al.* 2010, Martin-Olmos *et al.* 2012, Teixeira *et al.* 2007, Zhang and Dong 2012), silicon (Khurshudov *et al.* 1996, Santinacci *et al.* 2003), metal (Fang and Chang 2003, Sumomogi *et al.* 1995, Versen *et al.* 2000a, Yan *et al.* 2007), oxides (Lu *et al.* 2010), semiconductors (Santinacci *et al.* 2001, Zhao *et al.* 2001, Zhao and Bhushan 1998) and biomaterials (Firtel *et al.* 2004, Muir *et al.* 2006). In addition, different types of tip materials have been investigated such as silicon tip (Kato *et al.* 2001, Schumacher *et al.* 1995, Teixeira *et al.* 2007), and silicon nitride tip (Jin and Unertl 1992, Tseng *et al.* 2005). The quality of the machined grooves depends on the tip geometry during scratching and both silicon and silicon nitride tips have limitations. Silicon tips suffer from wear which increase relatively quickly with time and cause a reduction in the accuracy of the produced channels. High tip wear also leads to a reduced repeatability to produce scratches. Indeed, differences in tip geometry due to wear can result in different stress distribution in the contact area for a given vertical probe deflection and thus, for a given normal load (Hassani and Aghabozorg 2011, Hu *et al.* 1998). To overcome this issue, the tip life can be increased by coating its surface with hard materials (Tseng *et al.* 2005) such as diamond (Santinacci *et al.* 2001) or diamond-like carbon (DLC) (Jiang *et al.* 2011a).

As a result of the numerous studies published in the past two decades where the tip-based nano machining process had been employed, a few state-of-the-art reviews have

been published recently in this specific field (Tseng 2011), (Yan *et al.* 2015), (Yan 2016). In this thesis, it is not intended to replicate yet another review. Instead, the focus of this section is to present the main challenges which are still faced by the research community for improving the predictability and accuracy of the process. In particular, these challenges stem from the fact that a flexible probe is used as the cutting tool to implement the process. As a result, the following four main issues, which will be expanded upon in the following sub-sections, have been identified:

1. Imprecise control of the groove depth;
2. Knowledge of scratching mechanisms;
3. Influence of the curvature of the deflected shape of the cantilever;
4. Understanding of the tip cutting angles.

2.3.1 First challenge: Control of the groove depth

In traditional machining, the edge of the cutting tool moves along a well-controlled path to insure that the workpiece is machined at a desired depth. In this case, the cutting edge geometry is known a-priori and constant throughout the machining process. However, for AFM tip-based nano mechanical machining, the geometric configuration of the cutting tool, i.e. of the AFM probe tip, cannot be considered to be constant. In particular, it should depend on the relative direction of cutting as well as the elastic bending and torsion of the cantilever. Thus, the resulting depth of the groove may vary even though, the V_{A-B} voltage corresponding to the vertical deflection of the cantilever is controlled and kept constant via the feedback loop of AFM instruments. Moreover, the depth of groove may be affected by the cutting conditions and workpiece material. Mostofa *et al.* 2013

To minimise this issue, a number of researchers have studied the effect of different factors on the outcome of AFM scratching operations. The relationship between the cutting parameters (i.e. the cutting velocity and the applied force) and the depth of groove were investigated by Mostofa *et al* (2013). Based on experimental trials conducted on a soda-lime glass workpiece, the authors found that the depth of groove exhibited a nonlinear relationship with the applied normal force, as shown in Figure 2.7.

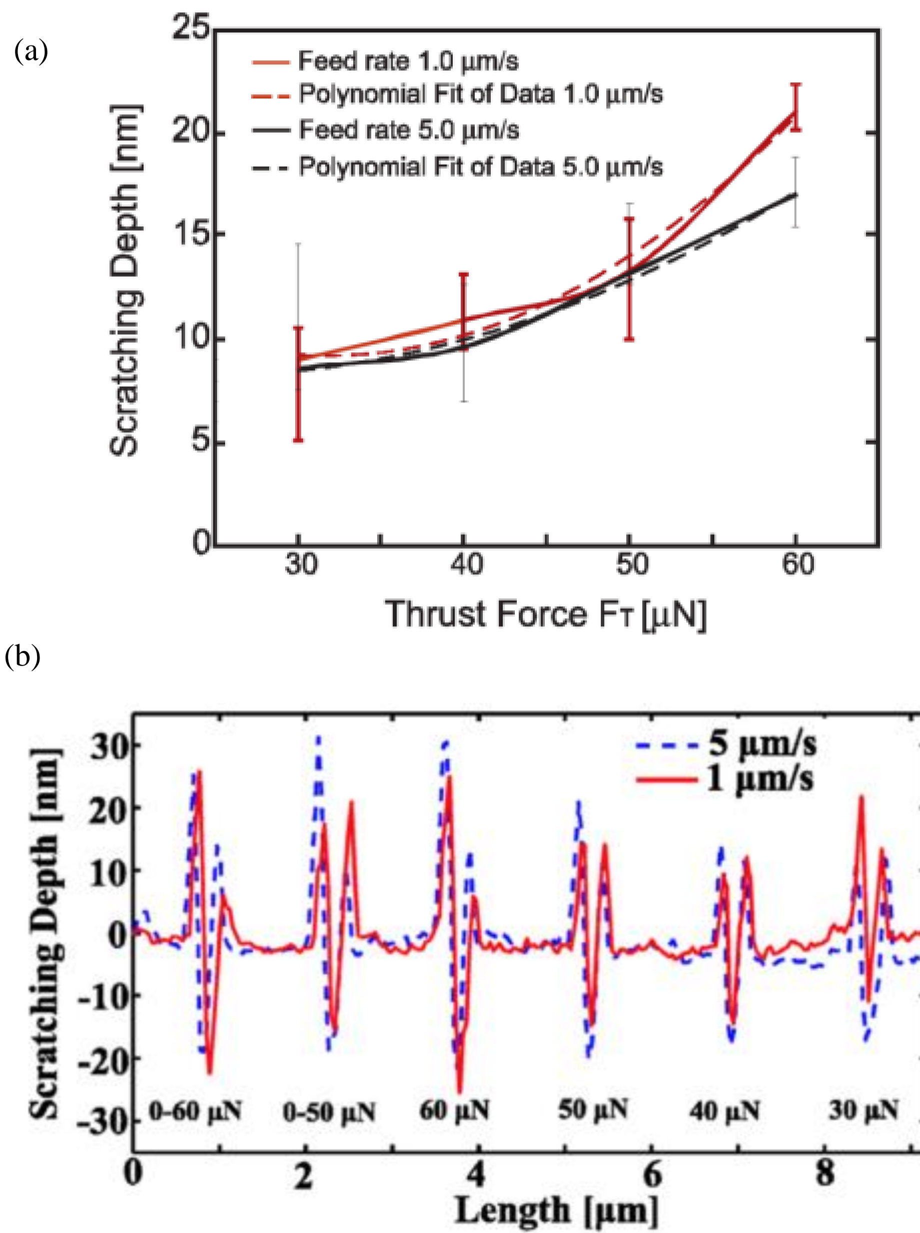

Figure 2.7 a) Scratching depths with variation in the normal force and feed rate; (b) scratch depths with pile-up heights for different loads (Mostofa *et al.* 2013)

The influence of the applied force on the groove geometry was investigated on the soft thin films of PMMA polymer coated on two substrates, silicon and glass, as well as another studied on the PE substrate (Hassani *et al.* 2010, Hassani and Aghabozorg 2011, Sadegh Hassani *et al.* 2008a, Sadegh Hassani *et al.* 2008b). The thickness of thin film coating was scanned using an AFM and found to be approximately 150nm. The PMMA thin film was scratched by using the AFM single crystal probe. The experimental observations of these studies show that increase in the applied force produced deeper groove. Moreover, the depth of groove exhibited linearly with increasing applied force as shown in Figure 2.8. Moreover, the depth of the groove on PMMA/silicon is lower than that obtained on the PMMA/glass substrate for identical process parameters. In the studies from Tseng et al. (2009) and Tseng (2010), the scratching characteristic of permalloy (NiFe) and silicon were investigated by using AFM diamond –coated silicon probe. The permalloy was deposited on the Sio_2/Si with a thickness about 32 nm. The results shown that the logarithmic relationship was found experimental between the depth of grooves and the applied normal force as shown in Figure 2.9. The depth of groove for permalloy was approximately seven times larger the depth of the Si substrate at the same applied force. The indium phosphide crystal was machined with AFM sharp diamond tip along <110> and <100> crystal directions in order to study the influence the crystal orientations on the plastic deformation groove size (Huang *et al.* 2013). The investigations show that the depth of groove in <100> orientation was always smaller than in the <110> direction due to the dislocation locking in this direction as shown in Figure 2.10.

(a) PMMA/Silicon

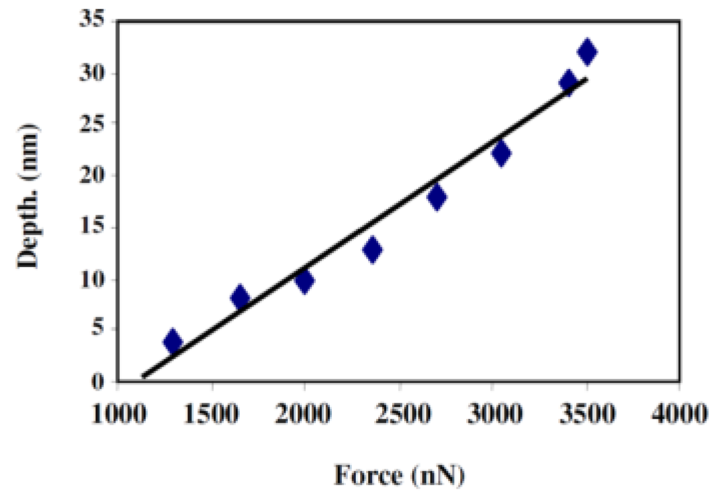

(b) PE

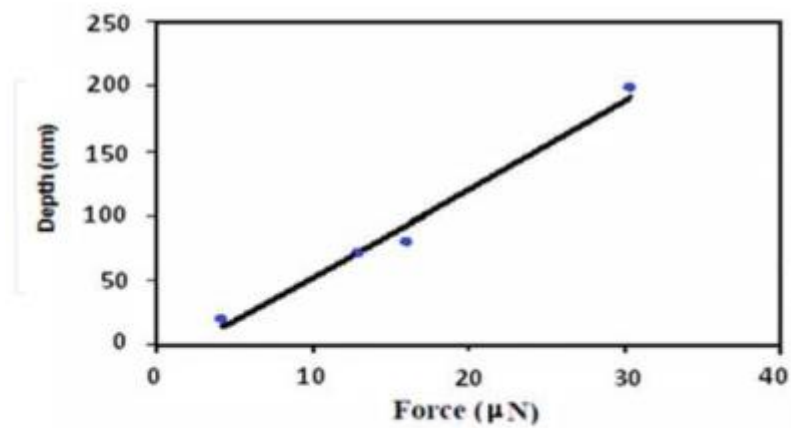

(c) PMMA/glass

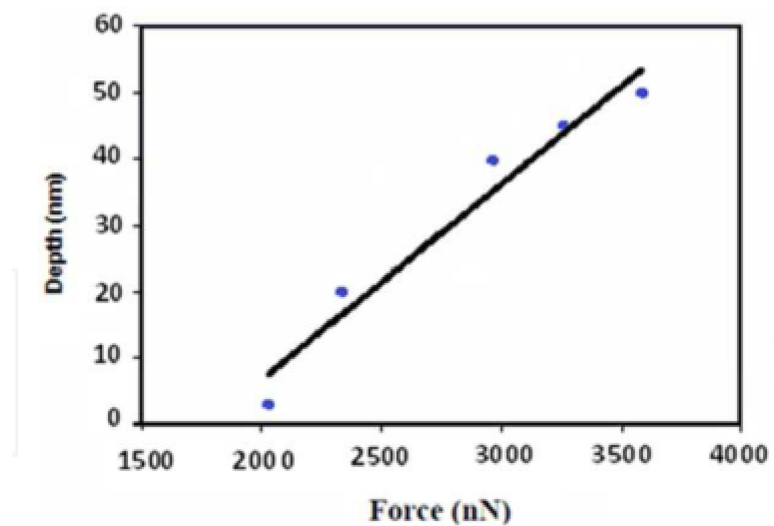

Figure 2.8 The relationship between the depth groove and normal force for (a) PMMA/Silicon (b) PE and (c) PMMA/glass (Hassani and Aghabozorg 2011)

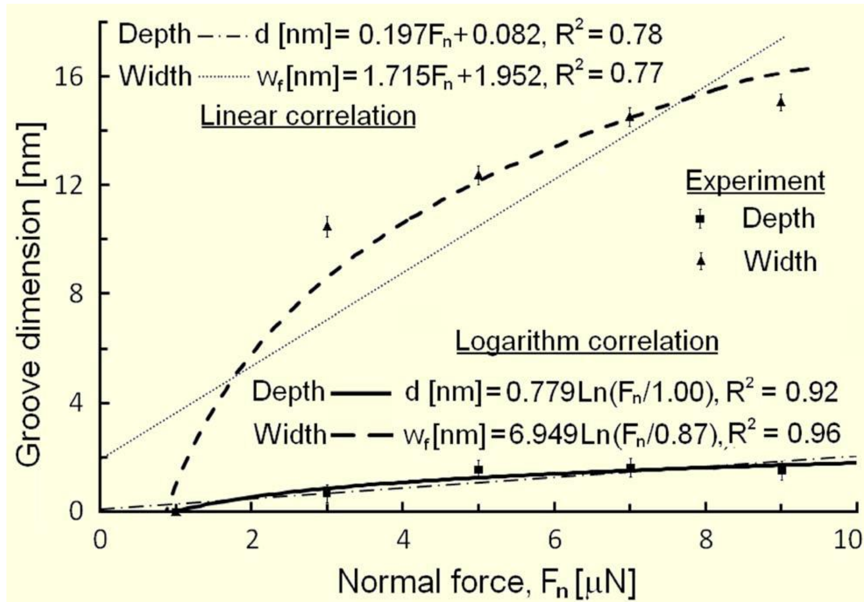

Figure 2.9 The relation between the groove dimensions and applied load for Si substrate (Tseng *et al.* 2009a)

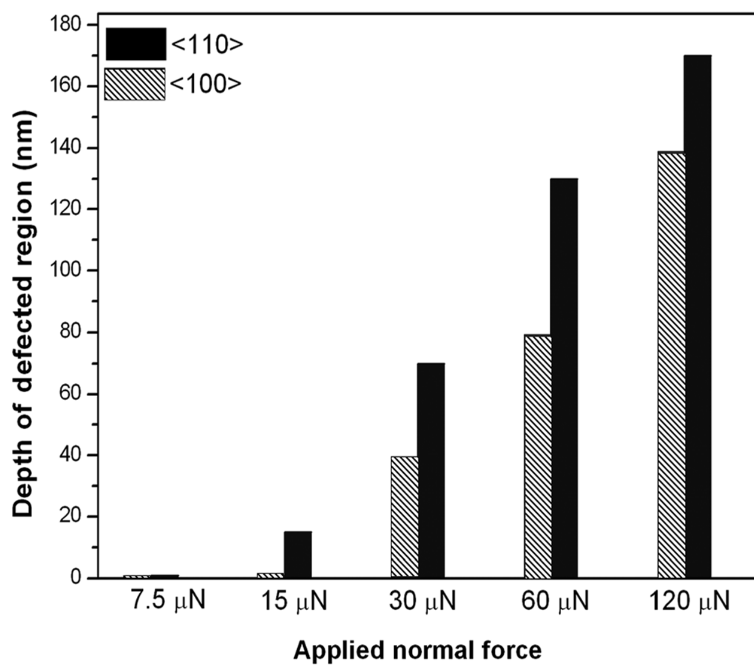

Figure 2.10 Depth of grooves at various applied load on the InP crystal (Huang *et al.* 2013)

The AFM scratchings were conducted on an aluminium film, which coated on a silicon substrate with thickness greater than 500nm to avoid film-substrate interfacial effects (Fang *et al.* 2000). In this study, the diamond tip radius was 15 nm, and the scribing direction was perpendicular to the long axis of cantilever (lateral direction). The normal loads applied by the tip onto the sample ranged between 4 µN and 20 µN, while the range of the scribing cycles was between 10 to 500 cycles. A nonlinear relationship was found between the depth of cut and the applied load. The higher value of applied force created a deeper groove. On the other hand, the increasing of tool pass reduced surface roughness as reported in Figure 2.11. The influence of the velocity and applied force of the AFM machining was studied using AFM diamond tip on metallic mask, which deposited on the a Si substrate (Fonseca Filho *et al.* 2004). The depth of groove reduced when the scratches speed increase. On the other hand, the increasing applied force produced a deeper groove as shown in Figures 2.12 and 2.13. The scratching speed or number of scratches was conducted using a diamond tip on the Al-surface. In investigations conducted by (Hassani and Aghabozorg 2011, Jiang *et al.* 2011a), it was shown that increasing the scratching speed caused a reduction in the depth of grooves. However, AFM scratching was performed on the Si surface with a diamond –coated tip by applied load less than 9 µN (Ogino *et al.* 2008). It was concluded that there is no effect of the scratching speed on the groove size.

From previous studies, it can be concluded that,they have neglegted the influence of mechanical behaviour of cantilever on the groove geometry.

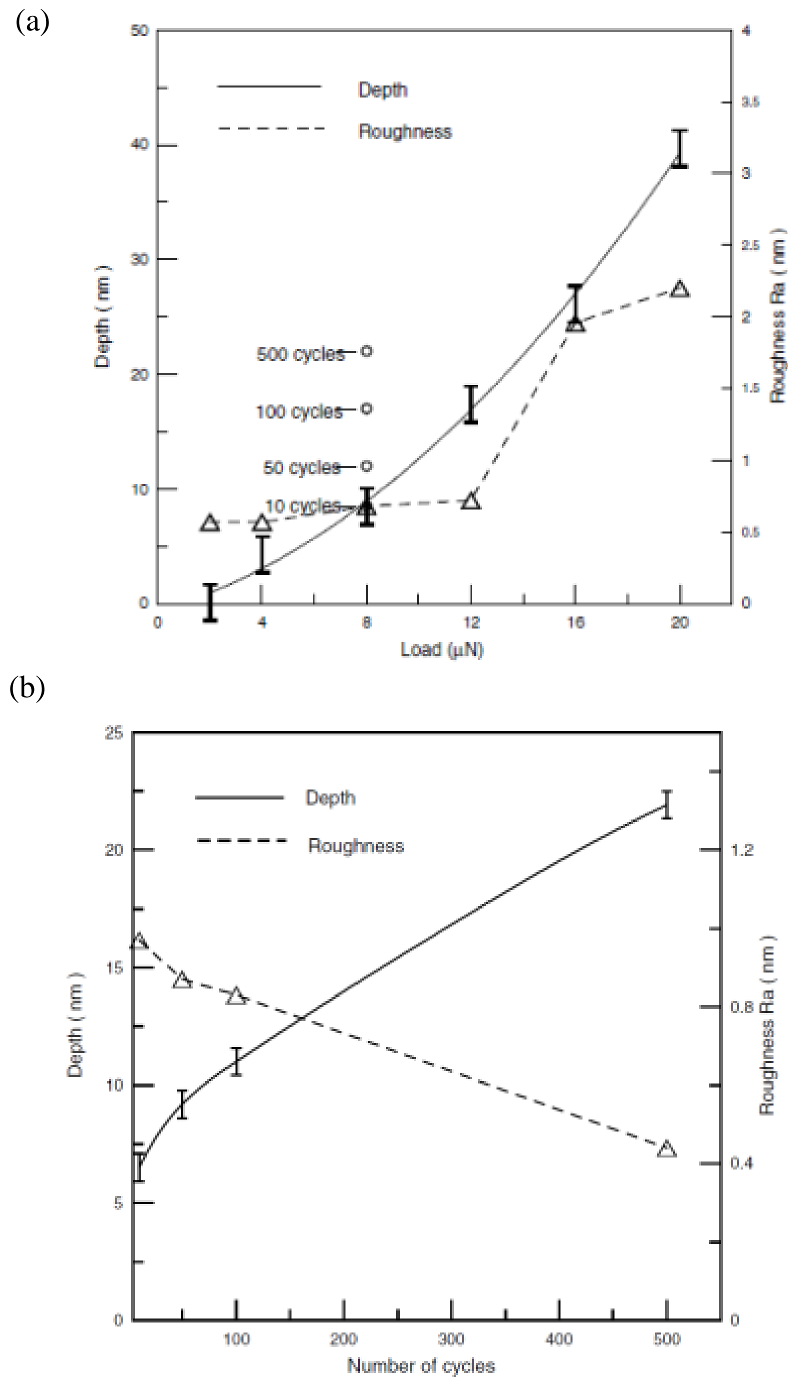

Figure 2.11 (a) influence of applied load on depth of groove and surface roughness (b) the effect of the cycles number of both depth and roughness of groove (Fang *et al.* 2000).

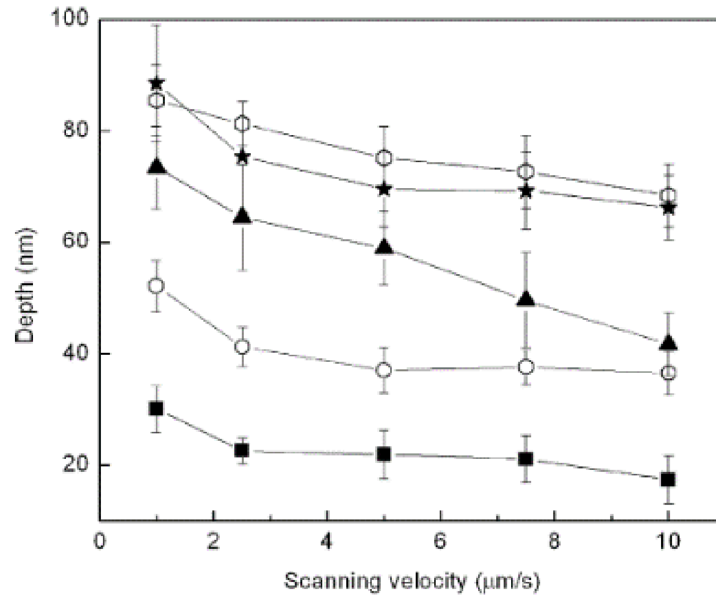

Figure 2.12 The influence of cutting speed on the depth of groove. The square, circle, triangle, hexagon and star symbols show the applied force at 30.5, 26.7, 19.1 and 15.2 μN respectively (Fonseca Filho *et al.* 2004)

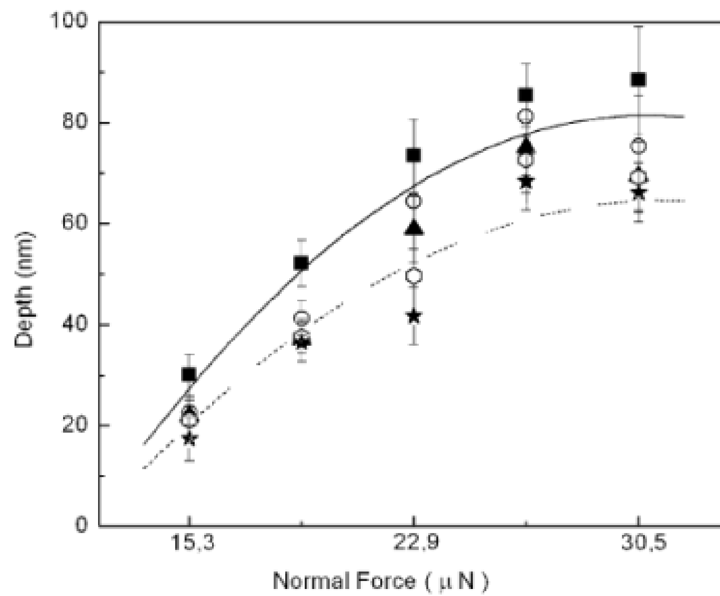

Figure 2.13 The influence of applied force on the depth of groove. The square, circle, triangle, hexagon and star symbols show the cutting speed force at 1, 2.5, 5 and 7.5 μm/s respectively (Fonseca Filho *et al.* 2004)

2.3.2 Second challenge: Understanding of scratching mechanisms

The mechanical interaction between an AFM probe tip and a workpiece leads to several regimes of material deformation depending on the processing conditions as demonstrated in an early study from (Zhang and Tanaka 1997). In particular, using molecular dynamics simulation, these authors showed that four distinct regimes of deformation exist when sliding a moving diamond asperity with a tip radius of a few nm over a copper surface, namely no-wear, adhering, ploughing and cutting. They reported that the transition between these regimes is governed by the tip radius, the speed and the engagement depth of the diamond asperity as well as the degree of lubrication or contamination at the diamond-copper interface. In the no-wear and adhering regimes, only elastic deformation takes place. This is the conventional regime for an AFM scan when the instrument is used to measure the surface topography of a sample in contact mode. Plastic deformation occurs in the other two regimes. The ploughing regime is characterised by some of the workpiece material being pushed out on the edges of a machined groove and some being compressed under the tip and recovering back after the tip passes (Elkaseer and Brousseau 2013). The occurrence of this mechanism is well documented and explained in the literature on micro mechanical machining. As illustrated in Figure 2.14, ploughing takes place when the engagement depth of the tip is below a certain value of the undeformed chip thickness. This value is conventionally referred to as the minimum chip thickness. In particular, no chips are formed and material is not physically removed from the workpiece (although plastic deformation can still occur) if the uncut chip thickness is less than this critical value (Liu *et al.* 2004). For example, the minimum uncut chip thickness was found about 12.5 to 14.5 nm for soda-lime glass (Mostofa *et al.* 2013). In the cutting regime, a chip is formed through the shearing of the workpiece material. If the tip engagement depth is equal to or just above the minimum chip thickness, this can be accompanied by a small amount of elastic recovery as reported by (Chae *et al.* 2006) in the case of micro machining and observed experimentally for AFM tip-based machining by (Elkaseer and Brousseau 2013). For fixed values of tip radius, cutting speed and surface lubrication or contamination conditions, (Zhang and Tanaka 1997) also predicted that the transition from the ploughing to the cutting regime occurs by increasing the engagement depth of the diamond tip.

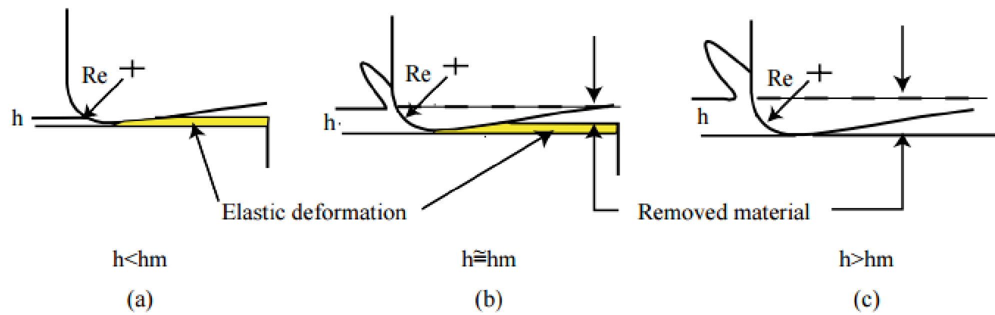

Figure 2.14 Schematic of the effect of the minimum chip thickness (Mostofa *et al.* 2013)

This regime transition is a direct consequence of overcoming the minimum chip thickness effect. In addition, it was observed experimentally in (Ahn and Lee 2009) that the height of the material being pushed out on the edges for the ploughing regime is inversely proportional to the depth of the groove when machining a silicon workpiece with a 100 nm radius AFM probe tip coated with diamond. As the processing regime moves from ploughing to cutting, the ratio between the height of such pile-ups and the depth of the grooves decreases and material starts being removed from the workpiece in the form of chips.

Investigations have been shown that it is possible to implement the AFM based-nano mechanical machining along different processing directions namely; forward, backward, and lateral refer to Figure 2.15 when considering the relative displacement of the tip over the material surface (Jiang *et al.* 2011a, Sun *et al.* 2013). The researchers, who investigated the process on a silicon specimen, experimentally reported three material removal regimes when using a sharp diamond tip. Firstly, with an applied normal force of at least 14μN, a sharp tip and while machining in the lateral direction, (Santinacci *et al.* 2001) reported that the scribing took place in the ploughing regime. In a separate experiment, machining was reported to occur for normal loads higher than 40μN by (Zhao and Bhushan 1998) based on the observation of coarser chip-debris. In this case, the tip radius was 160 nm and the direction was orthogonal to the axial axis of the cantilever. By

increasing the load to approximately 190 μN, these authors found a transition to brittle behaviour, which resulted in a poorer surface finish (Zhao *et al.* 2001). Yan et al. (2009) investigated specifically the effect of tool geometry and direction of scratching on the mechanism of AFM nanomachining on a single crystal silicon surface. The tip was a three side pyramidal diamond with a radius of 30 nm. The results showed that as the tip moved along the long axis of cantilever in the backward direction, the process displayed a cutting behaviour, whilst in forward direction; it exhibited a ploughing mechanism as clearly shown in Figure 2.16.

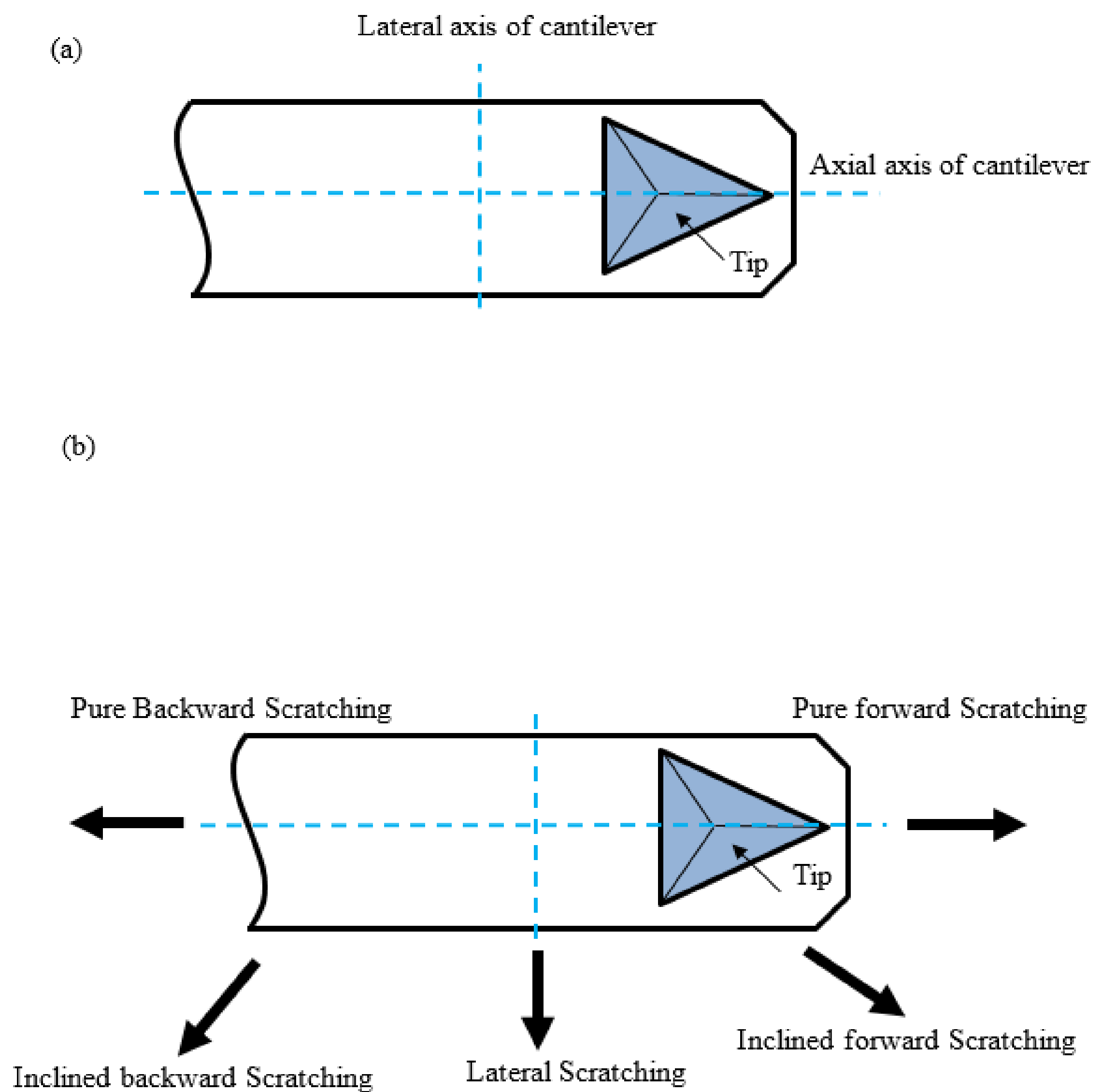

Figure 2.15 Schematic of the cantilever axes and direction motion (a) Main axis of cantilever (b) The direction of tip motion relative to main axis

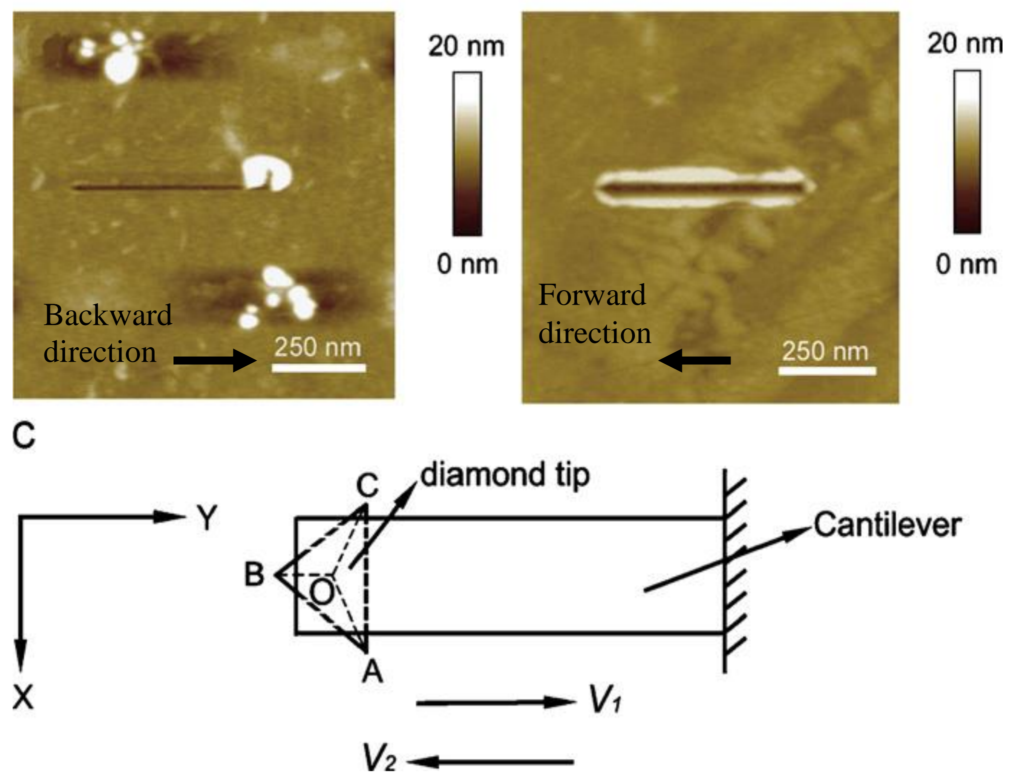

Figure 2.16 Effects of tip geometry on materials removal states along the scratching direction (Yan *et al.* 2009).

2.3.3 Third challenge: Influence of the curvature of the deflected shape of the cantilever

For the conventional cutting process, the components of a machine tool suffer from elastic deformation because of the kinematic linkage between the motion of the cutting tool and the sample, which is subjected to various cutting forces. Therefore, the machine tool components such as the tool holder are designed to be rigid (i.e. $K_1 \approx K_2$) as presented in Figure 2.17.

In AFM tip-based nanomechanical machining, the AFM tool holder is a flexible cantilever and in this case $K_1 << K_2$ (see Figure 2.17). Thus, the AFM scratching process is not achieved with a rigid tool. Besides, the V_{A-B} voltage output of the PSPD is controlled via the feedback loop of the AFM system for the purpose of keeping a constant normal force between the tip and the sample. In this case, the AFM instrument is operated under the force controlled mode as mentioned earlier. However, the fact that machining operations are performed with a non-rigid cutting tool and thus, the understanding of the mechanical behaviour of the cantilever, is often neglected in AFM-based machining studies. As mentioned in the previous section, the AFM nanomachining can be used in different directions. Two of these directions, which are typically found in the literature, are illustrated in Figure 2.15. The current body of experimental and theoretical studies, which investigated the process is relatively large as reported earlier. The displacement along the "forward direction", which is the terminology adopted from (Jiang *et al.* 2011a), is of particular interest (see Figure 2.18). Indeed, for this direction, it is generally assumed, such as in (Geng *et al.* 2013b, Geng *et al.* 2014, Hassani and Aghabozorg 2011, Malekian *et al.* 2010, Ruan and Bhushan 1994) that the bending of the cantilever is concave as illustrated with Figure 2.18b. Thus, from a theoretical point of view, there is no a-priori reason to make this assumption. Indeed, the deformed shape of the cantilever during AFM tip-based nanomachining along the forward direction should depend on the particular loading conditions acting on the tip.

The cantilever shape deflection could be affected by several factors such as the workpiece material, the applied normal force, direction of scratching and the dimension of the cantilever itself. This issue will be studied in detail in this research.

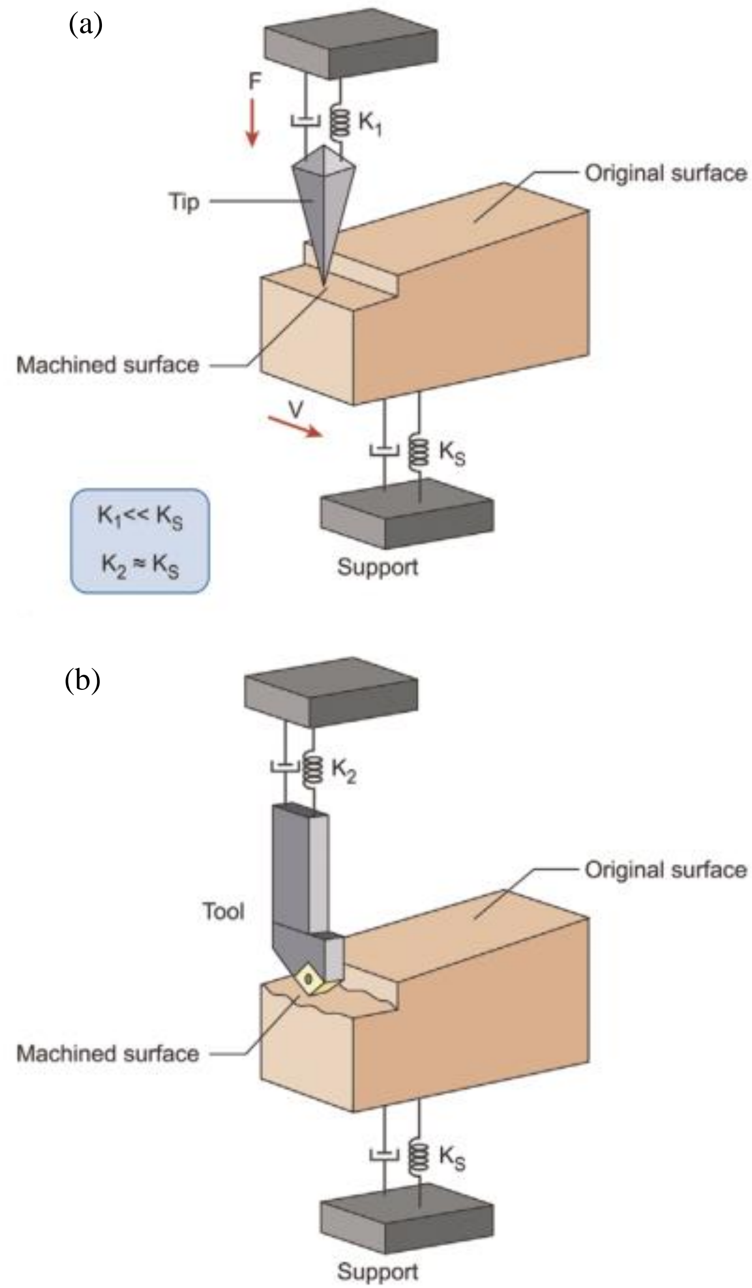

Figure 2.17 a) schematic of the AFM tip-based nano mechanical machining system b) schematic of the conventional cutting system (Yan *et al.* 2015)

(a) Top view

Possible directions of motion along the long axis of the cantilever:

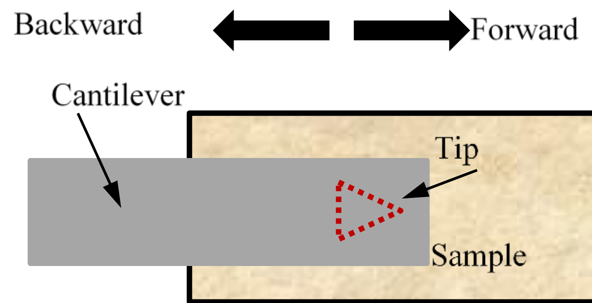

(b) Side view

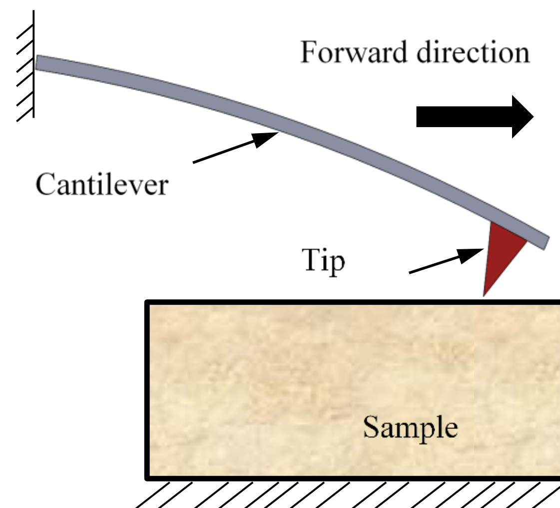

Figure 2.18 (a) Illustration of the backward and forward AFM tip-based machining directions using a top view perspective and (b) side view of the commonly assumed concave cantilever deflection when processing in the forward direction

2.3.4 Fourth challenge: Understanding of the tip cutting angles

In macro machining, there are two established tool geometries, namely the ISO and ANSI standards. According to these standards, two types of systems can be considered when describing the tool geometry, namely, the *Tool–in–hand System (T-hand-S)*, and the *Tool–in-use System (T-use-S) (Astakhov 2010).* The *T-hand-S* relates to the static geometry of the tool, whilst the *T-use-S* is based on the consideration of the tool motion with respect to the sample. The analysis of tool angles for both of these systems assumes that the tool holder is rigid. However, for AFM tip-based nanomachining, the tool holder is a flexible cantilever. Thus, using such flexible tools raises complexity when analysing the cutting angles. For example, the rake angle of a flexible tool varies as a function of the cantilever deflection and of the direction of scratching.

Previous investigations have established that a worn tip increases the friction force between the sample surface and the tip (Bhushan and Kwak 2008, Tao and Bhushan 2006). Moreover, a worn tip with a large apex radius produces a shallower groove for a given applied load (Yan *et al.* 2012).

The influences of the cutting angles (rake, wedge angle and inclined angle) on the deformation of the cantilever were investigated in micro-machining by (Herrera-Granados *et al.*). The operating system was proposed similarly to the AFM, where a sharp tool fixed at the free end of a flexible cantilever as shown in Figure 2.19. The experimental results conducted that the effects of rake angle on the mechanism of micro machining are similar to traditional cutting. The authors recommended that the rake face angle should be used between the -15° to 0°, because of the not-rigid body of the cantilever.

Thus, the fourth challenge arise from the fact that the probe is actually flexible tool. Consequently, the tool geometry (i.e. angles and radius) may be changed depending on the cantilever deflected shape and the direction of scratching. Thus, the issue will be studied in detail in this thesis.

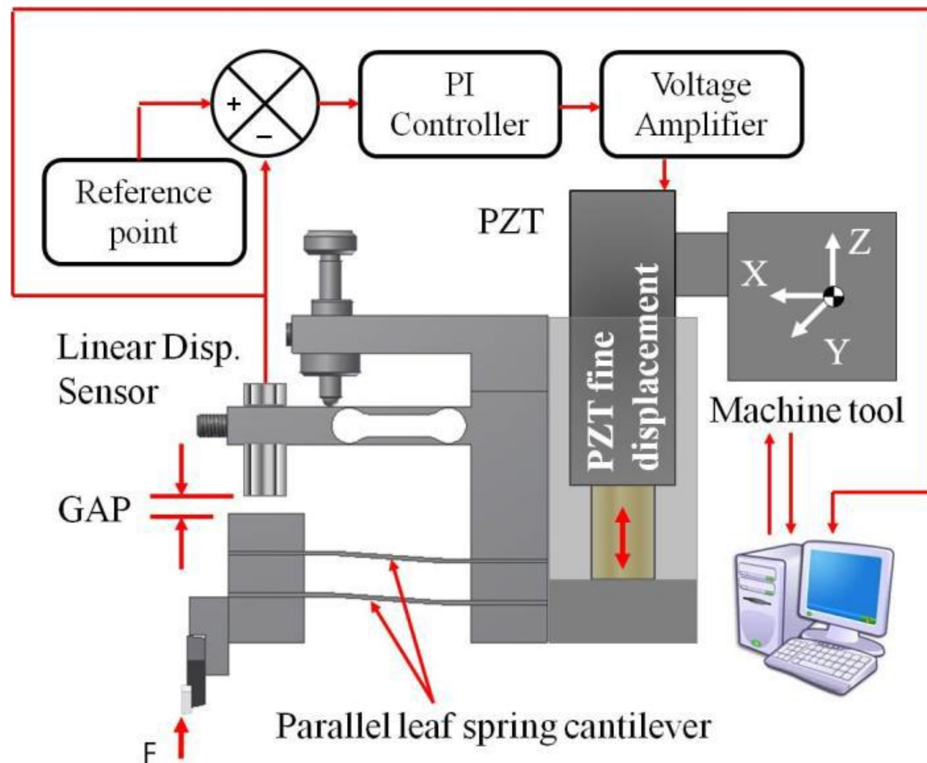

Figure 2.19 Constant load cutting mechanism with control loop (Herrera-Granados *et al 2014).*

2.4 Force measurements during AFM probe-based machining

As with all conventional machining process, e.g. turning, end milling, ball end milling, etc., many studies have been carried out to predict the cutting forces. An understanding of the cutting forces during machining is important to analyse the effect of process inputs, such as cutting conditions and tool geometry, on process outcomes such as machining stability, tool wear and tool breakage. Based on such analysis, the tool life and surface quality can be optimised by choosing suitable machining conditions.

In the field of AFM-based nanomachining, the study of cutting forces is also a critical aspect that should be considered when attempting to understand the material processing mechanisms that result from the interactions between the workpiece surface and the AFM tip. Moreover, such a study can provide insightful information to achieve better process performance, less tip wear and higher throughput. To conduct such a study, it is important

to define first the different force components which are present during the process along different directions. As illustrated in Figure 2.20(a), when the tip describes a horizontal motion in the axial plane, it is subjected to two force components, namely the axial force, F_a, which is parallel to sample surface and measured in the axial plane and the normal force, F_n, which is perpendicular to the sample surface. When the tip motion is perpendicular to the longitudinal axis of cantilever, two force components are generated, as shown in Figure 2.21(b), namely the lateral force, F_L, which is perpendicular to the axial plane and parallel to the sample surface and the normal force, F_n. Thus, in the subsequent sub-sections, currents approaches reported in the literature to assess such normal, lateral and axial force are presented.

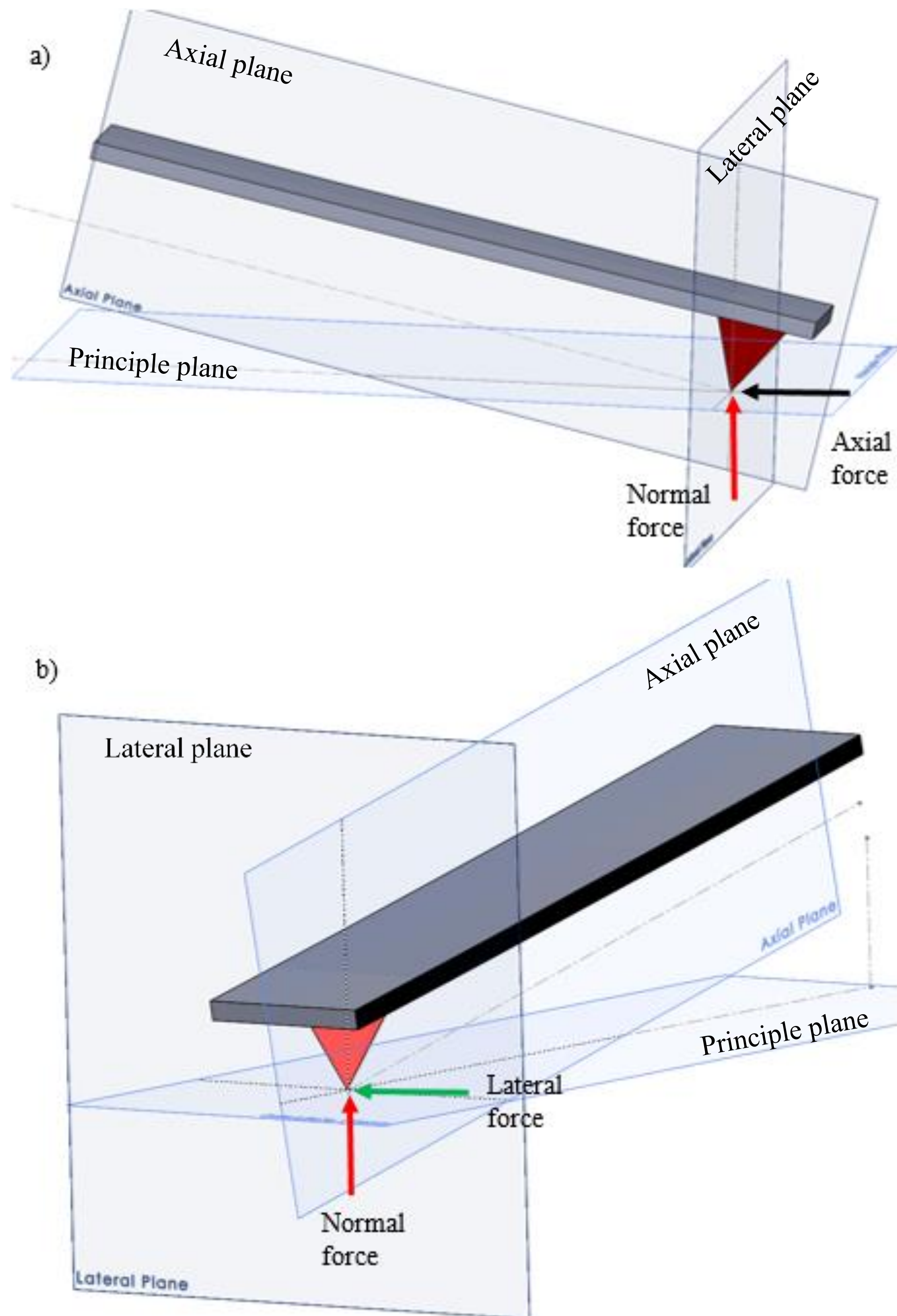

Figure 2.20 Schematic of the different planes and axes based on the geometry of an AFM probe along (a) the forward direction and (b) the lateral direction of the probe movement

2.4.1 Determination of the normal force, F_n

As described previously, the tip is mounted at the end of the cantilever (which is assumed as a spring). In this case, the tip-specimen force follows Hooke's law (Butt *et al.* 2005, Ducker *et al.* 1992), and depend on the spring constant of the cantilever and the distant between the tip an sample. Thus, the normal force F_n can be described as follows;

$$F_n = K.\delta_n \tag{2.1}$$

where *K* is the spring constant (N/m) of the cantilever and δ_n is the vertical deflection (m) at the free end of the cantilever. Based on AFM components, the force sensor is relied on the optical level method. Thus, F_n can be obtained by converting the output of the $V_{A\text{-}B}$ voltage vertical deflection as follows (Butt *et al.* 2005, Ducker *et al.* 1992).

$$F_n = K.S_n.V_{A-B} \tag{2.2}$$

where V_{A-B} is the PSPD voltage (V) and S_n (m/V) is normal sensitivity of the PSPD. Thus, measuring the normal force relies on the determination of two constants, namely *K* and S_n. A number of methods have been proposed to determine the spring constant of cantilevers as reviewed by (Clifford and Seah 2005). In this research, the widely used method from Sader et al (1999) is adopted to assess the spring constant of the cantilever used. In the following section, the conventional method used to calibrate S_n and its associated drawback is presented.

2.4.1.1 Calibration of the normal sensitivity of the PSPD, S_n

The calibration of the normal sensitivity can be achieved by approaching and lightly pressing the tip onto the surface of a hard substrate (such as sapphire, which has a Young's modulus of about 435GPa) and then lifting the tip back. During this process, both the $V_{A\text{-}B}$ signal and the displacement of the Z scanner are monitored. Given the fact that this procedure is realised on a hard surface and that the tip is only pressed gently on this surface, it can be assumed that the Z scanner displacement corresponds to the deflection of the probe. In this way, the slope, m, of the curve $V_{A\text{-}B}$ against δ_n can be obtained as illustrated in Figure 2.22. The normal sensitivity is equal to the inverse of this slope and thus, it is expressed as follows:

$$S_n = \frac{1}{m} = \frac{\delta_n}{V_{A-B}} \quad (2.3)$$

However, in all commercial AFM systems, the cantilever is generally fixed in the AFM head at a certain inclination angle defined between the long axis of the cantilever and the sample surface. This is to ensure that only the tip is in contact with the sample surface and not some parts of the cantilever as a result of its deflection. From the analysis of the literature, it is reported that the range of values for this angle is generally comprised between 7° and 20°. Based on published literature, it is also reported that the combined influence of the cantilever geometry and of this inclination angle is normally not taken into account when determining the applied normal force. Thus, the focus of Chapter 5 is to present a refined theoretical model to determine this force component when the AFM stage is static by considering the influence of the inclination angle and of the cantilever geometry.

Moreover, as mentioned previously, the determination of the normal force during the motion of the tip across the sample surface is normally carried out by assuming the absence of any horizontal force components. For this reason, the study reported in Chapter 5 also aims at investigating the validity of this assumption. Based on the findings reported in Chapter 5, the objective of Chapter 6 is to propose a novel approach to measure the normal force acting on the tip when conducting the AFM tip-based nanomachining process along different directions. The next section presents the current approaches, which have been reported in the literature to assess the axial force, F_a, and the lateral force, F_L.

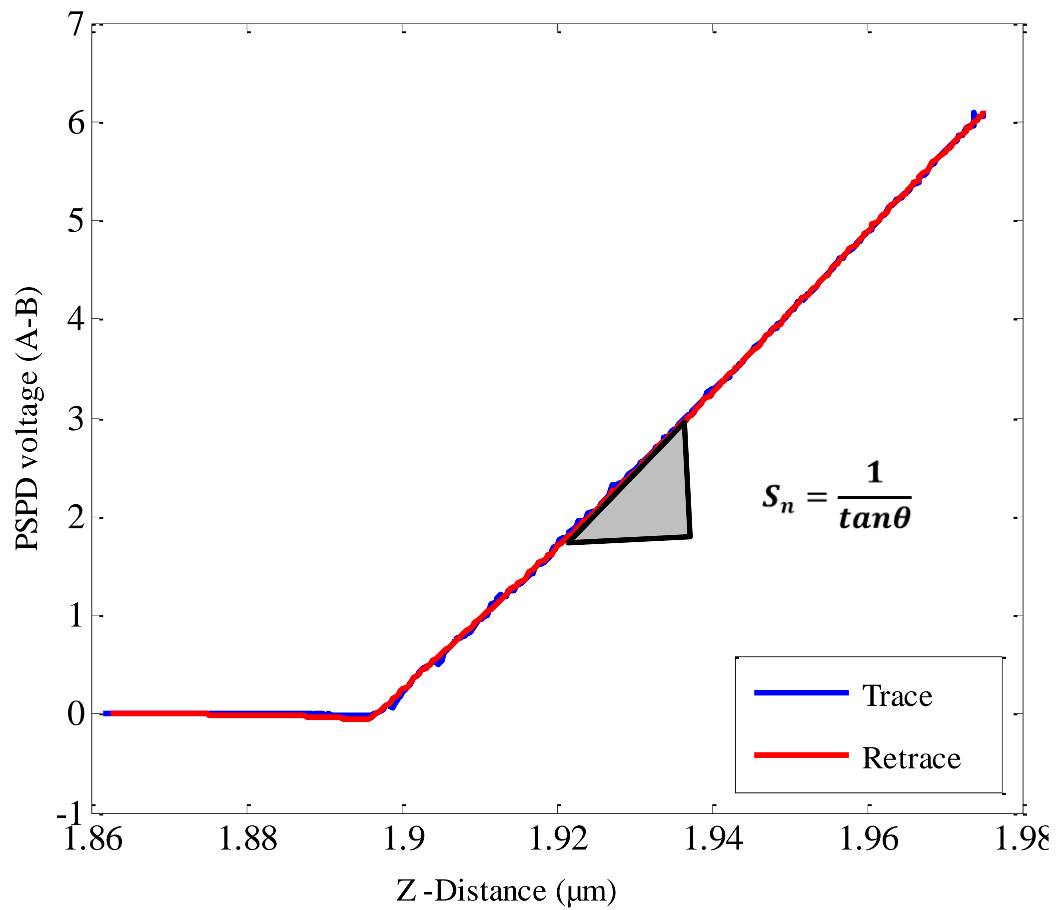

Figure 2.21 Illustration of the evolution of $V_{A\text{-}B}$ as a function of the displacement of the Z scanner during the calibration of the PSPD normal sensitivity

2.4.2 Determination of the lateral force, F_L

When the sample moves relative to the tip, the assessment of the lateral force becomes more complex. The calibration of the AFM force sensor to extract F_L during the process is a nontrivial task because the lateral sensitivity of the PSPD is more difficult to determine than the normal sensitivity. Prior to the start an AFM tip-based nanomachining operations, the calibration procedure to measure the lateral force typically includes two steps (Feiler *et al.* 2000). First, the relationship between the torsional angle of the cantilever and the lateral response of the PSDP must be established. Second, the torsional spring constant of the cantilever must be also be determined. Only a few methods have been presented in the literature to perform this type of calibration. These are reported below.

The most commonly employed approach for this purpose is the wedge method (Ogletree *et al.* 1996). The method relies on scanning a sample, which exhibits both flat and sloped surfaces with known angles with a constant normal force (Wang and Zhao 2007). This enables the measurement of the difference in friction forces between the flat and the sloped surface as shown in Figure 2.22a. A friction loop can thus be obtained by plotting the lateral voltage $V_{C\text{-}D}$ against the lateral position of the tip, for a reciprocating scan as shown in Figure 2.22b. Calculation the friction coefficient, μ_w, with this method can be realised based on the following expression ;

$$\sin\theta(L\cos\theta + A)\mu_w^2 - \frac{\Delta_{slope} - \Delta_{flat}}{W_{slope}}(L + A\cos\theta)\mu_W + L\sin\theta\cos\theta = 0 \tag{2.4}$$

where θ is the angle of the sloped surface; L is the applied load (N); A is the adhesive force (N) ; Δ_{slope} is the offset from the friction loop (V) in slope surface of sample; , W_{slope} is the half width of friction loop (V) in the slope surface of sample and Δ_{flat} is the offset from the friction loop (V) in flat surface of sample. Solving this equation gives two value of μ_w. Using these two values in equation 2.5 gives two value α

$$\frac{\mu_W(L + A\cos\theta)}{\cos^2\theta - {\mu_W}^2\sin^2\theta} = \alpha W_{slope} \tag{2.5}$$

To find the value of the friction coefficient on the flat surface μ_{flat}, the two value of α substitute in equation below

$$\mu_{flat} = \frac{\alpha \, W_{flat}}{(L + A)} \tag{2.6}$$

To select the correcting value of the α, the coefficient of friction on the flat surface is compare with friction on the slope surface as following:

$$\langle |\mu_{W1} - \mu_{flat1}| < |\mu_{W2} - \mu_{flat2}| \rangle \tag{2.7}$$

If the result of above equation is true, the α_1 is correct, otherwise, the α_2 is correct

Once the lateral calibration constant is determined, the lateral force can be measured by using lateral equation as below.

$$F_L = \alpha \, V_{C-D} \tag{2.8}$$

where V_{C-D} is lateral voltage of the PSPD

Similarly, to the previous section, another approach has been used to determine the lateral force is theoretical. Based on Hooke's law, the lateral applied force, F_L, is described by

$$F_L = K_L . \delta_L \tag{2.9}$$

where K_L is the lateral spring constant of cantilever and δ_L is the lateral deflection of the cantilever. Based on the optical lever method, this deflection is expressed as follows:

$$\delta_L = S_L . V_{C-D} \tag{2.10}$$

where S_L is the lateral sensitivity of the PSPD (μm/v) and V_{C-D} is lateral voltage output,

Substituting equation 2.10 in 2.9, we get:

$$F_L = K_L . S_L . V_{C-D} \tag{2.11}$$

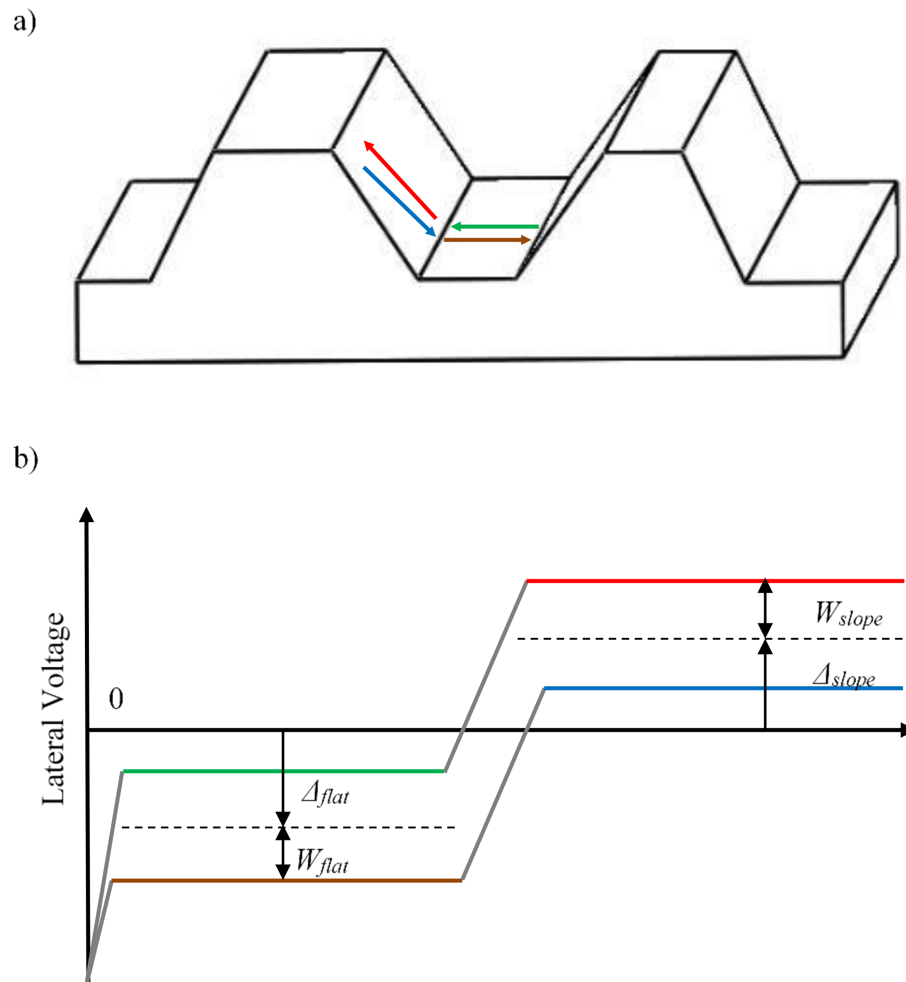

Figure 2.22 a) wedge sample and b) friction loop

In practice, both K_L *and* S_L are difficult to determine. Thus, these two constants are often combined and expressed as one parameter, which is called the lateral force calibration factor α (μN/v). In this way, the lateral force is expressed as:

$$F_L = \alpha . V_{C-D} \tag{2.12}$$

Therefore, the aim of a calibration method is to find this factor.

For cantilever with rectangular cross-sections, based on beam theory, the lateral spring constant is given by:

$$K_L = \frac{G.w.t^3}{3.L.(h+\frac{t}{2})^2} \tag{2.13}$$

where *G* is the shear modulus and *h* is the height of tip , t is the thickness of cantilever, L is the length of cantilever and h is the tip height.

Substituting equation (2.13) in (2.11) lead to

$$F_L = \frac{G.w.t^3}{3.L.(h+\frac{t}{2})^2}.S_L.V_{C-D} \tag{2.14}$$

The relation between the lateral sensitivity and normal sensitivity is given by (Liu *et al.* 2007);

$$S_L = \frac{E.(h+\frac{t}{2})}{2.G.L}.S_n \tag{2.15}$$

In this case, the PSPD is assumed symmetric rotationally, the shift of lateral beam by displacement φ in the up-down or left-right direction will produce same the photocurrent

$$F_L = \frac{G.w.t^3}{3.L.(h+\frac{t}{2})^2}.\frac{E.(h+\frac{t}{2})}{2.G.L}.S_n.V_{C-D} \tag{2.16}$$

By compare with equation 2.11, the lateral force calibration α can be found by

$$\alpha = \frac{E.w.t^3}{6.L^2.(h+\frac{t}{2})}.S_n \tag{2.17}$$

It is argued that the previously mentioned methods suffer from limitations when applied to the AFM tip-based nanomachining process. First, they assume that the normal force and the normal sensitivity stay constant during the tip motion. Second, they are not taking into account the mechanical behaviour of the cantilever as the AFM tip moves relative to sample. Moreover, the disadvantage of the theoretical approach reported in Liu et al (2007) is that it is restricted to cantilevers with perfectly rectangular cross sections, which is not the case in practice.

2.4.3 Determination of the axial force, F_a

When the sample moves in a direction parallel to the long axis of the cantilever, an axial force is generated on the tip. In this case, the generated axial force induces a moment on the free end of the cantilever. Thus, the accurate measurement of this axial force is necessary in order to better understand the tip-based nanomachining process. In constant force mode (Bhushan and Marti 2010) proposed a simple way to determine the axial force and the coefficient of friction between the sample and the tip when the probe moves in the axial plane. As shown in Figure 2.24, the direction of the axial force, F_a, is opposite to the direction of motion of the probe. (Bhushan and Marti 2010) assumed that the total moment, M_A, on the fixed end of the AFM probe is constant because the vertical deflection is kept constant during the scanning. This means that:

$$\sum M_A\ (forward\ direction) = \sum M_A\ (backward\ direction) \tag{2.18}$$

Based on this assumption and on the notations used in Figure 2.24, which were presented in (Bhushan and Marti 2010), these authors reported that:

$$(F_n - \Delta F_{n1})L + F_a l = (F_n + \Delta F_{n2})L - F_a l \tag{2.19}$$

thus

$$(\Delta F_{n1} + \Delta F_{n2})L = 2F_a l \tag{2.20}$$

And finally

$$F_a = \frac{(\Delta F_{n1} + \Delta F_{n2})L}{2l} \tag{2.21}$$

Where ΔF_{n1} and ΔF_{n2} are the absolute values of the changes in normal force when the sample is moved in the forward and the backward direction, respectively. L is the length cantilever a, *l* is the vertical distance between the tip end to the point *A*. As shown in Figure 2.24, if there is no effect of the adhesive force and the interatomic attractive forces between the sample and tip, the normal force F_n can be said to be equal to the initial cantilever deflection (i.e. H_o in Figure 2.24) multiplied by the spring constant of the cantilever. Thus, $\Delta F_{n1} + \Delta F_{n2}$ is equal $(\Delta H_1 + \Delta H_2)$ multiplied the cantilever spring constant.

Thus, the axial force can be found as follows:

$$F_a = \frac{K(\Delta H_1 + \Delta H_2)L}{2l} \tag{2.22}$$

The coefficient friction (μ) between the sample and tip is given as

$$\mu = \frac{F_a}{F_n} = \left(\frac{\Delta H_1 + \Delta H_2}{H_0}\right)\left(\frac{L}{2l}\right) \tag{2.23}$$

It is argued that the presented analysis has a number of limitations. First, the authors assumed that the axial force had the same magnitude in both the forward and the backward directions for an identical voltage output of the PSPD, i.e. $V_{A\text{-}B}$. However, this may not be the case for AFM tip-based nanomachining because it is expected that the rake angle should be different along both directions. In addition, AFM probes are not generally axis-symmetric. Thus, the contact area between the material and the tip should be different depending on the considered processing direction. Indeed, the authors neglected the influence of the axial force on the vertical deflection of the cantilever because they assumed, without supporting justification, that this deflection was kept constant during the process. However, it is argued that the reported experimental investigations were not sufficient to prove the validity of this assumption. Thus, this method may be not suitable for measuring the axial force during the AFM based nanomachining process.

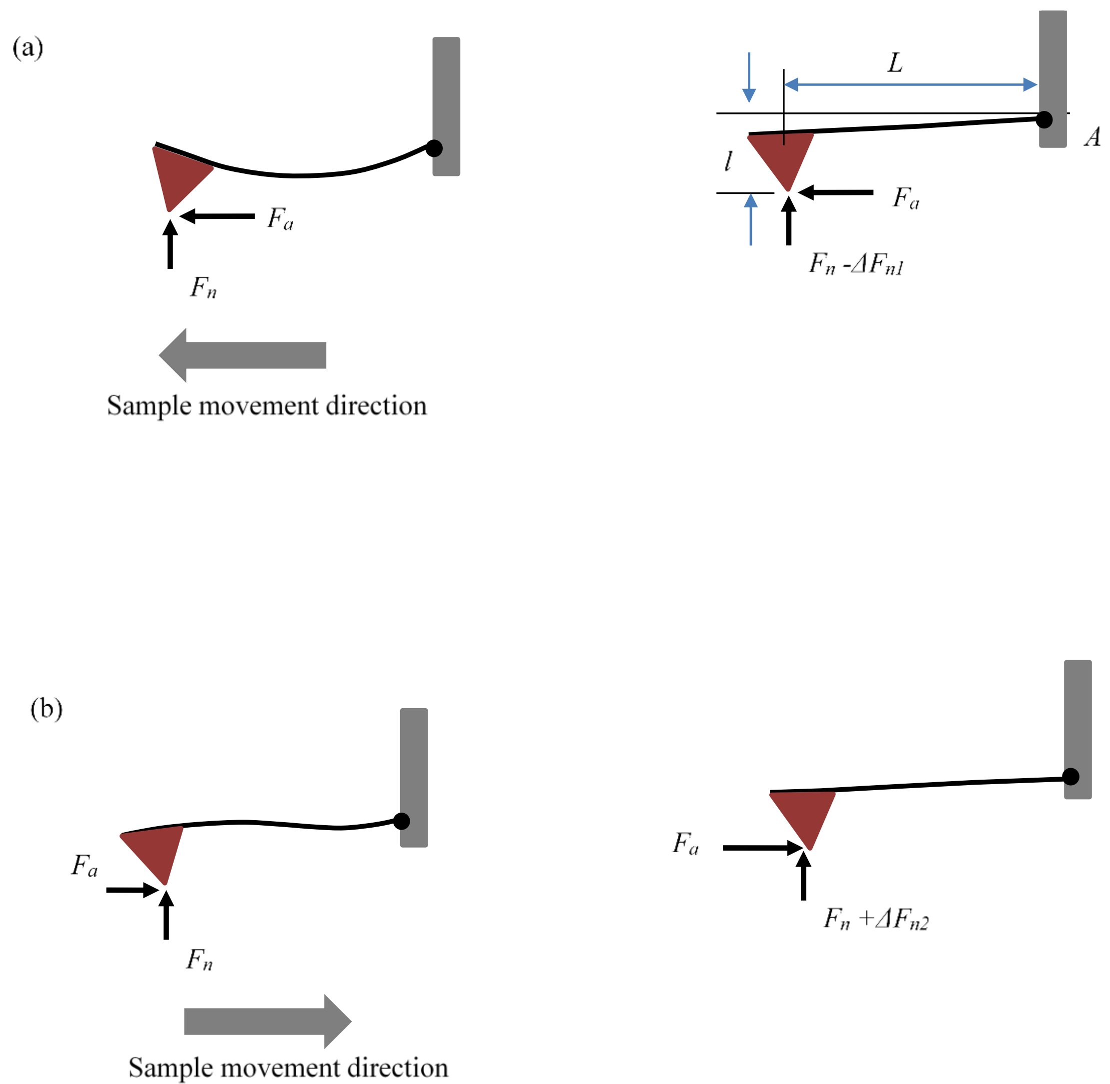

Figure 2.23 Schematic showing the cantilever deflected shape due to the axial force (a) during backward scanning and (b) forward scanning (adapted from (Bhushan and Marti 2010)).

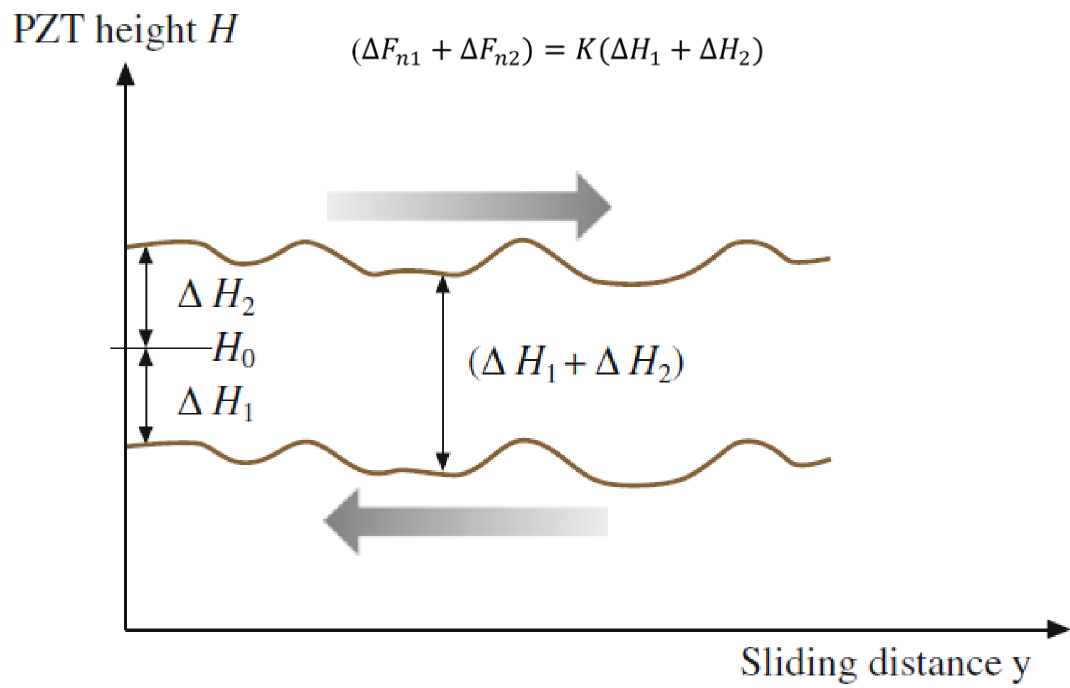

Figure 2.24 Schematic illustration the Z-scanner movement in both forward and backward scanning direction (from (Bhushan and Marti 2010))

2.5 Summary and identified knowledge gaps

In this chapter, the basic operating principle and key hardware components of AFM instruments were introduced first. Then, based on the body of literature in of AFM tip-based nanomachining, an analysis of previous studies was reported in the context of four research challenges, which are still current in this field. Following this, particular issues to acquire the accurate measurements of machining forces during the process were discussed. To complete this chapter, a summary of the identified knowledge gaps is now given below.

As it was reported in this chapter, a key issue faced by researchers when implementing AFM tip-based nano machining is to be able to predict the depth of a produced groove based on the particular combination of probe, workpiece material and processing conditions utilised, such as the relative orientation between the probe and the sample and the machining forces. Currently, the empirical trial and error approach is the conventional technique adopted to determine the machined depth as a function of such parameters. In practice, the achieved depth depends on the machining mechanism involved, which in turn depends on the orientation between the tip and the sample. Ultimately, this orientation depends on the deflected shape of the cantilever. However, the review of the literature presented here reveals that studies in this field neglected the fact that AFM probes should be considered as flexible tools when investigating the tip-based nanomachining process. Therefore, the main objective of this thesis is to focus on studying the influence of the quasi-static behaviour of AFM probe cantilevers on the process outcomes. In this context, the specific knowledge gaps that have been identified are as follows:

1. It is normally assumed that the bending of the cantilever is concave in the forward direction. However there is no a-priori reason to make this assumption. Indeed, the deformed shape of the cantilever during AFM tip-based nanomachining along the forward direction should depend on the particular loading conditions acting on the tip.

2. When the AFM stage is static, the combined influence of the cantilever geometry and of the tilt angle between the long axis of the cantilever and the sample surface is

generally not taken into account for determining the applied normal force. In practice, this leads to erroneous assessments of the normal load applied by the tip on the sample based on the voltage output of the PSPD.

3. When the stage is not static, i.e. during actual tip-based nanomachining operations, an axial force is also generated on the tip. This creates a moment on the free end of the cantilever. The influence of this moment on the normal force, vertical deflection and normal sensitivity of the PSPD has been neglected in tip-based nanomachining studies.

4. The above knowledge gap also means that current approaches have deficiencies for determining accurately the loads acting on the tips during nanomachining.

5. The last knowledge gap identified is that further investigations are required to explore the machining phenomena that lead to a given groove geometry as a function of the cutting conditions and their influence on the quasi-static behaviour of the cantilever.

Chapter 3

Experimental Setup

3.1 Introduction

The purpose of this chapter is to describe the experimental set-up and machining conditions implemented in this study. In particular, the specific methodology developed to gain insights into the quasi-static behaviour of AFM probe cantilevers during tip-based nano mechanical machining is described first. This description includes the atomic force microscope instrument utilised and the data acquisition set-up implemented. Then, the experimental conditions followed to perform the tip-based nanomachining tests are explained. Finally, the microscopy techniques utilised to characterise the topography of machined grooves are described.

3.2 Experimental platform

3.2.1 Atomic Force Microscope

The AFM instrument employed in this research is the XE-100 model from Park Systems (see Figure 3.1). The AFM is positioned on an active anti-vibration table (model TS 150 from Table Stable Ltd). In addition, it is located inside a full acoustic enclosure to eliminate noise and light interferences. In the XE-100 model, the Z-scanner is independent from the XY Scanner as shown in Figure 3.2. The XY scanner is fabricated from aluminium and is designed with a flexure hinge structure, which ensures highly orthogonal two-dimensional movement with minimal out-of-plane motion. The XY scanner has a range of motions which is 50 µm × 50 µm. The maximum movement of the probe in the Z direction relative to the specimen surface is limited by the range of motion of the Z-scanner range, which is 12 µm for the XE-100 AFM system. The vertical resolution of the Z-scanner is determined by the control unit and applied voltage to the Z-scanner.

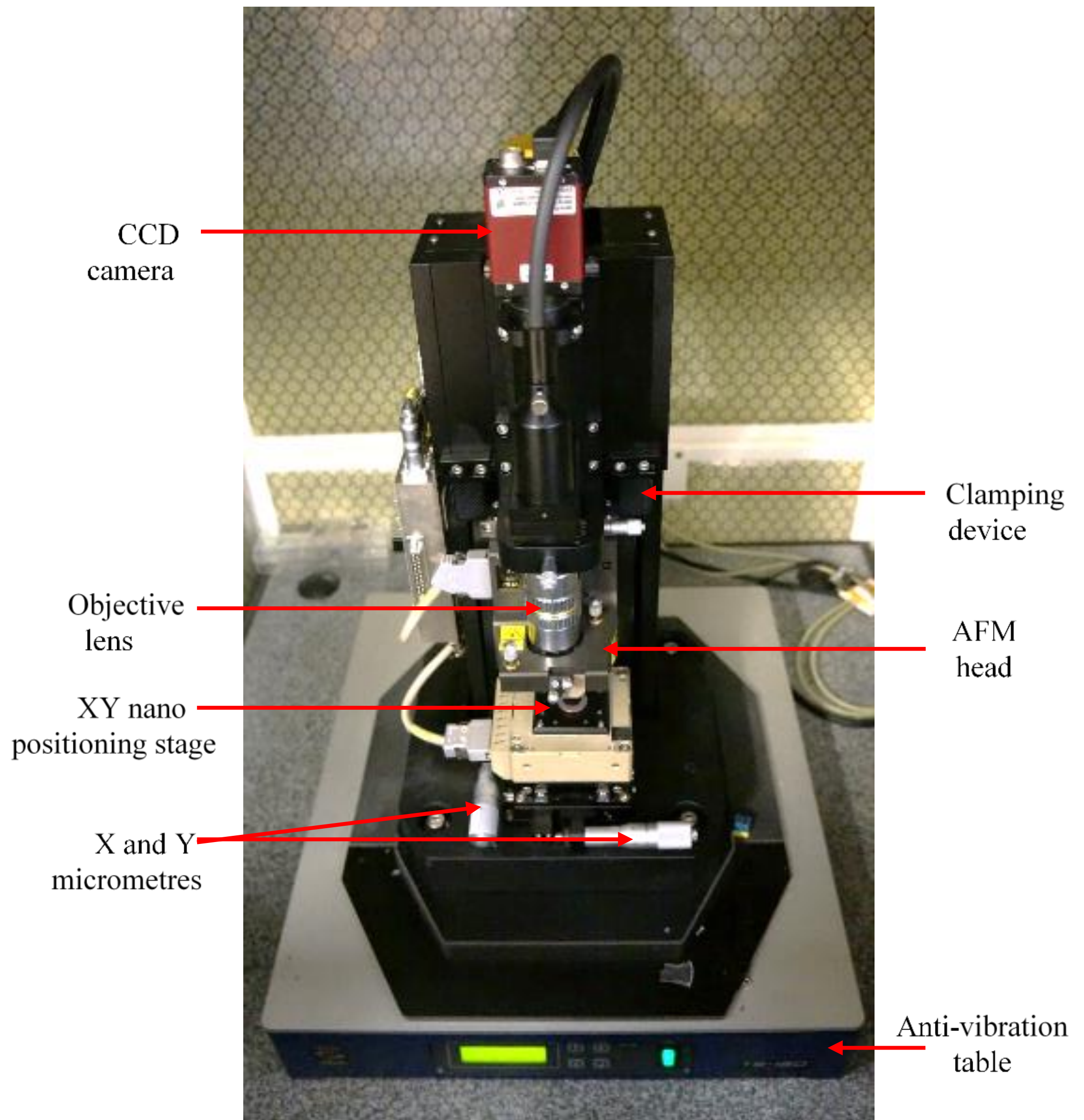

Figure 3.1 Park XE-100 AFM instrument

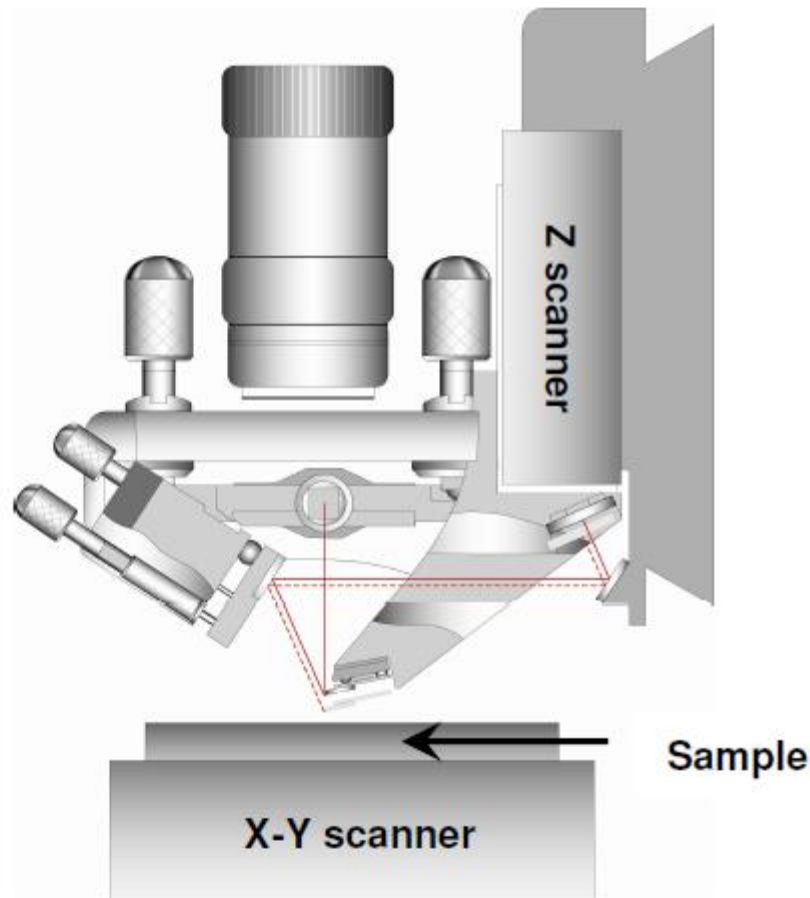

Figure 3.2 Configuration of the X-Y and the Z scanners (Park-systems)

3.2.2 Data Acquisition System

The complete data acquisition system (DAQ) was composed of the Signal Access Module (SAM) from Park Systems used in combination with a NI 9223 module from National Instrument and the LabVIEW software. The SAM can be utilised to access a number of signals when operating the AFM. In particular, it allows the monitoring of the voltage inputs sent by the controller to the piezoelectric actuators, which define the vertical motions of the Z-scanner and the horizontal displacements of the stage. In addition, the voltage outputs from the strain gauge mounted of the Z-scanner and from the PSPD can also be recorded. The NI 9223 module is connected to the SAM via BCN cable and provides four analog signal to be recorded at a sampling rate of 1MS/s per

channel. In Figure 3.3 the specific four output channels on the SAM to which the NI 9223 module was connected. In particular, the channels named “Y DET”, Z DET”, “LFM”, and “A-B(DC)” in this picture were utilised to record respectively 1) the horizontal motion of the stage, 2) the strain gauge output, 3) the “C-D” voltage and 4) the V_{A-B} voltage on the PSPD. Further physical interpretation of these four signals and the terminology adopted In the remainder of this thesis for each of them is given below:

The DAQ is connected to the computer via a USB interface as shown in Figure 3.4. In particular, this system was utilized to capture four outputs during the nano-machining operations as described below:

1) Y-detector signal. This corresponds to the voltage sent by the controller to the horizontal piezoelectric actuator that drives the in-plane motions of the AFM stage. Monitoring of this signal enables the accurate time determination of the beginning and end of nano-machining paths.
2) Z-detector signal. This voltage is provided by the strain gauge sensor, mounted on the Z scanner. Given that the Z-scanner defines the vertical displacement of the AFM probe, the monitoring of the Z-detector signal enables the assessment of the motions of the fixed end of the cantilever.
3) LFM signal. This corresponds to lateral bending of cantilever and it is provide by the lateral voltage ($V_{\text{C-D}}$) of the PSPD and used to monitor it.
4) A-B signal. This voltage output is given by the PSPD and it was used to monitor the vertical deflection of the free end of the probe cantilever.

The actual experimental set-up utilised in this research which comprises the different components presented in this section is illustrated in Figure 3.4 while a schematic description of the entire set-up is given Figure 3.5.

Figure 3.3 Signal Access Module from Park Systems

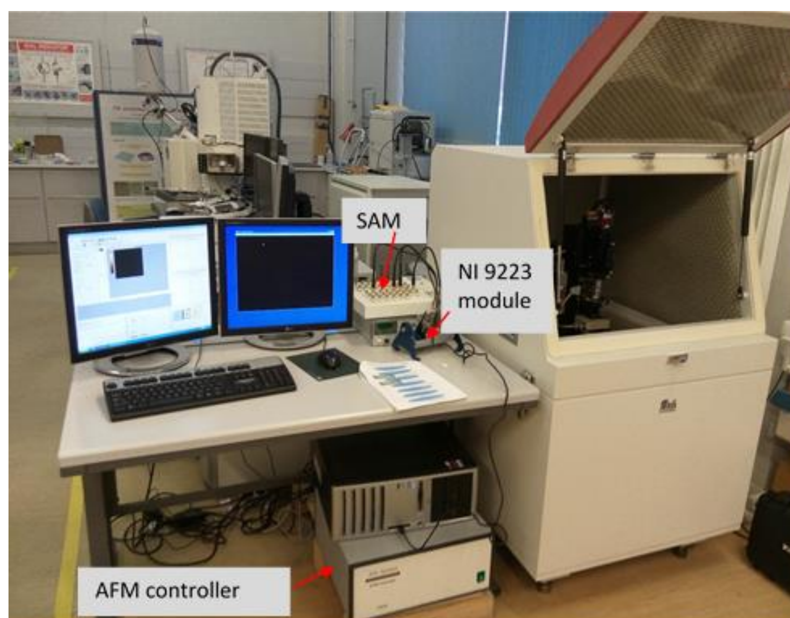

Figure 3.4 Actual experimental set-up

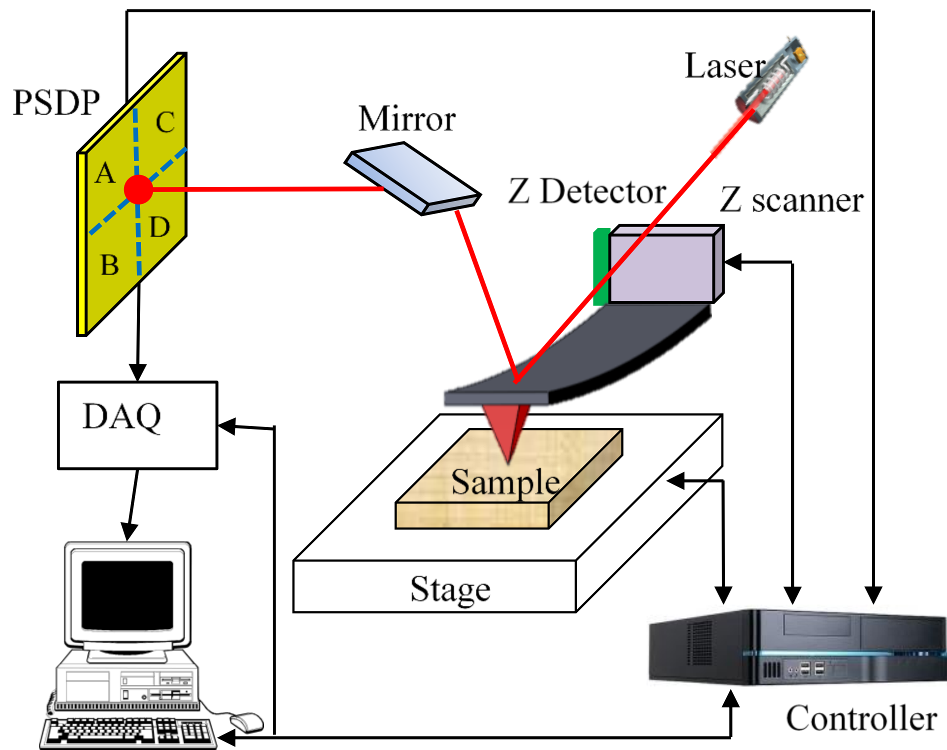

Figure 3.5 Schematic description of the AFM probe-based nano-machining set-up.

3.3 Operating conditions

3.3.1 Workpiece materials

A single crystal copper sample with 99.999 % purity was used as a workpiece. The majority of the experiments were performed on this sample. As reported in Chapter 4, another specimen made of polycarbonate (PC) was also employed to confirm the results observed with the copper workpiece. The Cu surface sample is prepared by polishing in order to use later in AFM based nano machining. The PC sample is produced by injection moulding polycarbonate. The surface roughness (R_a) of Cu and PC sample is measured by AFM scanning and it found 3.2nm and 6.2nm respectively.

3.3.2 AFM probes

The probe used for conducting the machining operations on the copper sample was the DNISP type from Bruker. Figure 3.6 shows SEM micrographs of this type of probes. Such probes are typically utilised for nano indentation and nano scratching tests since they are designed with a relatively high spring constant. In this study, the spring constant of the DNISP probe employed had been assessed by the manufacturer and reported to be 221 N/m. This probe had a rectangular cantilever made of stainless steel, while its tip was a 3-sided diamond pyramid formed by 3 right angle planes. The tip apex may be reasonably approximated by a sphere. In this way, it was determined to have a radius of 70 nm using Scanning Electron Microscopy (SEM) imaging.

In the case of the PC specimen, the nanomachining operations were conducted with a different probe. This was a TESPD type from Bruker (see Figure 3.7). For such probes, the tip is coated with a diamond-like carbon layer for increased tip lifetime. The particular TESPD probe utilised had a nominal tip radius of 15 nm. Its normal spring constant was determined using the Sader method (Sader *et al.* 1999) and found to be 56 N/m.

The specifications for the probes utilised during the nanomachining trials are given in Table 3.1 A third type of AFM probe, namely the CSG model from NT-MDT, was utilised after the nanomachining experiments for the purpose of recording the topography of the obtained grooves. This was done with the same AFM instrument (i.e. the XE-100 model from Park Systems) using its surface imaging functionality in conventional contact mode.

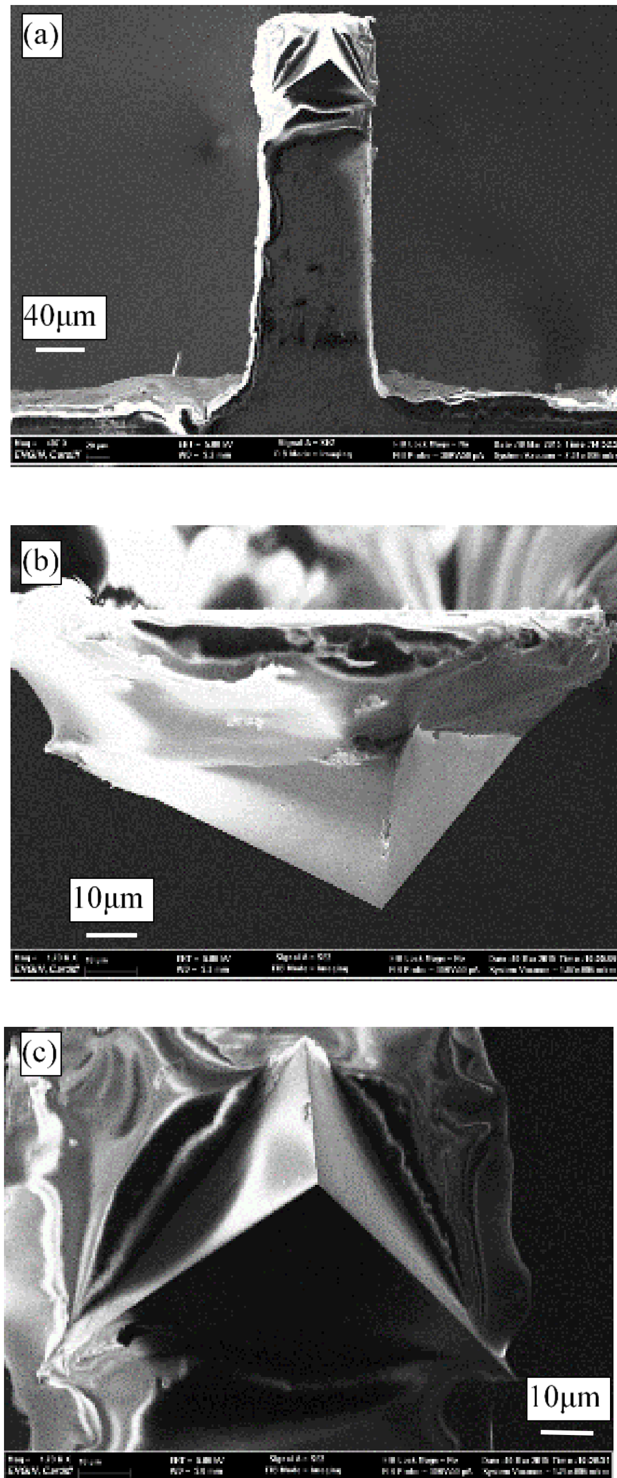

Figure 3.6 SEM micrographs of the utilised DNISP probes (a) top view of cantilever (b) side view of the tip apex (c) top view of tip apex

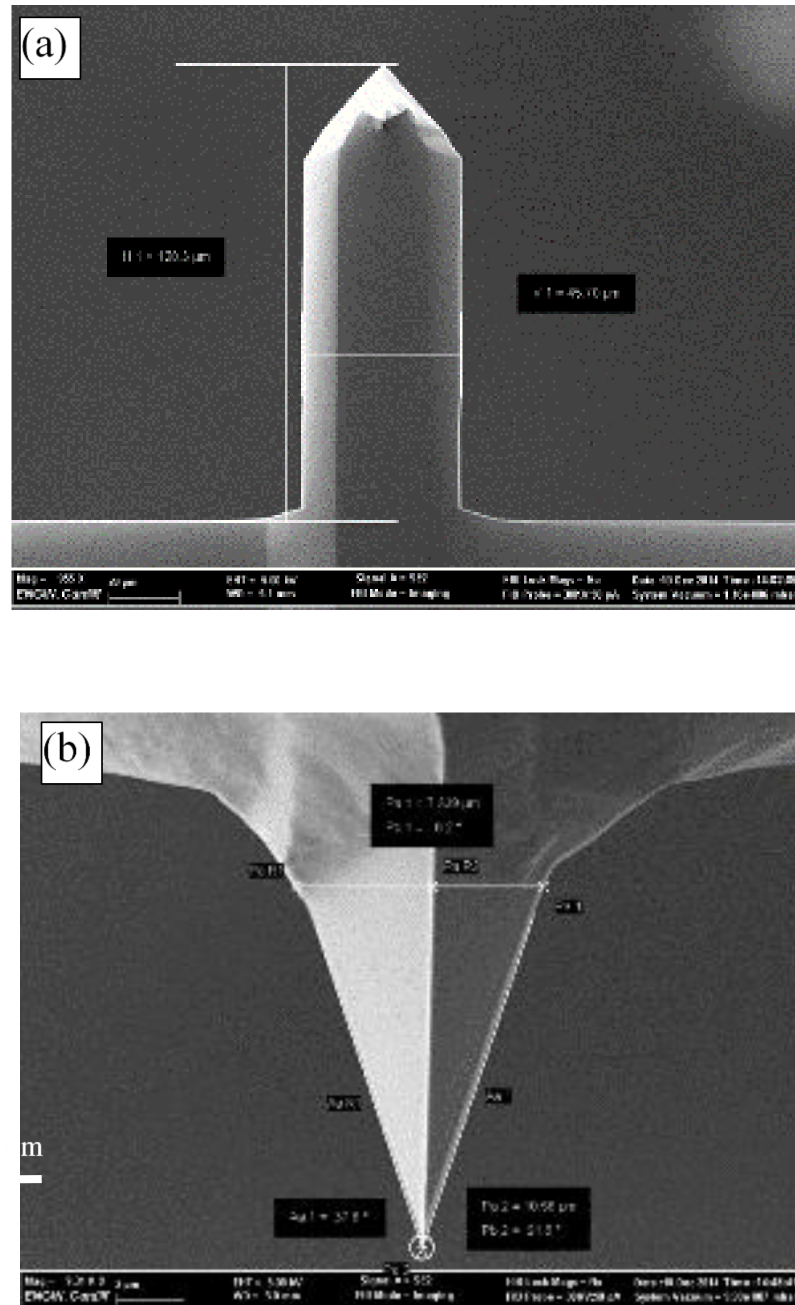

Figure 3.7 TESPD type from Bruker (a) top view of cantilever (b) side view of the tip apex

Table 3.1 Probe specifications

Specifications	**DNISP**	**TESPD**	**CSG**
Tip geometry	Three sided	Three sided pyramid	Three side pyramid
Tip material	Diamond	Silicon (DLC)	Single crystal silicon
Cantilever geometry	Rectangular	Rectangular	Rectangular
Cantilever material	Stainless Steel	Silicon	Silicon
Length of cantilever	352 µm	128.3 µm	190 µm
Width of cantilever	110 µm	45.7 µm	30 µm
Thickness of ccantilever	10.7 µm	Not provided	1.5 µm
Tip height	50 µm	10.5 µm	14.4 µm
Spring constant	221 N/m	56 N/m	0.6 N/m

3.3.3 Experimental cutting conditions and parameter settings

The so-called XEP software from Park Systems was used to operate the AFM when used in imaging mode while the XEL software (also from Park Systems) was employed to set-up the nanomachining experiments.

Prior to the start of a nanomachining operation, a scan of the sample surface is achieved first in order select a suitable location on the surface and thus and to avoid the tip coming into contact with any contaminants that may affect the results.

XEL is a software package which is designed for performing lithography tasks using the XE-100 AFM. Three types of mode are supported by XEL namely "*Z-scanner*" mode, "*set-point*" mode and "*bias*" mode. In the "*set-point*" mode, the user can specify a

particular value for the interaction force between the tip and the sample. Thus, this mode depends on the feedback loop of the AFM instrument, which ensures that the reflected laser spot position on the PSPD is kept constant, as mentioned in Chapter2. In this work, the set point mode is selected as it allows to perform the trial in the so-called force-controlled mode. In this case, the feedback loop ensured that V_{A-B} signal on the PSPD is kept constant throughout the nanomachining operations by moving the probe closer or further away from the sample surface. This software also enables the user to define customised tip trajectories. Following the definition of the scratching path within the XEL software, the user must first bring the tip of the AFM probe into contact with the sample/workpiece until a predefined load is reached. Next, using XEL, the tip is moved horizontally across the sample surface along a pre-defined path via the displacements of the stage along the x and y axes. During these operations, the required signals are recorded in real time using the LabVIEW Signal Express interface as shown in Figure 3.8. In these experiments, the sample rate utilised was 1 KHz for all recorded signals. After the performing the scratching process, the captured signal data are stored in LabVIEW and the AFM tip is lifted up for subsequent machining.

The terminology employed throughout the thesis and which is related to the considered cutting parameters is described below:

- ***Pre-Set applied load***. This is the force applied on the sample surface. This value is defined by the AFM user prior to performing an AFM machining operation. It corresponds to the normal force applied by the tip on a specimen (interaction force between the tip and sample) when the tip is engaged vertically into the material without horizontal motion of the probe with respect to the sample. If the set point is set too high, the tip may be penetrate too deep into the sample surface, possibly destroying the tip. On the other hand, if the normal load is set too low, the tip will not induce plastic deformation on the sample surface. In this study, the range of applied normal force values was considered shown in Tables 3.2 and 3.3.

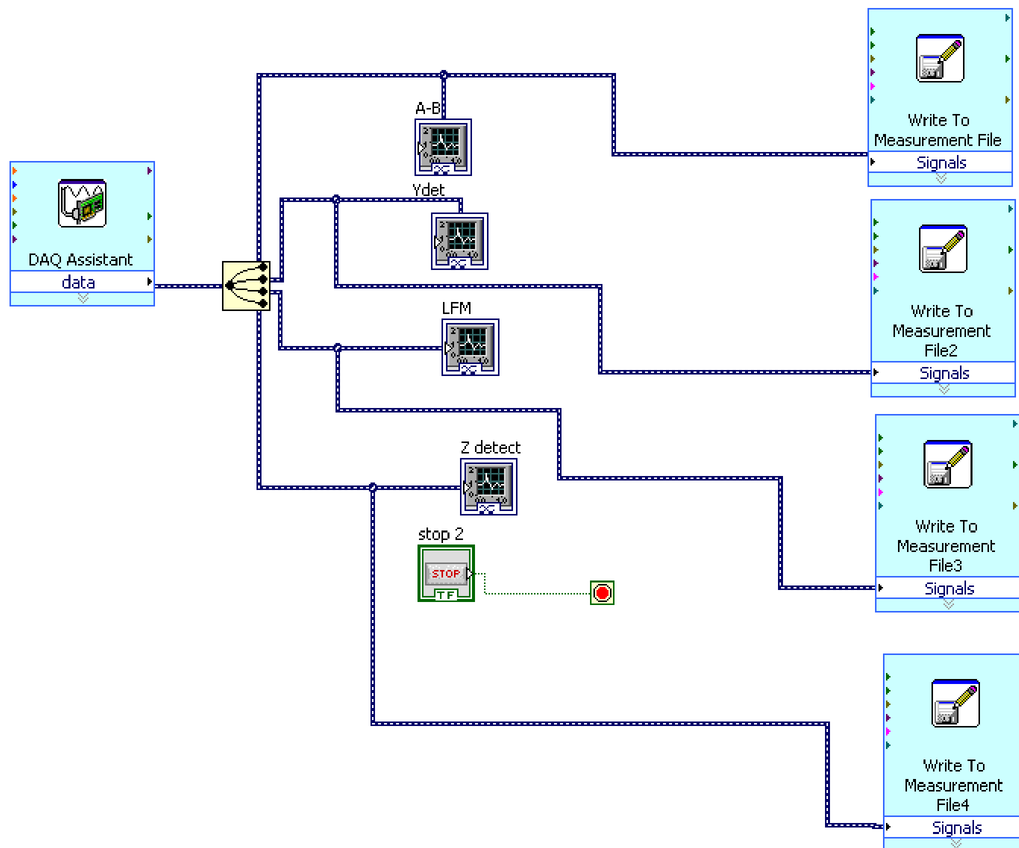

Figure 3.8 LabVIEW block diagram of get voltages

- ***Machining direction***. A large number of scratching directions can be implemented as the tip is moved horizontally relative to the sample. However, in the majority of studies on AFM-based nano mechanical machining, fundamentally four different directions are employed. As described in Tseng *et al*. (2011), these can be parallel to the axial axis of the cantilever while towards to or away from the probe as well as perpendicular to the lateral axis of cantilever. In this work, the machining tests were conducted along different orientations, namely in the pure forward and backward directions as well as at inclined angles with respect to the main axis of the cantilever, as illustrated in Figure 3.9.

- ***Machining speed***. This is relative velocity between the tip and the sample surface during a nanomachining operation. In this work, the scratching speed was fixed at 5 µm/s for all tests.
- ***Machining length***. This is the length of the produced grooves. This length is restricted by the range of motions allowed the XY scanner. Typically, the machined length is set in all the tests to a value of 15 µm. Machined grooves were separated by a distance of approximately 20 µm to avoid any influence of a previous cut on the current groove being machined, such as the presence of material pile-ups or residual stress.

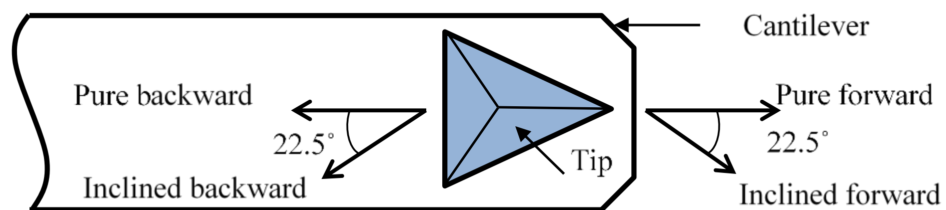

Figure 3.9 Considered cutting directions with respect to the cantilever orientation and tip geometry

Table 3.2 Cutting conditions for the Cu sample

Probe type		DNISP
Groove length (µm)		15
Machining speed (µm/s)		5
Normal force (µN)	Forward direction	20, 23, 24, 26, 27, 30, 31, 34, 36, 39
	Backward direction	13, 20, 27, 34

Table 3.3 Cutting conditions for the PC sample

Probe type		TESPD
Groove length (μm)		15
Machining speed (μm/s)		3
Normal force (μN)	Inclined forward (22.5°)	3.1, 3.4, 3.8, 4.1, 4.4
	Inclined backward (22.5°)	3.1, 3.4, 3.8, 4.1, 4.4

3.4 Microscopy techniques

Qualitative observations of the groove geometry and chip morphology were made using a scanning electron microscope (SEM). The particular SEM instrument utilised in this research was the XB 1540 model from Carl Zeiss (see Figure 3.10). This system allows two kinds of detectors of secondary electrons to be utilised, namely the so-called "Inlens" –detector and the "SE2" detector. The Inlens detector is located in line with the primary beam so it receives the higher energy secondary electrons and therefore usually produces better images. The SE2 detector is located on the wall of the SEM chamber, at an angle to the sample, so is less efficient in the collection of secondary electrons.

Finally, quantitative measurements (i.e. the depth and width of the grooves) were achieved on the XE-100 AFM instrument using CSG probes in contact mode. The XEI software (also from Park Systems) digital was utilised to convert the acquired AFM data into topography information and thus, to extract dimensional information about the produced grooves.

Figure 3.10 The Scanning Electron Microscope utilised

Chapter 4

New insight into the quasi-static behaviour of cantilevers during AFM tip-based nanomachining

4.1 Introduction

The review of the literature presented in Chapter two revealed that studies in the field of AFM tip-based nanomachining have neglected the fact that AFM probes should be considered as flexible tools in investigating the process. In particular, it was reported that, so far, the bending of the cantilever has been assumed to be concave in the forward direction. However there is no a-priori reason to make this assumption. Indeed, the deformed shape of the cantilever during AFM tip-based nanomachining along the forward direction should depend on the particular loading conditions acting on the tip. Thus, the aim of this chapter is two-fold. The first objective is to report a refined theoretical analysis to express the sign of the slope of the cantilever at the tip end as a function of loading conditions corresponding to a nanomachining operation conducted in the forward direction. The second objective is to verify experimentally that both concave and convex deformed shapes of the cantilever can be observed during actual AFM tip-based nanomachining tests along the forward and inclined forward directions depending of the processing conditions utilised.

The chapter is organised as follows; in the following section, a theoretical analysis of the bending orientation of a cantilever is presented that takes into account the specific tilt angle that the probe is mounted within an AFM device. This analysis allows to specify the actual directions of forces acting on the tip during a nanomachining operation. It is shown that under certain processing conditions, the deformed shape of the AFM cantilever probe working in the forward direction may change from a convex to a concave orientation. It should be noted that in practice, one cannot observe directly whether the cantilever experiences convex or concave bending. Hence, one needs to interpret correctly the signals obtained. The reasoning behind such interpretation is provided first in section 4.3. In particular, because the deflected shape of the cantilever in the backward and inclined backward directions is always convex, this can be used for the understanding of obtaining signals. In turn, this knowledge is used to identify if concave bending is observed. Next, the experimental results obtained when scratching in different directions for varying loads are presented. The work conducted and the main findings obtained in this chapter are summarised in the final section.

4.2 Theoretical analysis of the deformed shape of the cantilever

The theoretical development reported in this section is based on the classic differential equation of the deflection curve of a beam (Timoshenko 1940). The principal difference between the usual schemes for a tip-based nanomachining cantilever and the refined scheme of this thesis is that the inclination angle, α, between the cantilever and the surface of a sample is also considered in order to take into account the actual configuration of AFM systems. To the best knowledge of the author, similar refined schemes were used only for lateral force analysis in the case of frictional force AFM (Varenberg *et al.* 2003), (Asay and Kim 2006) while the aim of the analysis here is to identify loading conditions on the tip during the AFM nanomachining process that determine the sign of the slope of the deflected cantilever at its free end.

A schematic illustration of the forces acting on the tip during nanomachining in the forward direction is given in Figure 4.1a and the corresponding free-body diagram is shown in Figure 4.1b. According to the literature for AFM machining, the y axis is directed along the beam and it is positive to the right; the z axis and the corresponding deflection are positive downward; the bending moment is positive when it causes compression in the upper part of the cantilever; and the curvature is positive when the cantilever is bent concave downward.

Here F_{th} and F_a represent respectively the vertical and the horizontal forces acting at the pyramid tip, i.e. the force needed to keep the tip in the workpiece (the thrust), and the cutting force acting on the tip in the direction of cutting. These notations and terminology are adopted here to be consistent with notations used in the literature for conventional machining (Merchant 1945), (Manjunathaiah and Endres 2000). Because the forces F_{th} and F_a are shifted from the axis of the cantilever beam, they produce a moment at the free end of the cantilever M_{axial}, i.e. M_{axial} is generated by components of the forces of interaction between the probe pyramid tip and the material of the sample. This is shown in the free body diagram (Figure 4.1b). Due to the inclination angle, α, between the horizontal axis and the axis y of the cantilever, both F_{th} and F_a contribute to M_{axial} as follows:

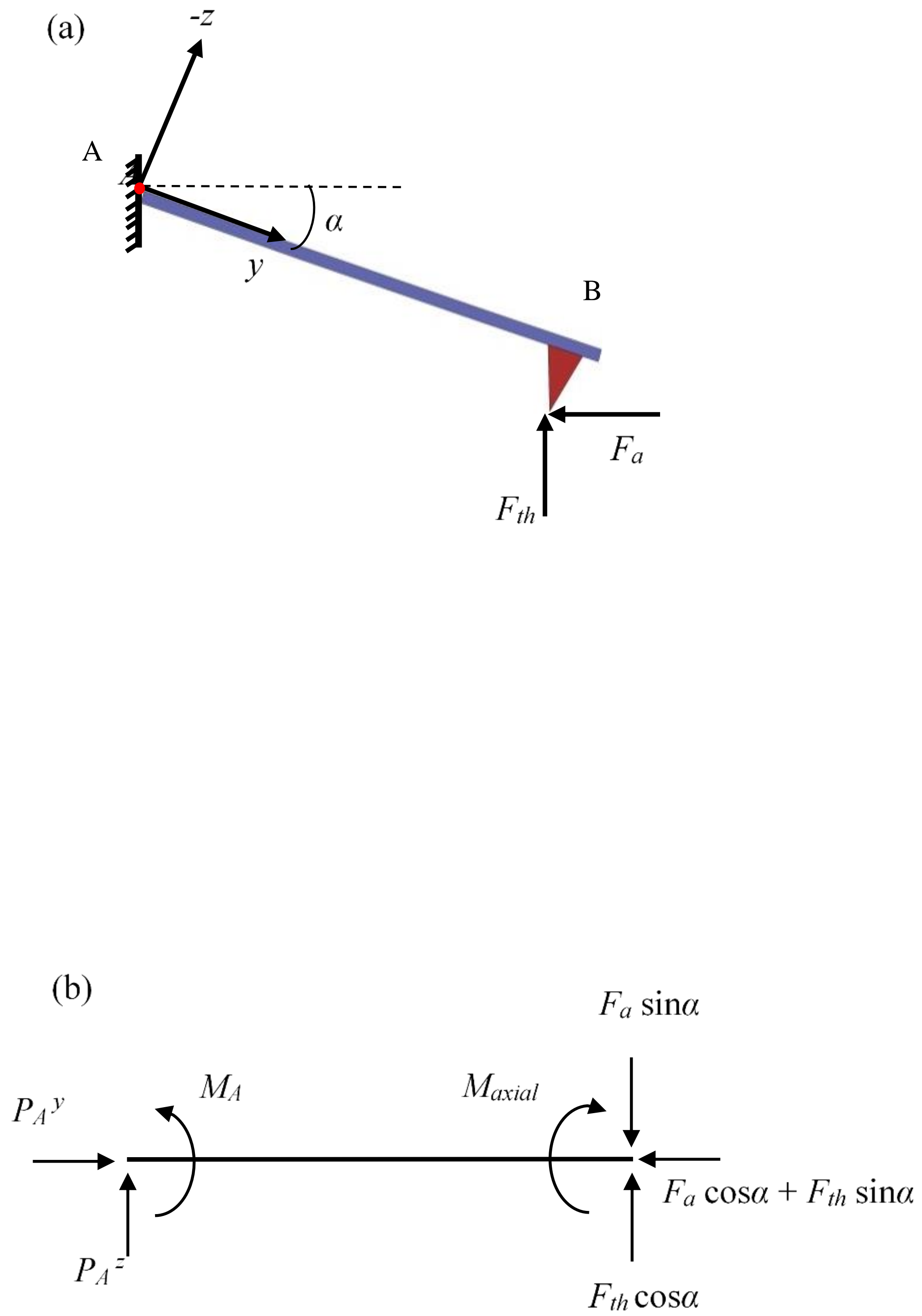

Figure 4.1 (a) Schematic representation of the AFM probe during nanomachining in the forward direction and (b) corresponding free body diagram.

$$M_{axial} = (h + t/2).F_a\cos\alpha + (h + t/2).F_{th}\sin\alpha \quad (4.1)$$

where *h* is the height of the tip and *t* is the thickness of the cantilever. Considering the equations of equilibrium, one can find the reaction moment M_A and reaction forces P_A^z and P_A^y at the built-in end of the cantilever

$$\begin{cases} P_A^y = F_a\cos\alpha + F_{th}\sin\alpha \\ P_A^z = F_a\sin\alpha - F_{th}\cos\alpha \\ M_A = M_{axial} + L(F_c\sin\alpha - F_{th}\cos\alpha) \end{cases} \quad (4.2)$$

where *L* is the length of the cantilever. Next, by cutting the cantilever at some point along its length and considering the equilibrium along the cut face, the bending moment, *M(y),* at a distance, *y*, from its fixed end is expressed as:

$$M(y) = -M_A + yP_A^z \quad (4.3)$$

Combing equations (4.2) and (4.3) leads to:

$$M(y) = -M_{axial} - L(F_a\sin\alpha - F_{th}\cos\alpha) + y(F_a\sin\alpha - F_{th}\text{hcos}\alpha) \quad (4.4)$$

The sign in the differential equation of the elastic (deformed) curve of the beam must be chosen to be consistent with the choice of coordinate directions and with the existing definition of positive bending (Timoshenko 1940), (Megson 1987) as that which produces curvature concave downward (hogging). Based on the coordinate directions used in Figure 4.1b and the fact that the angle of rotation of the cantilever, θ, is considered positive when clockwise with respect to the positive *y* axis, the basic differential equation of the deflection curve of the cantilever is expressed as

$$EI\frac{d^2z}{dy^2} = -M(y) \quad (4.5)$$

Its solution z = *w(y)* defines the shape of the deflection curve. By combining equations (4.4) and (4.5), it follows:

$$EI\frac{d^2w}{dy^2} = (h + t/2)(F_a\cos\alpha + F_{th}\sin\alpha) + (L - y)(F_a\sin\alpha - F_{th}\cos\alpha) \quad (4.6)$$

The AFM probe is assumed to be rectangular, and hence the flexural rigidity *EI* is fixed. This case represents the majority of probe designs. Then, the slope of the deflection curve may be found by integration of equation (4.6):

$$EI\frac{dw}{dy} = y(h+t/2)(F_a\cos\alpha + F_{th}\sin\alpha) + (F_a\sin\alpha - F_{th}\cos\alpha)(yL - y^2/2) + C \tag{4.7}$$

where *C* is a constant of integration. It follows from the boundary condition that the cantilever is built-in at the fixed end *A*, i.e. the slope is zero, that *C*=0. By substituting *y* = *L* in the equation (4.7), one obtains the slope at the free end of the deformed cantilever:

$$\frac{dw}{dy}(L) = \frac{L}{EI}[(h+t/2)(F_a\cos\alpha + F_{th}\sin\alpha) + (F_a\sin\alpha - F_{th}\cos\alpha)(L/2)] \tag{4.8}$$

It should be noted that the thickness of the cantilever, *t*, is generally much smaller than its length, *L*, and the tip height, *h*. Hence, the above equation can also be simplified to:

$$\frac{dw}{dy}(L) = (L/EI)[h(F_a\cos\alpha + F_{th}\sin\alpha) + (F_a\sin\alpha - F_{th}\cos\alpha)/(L/2)] \tag{4.9}$$

The moment generated at the fixed end of the probe by the force components acting on the tip and oriented in a direction perpendicular to the long axis of the cantilever is denoted as M_{normal}, i.e. $M_{normal} = L(F_{th}\cos\alpha - F_a\sin\alpha)$. Because $M_{axial} \approx h(F_a\cos\alpha + F_{th}\sin\alpha)$, one gets

$$\frac{dw}{dy}(L) = (L/EI)[M_{axial} - M_{normal}/2] \tag{4.10}$$

It follows from equation (4.10) and the sign convention of the slope of the deflected cantilever refer to Figure 4.2 that

$$\begin{cases} \text{If } M_{axial} > (M_{normal}/2) \text{ then } \theta < 0; \text{ the shape at the tip end is concave} \\ \text{If } M_{axial} < (M_{normal}/2) \text{ then } \theta > 0; \text{ the shape at the tip end is convex} \end{cases} \tag{4.11}$$

One can see from equation (4.9) that in the general case, the orientation of the deformed shape of the cantilever depends on three geometric parameters, namely, *α*, *h*, and *L* and two processing parameters, F_{th} and F_a. As a first approximation, it can be considered that the angle α is rather small, i.e. $\sin\alpha \approx 0$ and $\cos\alpha \approx 1$. Indeed, it is about 12° for actual AFM instruments. Putting $\sin\alpha = 0$ and $\cos\alpha = 1$, the equation (4.9) may be further simplified as

$$(EI/L)\frac{dw}{dy}(L) \cong hF_a - (L/2)F_{th} \tag{4.12}$$

Based on these coarse assumptions, it can generally be said that the bending of the cantilever during nanomachining in the forward direction is likely to be concave for increased values of axial cutting force, F_a, relatively to the thurst force, F_{th}.

Thus, it has been shown above that contrary to the assumption normally made in the AFM tip-based nanomachining literature, the deformed cantilever shape may be convex, especially for values of F_a that are small relatively to F_{th}. In the remainder of this chapter, experiments are reported to verify whether both bending orientations can be observed in practice.

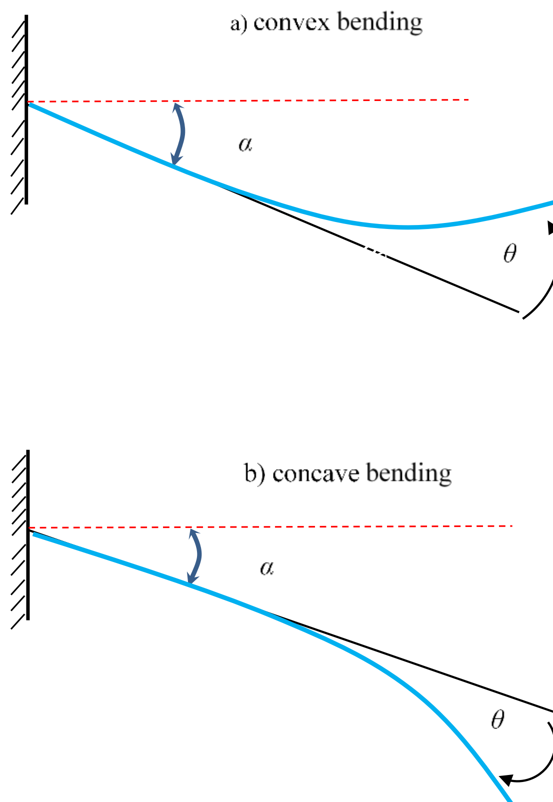

Figure 4.2 The shape of cantilever deflection and slope angle a) convex bending and b) concave bending

4.3 Illustration and analysis of the Z-detector output signal

The experimental observations reported in the next section rely significantly on the analysis of the Z-detector signal. This is due to the fact that the information content of this particular output is relatively rich and provides valuable data to understand the mechanical behaviour of cantilevers during nanomachining. For this reason, this section presents a detailed time-dependence analysis of a typical Z-detector output. The Z-detector signal used in this example is shown in Figure 4.3. It was obtained when cutting a groove in the PC sample along the backward direction. As noted in this figure, such a signal can be divided into five consecutive stages, which correspond to the regions “A”, “B”, “C”, “D” and “E”. The physical interpretation of each of them is given below.

- First stage (region A). This stage takes place after the initial approach of the tip onto the surface of a specimen. In this case, the tip is in static contact with the sample and the applied normal force is very low. More specifically, it is typically in a range between a few nN to a few tens of nN as defined by the AFM user. This results in the generation of the thrust force, F_{th}, as mentioned in Section 4.2. Based on the knowledge of the normal spring constant of the probe and the sensitivity of the PSPD, this load corresponds to a given A-B output voltage, V_0, as illustrated with Figure 4.4a. Thus, at the end of the tip approach, the Z-detector signal is constant as observed in Figure 4.3.

- Second stage (region B): Between point 1 and point 2 in Figure 4.3, the normal load is increased to another user-defined value, which is sufficiently high to induce plastic deformation. In this example, it was set at 3.4 μN. Thus, through this stage, the tip penetrates into the processed material as the probe is moved down vertically towards the sample due to the extension of the Z-scanner. Also, the XY stage of the AFM is static during this time. Therefore, this step also corresponds to the loading cycle of a nanoindentation process. The vertical motion of the probe stops when the V_{A-B} signal of the PSPD reaches a value, V_1 in Figure 4.4b, which matches the load set by the user and which will be the target value for the feedback loop during machining. At the same time, the extension of the Z-scanner is monitored by the strain gauge and as a result, the Z-detector signal increases sharply between point 1 and point 2 in

Figure 4.3. Based on the experimental data reported here, the evolution of the Z-detector output as a function of the Z-scanner movement, when the tip is in contact with a sample, is shown Figure 4.5. For the analysis presented later on in this chapter, it is important to note that, when the Z-scanner extends and thus, the probe moves towards the sample surface, the Z-detector voltage increases. When the probe moves away from the sample, as a result of the contraction of the Z-scanner, this signal decreases.

- Third stage (region C): This may be referred to as a transition stage. In particular, at point 2 in Figure 4.3, the horizontal motion between the sample and the probe starts. Thus, a horizonatl cutting force (axial force), F_a, is now also applied on the tip in addition to the thrust force, F_{th}. As presented in section 4.2, the resulting change in the moment M_{axial} on the free end of the cantilever also modifies its deflection angle, θ. Consequently, the generation of F_a also modifies the $V_{A\text{-}B}$ signal on the PSPD as a result of the optical lever principle. For this reason, the vertical position of the probe is automatically adjusted through the feedback loop of the AFM system. In this example, contraction of the Z-scanner takes place to raise the probe until the A-B output reaches a target value, which corresponds to the voltage attained prior to the start of the horizontal motion of the stage. Thus, this voltage value also corresponds to V_1 as referenced in Figure 4.4. During this transition stage, the Z-detector signal output varies until a steady-state configuration is reached, which is illustrated with point 3 in Figure 4.3.

- Fourth stage (region D): The time elapsed between points 3 and 4 corresponds to the actual machining of a groove as a relative motion between the AFM tip and the surface of the sample takes place along a pre-defined path as shown in Figure 4.6.

- Fifth stage (region E): This step is reached when the horizontal motion of the stage is stopped. In this case, the tip stays inside the groove but the normal load applied is reset to the value defined for the approach process. This value corresponds to the $V_{A\text{-}B}$ output voltage V_0 in Figure 4.7.

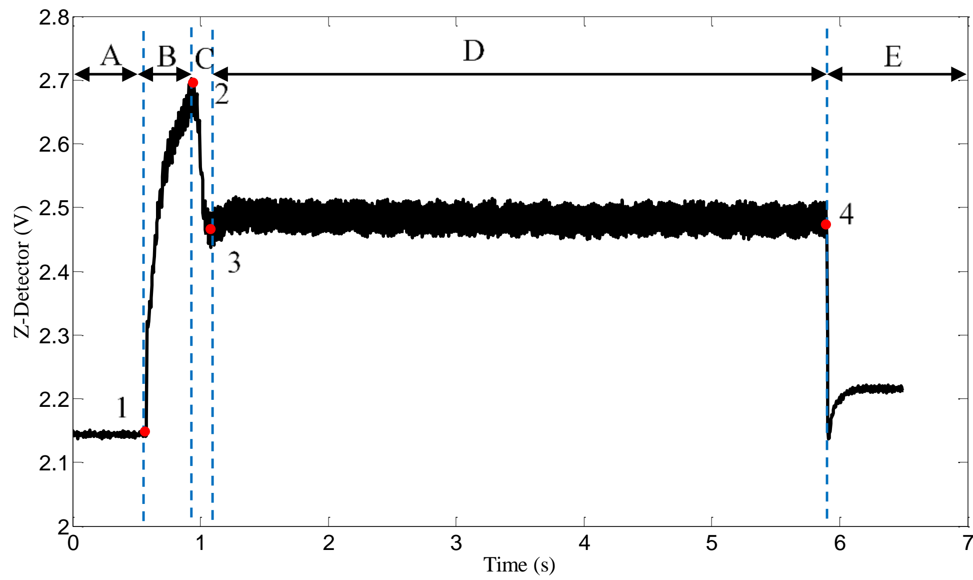

Figure 4.3 Example of Z-detector signal during nanomachining in the backward direction

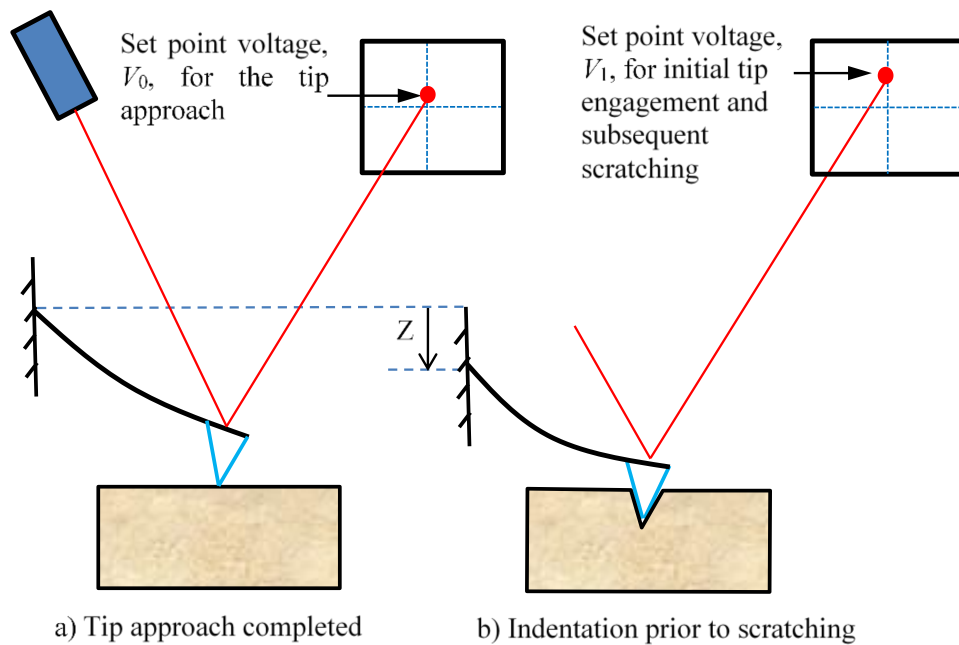

Figure 4.4 Illustration of the probe and the PSPD status following a) the approach process and b) the initial tip penetration into the specimen.

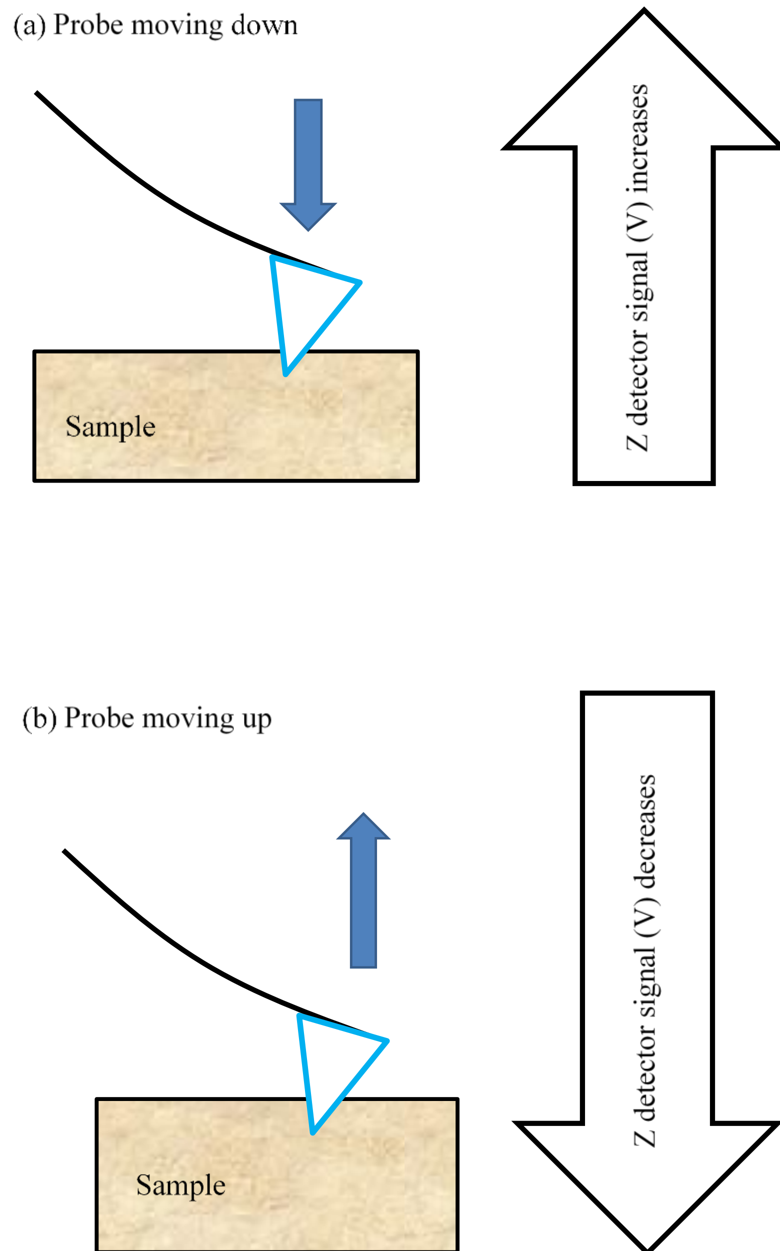

Figure 4.5 The evolution of the Z-detector output as a function of the Z-scanner movement

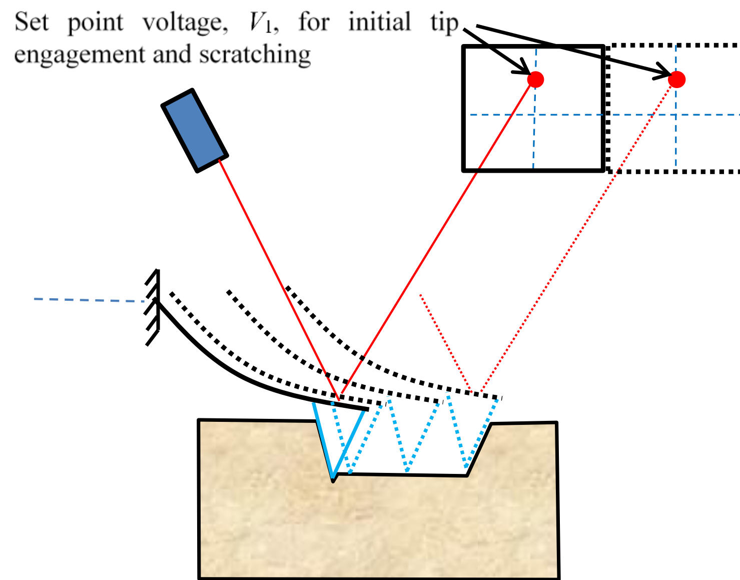

Figure 4.6 Illustration of the probe and the PSPD status during the machining stage

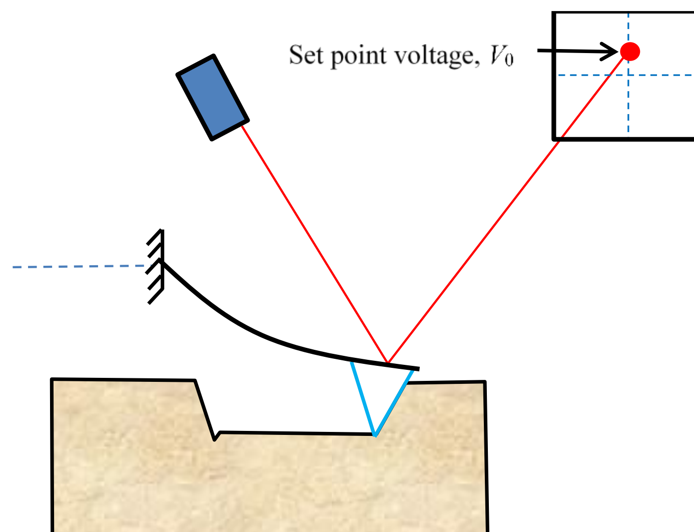

Figure 4.7 Illustration of the probe and the PSPD status following the retraction stage

4.4 Experimental studies of nanomachining with different process directions

In this section, experimental results when nanomachining in different direction and for varying loads are presented. Due to the fact that the deflected shape of the cantilever in the backward and inclined backward directions is always convex, first, the Z-detector and $V_{A\text{-}B}$ voltage signals in these directions are monitored and analysed. This analysis is performed mainly to help the further understanding of the physical meaning of these signals. Then, the knowledge about AFM output voltages gained is used to identify if concave bending is taking place during nanomachining in the forward direction.

4.4.1 Nanomachining with backward and inclined backward directions

Figures 4.8 to 4.11 show Z-detector output signals when machining the Cu sample in the backward direction and the PC specimen in the inclined backward direction. In particular, these plots correspond to those obtained for both the smallest and the highest normal loads set for each material (see Table 3.2 and 3.3 in Chapter 3). In addition, Figure 4.12 displays an example of a typical A-B voltage signal monitored when processing along these directions. The recorded Y-detector signal is also superimposed in this figure in order to associate the fluctuation of the A-B voltage with the start and end of the horizontal motion of the AFM stage. For information, the data used in this illustrative example are those obtained when machining the Cu sample with a set applied load of 13 μN.

From the inset shown with Figure 4.12, it is observed that the A-B signal increases as soon as the horizontal motion of the stage begins. As discussed in section 4.3, this increase is the result of the change in the deflection angle of the cantilever at its free end following the introduction of the horizontal force, F_a, on the tip. In particular, for the backward and inclined backward machining configurations, the direction of F_a is always pointing away from the fixed end of the probe. Consequently, the deflection angle of the cantilever increases upon the start of the stage motion. As observed in Figure 4.12, and as explained with Figure 4.13, this increase in the deflection angle also leads to the increase of the $V_{\text{A-B}}$ signal on the PSDP. In this case, it is expected that the Z-scanner should raise the probe to return the $V_{\text{A-B}}$ voltage to its set value. This can indeed be

observed with all the experimental plots shown in Figures 4.8 to 4.11 as the Z-detector signal decreases in all cases during the time interval referred to as "region C" in the previous section. Thus, the resulting shape of the deformed cantilever stays convex throughout machining in the backward and inclined backward directions due to the fact that F_a is pointing away from the fixed end of the cantilever along these cutting directions.

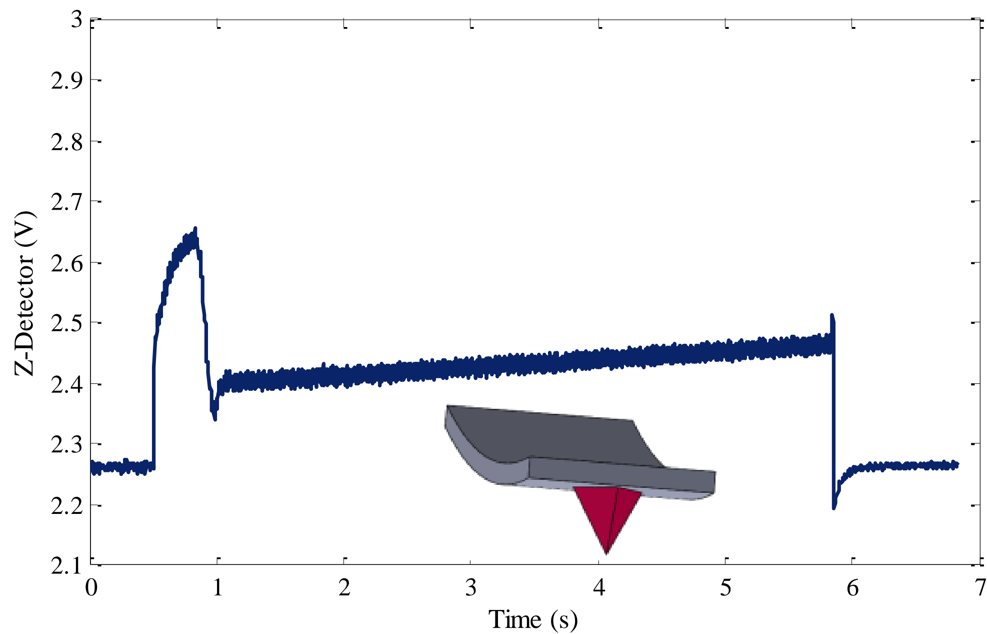

Figure 4.8 Z-detector output signals when processing the PC sample along the backward direction for a set normal load of 3.1 μN

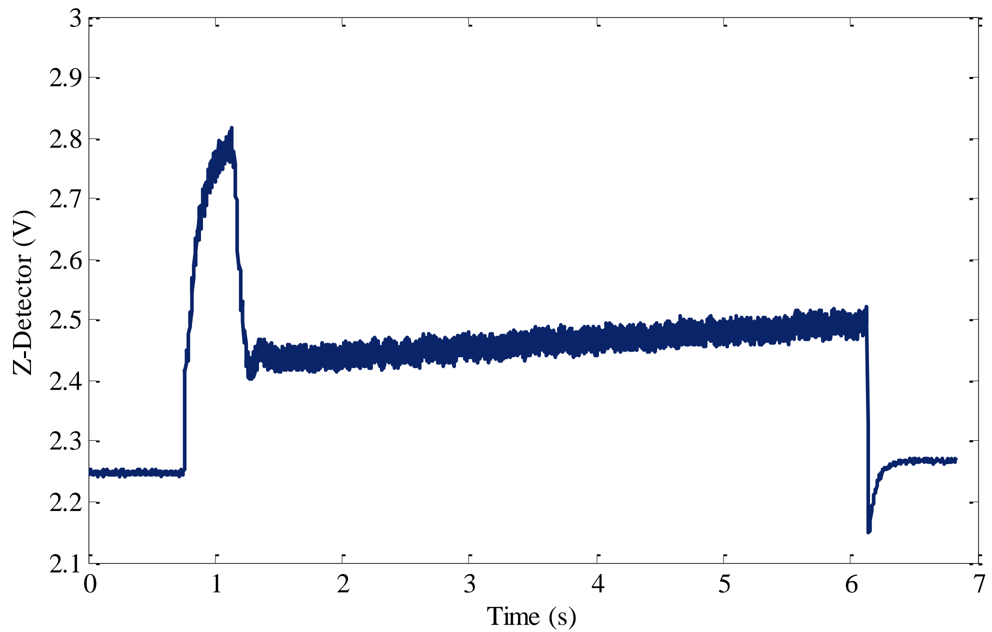

Figure 4.9 Z-detector output signals when processing the PC sample along the backward direction for a set normal load of 4.4 μN

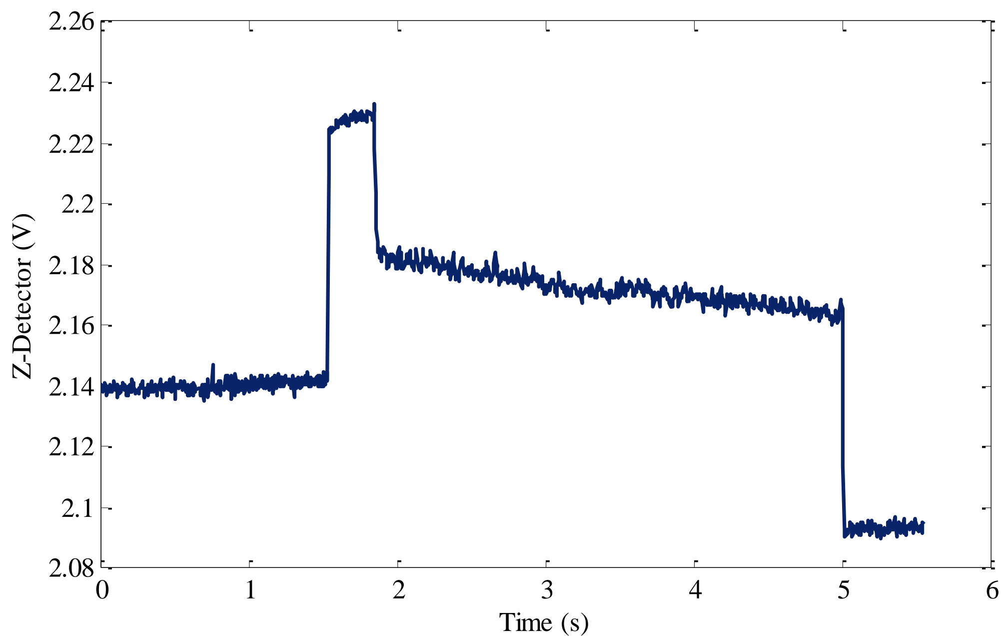

Figure 4.10 Z-detector output signals when processing the Cu sample along the backward direction for a set normal load of 13 μN

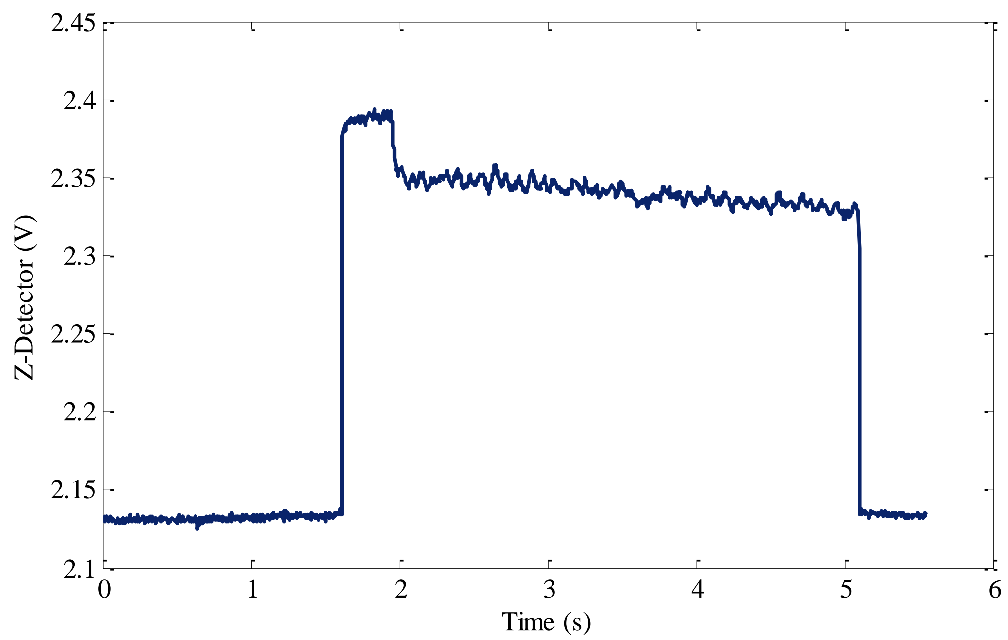

Figure 4.11 detector output signals when processing the Cu sample along the backward direction for a set normal load of 34 μN

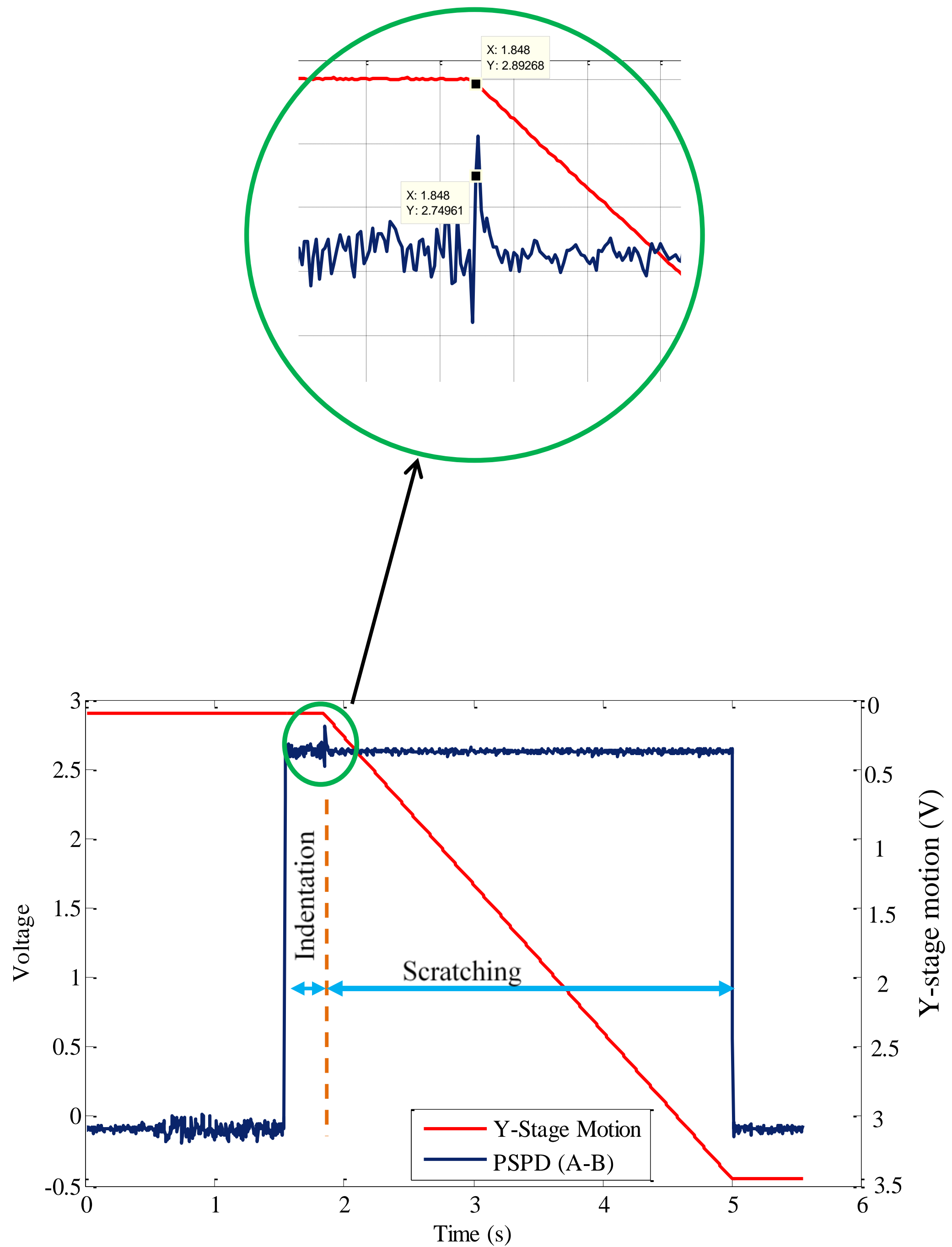

Figure 4.12 Typical A-B and Y stage signals representative of processing in the backward and inclined backward directions. The inset plot shows the change in the A-B voltage as soon as the lateral motion of the stage starts.

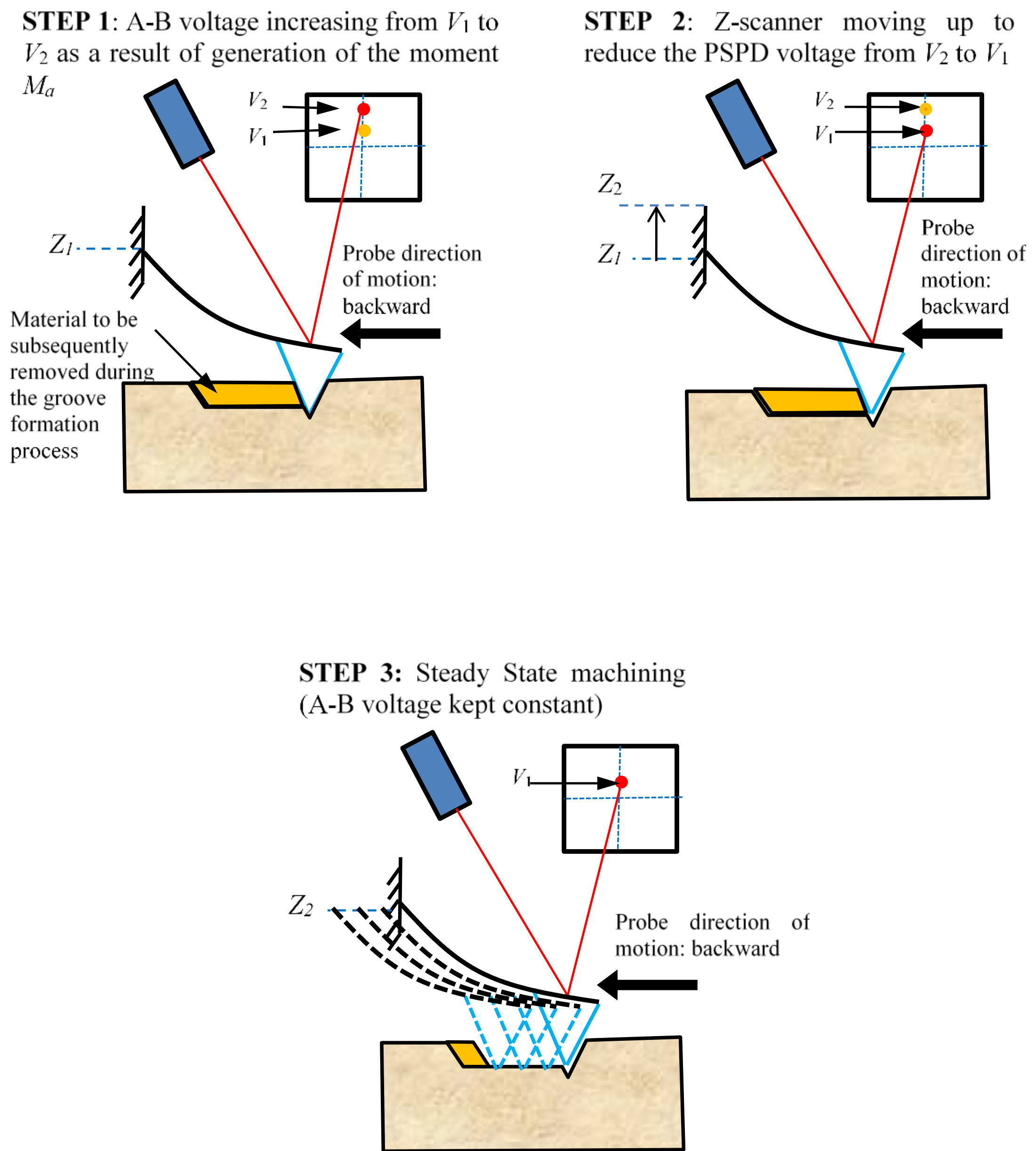

Figure 4.13 Illustration of the probe being raised as a result of the moment M_a being Generated when the lateral motion of the stage is initiated.

4.4.2 Shape of the deflected cantilever during nanomachining in the forward direction

In this section, profiles of the Z-detector voltage corresponding to machining in the forward direction are reported and compared with these obtained in the backward direction. The results presented are those obtained when processing the Cu sample in a pure forward direction. Depending on the load applied, three different types of voltage profiles may be observed corresponding to the quasi-static behaviour of the cantilever. These three types are associated with normal loads that are 1) relatively low (between 20 μN and 23 μN), 2) intermediate (between 24 μN and 27 μN) and 3) high (between 31 μN and 39 μN).

4.4.2.1 The deflection of the cantilever at low loads

As the above theoretical analysis shows, it would be reasonable to expect that the V_{A-B} voltage of the PSPD drops as soon as the motion of the XY stage begins. Indeed, the axial force F_a is pointing towards the fixed end of the probe in this case. As a result of this orientation, the deflection angle of the cantilever should decrease once the displacement of the stage is initiated. Consequently, it would also be expected that, the probe should be lowered towards the sample by the Z-scanner in order to raise the PSPD voltage back to its set value. Should this downward vertical motion of the probe take place, an increase in the Z-detector signal should be recorded with the data acquisition system. However, it is the opposite result which was observed when processing in this lower range of set normal forces as observed in Figures 4.14 and 4.15. To illustrate this in more detail, the recorded Z-detector and Y stage signals are reported in Figure 4.16 when processing with a set normal load of 20 μN. In particular, it can be seen with the inset image in this figure that the Z-detector decreases once the motion of the lateral stage begins.

This means that the probe was raised, and not lowered as it could have been expected, immediately after the initiation of the stage motion. A possible reason for such behaviour is that the initial stage displacement results in a sliding motion of the tip along the face of the indent formed during the previous time interval when the AFM stage was still static. This sliding motion results in the PSPD voltage to increase, as illustrated in Figure 4.17.

Consequently, the Z-scanner raises the probe until the $V_{A\text{-}B}$ voltage reduces back to its set value. Therefore, based on the fact that the probe is moved up at the start of the groove and that the overall profile of the Z-detector signal is similar to that obtained in the backward direction, it is concluded that the deformed shape of the cantilever is convex during the machining process for this lower range of set normal forces. Thus, the value of the force F_a was too small to change the cantilever shape (see equation (4.12)).

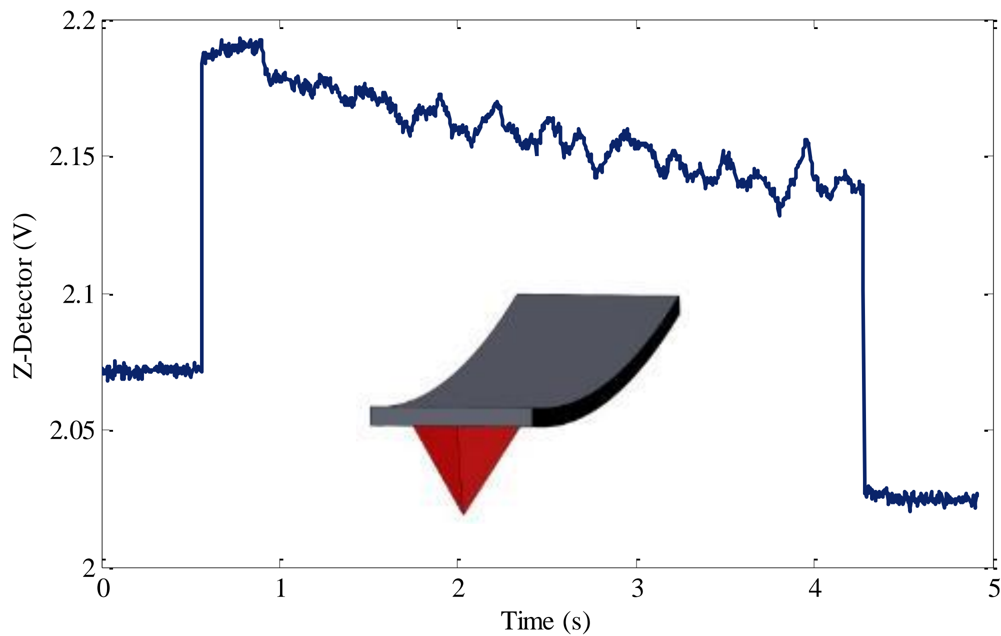

Figure 4.14 Z-detector output signals when processing the Cu sample along the backward direction for a set normal load of 13 μN

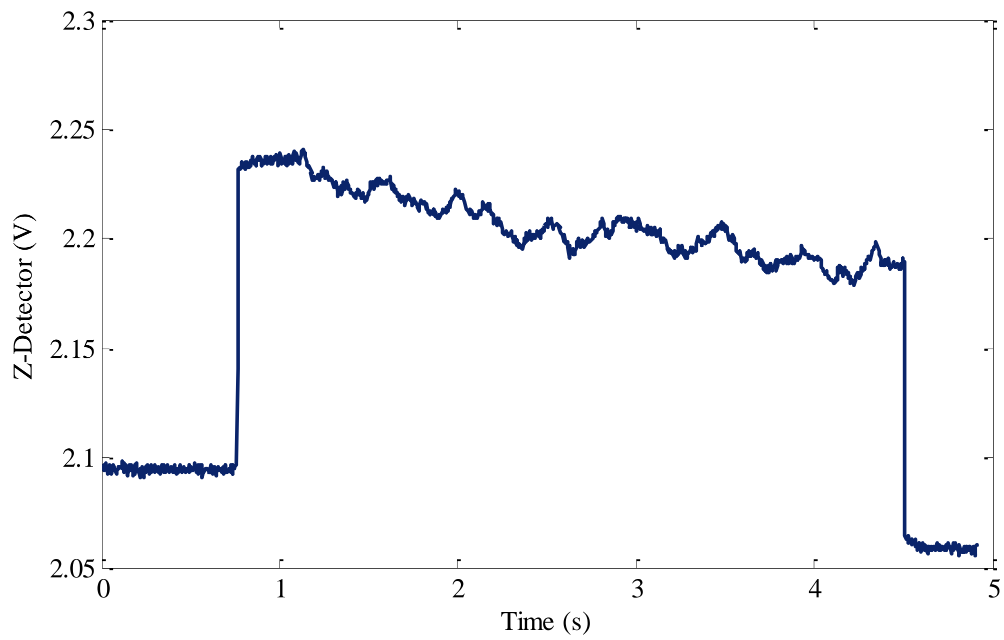

Figure 4.15 Z-detector output signal when processing the Cu sample along the backward direction for a set normal load of 27 μN

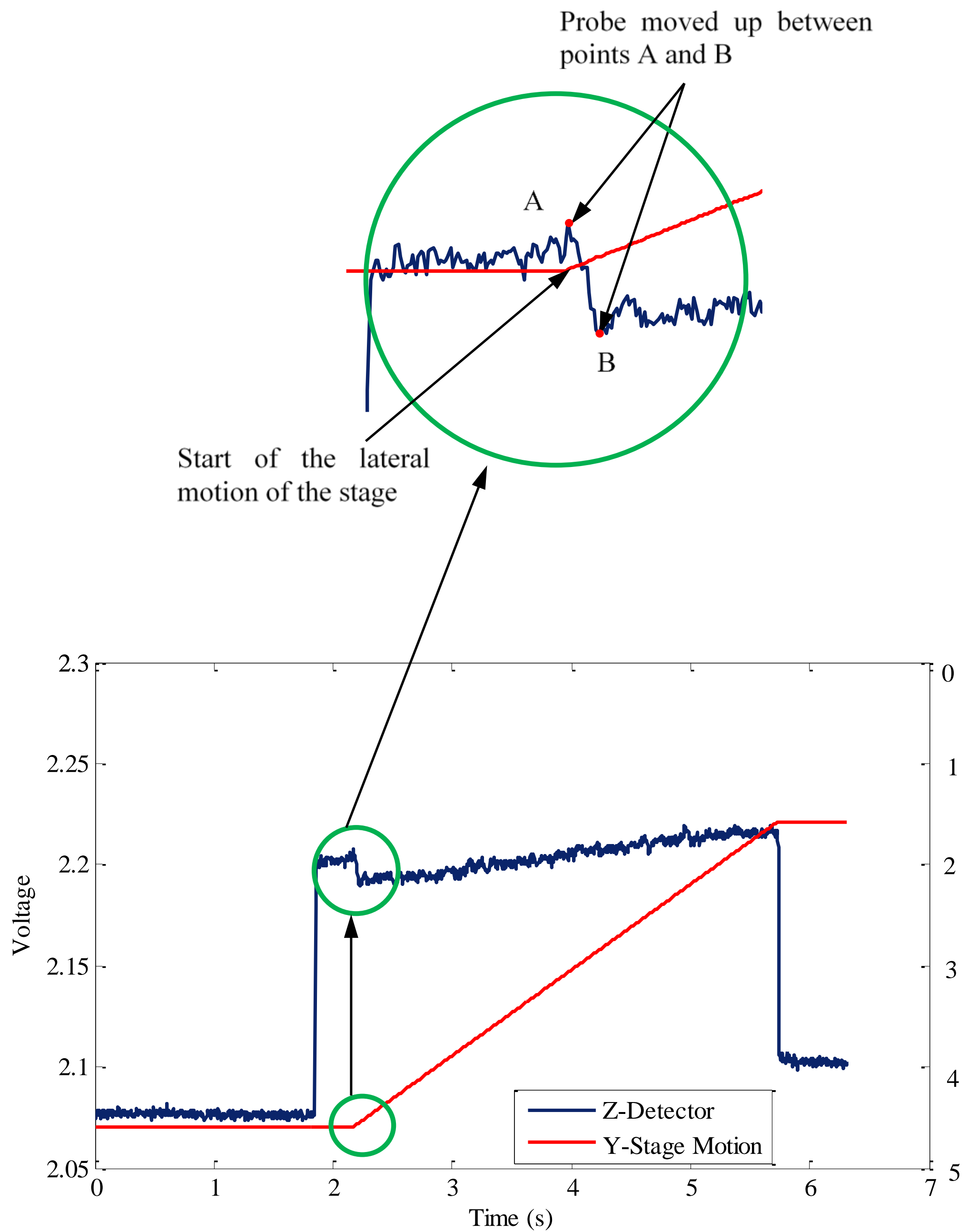

Figure 4.16 Z-detector and Y stage output signals when processing the Cu sample along the forward direction for a set normal load of 20 μN. Note that for the inset higher magnification image, the Y stage signal was deliberately shifted up for illustration purpose.

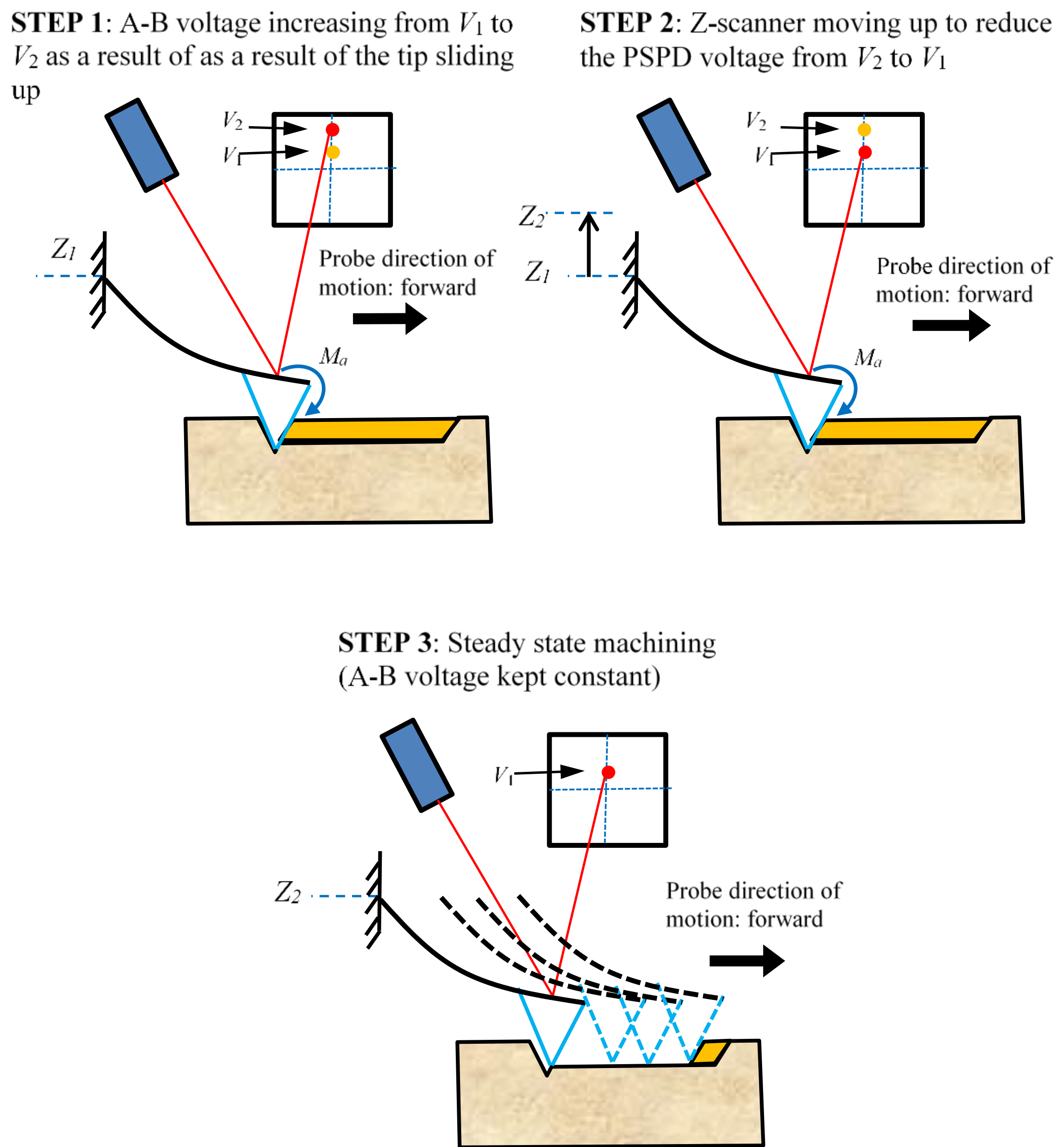

Figure 4.17 Illustration of the probe sliding up the face of the initial indent and the subsequent series of events with respect to the $V_{A\text{-}B}$ voltage variation on the PSPD and the associated response of the Z-scanner via the force-controlled feedback loop

4.4.2.2 The deflection of the cantilever at medium loads

In this range of loads, one can observe the different behaviour of the profiles of the Z-detector output voltage in comparison with the behaviour of these profiles recorded in the backward direction. For example, the signals in Figure 4.18 were captured during machining along the pure forward direction for an applied load 24 μN. It can be seen from this figure that the probe is brought down towards the sample as soon as the Y stage initiates its displacement. This is the opposite motion to that reported earlier in section 4.4.2.1 when conducting experiments with smaller loads. Indeed, the lowering of the probe via the feedback loop of the AFM at this particular stage of the process is realised in response to a reduction in the deflection angle at the free end of the cantilever. This decrease in the deflection angle at the start of the displacement of the stage is a consequence of the generated axial force, F_a, being induced on the tip while the tip is also sticking on the initial indent (as opposed to sliding along it). The sequence of events leading to the observed output signals upon initiation of the stage motion is illustrated with Figure 4.19. It should be noted that this observation could also be made when processing with a set normal load of 26 μN. However, for 27 μN, it is the sliding motion of the tip, which was found to govern the response of the Z-scanner motion upon the initiation of the lateral displacement of the stage (see Figure 4.20). Thus, it can be said that, in this intermediate range of set normal loads, a mix between tip sliding and tip sticking phenomena was obtained when initiating the machining operations. In addition, the cantilever shape also stayed convex during machining in this range of medium loads. Thus, the generated axial force F_a was not enough to change the cantilever deflected shape.

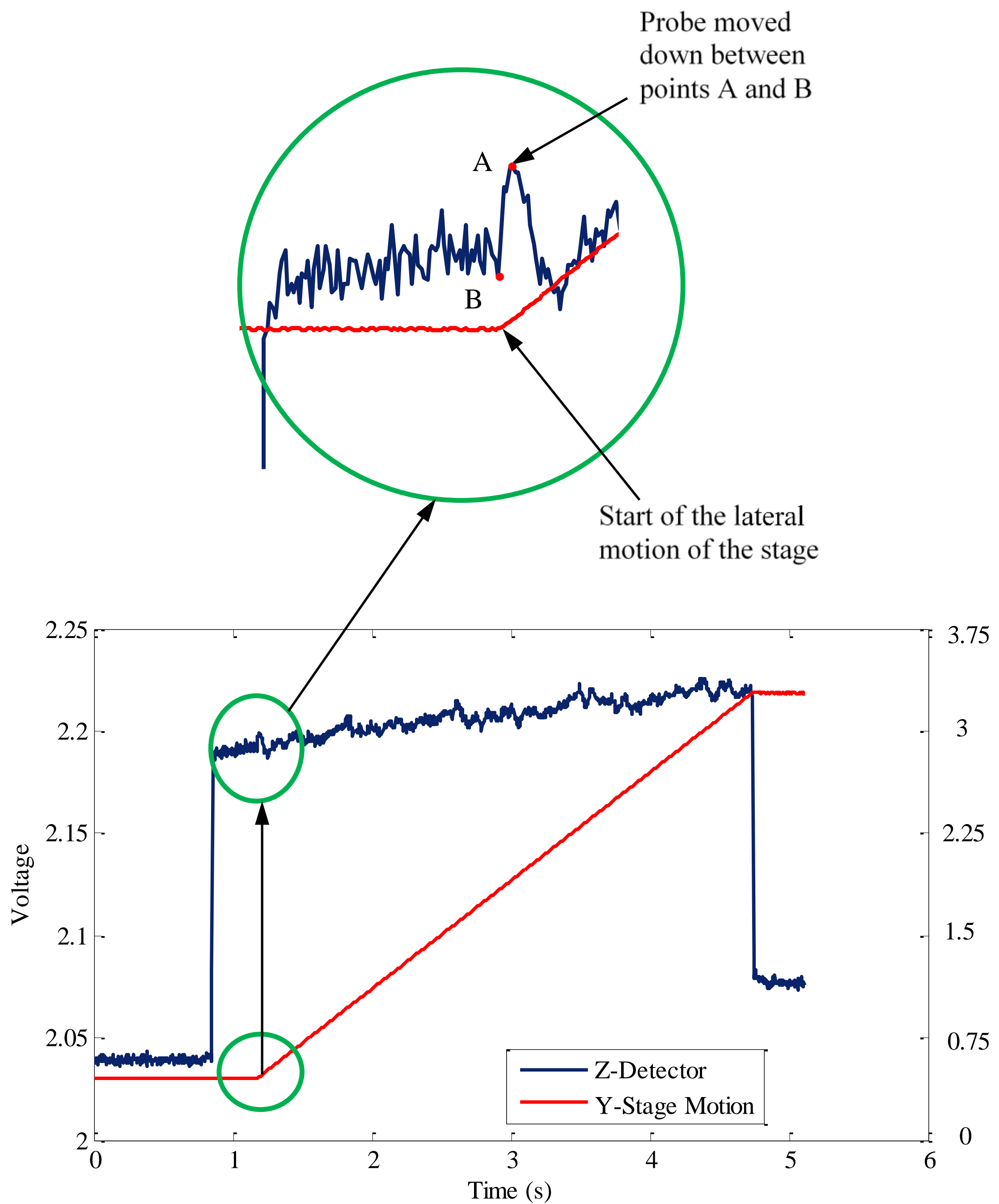

Figure 4.18 Z-detector and Y stage output signals when processing the Cu sample along the forward direction for a set normal load of 24 μN.

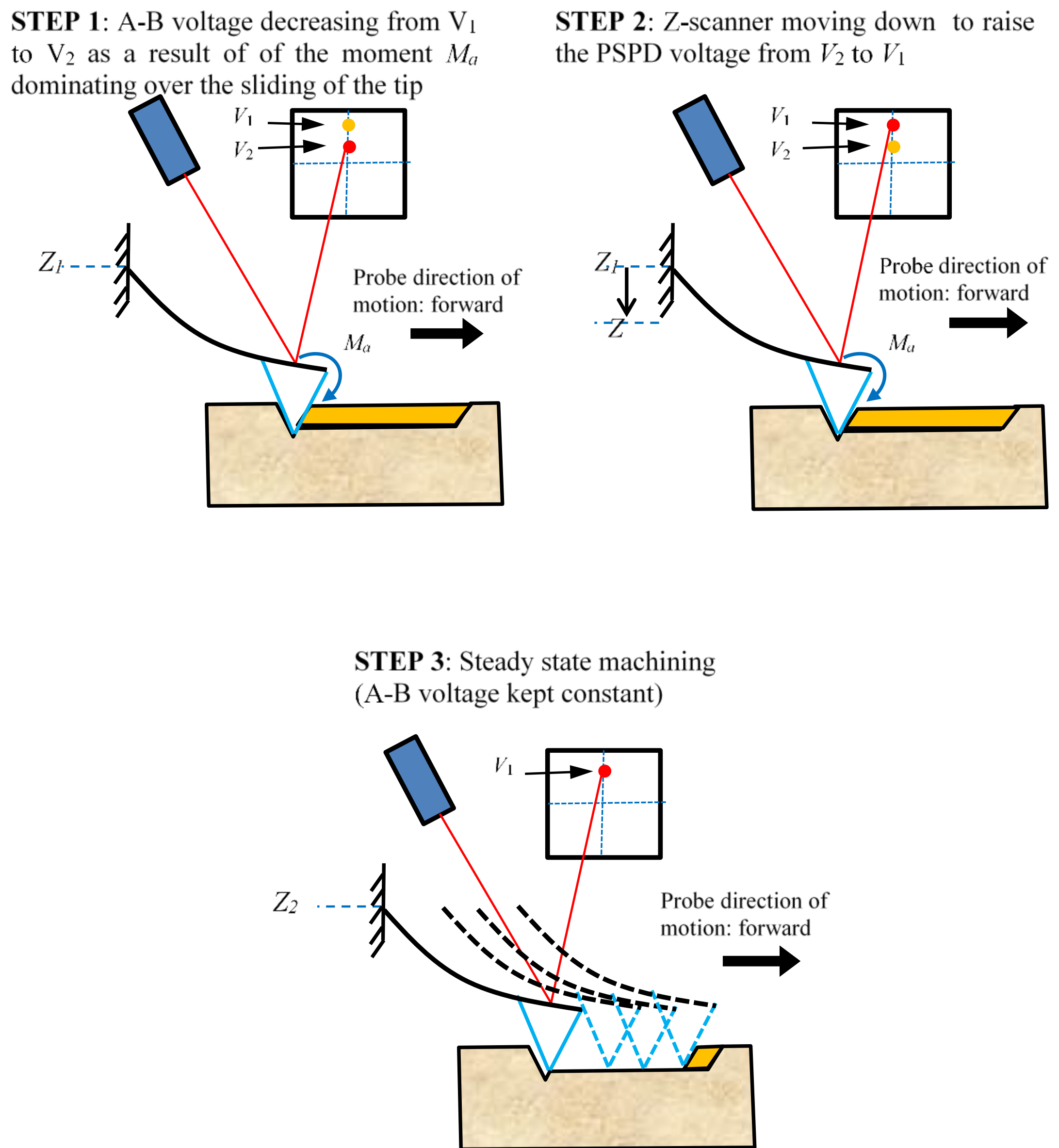

Figure 4.19 Illustration of the probe being lowered upon the start of the lateral motion of the stage as a result of the effect of the moment Ma dominating over the sliding of the tip.

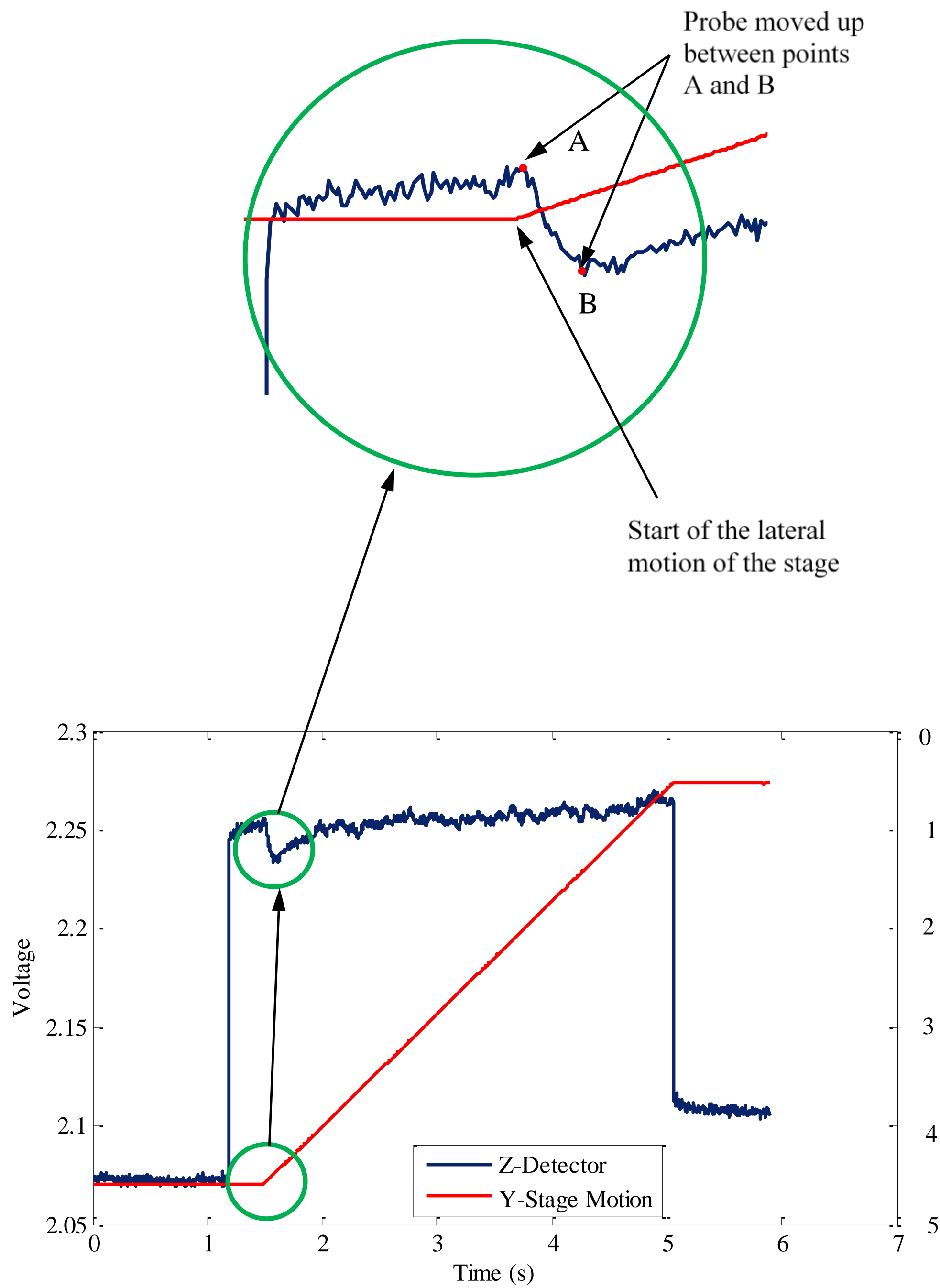

Figure 4.20 Z-detector and Y stage output signals when processing the Cu sample along the forward direction for a set normal load of 27 μN.

4.4.2.3 The deflection of the cantilever at high loads

In this third and highest range of set normal forces, the recorded data showed that the tip sticking effect consistently dominated the behaviour of the AFM probe during the initial motion of the stage. Most importantly however, a significant phenomenon was observed during the subsequent groove machining process. This is illustrated with Figure 4.21 in the case of a set normal load of 31 μN. In particular, it can be seen from this figure that the Z-detector signal increases significantly about half-way through the cutting of the groove. This rapid increase in the Z-detector signal shows that the feedback loop of the AFM suddenly drove the probe down as the groove was being cut. This was realised to ensure the V_{A-B} voltage output of the PSPD was maintained to a set target value. At the same time point and as shown with Figure 4.22, the PSPD voltage also started displaying more pronounced oscillations around this target value.

The hypothesis put forward to explain such observation during this particular short time interval is that the bending of the cantilever at its free end changes from a convex orientation to a concave one. To support this hypothesis, it is argued that the axial force, F_a, acting on the tip is increasing along the length of a machined groove. Further investigations are required to elucidate in a comprehensive manner the reason behind this increase in F_a during the groove formation process itself. The hypothesis that may be put forward at this stage to explain such a change in the cutting force is that it could be the result of the combined effect of 1) the accumulation of piled-up material in front of the tip and 2) the strain hardening of the material ahead of the tip. In particular, the gradual accumulation of pile-up on the tip rake face augments the contact area between the tip and the material, which in turn, raises the force acting of the tip. Strain hardening of the material may also be considered as a possible effect. Indeed, when increasing the value of the set normal load, the resulting larger volume of material subjected to plastic deformation around the tip may also be expected to be associated with an augmentation of the dislocations density in this region. Consequently, when the tip moves across the surface of the sample, it can also be reasonably expected that the occurrence of dislocation entanglements should increase and thus, that the number of movable dislocations should reduce. Therefore, the cutting force in this case has to overcome the larger atomic bonding forces in the Cu crystal (Backer *et al.* 1952). Regardless of the specific physical phenomon at play, an increase in F_a results in a reduction of the deflection angle at the

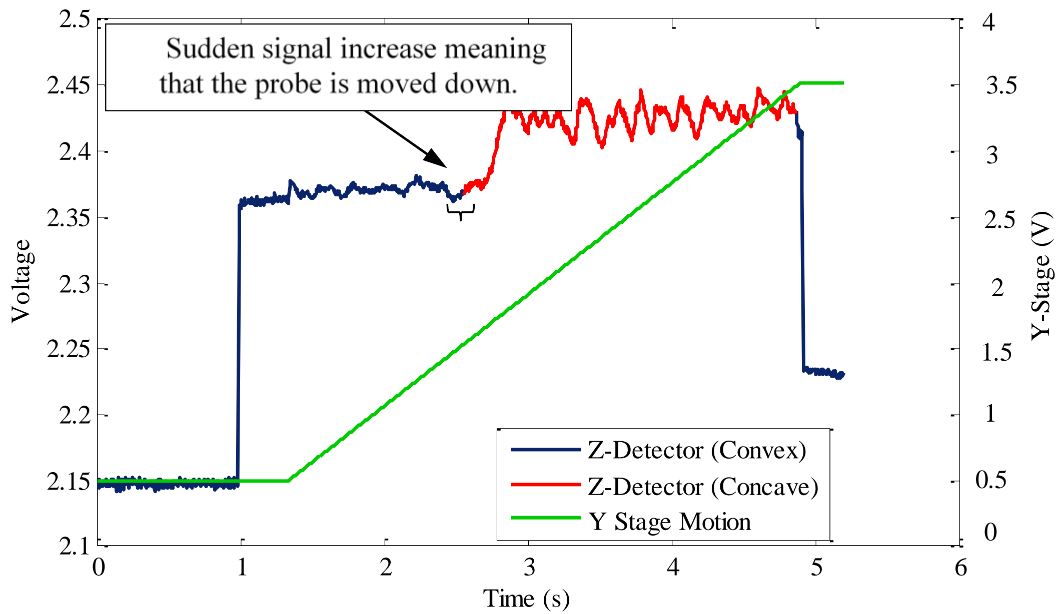

Figure 4.21 Z-detector and Y-stage voltage output signals when processing the Cu sample along the forward direction for a set normal load of 31 μN.

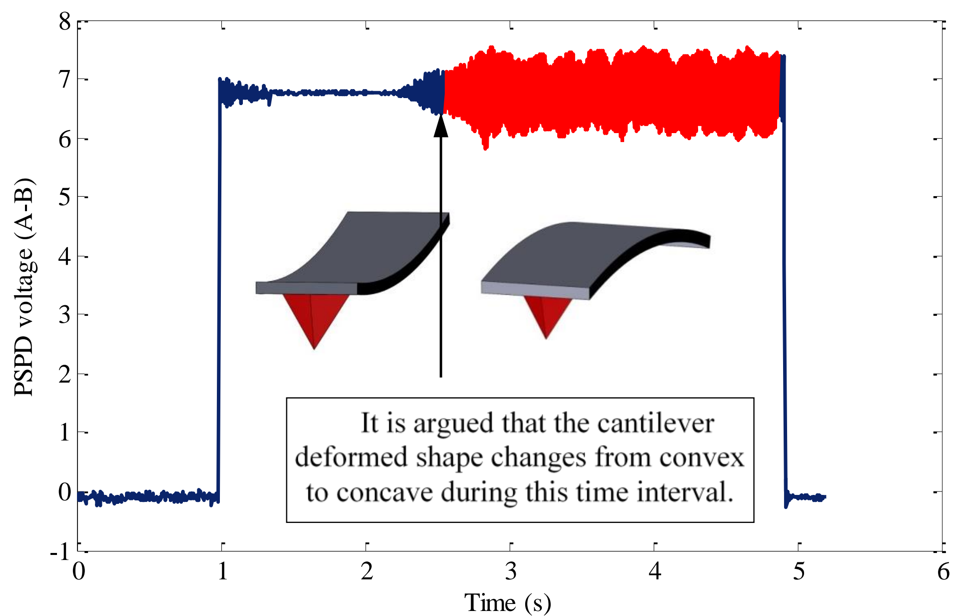

Figure 4.22 (A-B) PSPD voltage output signals when processing the Cu sample along the forward direction for a set normal load of 31 μN.

STEP 1: A-B voltage decreasing from V_1 to V_2 as a result of of the moment M_a dominating over the sliding of the tip

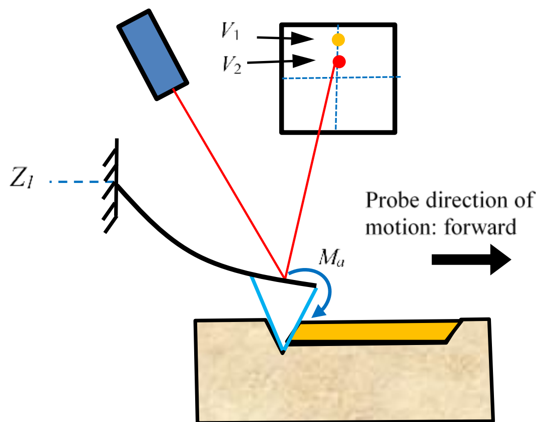

STEP 2: Z-scanner moving down to raise the PSPD voltage from V_2 to V_1

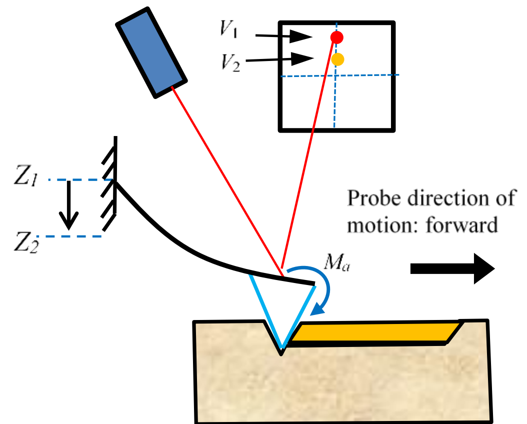

STEP 3: Steady state machining (the A-B voltage is kept constant). The shape of the cantilever is convex.

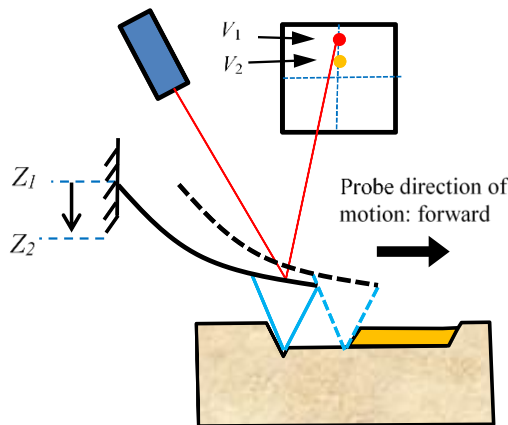

STEP 4: The increase of the moment M_a during cutting make the *Z*-scanner to move down again to keep the voltage at V_1

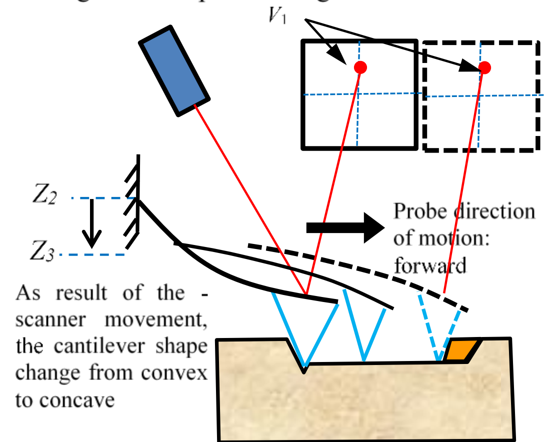

Figure 4.23 Illustration of the cantilever shape changing from convex to concave during the machining of a groove and the associated Z-scanner response

free end of the cantilever, which may eventually become negative and lead to feedback loop observed reaction, as illustrated with Figure 4.23. Based on the behaviour of the recorded Z-detector signals for these experiments, such convex to concave shape transition could also be found when machining with all the other considered loads in this higher range of applied normal forces, namely 34 µN, 36 µN and 39 µN. For example, Figures 4.24 and 4.25 display the signals obtained for the highest normal load tested. The main comment that can be added when analysing this figure is that the occurrence of the cantilever shape change occurs sooner along the groove with this higher load. In fact, the temporal dependence of the cantilever shape change as a function of the normal load value is clearly illustrated with the SEM micrographs of the grooves generated in this higher range of applied forces (see Figure 4.26). It is also interesting to notice from this figure that the convex to concave transition is obviously accompanied with a non-negligible modification of the topography of the groove. This is in spite of the fact that the force-controlled feedback loop ensures that the $V_{A\text{-}B}$ voltage is kept constant around a mean value set by the user. In particular, following the transition of the cantilever shape from convex to concave, AFM measurements indicate that the grooves became just over 50% deeper and wider on average.

In the following section, confirmation experiments were carried out to demonstrate that this change in the cantilever shape may also happen when processing along an inclined forward direction or when machining a different substrate or with a different type of probe.

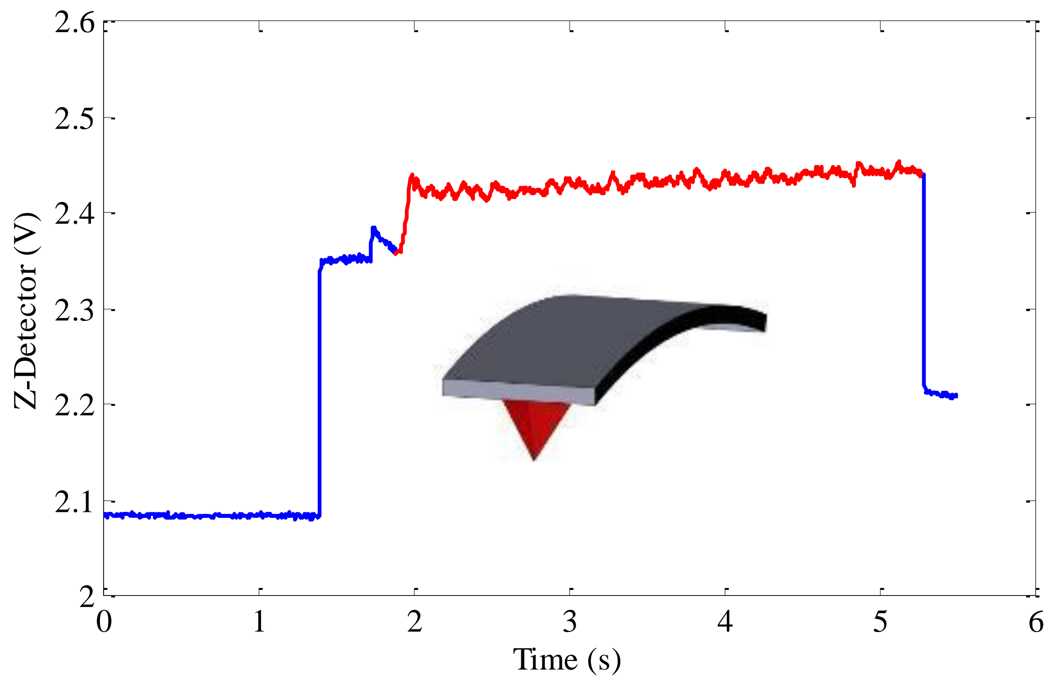

Figure 4.24 Z-detector recorded when using a set applied load of 39 µN.

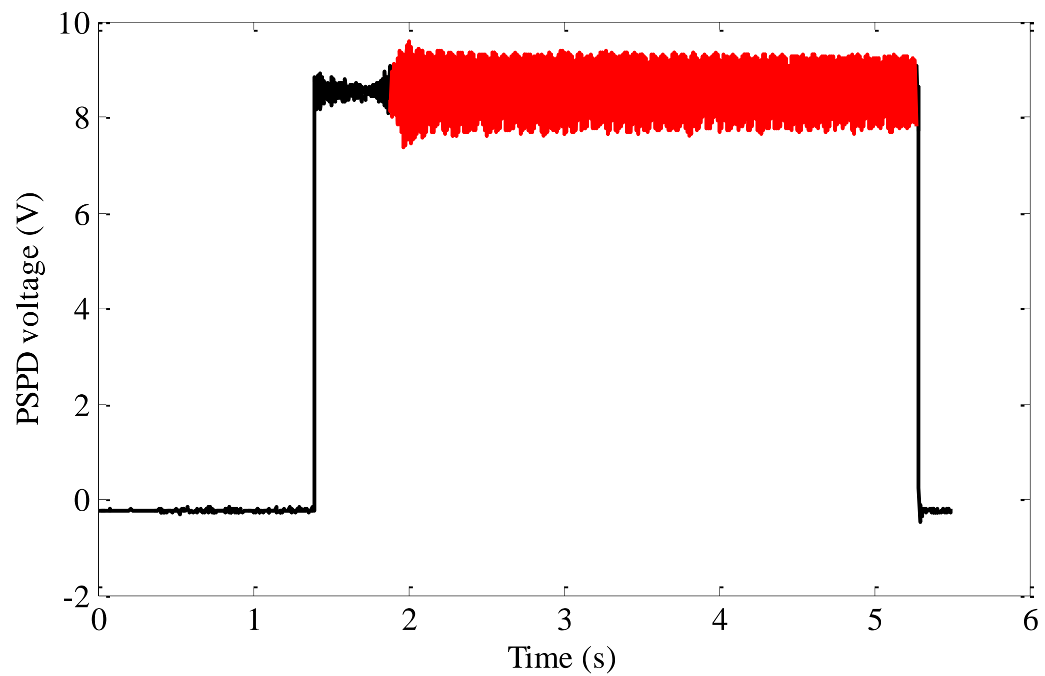

Figure 4.25 A-B signals recorded when using a set applied load of 39 µN.

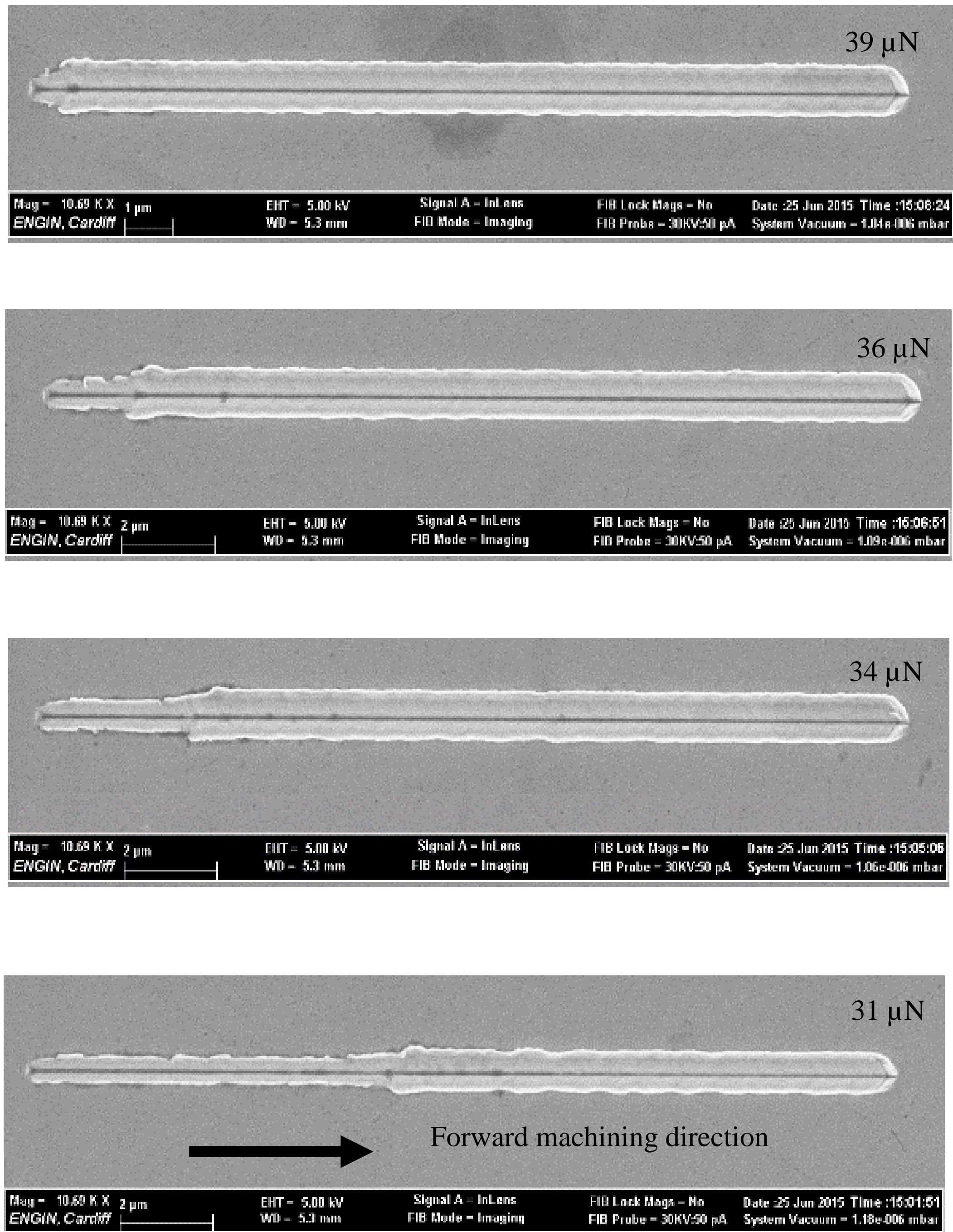

Figure 4.26 SEM micrographs of the grooves obtained when machining with the higher range of normal loads considered along the forward direction. Scale bar: 2 µm.

4.5 Verification experiment

4.5.1 Inclined forward direction

In this final experimental run, the PC and Cu samples were machined along an inclined angle of 22.5° with respect to the pure forward direction (see Figure 3.9). For the PC substrate, the set normal forces applied were comprised between 3.1 μN and 4.4 μN and the probe employed was the TESPD type. Until 4.1 μN, the recorded data for the Z-detector signal indicated that the bending of the cantilever kept a convex orientation throughout. As an example, the data obtained with a load of 3.1 μN are given with Figure 4.27. However, when the load was raised to 4.4 μN, a rapid increase in the Z-detector signal was recorded during the cutting of the groove as reported with Figure 4.28. In this case, the transition from convex to concave bending took place at the start of the groove. Thus, while the occurrence of the cantilever shape modification could be confirmed using a different set of experimental conditions compared to those reported in the previous section, it is interesting to note that, the transition from convex to concave bending was very sensitive to a small increment in the set normal load applied.

When processing the Cu sample along the same inclined forward angle, the Z-detector signal for applied loads between 14 μN to 32 μN was similar to that obtained in the pure forward direction for load lower than 31 μN. Therefore, the bending of the cantilever kept a convex orientation in this range of applied loads. However, when the load was raised to 33 μN, a rapid increase in the Z-detector signal was recorded during the cutting of the groove after about a quarter of the groove length as reported with Figure 4.29 The topography of the produced groove is illustrated in Figure 4.30. Quantitative AFM measurements of such grooves show that their depth and width increased up to 70% following such shape transition in the deformed cantilever.

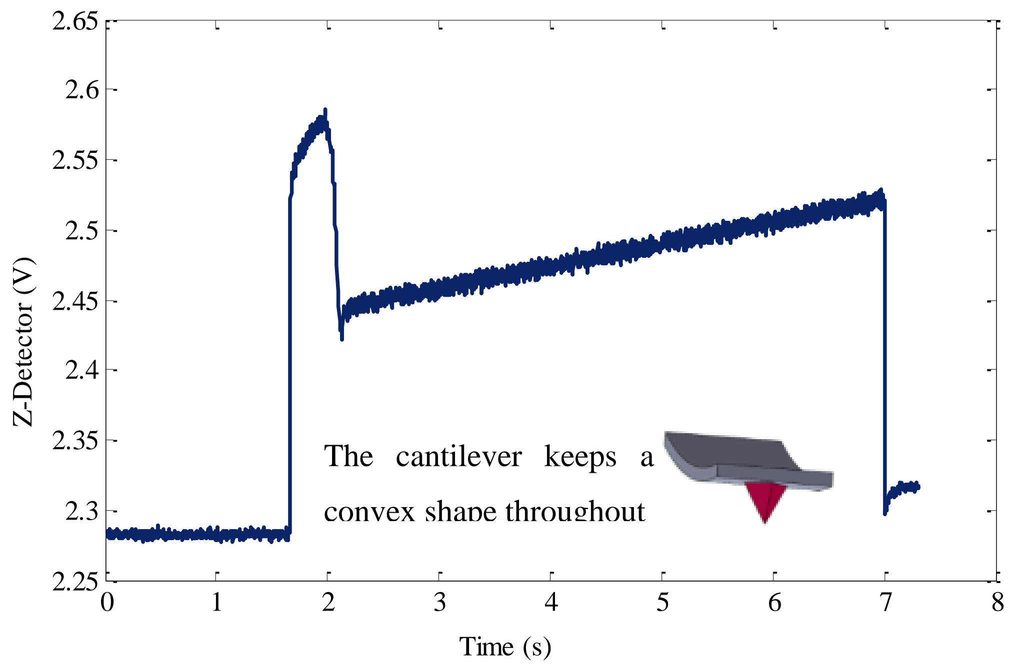

Figure 4.27 Z-detector signals obtained when machining the PC specimen along the inclined forward direction for a set normal applied load of 3.1 μN.

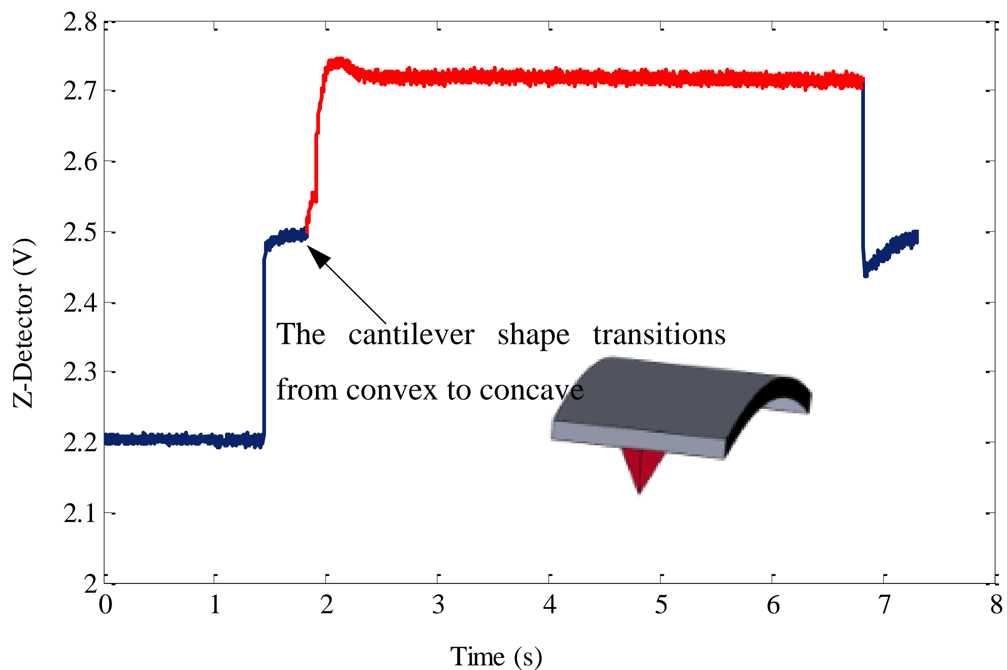

Figure 4.28 Z-detector signals obtained when machining the PC specimen along the inclined forward direction for a set normal applied load of 4.4 μN.

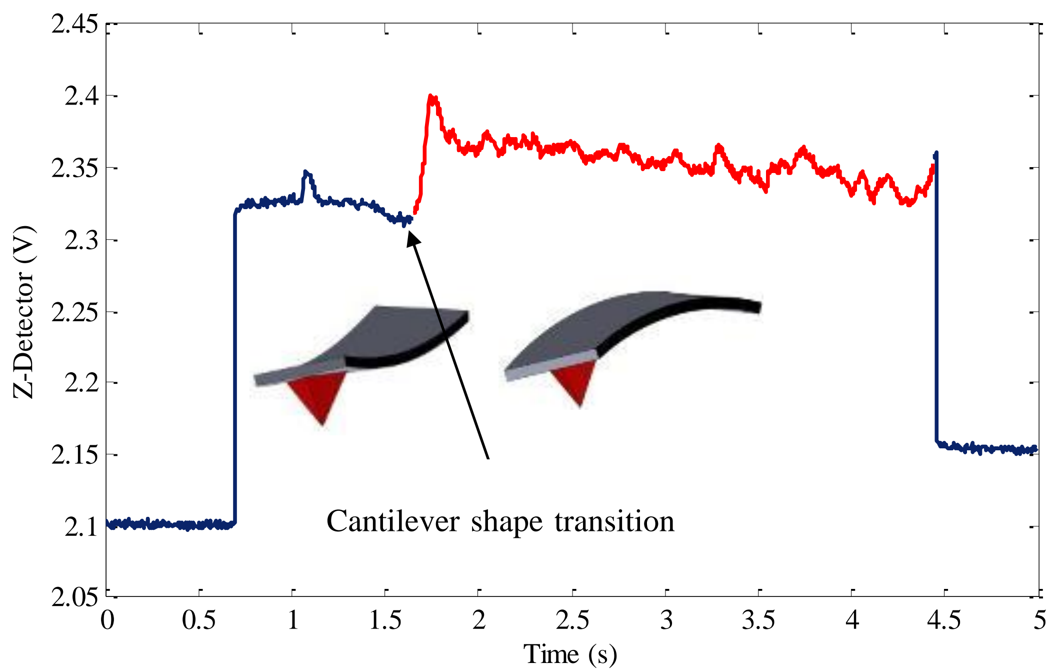

Figure 4.29 Z-detector signal recorded when machining the Cu specimen along the inclined forward direction for a set applied load of 33 μN

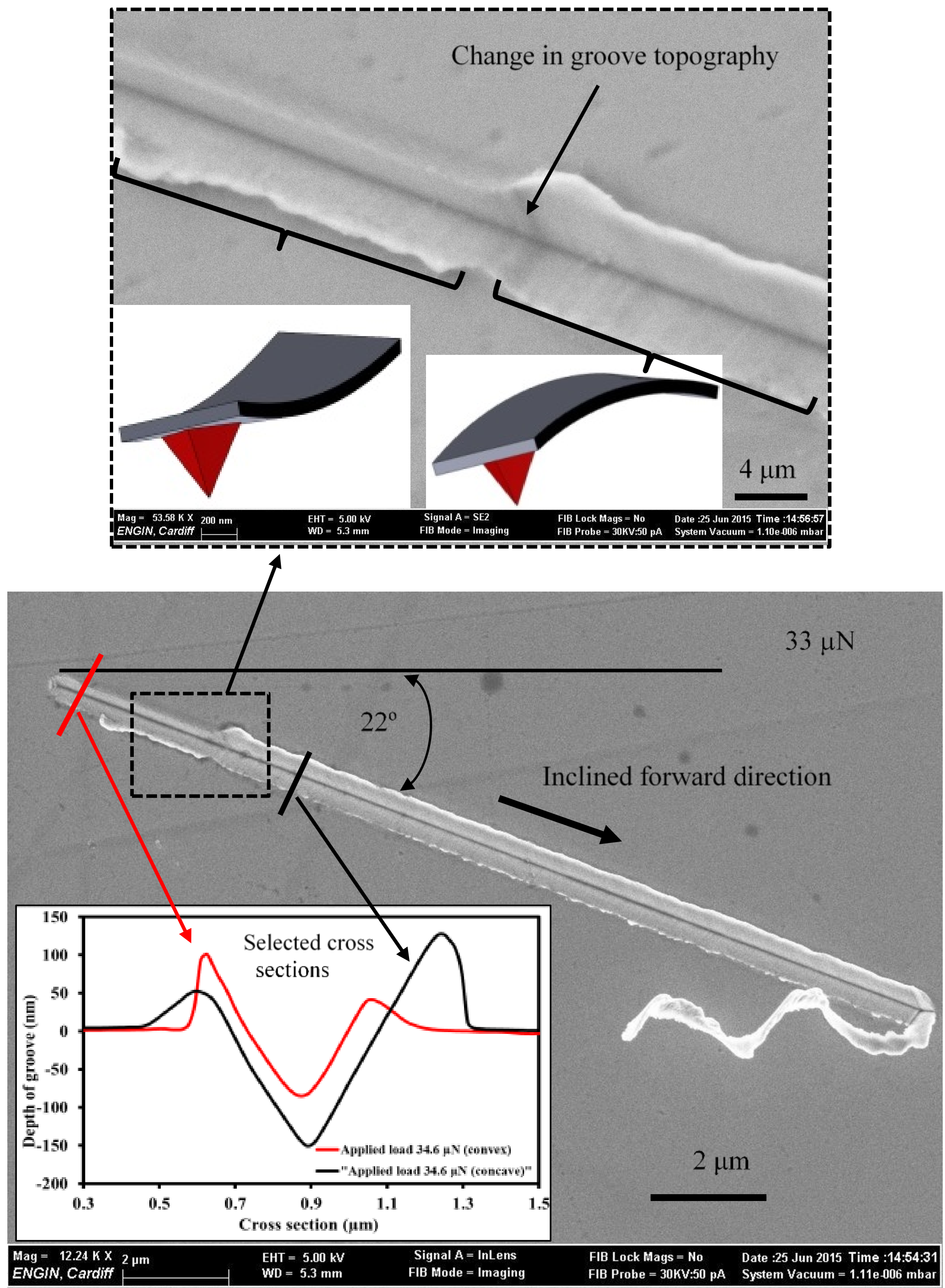

Figure 4.30 SEM micrographs of the grooves obtained when machining the Cu specimen with a normal load of 33 μN.

4.5.2 Measurements of the machining distance

Figure 4.31 shows an AFM scan and an SEM micrograph of a groove and the corresponding Z-detector obtained when processing the Cu specimen for a set normal load of 31 μN in the forward direction. The machined distance between the indentation step (A) and the point, (B), at which the cantilever deflected shape changed from convex to concave was measured and compared using three different methods. First, the AFM scan was analysed using a proprietary software (XEI from Park Systems) to measure the distance between point A and B. In this case, it was found to be approximately 7.55 μm. Second, the distance between these point was measured using the SEM micrograph and it was found to be about 7.66 μm. Third, in order to further confirm the reliability of Z-detector signals, the time interval between the starting point of indentation and the point at which the change in the shape of the cantilever could be noticed from such a signal was determined. It was found to be about 1.52 second. Then, the distance between this two points was calculated by multiplying the machining velocity, *V*, by this time. In this way this distance was found to be approximately 7.6 μm, which is in very good agreement with the estimations made from the AFM and the SEM data.

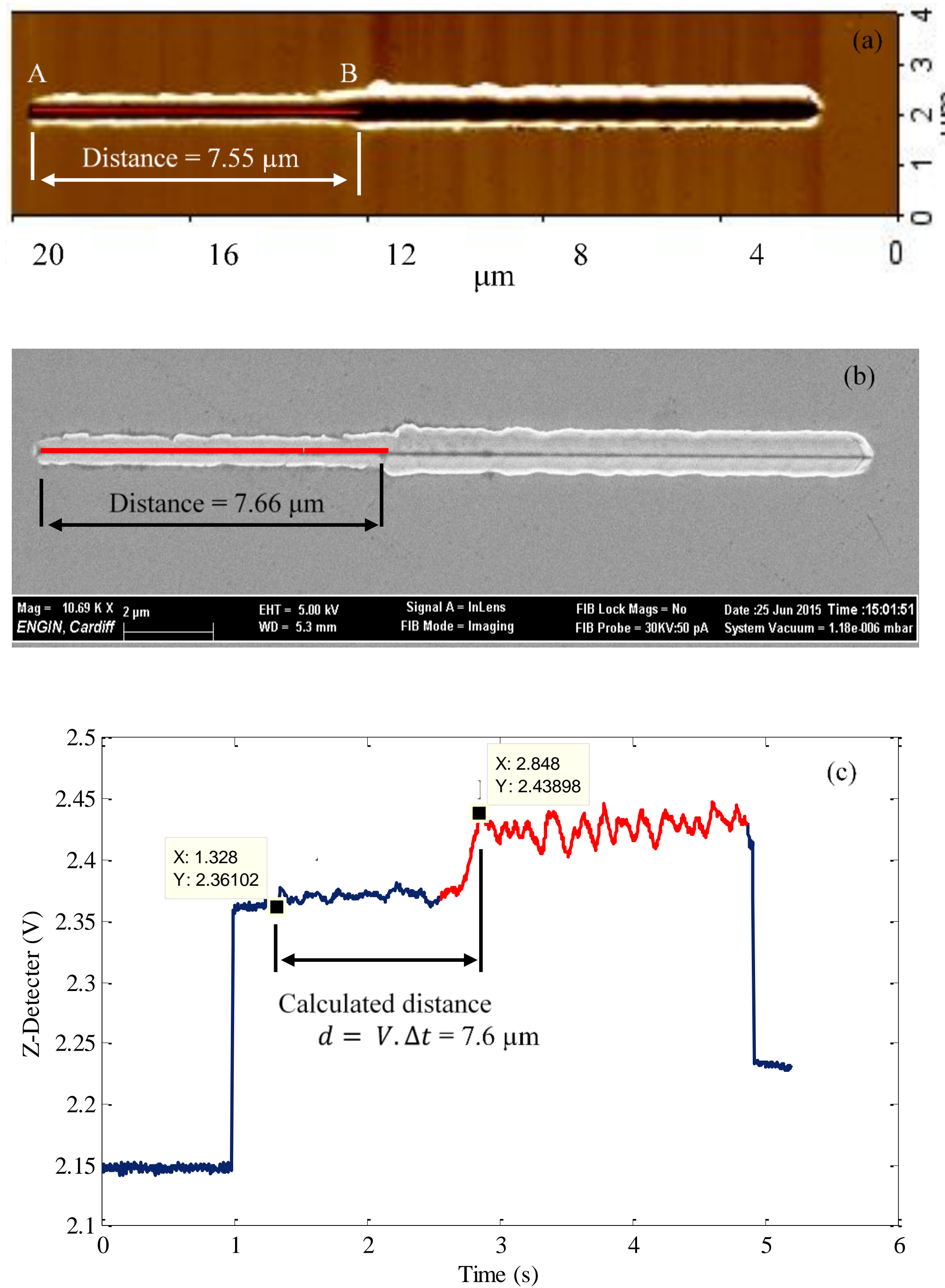

Figure 4.31 (a) AFM scan and (b) SEM micrographs of the groove and (c) recorded Z-detector signal when machining the Cu sample for a set normal load of 31 µN in the forward direction.

4.6 Summary

This chapter describes an important phenomenon specific for AFM nanomachining in the forward direction: under certain processing conditions, the deformed shape of the cantilever probe may change from a convex to a concave orientation. It is argued that the assumption commonly adopted in the literature that the deformed shape of the AFM cantilever used for tip-based nanomachining along the forward cutting direction, is always concave, is wrong. To explain and justify this claim, a refined theoretical analysis of the work of an actual AFM probe was performed, along with a novel interpretation of monitored signals from an advanced new experimental set-up for the determination of the actual cantilever deflected shape during AFM nanomachining. Based on the theoretical analysis, it is shown that the bending of the cantilever during nanomachining in this direction can be convex, especially for small value of the cutting force acting on the tip in the direction of cutting F_a relative to the force needed to keep the tip in the workpiece F_{th}.

The experimental evidence provided that both (concave and convex) bending orientations of the cantilever could be observed during actual machining tests. These results are based on the combined analyses of three different output signals monitored during processing in addition to the subsequent inspection of the machined topography by producing grooves.

The results provided from both theoretical analysis and experimental work can add other interesting outcomes. Firstly, this study indicates that the analysis of the Z-detector signal is relatively rich and provides valuable data for understanding the mechanical behaviour of the cantilever deflected shape. Secondly, this research suggests that following the initial vertical engagement of the tip into the substrate material, the tip may subsequently slide upwards on the face of the created indent when the lateral motion of the AFM stage begins. This observation was made for the small values of set normal loads considered. For increased values, the tip was more likely to stick onto the face of the indent at this specific stage of the process. Thirdly, the analysis of the Z-detector voltage suggests that AFM nanomachining is achieved in a minimum of five steps, namely, approach, indentation, transition, scratching and reset step. This analysis may be used to gain an improved understanding of the hardware and physical considerations of AFM.

Finally, using both SEM micrographs of the grooves and AFM topography studies, it was demonstrated that not only the applied load has an effect on the depth and width of the groove, but also the deflected shape of the AFM cantilever has a significant influence on the trench shape. The latter phenomenon may cause that the trench to become deeper and larger. For example, it has been observed that grooves becomes over 50% deeper and wider on an average when the cantilever deflected shape changes from convex to concave.

Chapter 5

Assessment of the applied normal force during the nanoindentation and the tip-based nanomachining processes

5.1 Introduction

As it was presented in Chapter 2, the determination of the normal force applied by the tip of an AFM probe onto a sample depends on the a-priori calibration of both the normal spring constant of the cantilever and the normal sensitivity of the PSDP. It was also highlighted that, when the AFM stage is static (i.e. during a nanoindentation operation), the combined influence of the cantilever geometry and of the tilt angle between the long axis of the cantilever and the sample surface is generally not taken into account in determining the applied normal force. Therefore, the first main objective of this Chapter is to present a refined theoretical model to determine the applied normal force when the AFM stage is static by taking into account the influence the tilt angle and the cantilever geometry.

In addition, it was also pointed out in Chapter 2 that, when the AFM stage is not static (i.e. during a tip-based nanomachining operation), the axial force, F_a, generated at the tip creates a moment on the free end of the cantilever. The influence of this moment on the normal sensitivity of the PSPD and consequently, on the determination of the applied normal force has been neglected in tip-based nanomachining studies. In this context, this Chapter reports theoretical and experimental analysis, which show that the conventional method for determining the applied normal load during AFM tip-based nanomachining is wrong. These analyses also reveal that the vertical sensitivity of the PSPD cannot be considered a constant parameter. Thus, the second main objective of this Chapter 5 is to propose a new theoretical model to determine the vertical sensitivity of the PSPD during nanomachining as a function of the machining direction.

This Chapter is organised as follows. The next section is concerned with the determination of the applied normal load when the stage of the AFM is static. In particular, a refined theoretical analysis is reported to modify the conventional approach for assessing the applied normal force in this case. In this section, experimental work is also reported to discuss the implications of the new formula. Then, the focus of section 3 is on the study of the assessment of the applied normal load when the tip is engaged into the sample material while the probe also describes horizontal motions relative to sample (i.e. during tip-based nanomanchining). In particular, experimental and theoretical evidences are reported to show that the applied normal load during nanomachining is not

equal to that set by the user prior to the start of the machining process. In this section, it is also shown that, consequently, the normal sensitivity value of the PSPD during nanomachining should also not be equal to the value determined when the AFM stage is static. Following this, a refined theoretical analysis of the cantilever is proposed to determine the actual value of the normal sensitivity of the PSPD during tip-based nanomachining.

5.2 Assessment of the applied normal force during nanoindentation.

5.2.1 Theoretical analysis

The refined theoretical analysis reported here is based on the basic beam theory. It is carried out in the scenario of the cantilever being subjected to endpoint loading without any relative horizontal motion between the tip and the sample. The principal difference between the usual formula used to express the normal force and the refined scheme presented in this section is that the inclination angle between the cantilever and the sample surface and the probe geometry (more specifically, the tip height, the cantilever thickness and length) are also considered in order to take into account the actual configuration of AFM systems. A schematic illustration of the force acting on the tip during nano indentation is given in Figure 5.1(a) and the corresponding free body diagram is shown with Figure 5.1(b)

Due to the indentation angle, α, between the cantilever and the sample surface, the applied normal load contributes to generate a moment, M_B, around at the free end of the cantilever, point B. By equilibrium, we express this moment as:

$$M_B = F_n.\left(h + \frac{t}{2}\right).sin\alpha \tag{5.1}$$

where F_n is the applied load on the tip, h is the height of tip and t is the thickness of cantilever. The bending moment, $M(y)$, at a distance, y, from the cantilever free end is obtained from the free body diagram of Figure 5.1(c):

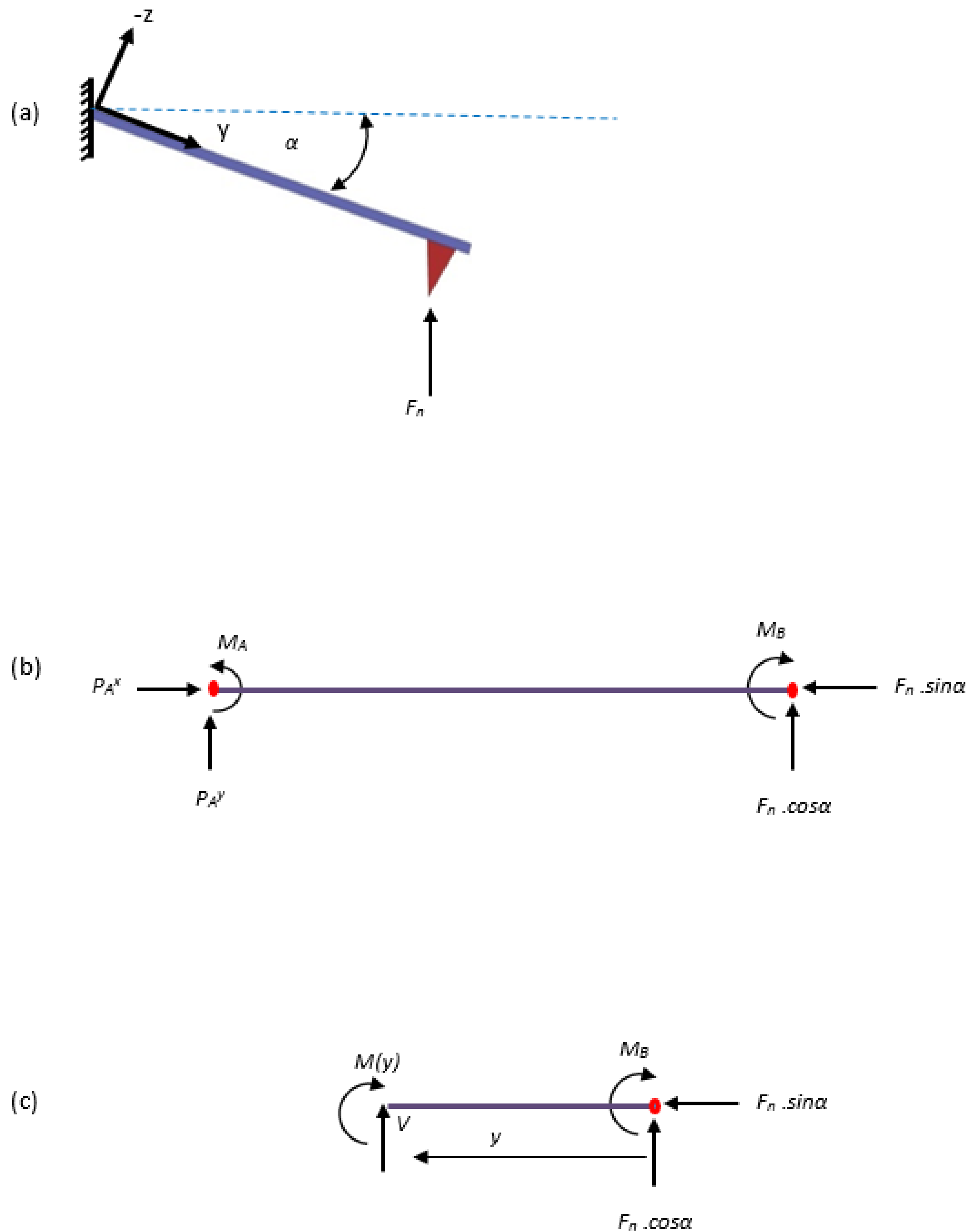

Figure 5.1 Schematic representation of the AFM probe during nanoindentation, (b) corresponding free body diagram and (c) free body diagram of cantilever portion.

$$M(y) = -M_B + F_n . cos\alpha . y \quad (5.2)$$

Substituting the proceeding expression for M_B in equation (5.2), it results

$$M(y) = -F_n . \left(h + \frac{t}{2}\right) . sin\alpha + F_n . cos\alpha . y \quad (5.3)$$

The basic differential equation of the deflected curve of the beam is:

$$EI \frac{d^2w}{dy^2} = -M(y) \quad (5.4)$$

When the expression for the bending moment in equation (5.3) is substituted into the differential equation, we obtain

$$EI \frac{d^2w}{dy^2} = F_n . \left(h + \frac{t}{2}\right) . sin\alpha - F_n . cos\alpha . y \quad (5.5)$$

Both sides of this equation are integrated to express the slope of the beam

$$EI \frac{dw}{dy}(y) = F_n . \left(h + \frac{t}{2}\right) . sin\alpha . y - F_n . cos\alpha . \frac{y^2}{2} + C_1 \quad (5.6)$$

where C_1 is a constant of integration. For the above integration, similarly to the theoretical development reported in Chapter 4, the flexural rigidity EI is also considered constant. This is the case for rectangular AFM probes, which represent the majority of probe designs. Applying the boundary condition that

$$y = L \quad (5.7)$$

and that the slope of the cantilever is zero at its fixed end, we can state

$$\frac{dw(L)}{dy} = 0 \quad (5.8)$$

we can express equation (5.6) as follows

$$0 = F_n . \left(h + \frac{t}{2}\right) . sin\alpha . L - F_n . cos\alpha . \frac{L^2}{2} + C_1 \quad (5.9)$$

Thus, the constant of integration becomes

$$C_1 = -F_n.\left(h+\frac{t}{2}\right).sin\alpha.L + F_n.cos\alpha.\frac{L^2}{2} \quad (5.10)$$

Substituting the proceeding expression for C_1 in equation (5.6), we get

$$EI.\frac{dw}{dy} = F_n.\left(h+\frac{t}{2}\right).sin\alpha.y - F_n.cos\alpha.\frac{y^2}{2} - F_n.\left(h+\frac{t}{2}\right).sin\alpha.L + F_n.cos\alpha.\frac{L^2}{2} \quad (5.11)$$

To obtain the angle of rotation, θ, at the free end of the cantilever (i.e. point B), we replace y by 0 in equation (5.11). With further simplification of the resulting equation, the slope at the free end of the deformed cantilever is:

$$\theta = \frac{dw}{dy} = \frac{1}{EI}\left[-F_n.\left(h+\frac{t}{2}\right).sin\alpha.L + F_n.cos\alpha.\frac{L^2}{2}\right] \quad (5.12)$$

Thus,

$$\theta = \frac{F_n.L}{2.EI}\left[L.cos\alpha - 2.\left(h+\frac{t}{2}\right).sin\alpha\right] \quad (5.13)$$

The equation (5.13) can be written as follows:

$$\frac{F_n.L}{2.EI} = \frac{\theta}{\left[L.cos\alpha - 2.\left(h+\frac{t}{2}\right).sin\alpha\right]} \quad (5.14)$$

Furthermore, to obtain the deflection of the cantilever at point B, both sides of the equation (5.6) are integrated. This leads to

$$EI\ w(y) = F_n.\left(h+\frac{t}{2}\right).sin\alpha.\frac{y^2}{2} - F_n.cos\alpha.\frac{y^3}{6} + C_1.y + C_2 \quad (5.15)$$

Substituting the proceeding expression for C_1 in equation (5.15), we get

$$E.I.w(y) = F_n.\left(h+\frac{t}{2}\right).sin\alpha.\frac{y^2}{2} - F_n.cos\alpha.\frac{y^3}{6} - F_n.\left(h+\frac{t}{2}\right).sin\alpha.L.y + F_n.cos\alpha.\frac{L^2}{2}.y + C_2 \tag{5.16}$$

The constant of integration C_2 can be found from the boundary condition that the deflection of the beam is zero at the support end. Thus, we have the following condition:

$$w(L) = 0 \tag{5.17}$$

Substituting equation (5.17) into equation (5.16) and simplifying, we obtain

$$C_2 = F_n.\left(h+\frac{t}{2}\right).sin\alpha.\frac{L^2}{2} - F_n.cos\alpha.\frac{L^3}{6} - F_n.\left(h+\frac{t}{2}\right).sin\alpha.L.L + F_n.cos\alpha.\frac{L^2}{2}.L \tag{5.18}$$

Further simplifications of equation (5.18) lead to

$$C_2 = \frac{F_n.L^2}{6}\left[-2.L.cos\alpha + 3.\left(h+\frac{t}{2}\right).sin\alpha\right] \tag{5.19}$$

By substituting equations (5.19) into equation (5.16), we obtain

$$E.I.w(y) = F_n.\left(h+\frac{t}{2}\right).sin\alpha.\frac{y^2}{2} - F_n.cos\alpha.\frac{y^3}{6} - F_n.\left(h+\frac{t}{2}\right).sin\alpha.L.y + F_n.cos\alpha.\frac{L^2}{2}.y + \frac{F_n.L^2}{6}\left[-2.L.cos\alpha + 3.\left(h+\frac{t}{2}\right).sin\alpha\right] \tag{5.20}$$

To express the deflection at the free end of the cantilever, point B, we substitute y=0 into equation (5.20). With further simplification, this deflection is given by

$$w(0) = \frac{F_n.L^2}{6.E.I}\left[-2.L.cos\alpha + 3.\left(h+\frac{t}{2}\right).sin\alpha\right] \tag{5.21}$$

The equation (5.21) can be written as follows:

$$\frac{F_n.L}{2.EI} = \frac{3.w(0)}{L.\left[-2.L.cos\alpha + 3.\left(h + \frac{t}{2}\right).sin\alpha\right]} \quad (5.22)$$

In order to find the relationship between the deflection and the bending angle at the free end of the cantilever, we substitute equation (5.22) into equation (5.14). In this way, we can write

$$\frac{\theta}{L.cos\alpha - 2.\left(h + \frac{t}{2}\right).sin\alpha} = \frac{3.w(0)}{L.\left(-2.L.cos\alpha + 3.\left(h + \frac{t}{2}\right).sin\alpha\right)} \quad (5.23$$

Thus, we can express θ as a function of $w(0)$

$$\theta = \frac{3.w(0)}{L}\left[\frac{L.cos\alpha - 2.\left(h + \frac{t}{2}\right).sin\alpha}{-2.L.cos\alpha + 3.\left(h + \frac{t}{2}\right).sin\alpha}\right] \quad (5.24)$$

Based on the work of Sarid (1994), we now express the vertical shift of the laser spot on the PSPD, d, as a function of θ

$$d = 2.\theta.D \quad (5.25)$$

where D is the spatial distance between the PSPD and the cantilever free end. Figure 5.2 provides a schematic illustration for these two parameters. Based on the study from Liu (2010), the vertical voltage differential, V_{A-B} due to d can be written as:

$$V_{A-B} = \beta_c.d \quad (5.26)$$

where β_c is a conversion coefficient, which depends on the parameters of the PSPD. Combining equations (5.24) and (5.25) into equation (5.26) and with further simplification, we obtain

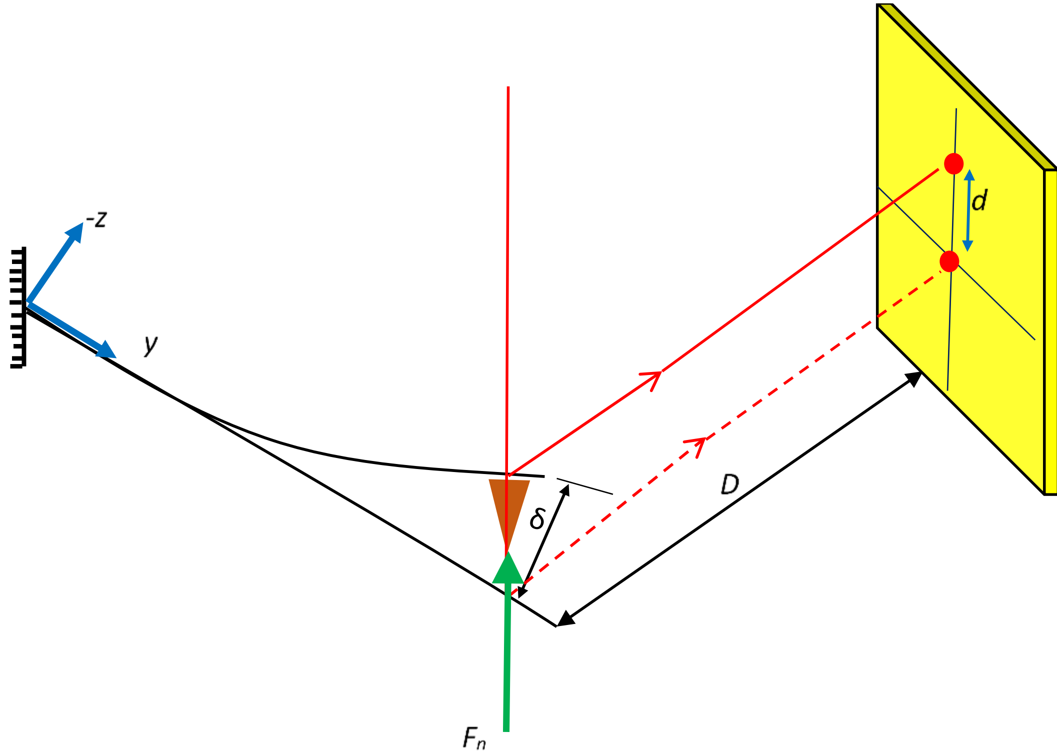

Figure 5.2 Illustration of the vertical shift of the laser spot on the PSPD

$$V_{A-B} = \beta_c.2.\theta.D = \frac{6.\beta_c.D}{L}\left[\frac{L.cos\alpha - 2.\left(h+\frac{t}{2}\right).sin\alpha}{-2.L.cos\alpha + 3.\left(h+\frac{t}{2}\right).sin\alpha}\right].w(0) \quad (5.27)$$

From the equation (5.27), we have expressed the vertical output signal as a function of the cantilever deflection at its free end. We introduce the constant, σ, to rewrite the equation (5.27) as follows:

$$V_{A-B} = \sigma.w(0) \quad (5.28)$$

Thus, the unit for σ is in V/m. Thus, this constant is also the inverse of the vertical sensitivity of the PSPD, which is normally expressed in m/V. The expression for σ is written below for completeness:

$$\sigma = \frac{6.\beta_c.D}{L}\left[\frac{L.cos\alpha - 2.\left(h+\frac{t}{2}\right).sin\alpha}{-2.L.cos\alpha + 3.\left(h+\frac{t}{2}\right).sin\alpha}\right] \quad (5.29)$$

As pointed out by Butt and Jaschke (1995), with the optical lever technique, it is the bending angle at the end of the cantilever, which is measured rather than the deflection itself. This is compatible with the result of an equation (5.27). Indeed, one could easily express V_{A-B} as a function of θ by rearranging equation (5.24) such that $w(0)$ is isolated on one side of the equation and by substituting $w(0)$ in equation (5.27) by the result of this rearrangement.

As stated above, σ is the inverse of the normal sensitivity of the PSPD. Based on equation (2.2), given in Section 2.4 (Chapter 2), the normal sensitivity is expressed as:

$$S_n = \frac{1}{\sigma} = \frac{w(0)}{V_{A-B}} \quad (5.30)$$

The spring constant of a rectangular cantilever, K, is given by (Cleveland *et al.* 1993, Clifford and Seah 2005)

$$K = \frac{3.E.I}{L^3} \quad (5.31)$$

Substituting equations (5.30) and (5.31) into equation (5.21) and simplifying, we obtain

$$S_n.V_{A-B} = \frac{3.F_n.}{6.L.K}\left[-2.L.cos\alpha + 3.\left(h+\frac{t}{2}\right).sin\alpha\right] \quad (5.32)$$

Based on this, we now express F_n

$$F_n = \frac{2.K.S_n.V_{A-B}.L}{\left[-2.L.cos\alpha + 3.\left(h+\frac{t}{2}\right).sin\alpha\right]} \quad (5.33)$$

This equation can be simplified as follows:

$$F_n = C.K.S_n.\ V_{A-B} \quad (5.34)$$

In contrast with the conventional equation used to define F_n , which is $F_n = K$ x S_n x $V_{A\text{-}B}$, (c.f. Section 2.4 in Chapter 2), we now have introduced a correction factor C, which is expressed as

$$C = \frac{2.L}{\left[-2.L.\cos\alpha + 3.\left(h + \frac{t}{2}\right).\sin\alpha\right]} \tag{5.35}$$

Thus, in the refined model presented here, the definition of the applied normal force not only depends on the spring constant of the cantilever and the normal sensitivity of the PSPD, but also on four geometric parameters namely, α, h, t and L. In the following sub-section, we study the implication of taking into account this correction factor when assessing F_n in practice.

5.2.2 Assessment of the applied normal load using the refined model

The correction factor, C, was calculated for a range of commercial probes based on the dimensions provided by the manufacturers. The results are given in Table 5.1. For each probe in this table, the thickness, length and the tip height are given a minimum, maximum and typical values. This is due to the fact that probes are fabricated with a certain degree of uncertainty. For this reason, manufacturers of AFM probes normally provide such a range of values for these dimensions. In addition, this table considers two possible values for the inclination angle, α, namely 12° and 20° because these are most commonly found in AFM instruments. The important outcome from this table is that the correction factor is always higher than unity. This means that the conventional approach to assess F_n leads to an under-estimation of the pre-set applied force. In addition, for the considered set of probes in Table 5.1, the lowest and highest values for C were calculated for the models named “PPP-CONTR” and “DNISP”, respectively. More specifically, it was found that, for an inclination angle of 12°, the value of F_n is conventionally under-estimated between 3% and 8.6 %. For the higher inclination angle of 20°, this range is increased from 7.8% to 18.3%.

Next, we present an example when the refined model is employed to extract a force-distance curve using AFM nanoindentation. This particular AFM application was selected because such curves are a common tool to extract a number of material properties from

indented substrates, such as Young's module and hardness (Borodich 2014). In this case, accurate knowledge of the maximum normal applied load, which is conventionally referred to as P_{max} in the indentation literature, and of the corresponding maximum depth of the indent, which is conventionally referred to as h_{max}, is required. Figure 5.3 shows the plots of two force-distance (f-d) curves obtained using the AFM instrumentation already described in Chapter 3. One of these curves was plotted using the conventional $F_n = K$ x S_n x $V_{A\text{-}B}$ relationship, while the other curve was obtained using the refined model. The probe used for this experiment was the model ND-DYIRS from Advanced Diamond Technologies. This probe is made of ultra nano crystalline diamond. SEM micrographs of the probe employed are given in Figure 5.4. The cantilever has a rectangular shape while the tip is a 4-sided diamond pyramid as shown in Figure 5.4. The respective procedures followed to determine both the spring constant value and the normal sensitivity were those already explained in Chapter 4. The spring constant was found to be 27 N/m. The probe dimensions required to determine the spring constant were measured using the SEM micrographs displayed in Figure 5.4. These are summarised in Table 5.2. Following the nanoindentation experiment, these dimensions were also used to assess F_n for both the conventional approach and for the refined model.

As with all AFM instruments, the compliance of the probe needs to be taken into account when extracting f-d curves (Capella and Dietler, 1999). This means that the deflection of the cantilever should be discarded from the obtained raw AFM nanoindentation distance data as follows

$$h_d = Z_{scanner} - w(0) = Z_{scanner} - (S_n \times V_{A-B}) \tag{5.36}$$

where h_d is the depth of the tip penetration and $Z_{scanner}$ is the vertical distance travelled by the fixed end of the probe which, in practice, is also equal to the displacement of the Z-scanner. In the equation above, h_d is expressed using the conventional approach. Below, we now define h_d by taking into account the inclination of the cantilever, α, and the correction factor, C, when expressing the deflection of the cantilever (see Figure 5.5). In this case, the depth of the tip penetration is

$$h_d = Z_{scanner} - w(0).cos\alpha = Z_{scanner} - \frac{(S_n \times V_{A-B})}{C}.cos\alpha \tag{5.37}$$

As expected, the applied normal load for the plot prepared using the refined model is higher than that using the conventional approach (see Figure 5.3). This is due to the correction factor, which is always higher than unity. Consequently, the penetration depth should be deeper than that assumed with the conventional approach. This is visible from Figure 5.3. This is also shown with equation (5.37) above because 1) $\cos \alpha$ is always lower than unity and 2) C is always higher than unity. Thus, the value substracted from the measured raw AFM nanoindentation data (i.e. the Z-scanner data) is smaller when considering the refined model in comparison with the traditional approach.

Table 5.1 Correction factor calculated for a range of commercial probes

Probe Types	Size	Dimension of probe (µm)			Correction Factor C	
		Length L	Thickness t	Height h	Inclination 12°	Inclination 20°
DCP11	Min	95	1.7	10	1.060	1.134
	Typical	100	2.0	12.5	1.068	1.148
	Max	105	2.3	15	1.075	1.161
DCP11	Min	125	1.7	10	1.051	1.117
	Typical	130	2.0	12.5	1.057	1.128
	Max	135	2.3	15	1.062	1.138
DCP20	Min	85	1.7	10	1.065	1.143
	Typical	90	2.0	12.5	1.073	1.159
	Max	95	2.3	15	1.080	1.173
DCP10	Min	90	1.5	10	1.062	1.138
	Typical	100	2.0	12.5	1.068	1.148
	Max	110	2.5	15	1.072	1.157
CSG01	Min	335	0.5	14	1.036	1.089
	Typical	350	1.0	15	1.036	1.090
	Max	365	1.5	16	1.037	1.091
CSG10	Min	215	0.5	14	1.044	1.104
	Typical	225	1.0	15	1.045	1.105
	Max	240	1.5	16	1.045	1.106
qp-CONT	Min	120	0.72	5.5	1.038	1.093
	Typical	125	0.745	7.15	1.042	1.100
	Max	130	0.78	8.5	1.045	1.105
PPP-CONTR	Min	440	1.0	10	**1.030**	**1.078**
	Typical	450	2.0	12.5	1.032	1.081
	Max	460	3.0	15	1.034	1.085
DNISP	Min	300	11	50	**1.086**	**1.183**
	Typical	350	13	50	1.077	1.167
	Max	500	15	50	1.061	1.135
ND-DYIRS-5	Min	125	2.5	5.6	1.040	1.096
	Typical	135	3.0	5.7	1.040	1.096
	Max	140	3.5	5.8	1.040	1.096
ND-SSCRL-5	Min	125	1.9	5.6	1.039	1.095
	Typical	130	2.3	5.7	1.039	1.095
	Max	135	2.8	5.8	1.040	1.096
ND-DYIRS-4	Min	115	2.5	5.66	1.042	1.100
	Typical	120	2.5	5.66	1.041	1.098
	Max	125	2.5	5.66	1.040	1.097

Note: The results highlighted in bold in the column "Correction Factor" correspond to the highest and lowest values calculated overall.

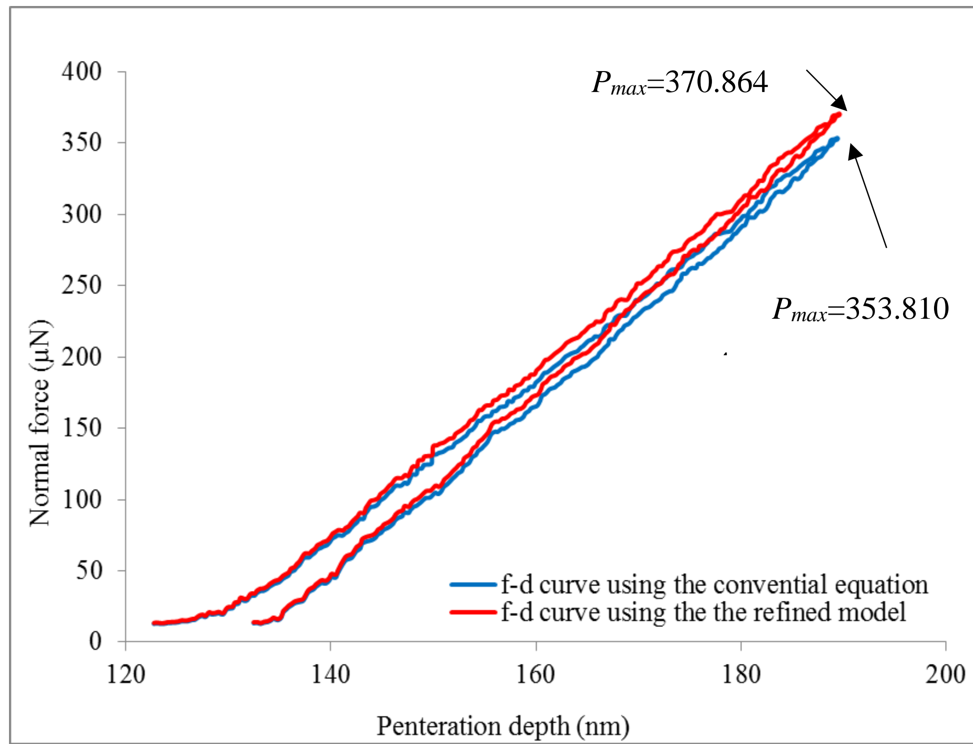

Figure 5.3 Curve of loading and unloading for PC sample

Table 5.2 Measured dimensions for the ND-DYIRS probe

Probe dimensions	Value
Length	141.6 µm
Width	35.3 µm
Thickness	3.4 µm
Tip height	9.3 µm

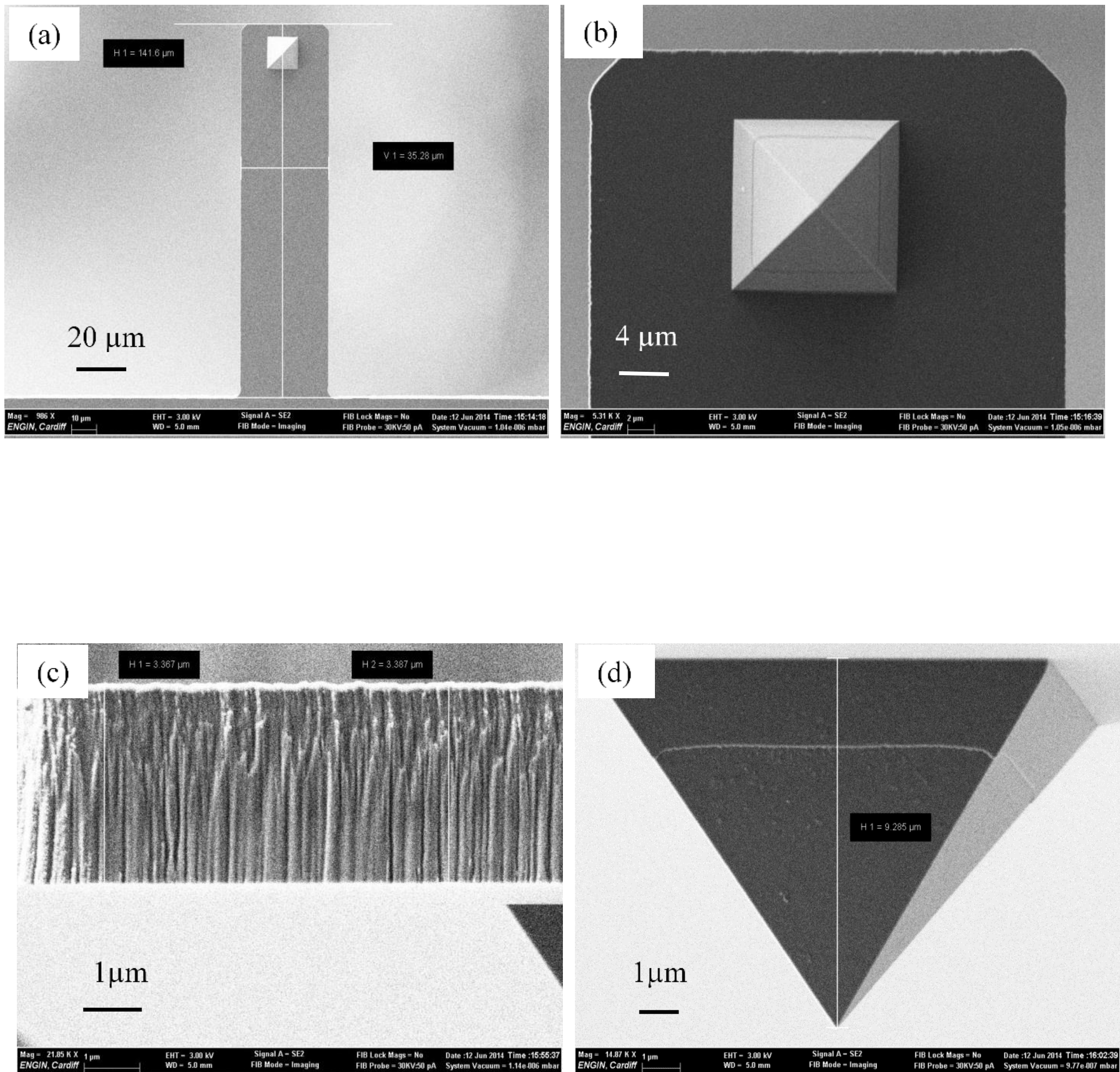

Figure 5.4 SEM micrographs of the probe ND-DYIRS utilised (a) overall view of the cantilever (b) tip geometry (c) cantilever thickness (d) tip height

5.3 Assessment of the applied normal force during tip-based nanomachining

A reported in Chapter 2, a common assumption made when using an AFM device in contact mode is that a given $V_{A\text{-}B}$ voltage output from the PSPD corresponds to a specific vertical deflection at the free end of the cantilever. Hence, it is also normally inferred that a given value of the A-B signal corresponds to a unique normal force value (see e.g. (Binnig *et al.* 1986b, Bowen and Hilal 2009, Christopher 2012, Eaton and West 2010, Meyer 1992, Mironov 2004, Wu *et al.* 2012)). However, it should be noted that, when scanning the tip across a sample, if the tip is in contact with the surface, or engaged within the surface as it is the case for tip-based nano machining, the cantilever deflection should also depends on the moment induced by a force acting on the tip. This force was defined in Chapter 2 and referred to as the axial force, F_a. Thus, it is argued that one should not assume that a given $V_{A\text{-}B}$ output obtained 1) with and 2) without tip horizontal motions in contact mode results in the same cantilever deflection in both cases, and thus, in the same value of applied normal load, F_n. To support this statement, the following two sub-sections respectively provide theoretical and experimental analyses of the influence of F_a on the resulting F_n.

5.3.1 Influence of the axial force: experimental analysis

The nanomachining tests presented here were performed on single a crystal copper sample along the backward direction and using a DNISP probe from Bruker. The cutting speed and length of the produced groove were 5 µm/s and 15 µm, respectively. The normal load set prior to the start of the machining operation, i.e. when the stage of the AFM instrument was static, was 29 µN. Following the completion of the machining process, another AFM probe, namely the CSG model from NT-MDT, was utilised for the purpose of recording the topography of the obtained groove. For this nanomachining experiment, the AFM instrument was operated in the “force-controlled” mode.

The AFM scan of the produced groove is displayed in Figure 5.5(a). In addition, Figure 5.5(b) shows the corresponding cross sections for this groove at the two successive processing steps, i.e indentation, which takes place first and the subsequent scratching of

the groove. In addition, the A-B signal recorded with the data acquisition system during the machining of this groove is shown in Figure 5.6. In particular, it can be seen from this figure that, for both the "Indentation" and the "Scratching" steps, the V_{A-B} signal of the PSPD stayed constant. This is an expected outcome because the AFM instrument was operated in the force-controlled mode.

Based on the analysis of the V_{A-B} signal alone, it could be assumed that the applied force, F_n, also remained constant throughout the nanomachining experiment. If this assumption was correct, then it would also be expected that the depth of the groove achieved during the indentation step would be identical to the depth obtained during the scratching step. However, as reported with Figure 5.5(b), this result was not observed. In particular, the depth obtained at the indentation step differs from that produced during the scratching step. More specifically, the depth of the groove was measured to be 75 nm during indentation, while it reduced to 42 nm, once the horizontal motion of the stage was initiated. Based on this experimental evidence, it is argued that the applied force, F_n, did not remain constant throughout the nanomachining experiment despite the V_{A-B} signal staying constant.

To explain the change in machining depth, and thus the variation in applied load, between the indentation and scratching step, it is necessary understand the mechanism of the feedback loop of the AFM instrument during the nanomachining experiment. This mechanism has already been elaborated upon when explain the results reported in Chapter 4. Thus, it is only briefly explain here. First, during the indentation step, the probe is moved down vertically towards the sample without any horizontal motion of the stage of the AFM instrument. This step is stopped by the feedback loop of the AFM device when the resulting applied load reaches a value set by the user prior to the start of the nanomachining experiment. Based on the knowledge of the normal spring constant of the AFM probe and on the sensitivity of the PSPD, this force corresponds to a given V_{A-B} output as expressed with equation (2.1). Second, for the scratching step, the horizontal motion between the sample and the probe is initiated. Thus, an axial force is also applied on the tip in addition to the normal force. This results in a change in the moment generated on the free end of the cantilever, which in turn, also modifies its deflection angle. Accordingly, this also changes the V_{A-B} output signal from the PSPD.

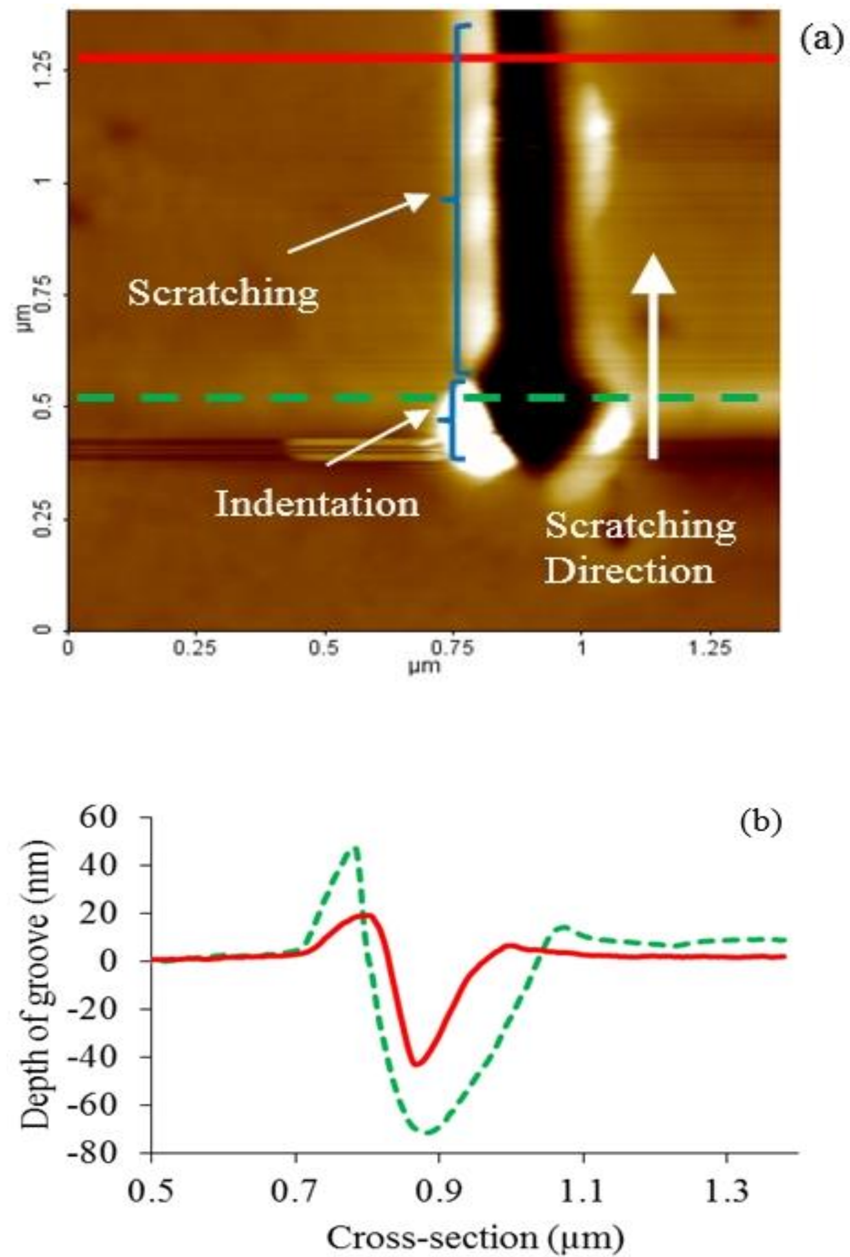

Figure 5.5 (a) AFM image of a groove machined with a normal force of 29 µN along the backward direction and (b) comparison of cross-section profiles obtained during the indentation and the scratching steps for this groove.

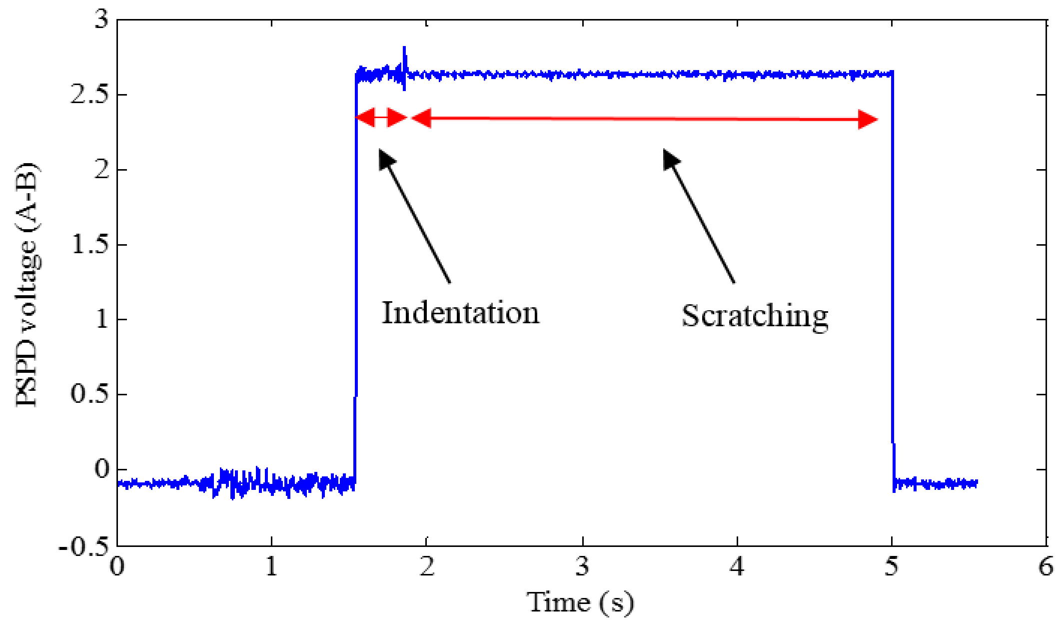

Figure 5.6 V_{A-B} signal measured when processing in the backward direction

As a result, the feedback loop of the AFM system ensures that the vertical position of the probe is adjusted to keep the V_{A-B} output signal equal to that set during the indentation step. In the experiment reported here, which was along the backward direction, the moment induced by the axial force increases the deflection angle of the cantilever, and thus the V_{A-B} signal increases too. Therefore, to reduce the V_{A-B} signal, the probe is raised. This results in a reduction in the normal applied load and consequently, in a reduced depth of the groove in comparison with that achieved during the indentation step. This is indeed the outcome that can be observed in Fig. 5.5(b). Based on this experimental evidence, it is argued that a given value of the A-B signal does not corresponds to a unique normal force value. The following sub-section provide further support for this from a theoretical perspective.

5.3.2 Influence of the axial force: theoretical analysis

In order to simplify the analysis reported here, we shall assume that the cantilever is mounted parallel to the surface of the sample, i.e. that the angle α is equal to zero. In a first case, if we assume that the tip is only subjected to an axial force, as shown in Figure 5.7, the vertical deflection at the free end of the cantilever is given by

$$\delta = \frac{F_a.(h + t/2).L^2}{2EI} \tag{5.38}$$

If this particular situation could be implemented on an AFM instrument, this deflection would also lead to a given $V_{A\text{-}B}$ voltage output on the PSPD. Thus, one can realise that, for a certain value of F_a, a targeted $V_{A\text{-}B}$ output could be achieved despite the fact that F_n is equal to zero in this case. This theoretical situation does not correspond to a real tip-based nanomachining configuration. However, it is presented here to illustrate the fact that, when F_a is not null, then a pre-defined $V_{A\text{-}B}$ output does not necessary mean that a certain value of normal load, F_n, has been achieved.

In the remaining part of this sub-section, we provide a similar theoretical analysis but this time by considering the real tip-based nanomachining configuration where F_n is not equal to zero and when scratching along the backward direction (see Figure 5.8). In this case, the vertical deflection is written as follows:

$$\delta = \frac{F_n.L^3}{3EI} + \frac{F_a.(h + t/2).L^2}{2EI} \tag{5.39}$$

By substituting equation (5.30) into equation (5.39), we obtain

$$V_{A-B} = \frac{1}{S_n}.\left[\frac{F_n.L^3}{3EI} + \frac{F_a.(h + t/2).L^2}{2EI}\right] \tag{5.40}$$

However, when the AFM stage is static, i.e. when F_a is equal to zero, then the vertical deflection becomes

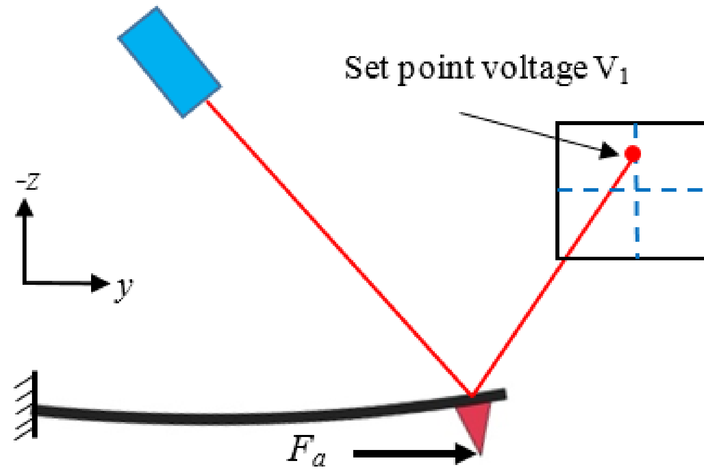

Figure 5.7 Schematic representation of the AFM probe being subject to an axial load only

$$\delta = \frac{F_n . L^3}{3EI} \tag{5.41}$$

In a similar way to the above treatment for equation (5.39), we get

$$V_{A-B} = \frac{1}{S_n} . \left[\frac{F_n . L^3}{3EI} \right] \tag{5.42}$$

It the previous section (refer to Figure 5.6), it was experimentally verified that the $V_{A\text{-}B}$ output from the PSPD when the AFM stage is static is equal to that during scratching (i.e. when the AFM stage is not static). This is a result of the mechanism implemented by the feedback loop of the AFM instrument. Thus, we can write that the equation (5.40) should be equal to the equation (5.42):

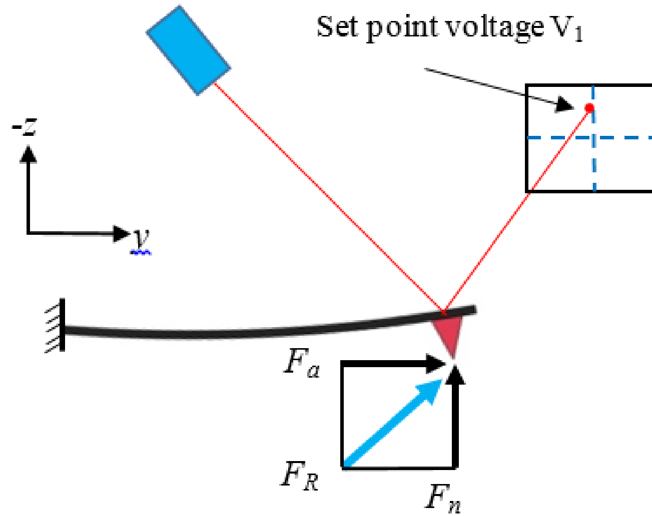

Figure 5.8 Schematic representation of the AFM probe during nanomachining in the backward direction

$$\frac{1}{S_n}.\left[\frac{F_n.L^3}{3EI}\right] = \frac{1}{S_n}.\left[\frac{F_n.L^3}{3EI} + \frac{F_a\,.(h+t/2).L^2}{2EI}\right] \quad (5.43)$$

The above relationship implies that the value of F_n on the left hand side of the equal sign is not equal to the value of F_n on the right hand side, otherwise the term $(\frac{F_a\,.(h+t/2).L^2}{2EI})$ would be equal to zero, which is not possible. In other words, the normal applied force (i.e. pre-set load) when the AFM stage is static is not equal to the normal applied force (i.e. thrust force) when there is a relative motion between the probe and the sample while the tip engaged into the sample.

There is an additional important implication associated with the finding reported here. This concerns how we should view the normal sensitivity of the PSPD during AFM tip-based nanomachining operations. In particular, considering that the cantilever normal spring constant, K, and the PSPD A-B voltage output, V_{A-B}, are both fixed physical quantities, further analysis of equation (2.2), i.e. $F_n = K \times S_n \times V_{A-B}$, suggest that the vertical sensitivity of the PSPD, S_n, cannot be considered constant between the

configurations where 1) there is and 2) there is not a relative horizontal motion between the sample and the tip.

In addition, this finding about the change in normal applied force is in agreement with the work of (Geng *et al.* 2013a). However, these authors assumed the vertical deflection at the free end of the cantilever stayed constant when using the AFM in the so-called "force controlled" mode. Besides, these researcher overlooked the fact that the generation of the axial force during tip-based nanomachining may also cause to change of the normal sensitivity of the PSPD.

Thus, it is argued that the using of the conventional method to determine the normal force applied to the AFM probe leads to wrong estimations when implementing the tip-based nanomachining process. Moreover, the calibration of the normal sensitivity of the PSPD using the traditional method, as described in Chapter 2, and which is based on the condition of static-end loading, is also not appropriate in this case. Therefore, in the next section a refined theoretical analysis is reported to propose a novel method to determine the actual normal sensitivity of the PSPD during tip-based nanomachining.

5.4 Determination of the quasi-static normal sensitivity during tip-based nanomachining

The refined model presented in this section is also based on classical beam theory. In the following sub-section, the model is developed for tip-based nanomachining conducted in the pure forward and inclined forward direction. In the subsequent sub-section, the analysis is carried out when the tip is scratching in the pure backward and inclined backward direction.

5.4.1 Pure and inclined forward direction

A basic illustration of the forces acting on the tip during nanomachining in the forward direction was already given in Figure 2.20 (Chapter 2). This schematic illustration is now further elaborated upon with Figure 5.9 with regard to the forces acting and the tip. The main difference between the refined scheme reported here and that

already presented in Chapter 4 is the fact that this analysis is concerned with the determination of the normal sensitivity of the cantilever rather that its deflected shape. In the pure and inclined forward direction, the axial force, F_a, is generated due to the tip movement with respect to sample and it is pointed towards the fixed end of the cantilever. This force is perpendicular to the normal force F_n as shown in Figure 5.9. Here, we define the force F_R which is the resultant force from F_n and F_a. Thus, F_R is given by

$$F_R = \sqrt{{F_n}^2 + {F_a}^2} \qquad (5.44)$$

As illustrated in Figure 5.9, we also define the resultant angle β between the resultant force, F_R, and the sample surface. In this way, we can write

$$\beta = \tan^{-1}\frac{F_n}{F_a} \qquad (5.45)$$

The angle β is measured in the plane which passes through the long axis of the cantilever (i.e. the axial plane as illustrated in Figure 2.20). We also define the angle γ, which is located between the resultant force and the longitudinal axis of the cantilever. It is also measured in the axial plane and is given by:

$$\gamma = \beta - 12° \qquad (5.46)$$

In the above equation, it was assumed that the inclination angle of the cantilever is 12° as this is the configuration of the AFM instrument used in this thesis. As noted earlier, based on the technical specifications provided by different AFM manufacturers, this angle could also be equal to 20°.

In the free body diagram shown in Figure 5.9(b), M_B is the moment induced at the free end of the cantilever. Similarly to the reasoning followed in Chapter 4, taking the balance of moments about B, we get

$$M_B = F_R(h + t/2).cos\gamma \qquad (5.47)$$

The bending moment at a cross sectional distance y from the right-hand side of tip is obtained from the free body diagram (see Figure 5.9(c))

$$M(y) = F_R.sin\gamma.y - F_R(h + t/2).cos\gamma \tag{5.48}$$

When this expression for the bending moment is substituted into the basic differential equation of the deflected beam (c.f. equation (5.4)) and both sides of the resulting equation are integrated we obtain the slope of the beam

$$EI\frac{dw(y)}{dy} = F_R\left(h + \frac{t}{2}\right).cos\gamma.y - F_R.sin\gamma.\frac{y^2}{2} + C_1 \tag{5.49}$$

The constant of integration C_1 can be found from the boundary condition already described earlier with equations (5.7) and (5.8)

$$C_1 = F_R.sin\gamma.\frac{L^2}{2} - F_R\left(h + \frac{t}{2}\right).cos\gamma.L \tag{5.50}$$

Then, substituting the preceding expression for C_1 in (5.49), we get

$$EI.\frac{dw(y)}{dy} = F_R\left(h + \frac{t}{2}\right).cos\gamma.y - F_R.sin\gamma.\frac{y^2}{2} + F_R.sin\gamma.\frac{L^2}{2} - F_R\left(h + \frac{t}{2}\right).cos\gamma.L \tag{5.51}$$

To obtain the angle of rotation θ at point B, we then substitute $y = 0$ into equation (5.51) and with further simplification, we can write:

$$\theta = \frac{L}{EI}\left[F_R.sin\gamma.\frac{L}{2} - F_R\left(h + \frac{t}{2}\right).cos\gamma\right] \tag{5.52}$$

Both sides of equation (5.51) are now further integrated to obtain the vertical deflection of the beam

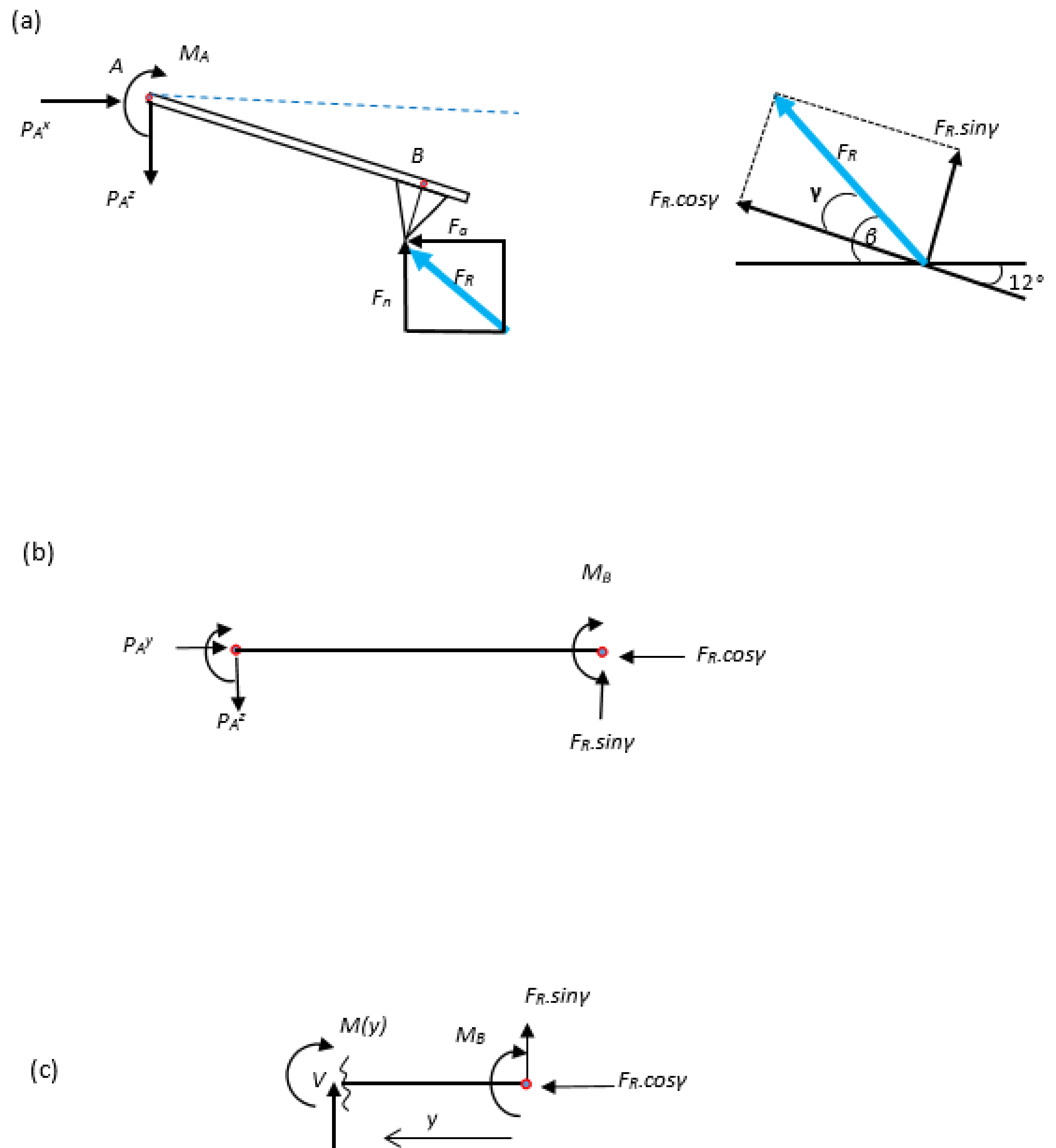

Figure 5.9 (a) Schematic representation of the AFM probe during forward nano machining (b) corresponding free body diagram and (c) free body diagram of cantilever portion.

$$EI.w(y) = F_R\left(h+\frac{t}{2}\right).cos\gamma.\frac{y^2}{2} - F_R.sin\gamma.\frac{y^3}{6} + F_R.sin\gamma.\frac{L^2}{2}.y - F_R\left(h+\frac{t}{2}\right).cos\gamma.L.y + C_2 \quad (5.53)$$

The boundary conditions defined earlier with equations (5.17) is now substituted in equation (5.53) in order to find C_2. Following that, the vertical deflection at the free end of the cantilever is determined for $y=0$ and thus, it is expressed as follows

$$w(0) = \left[\frac{2.L^3.F_R.sin\gamma - 3.L^2.F_R\left(h+\frac{t}{2}\right).cos\gamma}{6.E.I}\right] \quad (5.54)$$

Now, substituting equation (5.53) in (5.54), thus, the quasi-static normal sensitivity of the PSPD can be written as a function of the resultant force, F_R, and the angle, γ, as follows

$$S_{th} = \left[\frac{2.L^3.F_R.sin\gamma - 3.L^2.F_R\left(h+\frac{t}{2}\right).cos\gamma}{6.V_{A-B}.E.I}\right] \quad (5.55)$$

From the above equation, it is important to notice that the quasi-static normal sensitivity is not expressed as a constant, but instead, it is a function of two variables, namely, F_R and γ.

5.4.2 Pure backward and inclined backward direction

In this case, the axial force is pointing away from the free end of the cantilever. Figure 5.10 illustrates the forces acting on the probe tip in this configuration. The angle γ between the resultant force and the longitudinal axis of the cantilever is now given by

$$\gamma = \beta + 12° \tag{5.56}$$

In addition, based on the see the free body diagram given in Figure 5.10(b), the bending moment at a cross sectional distance *y* from the right-hand side of tip is now expressed as follows

$$M(y) = F_R.sin\gamma.y + F_R(h + t/2).cos\gamma \tag{5.57}$$

We then adopt the same procedure than that used in the previous sub-section from equation (5.49) until equation (5.54) to express the quasi-static normal sensitivity of the PSPD in the pure backward and inclined backward direction. This results in the following equation

$$S_{th} = \left[\frac{2.L^3.F_R.sin\gamma + 3.L^2.F_R\left(h + \frac{t}{2}\right).cos\gamma}{6.V_{A-B}.E.I}\right] \tag{5.58}$$

By comparing the above equation with equation (5.55), we notice that both expression are quite similar. Indeed, there is only a sign difference in front of the second term at the numerator when comparing S_n between the different directions considered. In addition, based on the theoretical analysis presented here, it can be said that for given values of F_R and γ, the normal sensitivity of the PSPD should always be higher in the pure backward and inclined backward direction in comparison with the pure forward and inclined forward direction.

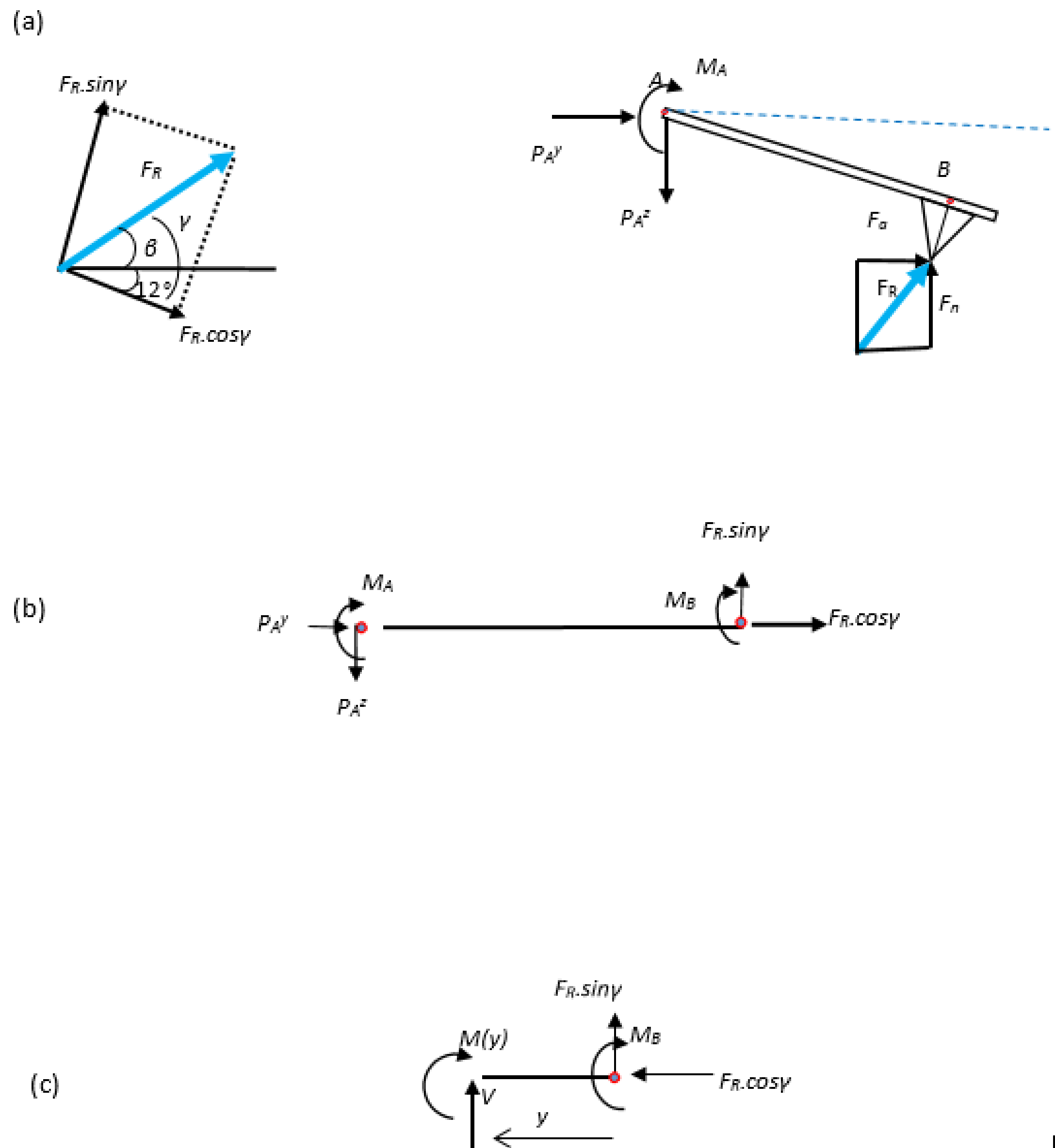

Figure 5.10 (a) Schematic representation of the AFM probe during backward nano machining (b) corresponding free body diagram and (c) free body diagram of cantilever portion.

5.5 Summary

In this chapter, a refined theoretical model was first presented to express the applied normal force when the tip is penetrating vertically into a sample material without any horizontal motion between the probe and the sample. This new model takes into account the inclination of the AFM probe with respect to the surface of the specimen. The main outcome was that a correction factor was introduced to the conventional equation for determining the normal load in this configuration. An important finding from this analysis was that the conventional approach always result in an under-estimation of the normal applied force. Subsequently, the practical importance of taking this correction factor into account was examined based on the nominal geometry of a set of commercial probes. In this way, it was shown that for an inclination angle of 12°, the normal force would conventionally be under-estimated by a maximum of 8.6 %. In the case of an inclination angle of 20°, this value was increased to 18.3%.

Next, using experimental and theoretical analyses it was demonstrated that, during actual AFM tip-based nanomachining operations (i.e. when the AFM stage is not static), the value of the applied normal load does not correspond to that set by the user prior to the machining trials. This is the combined consequence of the generation of an axial force on the tip and of the working mechanisms of the AFM feedback loop in the "force-controlled" mode. In particular, a simple experiment showed that the depth of the groove produced was not equal to the depth of the initial indent (at the beginning of the groove) even when the V_{A-B} voltage output of the PSPD was kept constant throughout. The difference in depth was found to be up to 40%. These results were based on the combined analyses of the cross-sectional profiles of the machined groove and of the corresponding V_{A-B} voltage signal from the PSPD during the two stages of machining, i.e. indentation and scratching. In addition, based on this analysis, it could be argued that, contrary to a common assumption in the literature, the normal sensitivity of the PSPD could not be considered constant between the nanoindentation and the scratching stages of the process. For this reason, another refined model was presented to express this important process parameter during tip-based nanomachining operations in different directions. The outcome of this theoretical analysis showed that the normal sensitivity of the PSPD depends on the combination of normal and axial forces as the tip is moved relative to the

sample as well as on the angle between the resultant force and the longitudinal axis of the cantilever.

Chapter 6

Measurements of cutting forces during AFM tip-based nanomachining

6.1 Introduction

The overall objective of this chapter is to report a novel procedure to estimate all three force components acting on the tip when probe-based nanomachining is conducted in any direction. As highlighted in Chapter 2, most approaches proposed to determine the axial and lateral forces (i.e. forces for which the directions are parallel to the sample surface) have assumed that the normal sensitivity, the normal force and the vertical deflection of the tip are constant (i.e. equal to those estimated during nanoindentation) when the AFM is operated in the "force-controlled" mode for nanomachining. It was already demonstrated in Chapter 5 that the conventional method to measure the normal force acting on the tip leads to wrong estimation of the applied load during AFM probe-based nanomachining operations (i.e. when the AFM stage is not static). This is due to the fact that this load does not correspond to the force set by the user prior to nanomachining.

In order to realise the overall objective of this chapter, two novel methods are proposed to calibrate and measuring the actual value of the normal force as the AFM probe is engaged into the material and moved horizontally relative to sample surface. As defined in Chapter 2, this force is referred to as the thrust force, F_{th}. Based on this, a refined model is reported to calibrate and measure the other two cutting force components, F_a, and F_L, in the context of AFM tip-based nano-mechanical machining. These correspond to the forces along the axial and lateral directions, respectively, as defined in Chapter 2. In addition, the lateral force calibration factor, α (c.f. Chapter 2), and the quasi-static normal sensitivity, S_{th}, are also determined in this chapter for particular experimental conditions.

This chapter is organised as follows. The next section describes in details the required steps to implement the proposed procedure to evaluate the forces acting on the tip during probe-based nanomachining. Then, the following section present and discusses the experimental results obtained when employing this approach for different cutting conditions (i.e. for various load values pre-set by the user and for different machining directions). Finally, a summary of the reported procedure and of the main findings is provided to complete the chapter.

6.2 Proposed procedure for calibrating and measuring AFM tip-based nano machining forces

In order to calibrate and measure the cutting forces during AFM tip-based nanomachining, the proposed procedure is shown in Figure 6.1. In particular, this procedure is divided into three main steps, as follows:

- First, the values of the deflection angle at the free end of the cantilever are considered during both indentation and scratching. These are referred to as θ_{in} and θ_{sc}, respectively. From this, a relationship that links both of these processing stages is found based on θ_{in} and θ_{sc}.
- Then, the actual normal force during the scratching stage. i.e. the thrust force, F_{th}, is assessed. To achieve this, two different methods are reported in this chapter.
- Next, a relationship is found between the axial force, F_a, and the thrust force, F_{th}, during AFM nanomachining, such that F_a can be estimated in practice. Following this, the results are used to extract the value of the lateral force, F_L. Finally, based on the determination of the three cutting forces components, namely F_{th}, F_a and F_L, the quasi-static normal sensitivity, S_{th}, and the lateral force calibration factor, α, can be assessed. More specifically, these calculations rely on equations (5.55) and (5.58) for S_{th} and on equation (2.12) for α.

Each of these steps is explained in details in the following sub-sections.

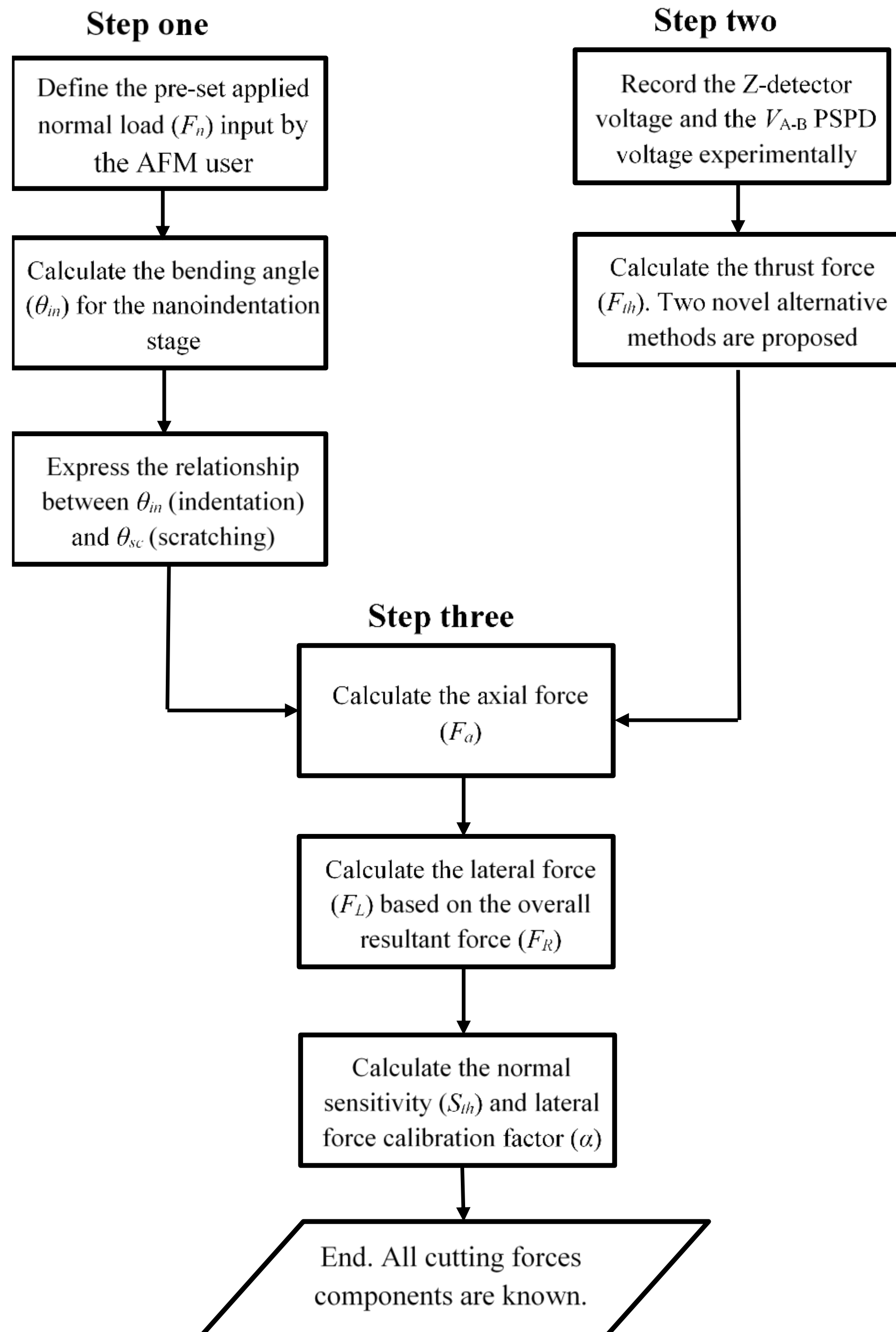

Figure 6.1 Flow chart developed for determining all cutting forces components during AFM tip-based nanomachining.

6.2.1 Step one: deflection angle for the indentation and scratching stages

A simple theoretical analysis is reported here in order to find the relationship between the configurations where the AFM stage is 1) static and 2) not static in contact mode. In particular, this analysis aims to express the deflection angle in both of these cases. When the AFM stage is static (i.e. the axial force, F_a, is equal to zero), this corresponds to the loading stage of a nanoindentation test, and thus, the deflection angle at the end this process is as follows:

$$\theta_{in} = \frac{2.w(0)}{3.L} \tag{6.1}$$

where θ_{in} is deflection angle as the probe is subjected to the normal force only. To calculate θ_{in} in practice, the vertical deflection $w(0)$ can be determined using equation (5.30).

As described previously in Chapter 4, when the AFM probe starts the horizontal motion relative to the sample (i.e. for the scratching stage), an axial force is generated and this creates a moment at the cantilever free end. This results in changing the (A-B) output voltage of the PSPD, i.e. $V_{A\text{-}B}$. Accordingly, the feedback loop mechanism of the AFM instrument automatically adjusts the vertical position of the fixed end of the probe such that $V_{A\text{-}B}$ is kept constant. This mechanism is illustrated Figure 6.2. We now consider the consequence of this working principle on the deflection angle at the free end of the probe. In particular, inspired from Butt and Jaschke (1995), we specifically argue that during machining, the resultant force F_R in the axial plane, composed of the two components F_a and F_{th}, has the same influence on the deflection angle of the cantilever as that of the normal force, F_n, during the nanoindentation stage. This is illustrated with Figure 6.3. In other words, according to basic principles of optical reflection, the fact that $V_{A\text{-}B}$ is kept constant throughout means that the surface of the cantilever where the laser is reflected keeps a fixed orientation in the axial plane. From the notation adopted in Figure 6.2, this implies that the segment $\overline{A'B'}$ is kept parallel to segment $\overline{AB}$ (i.e. that $\overline{A'B'} // \overline{AB}$). The important implication is that the bending angle, θ_{in}, produced by the applied load at the end of the indentation stage is equal to the bending angle, θ_{sc}, during the scratching stage as illustrated in Figure 6.3. Therefore, we can write that:

$$\theta_{sc} = \theta_{in} \tag{6.2}$$

In this work, this result is used to calculate the axial force, F_a. To achieve that, knowledge of the thrust force, F_{th}, is also required. This is the focus of the next section, which corresponds to step number two in the proposed overall procedure (c.f. Figure 6.1).

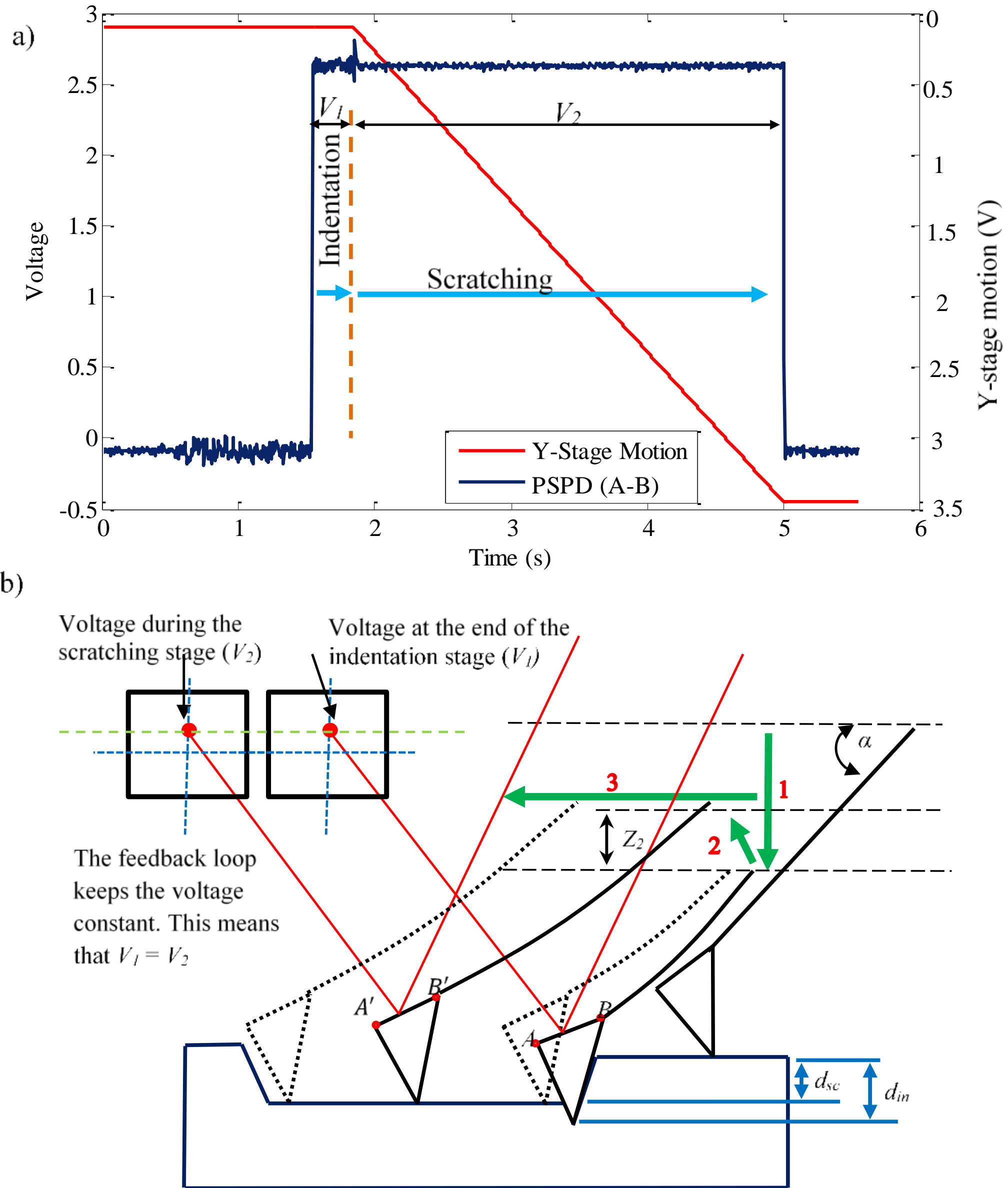

Figure 6.2 AFM tip-based nanomachining in the forward direction; (a) plot showing that the (A-B) voltage of the PSPD stays constant during scratching process and (b) corresponding schematic representation of the probe moving in the vertical direction to keep the voltage constant as a result of the feedback loop mechanism

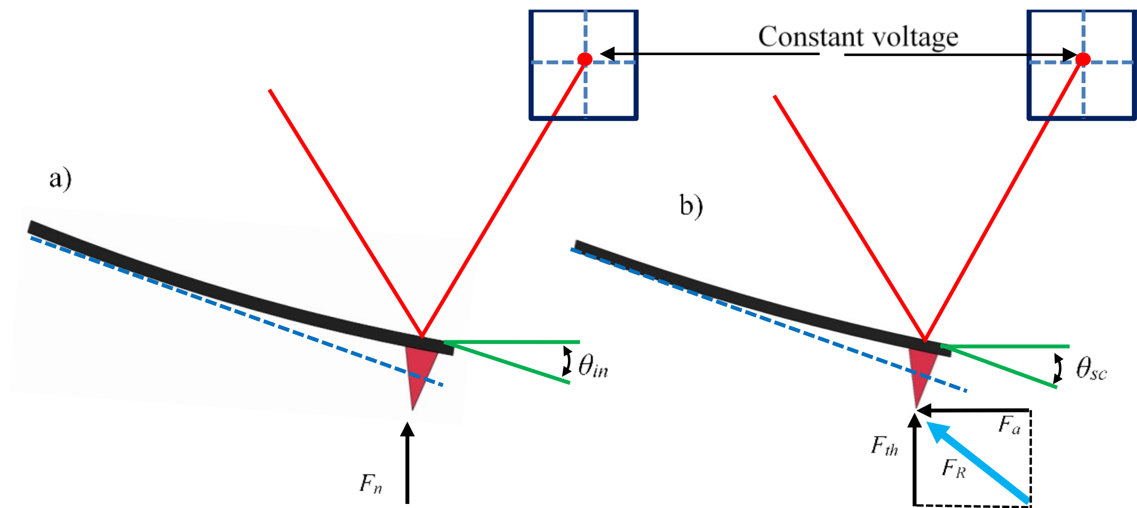

Figure 6.3 Schematic representation of a) the indentation stage and b) forward machining

6.2.2 Step two: thrust force measurement

In this section, we propose two novel methods to measure the thrust force, F_{th}, during scratching. These are referred to as the "fitting" and the "percentage" method, respectively. The main idea behind both of the proposed methods is to exploit the Z-detector voltage output to obtain the actual magnitude of F_{th}. This voltage signal can be easily recorded using the combined SAM and DAQ set-up employed in this research. It is generally known that the cutting forces are affected by many factors, such as the workpiece material, the length of the cantilever, the height of the tip, the radius of curvature of the tip, the shape of the cantilever deflection, the tool wear and the direction of cutting. Hence, it is important to consider the influence of these factors in any cutting force model. In this work, these factors are taken into account in an indirect way because they influence the Z-detector voltage. Each of the proposed methods is now explained and validated in the following sub-sections.

6.2.2.1 Method one: fitting method

Principle

As described in Chapter 2, the Z-scanner is a piezoelectric actuator and its extension and contraction along the vertical axis is obtained by applying a voltage to it. When the Z-scanner moves the probe towards the sample surface, this raises the normal force. Conversely, when the probe is moved away from the sample surface, the normal force is lowered. Thus, the increase or the decrease of the Z-scanner voltage signal and consequently, that of the Z-detector too, corresponds to a respective increase or reduction in the normal load. For this reason, the Z-detector voltage can be employed for measuring the thrust force (or the normal force during indentation) by establishing, a-priori, a relationship between the Z-detector voltage output and the normal applied force on the sample. This relationship can be extracted by conducting a nanoindentation experiment. The output of this experiment is the determination of a function $F_{\mathrm{n}} = f\,(V_{\mathrm{Z}})$ where V_{Z} is the output voltage of the Z-detector. It is argued that the same function $f\,(V_{\mathrm{Z}})$ can also be used to express F_{th} during scratching.

The proposed fitting method is described as follows:

1. Record the Z-detector and the $V_{\mathrm{A\text{-}B}}$ output voltage experimentally for a nanoindentation test.
2. Convert the $V_{\mathrm{A\text{-}B}}$ data to normal force values using the knowledge of the spring constant of the cantilever and the normal sensitivity of the PSPD.
3. Plot the calculated normal force values as a function the Z-detector voltage output.
4. Fit a regression curve to the data such that the normal force is now expressed as a function of the Z-detector output.

The application of this method is now demonstrated in practice. The probe and sample used here were the same as those employed in the experiment reported in Chapter 4. In particular, a nanoindentation test was realised by approaching the tip onto the surface first until a normal force value of 1.5 μN was reached. Next, the fixed end of the probe was further lowered by 0.8 μm at a speed of 0.3 μm/s. Following this, the probe was raised until the normal force value reached was again 1.5 μN. The Z-detector voltage and the $V_{\mathrm{A\text{-}B}}$ voltage were recorded throughout the experiment. Appendix A shows a screenshot

of the user interface of the Park Systems software used to realise this particular experiment.

Analysis of output signal and curve fitting

The signals recorded as a function of the time for the Z-detector and the $V_{A\text{-}B}$ voltages are shown in Figures 6.4 and 6.5, respectively. In particular, these signals can be divided into four stages, which correspond to the regions “A”, “B”, “C” and “D” in these figures. The physical interpretation for each stage is given below:

- First stage (region A): This corresponds to the situation where the normal load applied is 1.5 μN following the completion of the approach process. This stage is similar to the stage “A” described in Chapter 4.
- Second stage (region B): the tip penetrates into the material as the probe is further moved down vertically. This stage is also known to as the loading step of the indentation process. The maximum applied normal load is determined by the total distance travelled by the Z-scanner, which is pre-defined by the user, i.e. 0.8 μm in this experiment. The vertical motion stops when the Z-scanner reaches this target value.
- Third stage (region C): this stage corresponds to the unloading step. In particular, the probe is moved away from the sample surface until the initial normal load value is reached, i.e. 1.5 μN in this experiment.
- Fourth stage (region D): the vertical motion of the stage is stopped. The normal force is maintained at the same value as that defined for the first stage, i.e. 1.5 μN.

Based on these signals and on the proposed procedure described earlier for the fitting method, three important steps should now be completed to find the relationship between the normal force and the Z-detector. First, suitable data should be selected from both the Z-detector and the $V_{A\text{-}B}$ voltage plots. It is clear from Figures 6.4 and 6.5 that, at time T_1, both the Z-detector and the $V_{A\text{-}B}$ signals increase gradually as the tip penetrates into the sample surface. It is worth mentioning that, above a certain value of vertical displacement of the probe, the reflection of the laser beam may lie outside the detection range of the PSPD. This effect can be observed in Figure 6.5 where, at time T_2, the $V_{A\text{-}B}$ voltage reaches a plateau. This corresponds to a maximum voltage output limit of +10 V for the

particular PSPD built-in our AFM system. Therefore, the data selected in this experiment were those comprised between T_1 and T_2. The range of values considered for the Z-detector signal during this time duration is shown more clearly in Figure 6.6. Second, the $V_{A\text{-}B}$ data were also selected within this time range. In particular, these were used to express the normal force values achieved between T_1 and T_2 by employing equation (5.34). The resulting plot for this experiment is shown in Figure 6.7. We now have data where the applied normal force and the Z-detector voltage are given as a function the time within the same interval, i.e. from T_1 to T_2. Thus, we can combine these data to finally express the Z-detector output signal as a function of the applied normal force. For this experiment, the obtained plot is given in Figure 6.8. Next, a regression line was fitted to the data plotted in this figure using the least square method. When doing this, the metric R^2 can be used to assess the deviation between the experimental data and the fitted curve. Thus, the value of R^2 is an estimation of the quality of the fitting method. When the R^2 value is near or equal to 1, then a good fit is obtained as it is the case for the data shown in Figure 6.8 where R^2 is equal to 0.999808. For the experiment reported here, the relationship between the Z-detector voltage, V_z, and the applied normal force, F_n, can finally be given as follows:

$$F_n = 155.877 \times V_z^{2.811} + 146.73 \times V_z + 0.709 \tag{6.3}$$

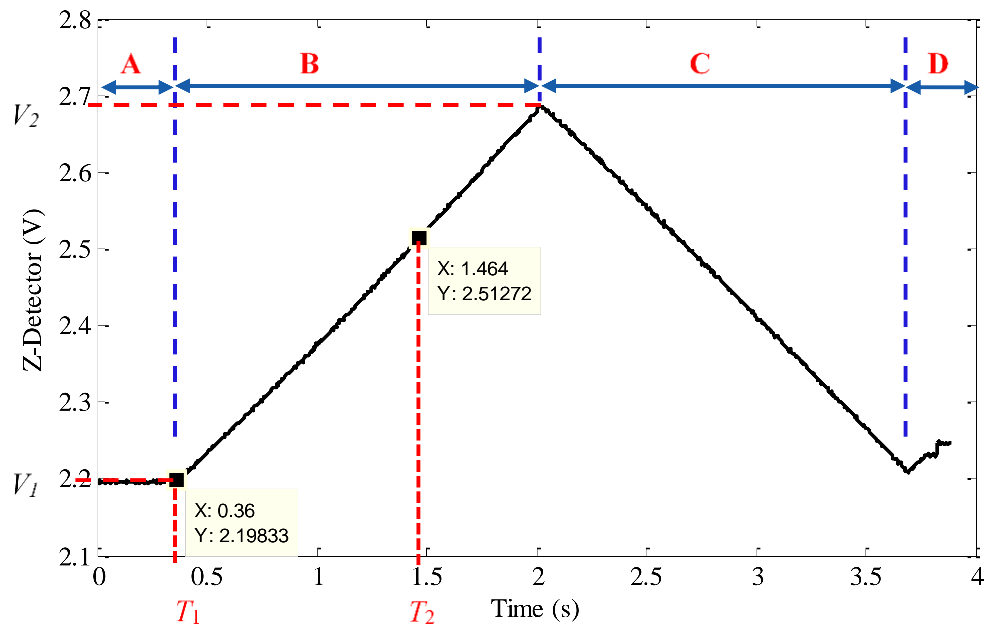

Figure 6.4 Z-detector output signal during the nanoindentation test

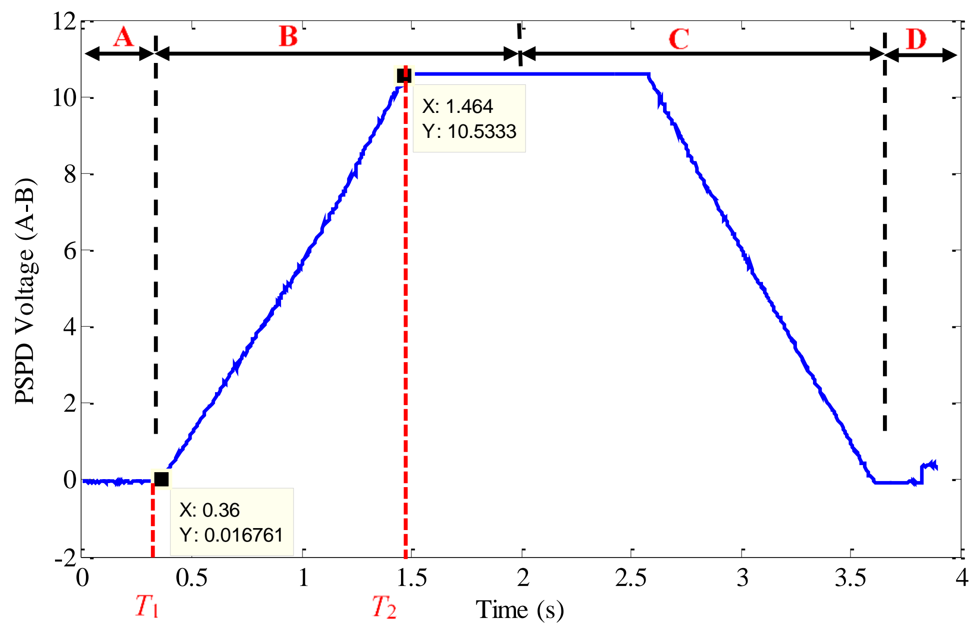

Figure 6.5 $V_{A\text{-}B}$ output voltage during the nanoindentation test

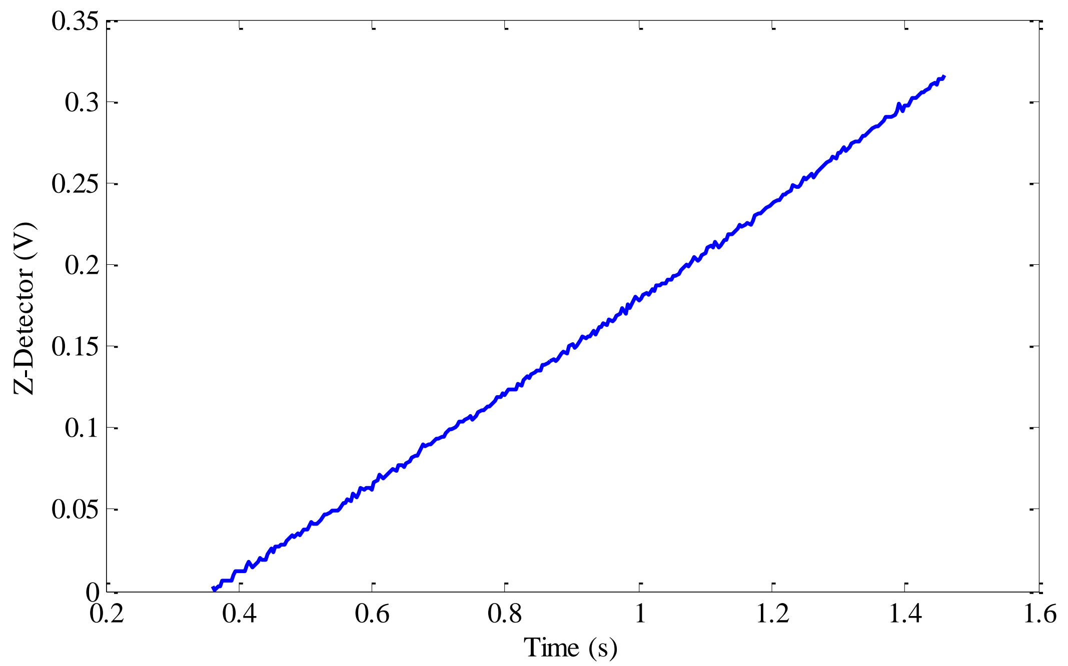

Figure 6.6 Z-detector output voltage between the selected T_1 and T_2

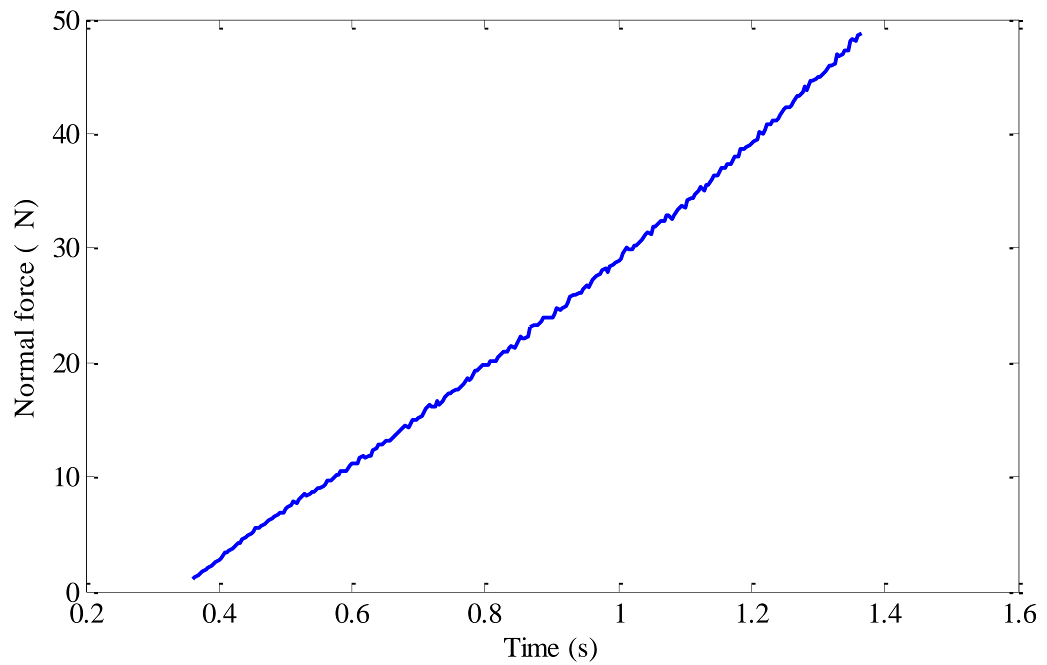

Figure 6.7 Applied normal force between T_1 and T_2

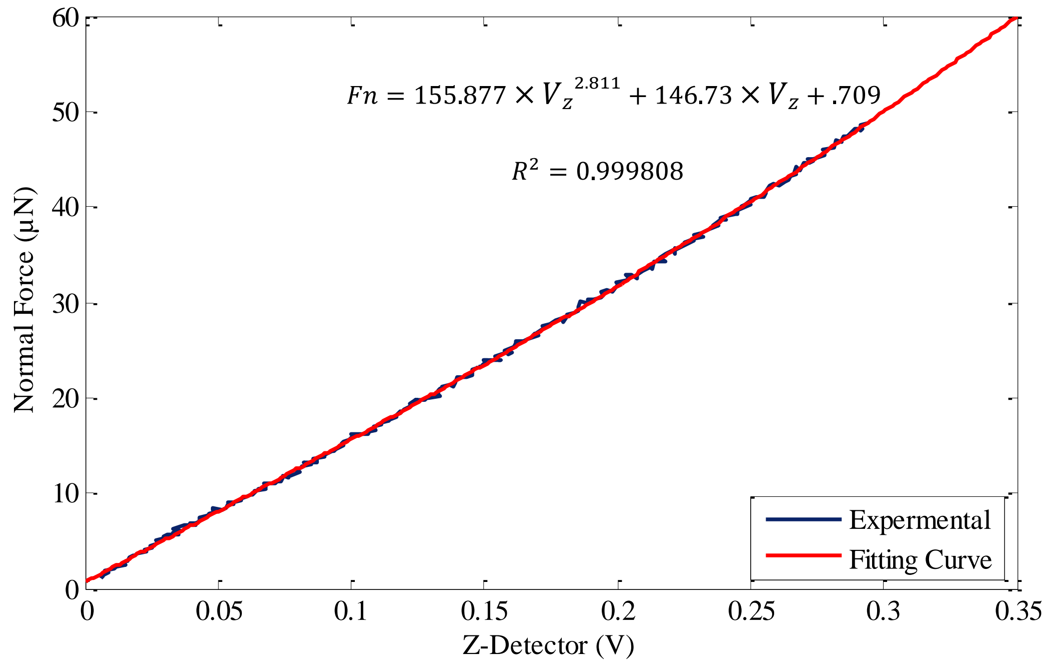

Figure 6.8 Extracted relationship between the Z-detector signal and the applied normal force between T_1 to T_2

Validation of the fitting method

Experimental data were extracted from different trials to compare the results when estimating F_n using the fitting method with those calculated using the refined equation (5.34), which was presented in Chapter 5. In particular, in this equation, a correction factor was introduced to take into account a number of geometric parameters that were identified to affect the determination of F_n. In these experiments, the normal force values were first calculated using equation (5.34). These theoretical values could also be used as references to compare the normal force estimated with the fitting method. The obtained results are presented in Table 6.1. This table also presents the percentage difference between the references values and the corresponding F_n extracted with the fitting method.

It can be seen from this table that a good agreement was found between the theoretical values and those obtained with the fitting method. Indeed, the percentage error was comprised between 1.1% and 4.6%. One of the sources of discrepancy between both sets of results is identified as follows. When implementing equation (5.34), it is assumed

that the initial $V_{A\text{-}B}$ voltage on the PSPD is null. However, this is difficult to achieve in practice as this requires the laser spot to be perfectly centred on the PSPD. For the particular probe used in these experiments, and according to equation (5.34), a small shift of ±0.5 V in $V_{A\text{-}B}$ results in a variation of 2 µN in the theoretical estimation of the normal force. Thus, it is acknowledged that a small uncertainty should affect the theoretical F_n values estimated with equation (5.34). In spite of that, it is concluded that the fitting method provides acceptable results when determining F_n. Thus, it is proposed that a reasonable estimation of F_{th}, defined as the normal load during the scratching process, could subsequently be obtained based on the a-priori knowledge of F_n as a function of the the Z-detector signal, which is established with the fitting method.

Table 6.1 Experimental normal force values obtained using the fitting method

F_n obtained from equation (5.34)	F_n obtained with the fitting method (i.e. equation (6.3))	Percentage difference between both approaches
21.5 µN	20.5 µN	4.6%
29.5 µN	28.7 µN	1.1%
36.5 µN	37.4 µN	1.9%
42.1 µN	43.7 µN	3.8%

6.2.2.2 Method two: percentage method

Principle

The proposed percentage method also relies on the knowledge of the Z-detector voltage to determine the applied thrust force, F_{th}, during nanomachining. In this method, this signal is analysed during both the indentation and the transition stages. As defined in Chapter 4, the transition stage takes place as the horizontal motion starts following the completion of the indentation of the tip into the workpiece material. As shown in Figure 6.9, the voltage output of the Z-detector during the indentation stage changes from V_0 to V_1. As discussed earlier, the value V_1 can be used to calculate the normal force, F_n, at the end of the indentation stage when the AFM stage is still static. It is worth mentioning again that, upon the start of the horizontal motion of the stage, the vertical position of the probe is automatically adjusted through the feedback loop of the AFM system. In the example shown in Figure 6.9, contraction of the Z-scanner takes place to raise the probe until the $V_{A\text{-}B}$ output signal reaches a target value, which corresponds to the voltage attained prior to the start of the horizontal motion. In this example, we can see that the Z-detector output is reduced from V_1 to V_2. Consequently, the normal force during machining, F_{th}, is reduced compared that pre-set by the user, i.e. F_n, prior to the start of the stage horizontal motion. Based on this observation, the percentage method relies on estimating the ratio between the voltage variation of the Z-detector during the transition stage and such a variation during the nanoindentation stage. Thus, the percentage change in the Z-detector voltage output can be determined by:

$$\Delta V = \frac{V_1 - V_2}{V_1 - V_0} \,.\% \tag{6.4}$$

The principle of this method is that the percentage change in ΔV is argued to be equal to the percentage change in the applied normal force ΔF. Based on this, the actual value F_{th} can be determined by the following equation:

$$F_{\mathrm{th}} = F_{\mathrm{n}} \pm (F_{\mathrm{n}}.\Delta V) \tag{6.5}$$

where F_n is a known pre-set value, which is calculated and defined by the user. As shown in Chapter 5, ideally, equation (5.34) should be considered to obtain a more accurate estimation of F_n in comparison with the application of the conventional method.

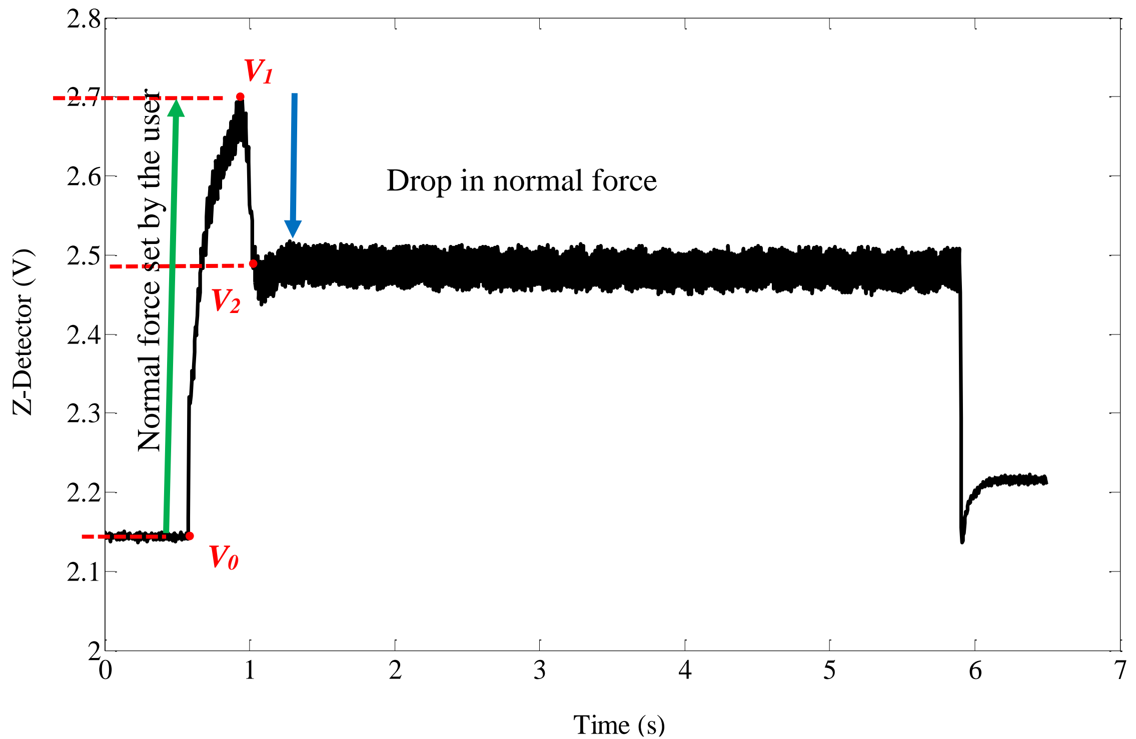

Figure 6.9 Illustration of employing the Z-detector output voltage to determine the actual normal load during machining

Validation of the percentage method

Thrust force values were estimated using both the fitting and the percentage methods for five different experimental trials. The results are presented in Table 6.3. In this table, the reported values for the applied load, F_n, at the end of the indentation stage were determined using equation (5.34). The maximum percentage error found between both methods was 6.6%. The minimum percentage difference was almost zero, for the applied load 29.1 μN when machining in the backward direction. The discrepancies between both methods are judged to be reasonable and should be, in part, due to the difficulty in ensuring a perfect alignment of the laser in the centre of the PSPD, as mentioned previously. Based on these results, it can be concluded that the percentage method is also a valid approach to estimate the thrust force, F_{th}, during AFM tip-based nanomachining operations.

Table 6.2 Thrust force, F_{th}, estimated by both the fitting and the percentage methods

Applied load, F_n, at the end of the indentation stage (μN)	Thrust force, F_{th}, during machining stage (μN)		Percentage difference between both the fitting and the percentage methods
	Percentage method	Fitting method	
21.6 (forward direction)	18.5	17. 7	4.3%
29.5 (forward direction)	26.5	25.9	2.0%
21.5 (backward direction)	14.4	13.9	2.8%
29.5 (backward direction)	23.0	23.3	≈ 0
36.5 (forward direction)	35.5 (convex)	36.9	3.7%
	45.2 (concave)	48.4	6.6%

6.2.3 Step three: axial force and lateral force measurements

In this section, a refined model based on the expression of the bending angle during machining, θ_{sc}, is presented. This model is based on the traditional beam theory and enables to determination of F_a and F_L. The following analysis is divided into three sub-sections depending on the considered directions of scratching:

- Pure forward and inclined forward direction;
- Pure backward and inclined backward direction;
- Pure lateral direction.

6.2.3.1 Pure forward and inclined forward

In the pure forward direction, the AFM tip motion is parallel to the axial plane as previously illustrated in Chapter 2 (see Figure 2.20). In this case, only two force components act on the tip, namely the axial and the thrust force. These were already illustrated in Figures 2.20, 4.1 and 5.9. Under this condition, the cantilever deformation is in pure bending. On the other hand, when the probe moves along the inclined forward

direction, the tip is subjected to three force components, namely the axial, the thrust and the lateral force. In this case, in addition to bending, the cantilever deformation is also affected by twisting. As described in Chapters 4 and 5, the axial force generates an axial moment, which affects the vertical position of the laser on the PSPD. Therefore, both the axial force, F_a, and the thrust force, F_{th}, are responsible for the vertical voltage variation of the PSPD voltage, i.e. V_{A-B}. Thus, only these two force components contained in the axial plane are considered in the refined model because the bending angle, θ_{sc}, is only influenced by these two forces. A mathematical expression for this angle was already described in Chapter 4 using equation (4.8). By rearranging this equation, we get:

$$\frac{\theta_{sc}.E.I}{L} = \left[\left(h+\frac{t}{2}\right).F_a.cos\alpha + F_a.sin\alpha.\frac{L}{2}\right] - \left[\left(F_{th}.cos\alpha.\frac{L}{2}\right) - \left(h+\frac{t}{2}\right).F_{th}.sin\alpha\right] \quad (6.6)$$

This can also be written as follows:

$$F_a = \begin{cases} \dfrac{F_{th}.A.L + E.I.\theta_{sc}}{B.L} & if\ the\ cantilever\ deflection\ is\ concave \\ \dfrac{F_{th}.A.L - E.I.\theta_{sc}}{B.L} & if\ the\ cantilever\ deflection\ is\ convex \end{cases} \quad (6.7)$$

In practice, the bending angle, θ_{sc}, can be determined with equation (6.1), F_{th} can be calculated using either the fitting or the percentage method. In equation (6.7), A and B are constants, which can also be easily estimated as they are given by:

$$A = (\frac{L}{2}.cos\alpha - \left(h+\frac{t}{2}\right).sin\alpha) \quad (6.8)$$

$$B = (\frac{L}{2}.sin\alpha + \left(h+\frac{t}{2}\right).cos\alpha) \quad (6.9)$$

Equation (6.7) applies for both the pure forward and the inclined forward directions. We now express the lateral force F_L. In the inclined forward direction, the lateral force can be calculated by following equation:

$$F_L = F_R.\tan(\emptyset).\cos(\beta) \quad (6.10)$$

where F_R is the resultant force, in the axial plane, from F_{th} and F_a. β is the resultant angle. F_R and β are determined by equation (5.44) and (5.45), respectively. $\emptyset$ is the inclined angle between the direction of tip movement and the axial axis. Obviously, in the pure forward direction, F_L, in this case, the angle $\emptyset$ is zero and equation (6.10) does indeed result in F_L being equal to zero.

Based on the knowledge of F_L, it is worth mentioning that it is also possible to derive the lateral force calibration factor of the PSPD as follows:

$$\alpha = \frac{F_L}{V_{C-D}} \tag{6.11}$$

where V_{C-D} is the average lateral voltage of the PSPD as described in Chapter 2. The study of this lateral force calibration factor is not pursued further in this Thesis. However, it should be noted that the application of equation (6.11) would represent an alternative approach to the conventional methods, which are used for this purpose (c.f. Chapter 2).

6.2.3.2 Pure backward and inclined backward analysis

In the pure and inclined backward directions, the axial force causes to increase the $V_{A\text{-}B}$ voltage because the direction of this force is now pointing away from the fixed end of the cantilever. In addition, the cantilever deflected shape is always convex. Thus, this force can be simply expressed as:

$$F_a = \frac{E.I.\theta_{sc} - F_{th}.A.L}{B.L} \tag{6.12}$$

In addition, the lateral force, F_L, and the lateral force calibration factor, α, can be determined as already described in the previous section.

6.2.3.3 Pure lateral direction

In this direction, the tip is moved perpendicularly to the longitudinal axis of the cantilever. Based on the particular geometry of the tip, an axial force component may still be generated and thus, may create an axial moment, M_{axial}, at the free end of the cantilever. For example, Figure 6.10 shows the 3-sided configuration of the tip used in

this work. It can be seen from this figure that the force component, F_1, which is oriented along the tip rake face would result in the generation of an axial force. Consequently, F_{th} would not correspond to the normal force set by the user, contrary to suggestions made in (Elings 1995, Liu *et al.* 2007, Meyer 1992, Yabing 2008) . Based on the configuration shown in this figure, the direction of axial force is similar to that of the forward direction (i.e. pointing towards the fixed end of the probe). In addition, the results of preliminary experiments in the pure lateral direction suggest that the magnitude of the generated F_a in this case is not enough to induced a shape change of the cantilever from convex to concave. Therefore, the axial force along this particular machining direction is given by:

$$F_a = \frac{F_{th}.A.L - E.I.\theta_{sc}}{B.L} \quad (6.13)$$

In addition, the lateral force is expressed as follows:

$$F_L = \frac{F_a}{\cos^2 \varepsilon} \quad (6.14)$$

where ε is the angle between the tip rake face and the cantilever longitudinal axis measured in the principle plane. The lateral force calibration factor can also be determined by equation (6.14).

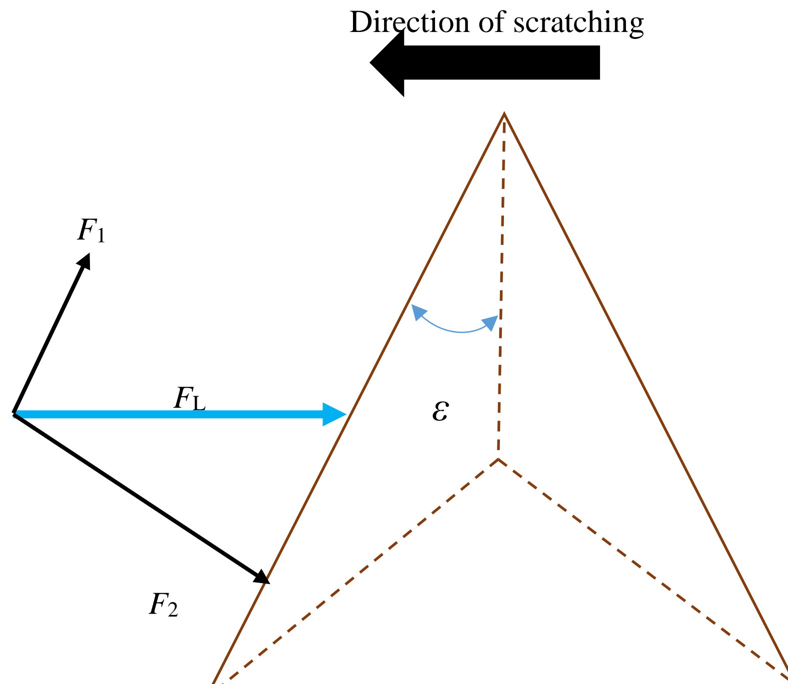

Figure 6.10 Forces analysis in the lateral AFM scratching

6.2.3.4. Case study

In this section, an example is given to illustrate the estimation of the different force components during an AFM tip-based nanomachining operation based on the equations and approaches developed in this Thesis. For this case study, a straight groove was cut in the copper sample along the forward direction using a pre-defined normal force of 36.5 µN, as set by the user. Two different cases are reported below for the different calculations because this cutting conditions also led to a shape change of the cantilever from covex to concave.

Convex deflection

The thrust force was first obtained from the fitting method (i.e. equation (6.3)):

$F_{th} = 36.92$ µN

Then, the bending angle at the end of the indentation stage was estimated using equation (5.24):

$\theta_{in} = 6.3 \times 10^{-4}$ rad

Following this, the axial force during machining could be obtained using equation (6.7):

$F_a = 14.3$ µN

Based on F_{th} and F_a, the resultant force F_R and the resultant angle β is determined from equations (5.44) and (5.45):

$$F_R = \sqrt{F_{th}^2 + F_a^2} = 39.59 \text{ µN}$$
$$\beta = tan^{-1}\frac{F_{th}}{F_a} = 68.83^{\circ}$$

Obviously F_L is null as machining is taking place along the pure forward direction. The quasi-static normal sensitivity of the PSPD can also be calculated. For this, equation (5.55) is used. This gives:

$S_{th} = 0.0188$ µm/V

Concave deflection

The same proceduere was followed here. The only difference is that the concave case was condisered when estimating F_a using equation (6.7). The results are given below.

$F_{th} = 48.4$ µN

$\theta_{in} = 6.3 \times 10^{-4}$ rad

$F_a = 127.46$ µN

$$F_R = \sqrt{F_{th}^2 + F_a^2} = 136.34 \text{ µN}$$
$$\beta = \tan^{-1}\frac{F_{th}}{F_a} = 20.79°$$

$S_{\mathrm{th}} = 0.0072 \mu\mathrm{m/V}$

Based on such calculations, it is proposed to use the recorded $V_{\text{A-B}}$ signal during nanomachining trials to further plot the variations of all force components along the groove (i.e. as a function of time). In this case, it is assumed that the forces acting on the probe tip are essentially constant following the completion of the transition stage and once a steady-state deflection of the cantilever is reached in case of forward or inclined forward machining.

6.3 Results and discussion

In this section, experimental data are reported and analysed to further investigate the different loads acting on the tip as a function and different cutting orientations and different initial normal force values as set by the user. The magnitude of the different force components were calculated based on the work reported so far in this Thesis. To complete this section, an investigation comparing the fitting and the percentage methods is also presented.

6.3.1 Backward direction

6.3.1.1 Normal force and thrust force

Figures 6.11 presents the profile for F_{n} and F_{th} for three different values of initial normal load. In these experiments, the fitting method was used to estimate the thrust force. It can be seen from this figure that, at the start of the indentation process, the applied load increased sharply as the tip penetrates into the sample surface and reached the target value set by the user after about 28 millisecond. This force also exhibits a small overshoot initially. Following this, it takes a further 332 millisecond to ensure that the $V_{\text{A-B}}$ voltage (and hence F_{n}) stays relatively stable until the horizontal displacement between the tip and the sample begins. This time delay may simply be the result of the specific procedure built by the equipment manufacturer within the controller of the AFM instrument.

When the movement between the tip and the sample starts, the plots in Figure 6.11 show that the actual normal load applied during scratching is lower than that set initially

by the user. For example, for a pre-set load of 21.5 μN, the obtained results show that this force was reduced to 13.9 μN as the thrust force during scratching (see Figure 6.11(a)). As discussed previously, this is due to the generation of the axial force on the tip. During the entire scratching stage, the feedback loop of the AFM maintained the thrust force constant. This means that steady state machining was achieved until the probe tip exits from the groove. Figure 6.12 presents the percentage reduction in the normal force as a function of the applied load set by the user. From these data, it can be seen that this percentage decreases sharply when the set force increase. One possible explanation for this phenomenon may be the result of the higher level of pre-stress in the cantilever prior to the start of machining as the normal load is increased. In particular, a pre-stressed cantilever tends to counteract the influence of the axial moment.

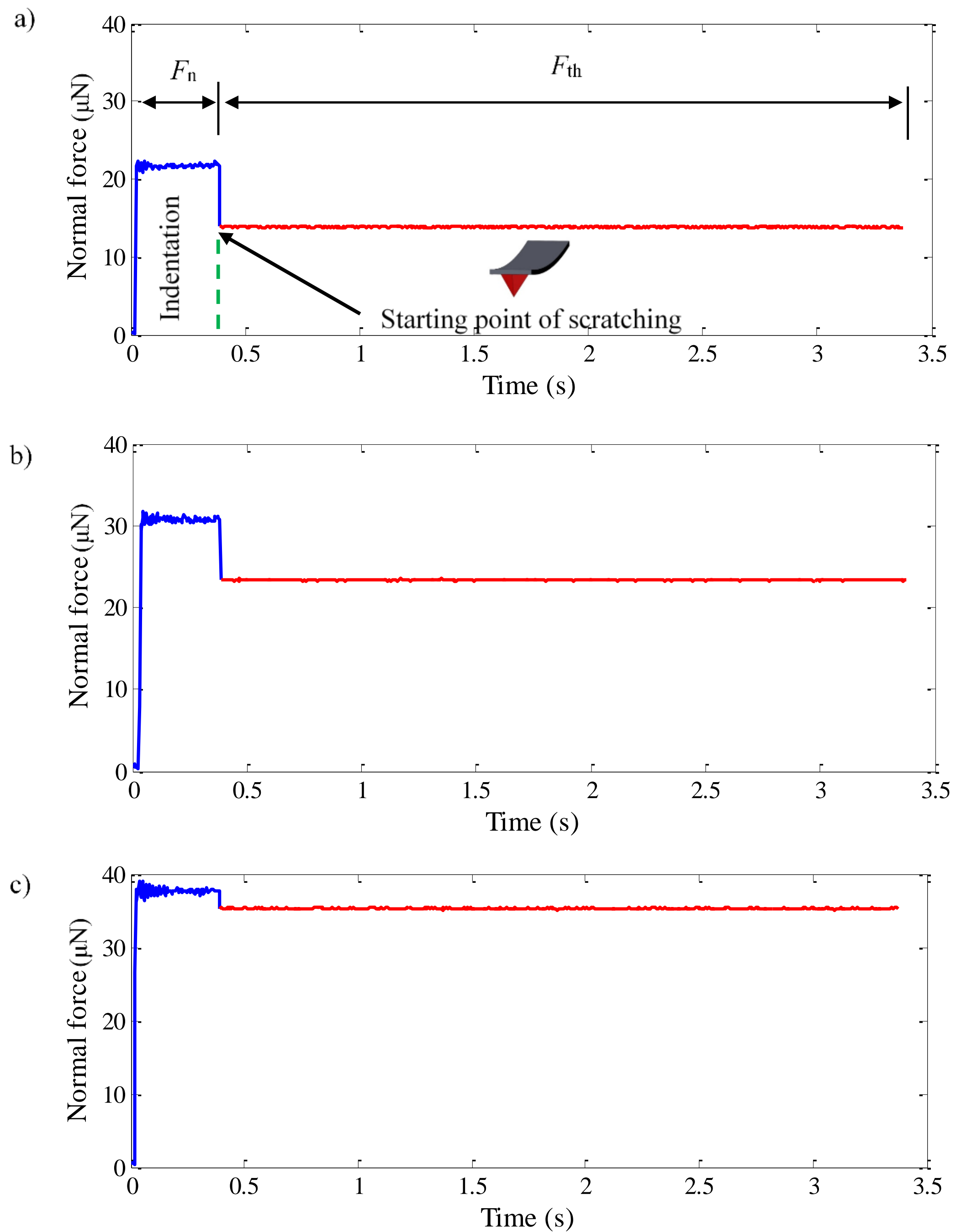

Figure 6.11 F_n, during indentation and F_{th} during scratching in the backward direction for a pre-set load (a) 21.5 µN. (b) 29.5 µN and (c) 37 µN

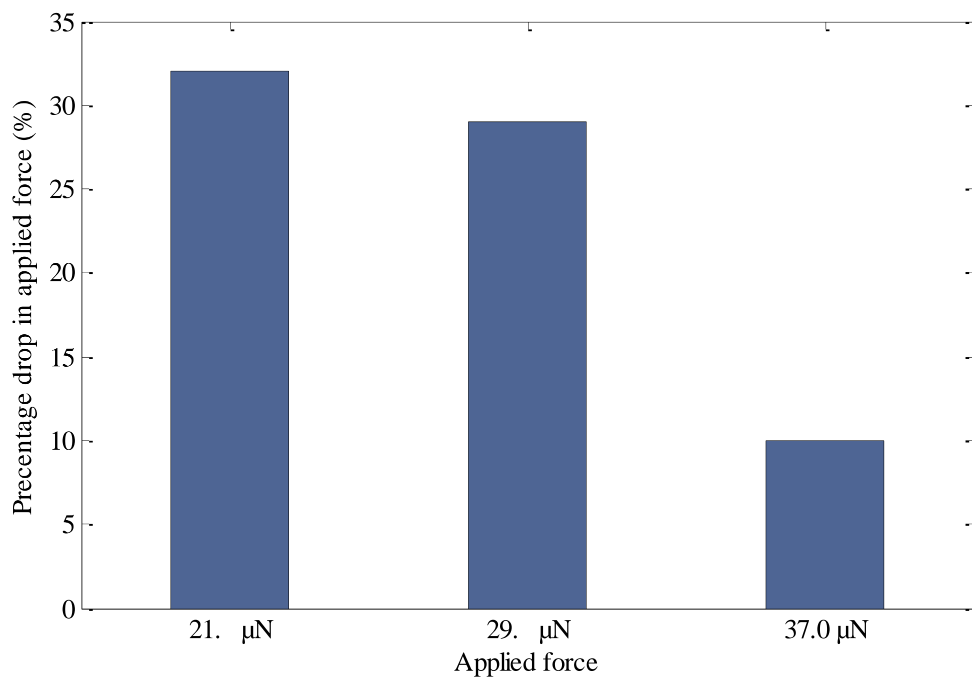

Figure 6.12 Percentage difference between the pre-set applied load value and F_{th} in the backward direction during scratching stage

6.3.1.2 Axial force and resultant force

The results for the axial force and resultant force measurements from these experiments are presented in Figures 6.13. From these data, it is obvious that both the axial and the resultant force are generated as soon as the horizontal motion of the stage begins and that they increase sharply to reach a steady-state value. This result may be explained by the fact that, at end of the indentation stage, the tip has reached a penetration depth corresponding to a given applied force. Thus, when the tip is moved horizontally, the contact stress on the rake face reaches a maximum values instantaneously. In other words, the tip does not gradually penetrate into the sample along the direction of motion as this would have resulted in a gradual increase of the axial force. In addition, it can be observed that the magnitude of the resultant force is always higher than that of the applied normal load during the indentation stage. Interestingly, it can also be seen from this figure that the axial force did not vary linearly with the increase in the applied load. For example, the axial force values were to 19.6 μN, 23 μN and 20 μN for applied load values of 21.5 μN, 29.5 μN and 37 μN, respectively. A possible explanation for this might be that changing the applied load causes both the rake angle and the radius of the contact to vary, which in turn modifies the cutting conditions. This will be explored further in Chapter 7.

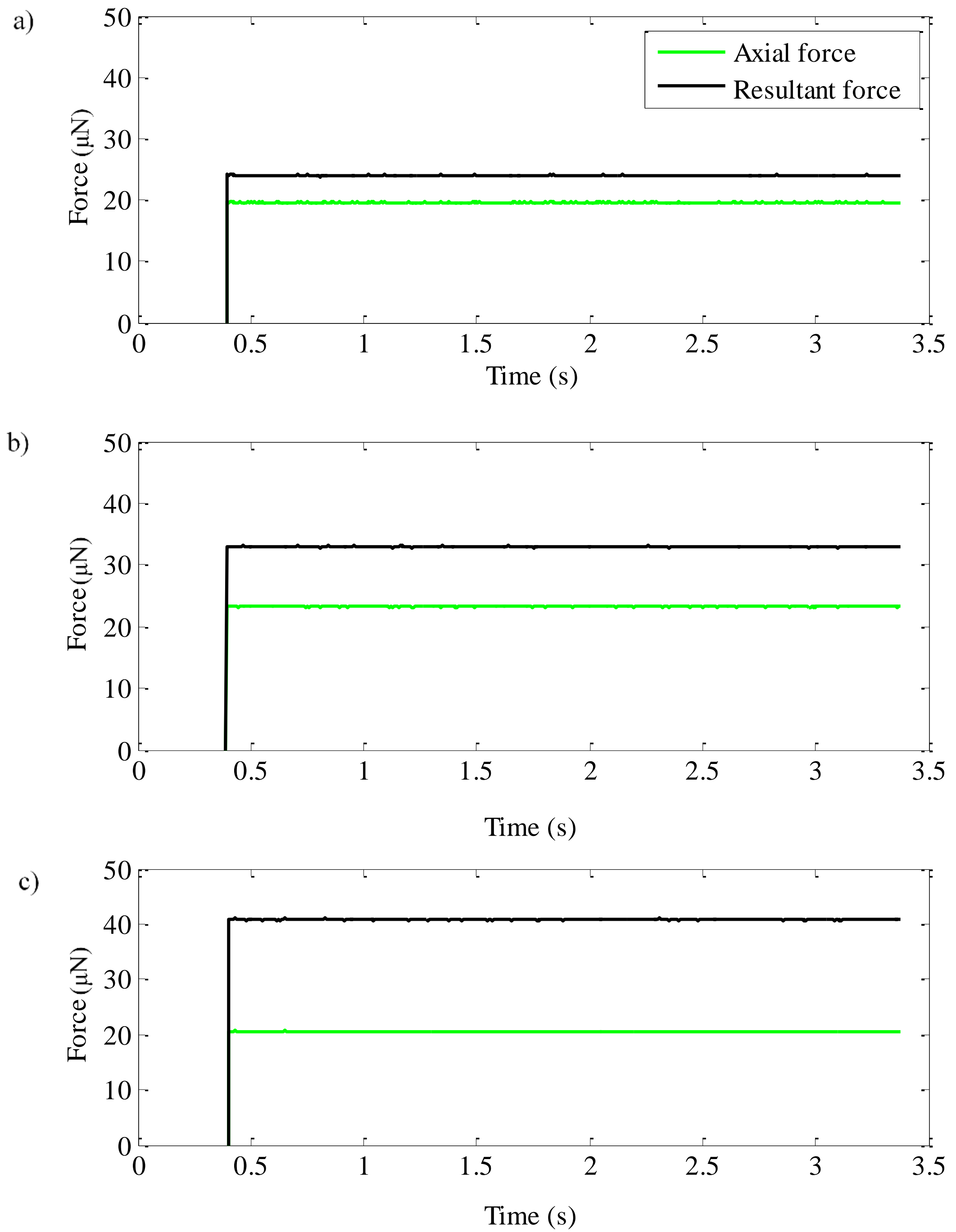

Figure 6.13 Resultant force , F_R, and axial force, F_a, during scratching in the backward direction for an applied force of (a) 21.5μN (b) 29.5μN and (c) 37μN

6.3.1.3 Quasi-static normal sensitivity and resultant angle

As depicted in the flowchart shown in Figure 6.1, to finish with, we can now calculate the quasi-static normal sensitivity, S_{th}, during nanomachining. As described in the previous chapter, this is important because the influence of the axial force causes a change in the normal sensitivity value compared to that defined during a nanoindentation experiment. The quasi-static normal sensitivity is determined using equation (5.55). To gain further understanding into the direction of the resultant force, F_R, the resultant angle, β, was calculated with equation (5.45). The results for both S_{th} and β are given in Figure 6.14.

As shown in Figure 6.14, the resultant force angle, β, increases when increasing the applied load. For this figure, it can also be observed that S_{th} during the scratching is not the same value as that obtained during the indentation stage. In addition, this values increases when the set applied load increases. A possible explanation for this is that the normal sensitivity of the PSPD during nanoindentation experiments is a constant physical quantity regardless of the applied normal load. For nanoindentation cases, this is due to the fact that the tip is only subjected to a vertical loading. Consequently, the relationship between the applied load and the bending angle is linear during nano indentation. Thus, the normal sensitivity, which represents the slope of this linear relationship (see equation 2.3) is constant. However, during scratching, the variation of the bending angle is no longer dependent on the normal load only. Indeed, it is also a function of the axial force F_a. For this reason, there is nonlinear relationship between the bending angle and the vertical force in this case. In turn, this also means that the slope of this relationship, and thence the normal sensitivity, is not constant anymore.

Another possible explanation for this might be that during scratching, the resultant force, F_R, is oriented at an angle relative to the principle plane, whilst, during nanoindentation, this force corresponds only to the load oriented perpendicular to that plane. Thus, this angle, which is referred to as β, changes as a function of both the axial and thrust forces while at the same time, the bending angle at the free end of the cantilever is kept constant by the feedback loop of the AFM instrument to ensure that the $V_{A\text{-}B}$ voltage remains fixed around a set value. This means that, under the force-controlled mode, the resultant force F_R has the same influence on the bending angle to that of F_n

during the indentation stage. For this reason, the normal sensitivity S_{th}, which is defined as a vertical displacement over a voltage output (i.e. μm/V) cannot be considered to be a fixed value if the bending angle at the end of the cantilever is forced to stay constant when a force, which is not perpendicular to the principle plane, acts on the tip.

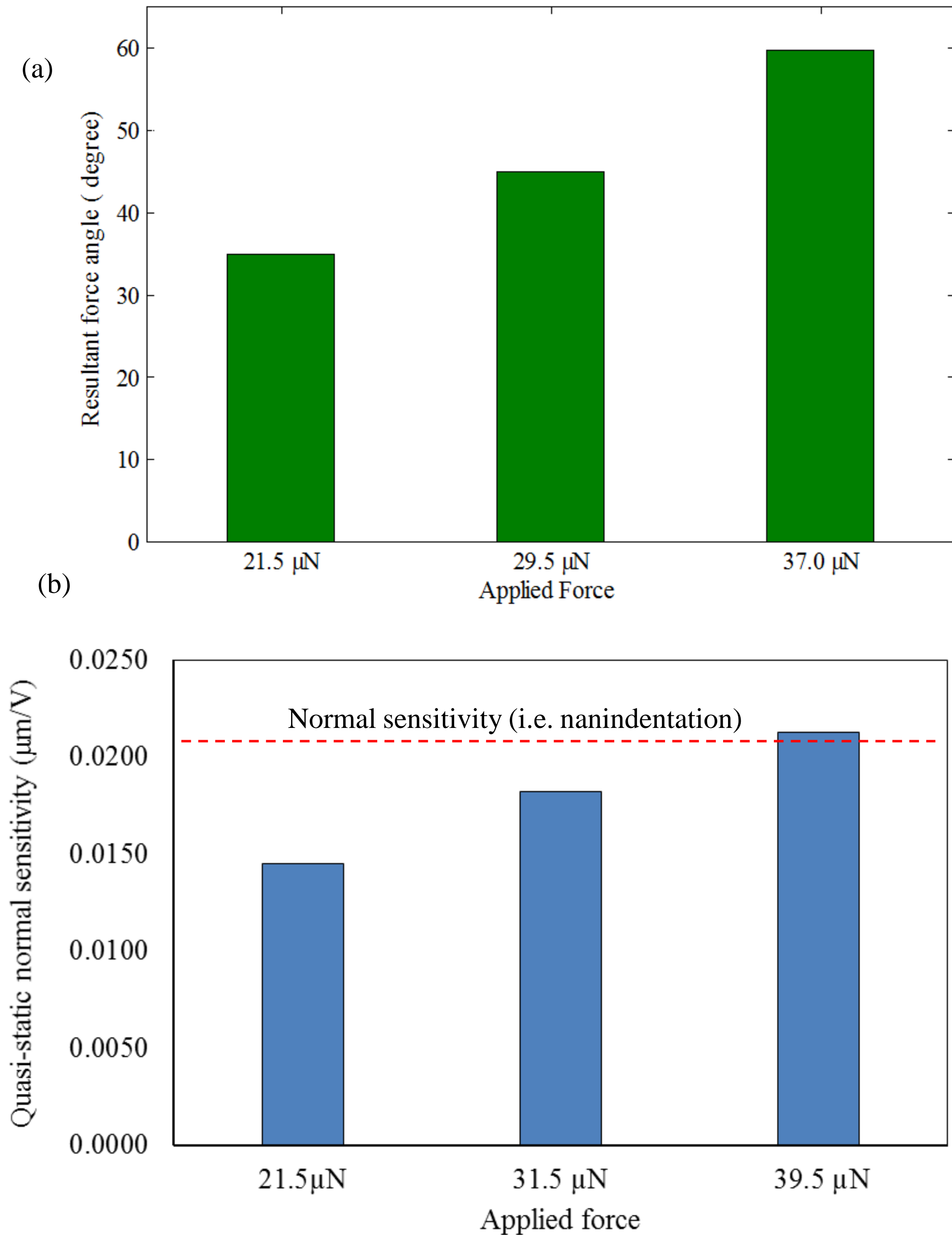

Figure 6.14 (a) Resultant force angle, β, and (b) quasi-static normal sensitivity, S_{th}, for different set normal applied loads during backward machining

6.3.2 Pure and inclined forward

6.3.2.1 Normal force and thrust force

In Figure 6.15, the normal force is plotted as a function of the scratching time for two different pre-set applied loads along the pure forward direction and for one applied load in the inclined forward direction. It is noticed from this figure that the time spent by the AFM instrument on completing the indentation stage, prior to the scratching stage, is similar to that observed earlier for the backward direction experiments. Figure 6.16 shows results for cases when the cantilever shape change from convex to concave occurs. In our experiments this corresponded to pre-set applied loads higher than 32 μN. It can be seen from Figure 6.15 that, as soon as the AFM stage initiates the horizontal displacement, the thrust force was found to be lower than the pre-set applied load. The explanation put forward for this result is that following the generation of the axial force, the tip subsequently slides upwards on the face of the created indent as already discussed in Chapter 4. Consequently, the feedback loop moves the tip away from the sample surface such that the resultant force during scratching stage would have the same influence on the bending angle as that of the normal force during the indentation stage.

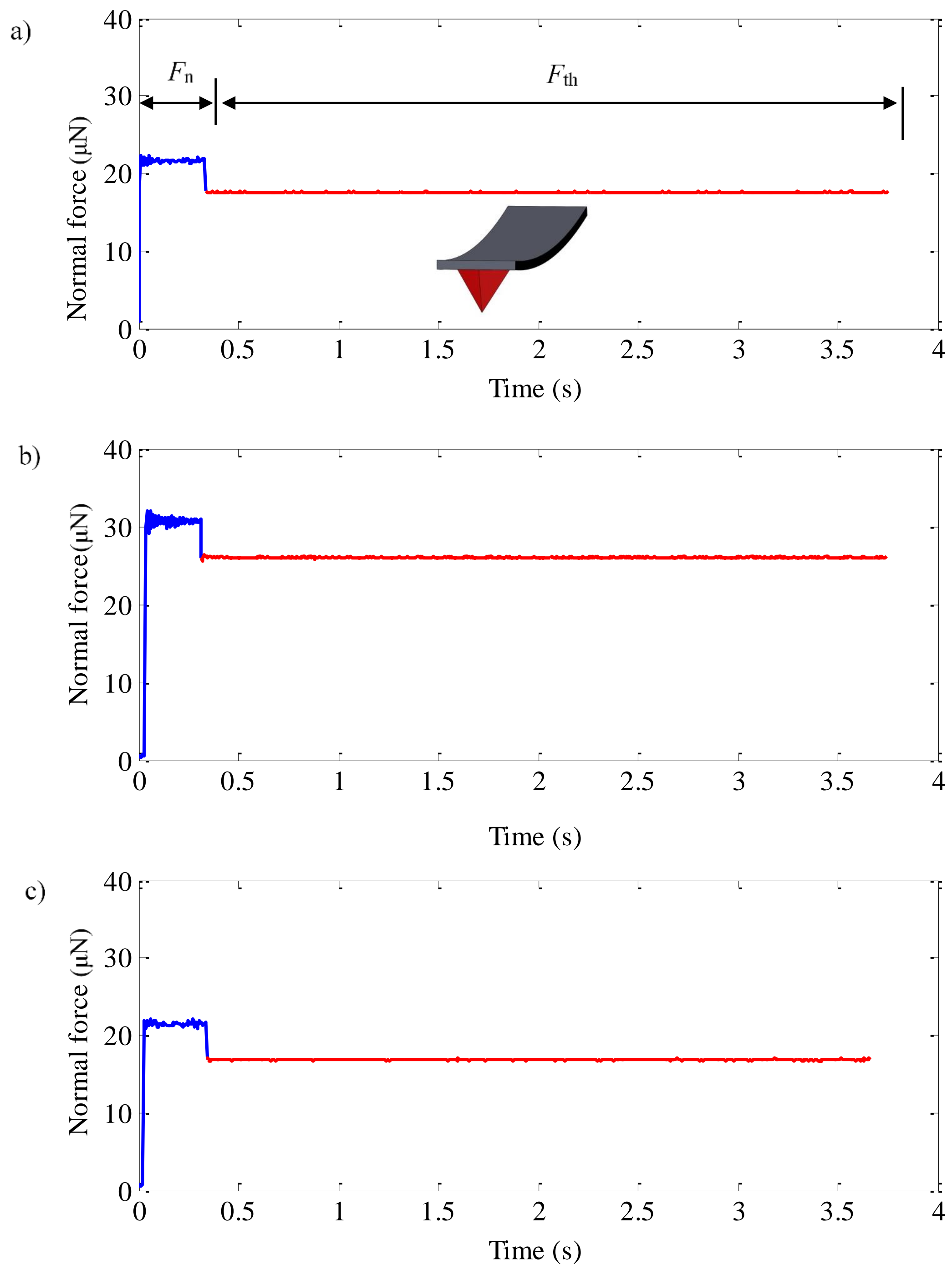

Figure 6.15 F_n, and F_{th} for a pre-set load of (a) 21.5 µN pure forward. (b) 29.5 µN pure forward and (c) 21.5 inclined forward direction µN

Figure 6.16 provides the plots of F_n and F_{th} for a pre-set applied load of 33.5μN in both the pure and inclined forward directions. The data show that in this case, the initial value of F_{th} is slightly higher that F_n. This is because the generated axial force caused a reduction of the bending angle while the tip was not affected by sliding. As explained in Chapter 4, this results in the V_{A-B} voltage to reduce compared to its target value. Therefore, the feedback loop minimises the distance between the probe and the sample via the extension of the Z-scanner to increase the bending angle until the V_{A-B} voltage returns back to its set value. Consequently, the thrust force during scratching stage was increased. In particular, for the pre-set applied force of 33.5μN, F_{th} was about 10% higher than F_n. From Figure 6.16, it is also observed that the cantilever shape stayed convex at the beginning of the scratching stage. However, at some point during scratching, the cantilever shape change occurred. This phenomenon was preceded by the occurrence of fluctuations in the value of F_{th}. This is attributed to the accumulation of pile-up in front of the tip, which caused to increase the axial force. Following the transition from convex to concave, F_{th} increased significantly. This is due to the fact that the probe was driven even closer to the sample as discussed in Chapter 4.

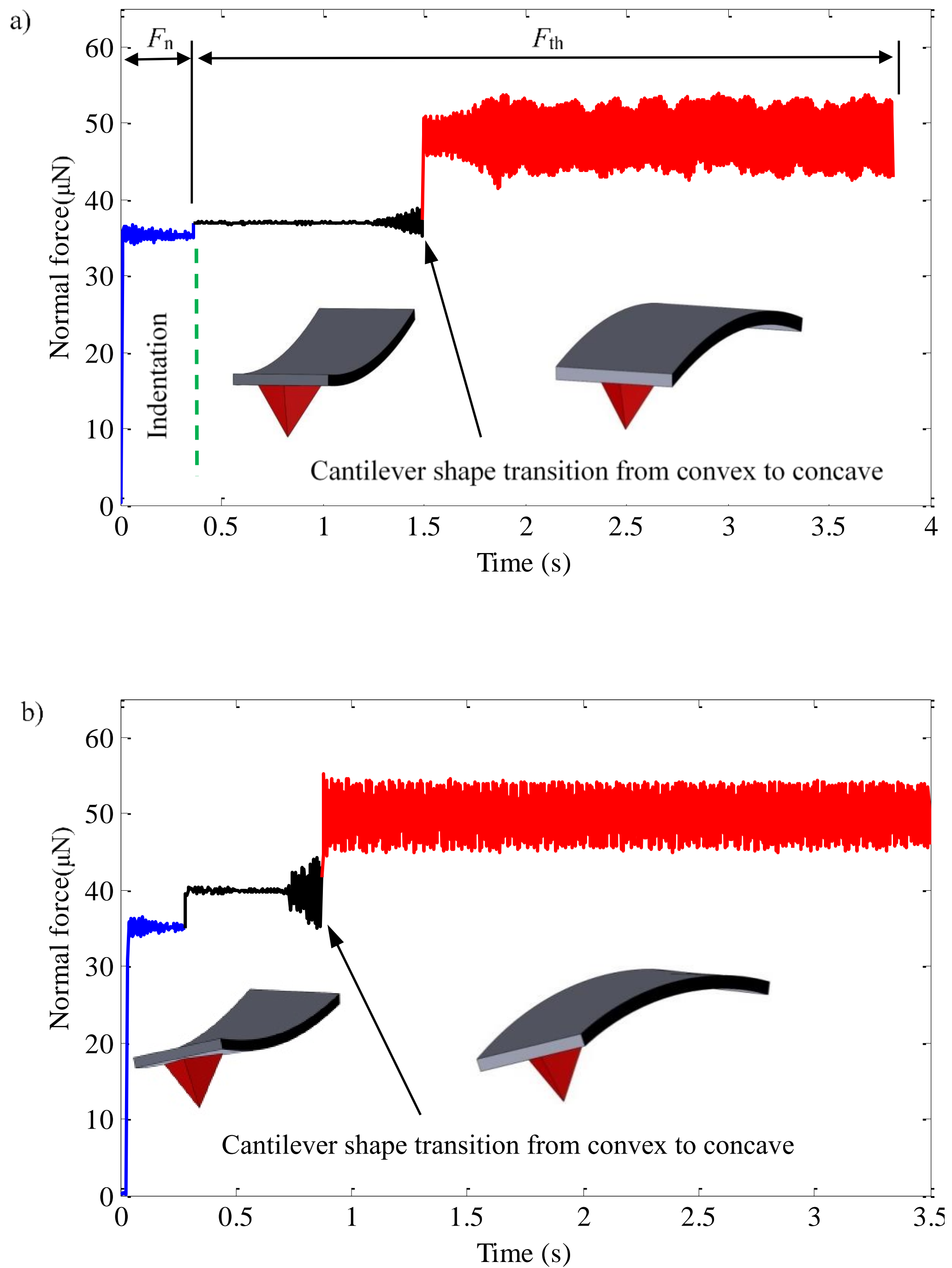

Figure 6.16 F_n, and F_{th} for a pre-set load of (a) 33.5 µN pure forward. (b) 33.5 µN inclined forward direction

6.3.2.2 Axial force, lateral force and resultant force

Figure 6.17 presents the plots of the resultant force and the axial force for a pre-set applied load of 21.5 μN along the pure and inclined forward directions. This figure shows that the overall profiles for both force components are similar to those reported in Figure 6.13 when machining in the backward direction. Thus, it is suggested that the shape of cantilever deflection stayed convex during these nano machining operations. Along the pure forward direction, the axial force and the resultant force generated at the tip were estimated to be 14.7 μN and 23 μN respectively. Figure 6.17 (b) provides the estimation of three force components, namely the axial, lateral and thrust force because the cutting direction was at an inclined angle with respect to the long axis of the cantilever. It can be seen that the lateral force value was the lowest of the three force component and equal to 5.7 μN. This should be due to the fact that the direction of machining was conducted at a small inclined angle (i.e. 22.5°). Naturally, if the inclined angle is increased, this force component should increase and reach and maximum value when the machining is performed along a pure lateral direction. In addition, it should be noted that the axial force was approximately 15.8 μN, which is higher than that calculated along the pure forward direction for the same pre-set applied load. This result may be explained by the fact that, in the pure forward direction, the scratching process is achieved under the ploughing regime only. However, in the inclined forward direction, both cutting and ploughing regimes are likely to be occurring as suggested with similar results of inclined forward machining shown Figure 4.30 in Chapter 4. Interestingly, the resultant force in the axial plane was found to be nearly 23 μN for both the forward and inclined forward directions. A possible explanation for this might be that this is the approximate magnitude required to keep the voltage of V_{A-B} voltage constant under the condition of a pre-set applied load of 21.5 μN.

Figure 6.18 shows the results for the axial and the resultant forces in the forward direction when the pre-set applied load was increased to 33.5 μN. This is a cutting condition which led to a shape change in the cantilever deflection from convex to concave. As a result of this phenomenon, the axial force and the resultant force increased significantly to reach approximately 125 μN and 138 μN, respectively. It is also observed that the magnitude of these two force components display more pronounced oscillations around these values. When the cutting was performed along the inclined forward direction

at the same pre-set applied load, the axial, resultant and lateral forces were also calculated as reported with Figure 6.19. It can be seen from these data that before the cantilever shape change, the axial and lateral force were found to be 14.3 μN and 5.2 μN, respectively. It is noticeable that following the change of the cantilever deflected shape these forces also increased substantially and oscillated around 132 μN and 49 μN, respectively.

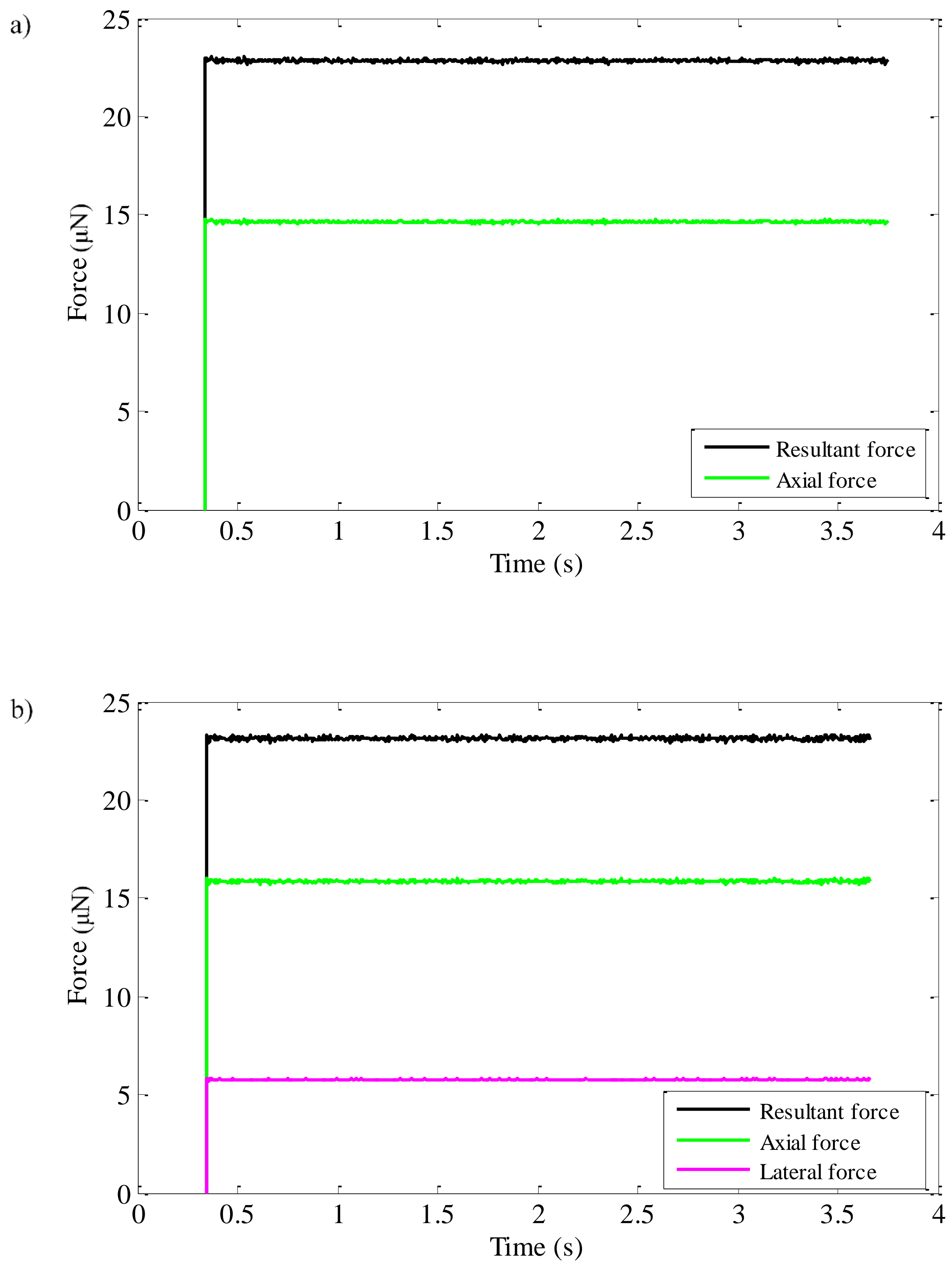

Figure 6.17 Forces during scratching for a pre-set applied load of 21.5 µN along the a) forward and b) inclined forward direction

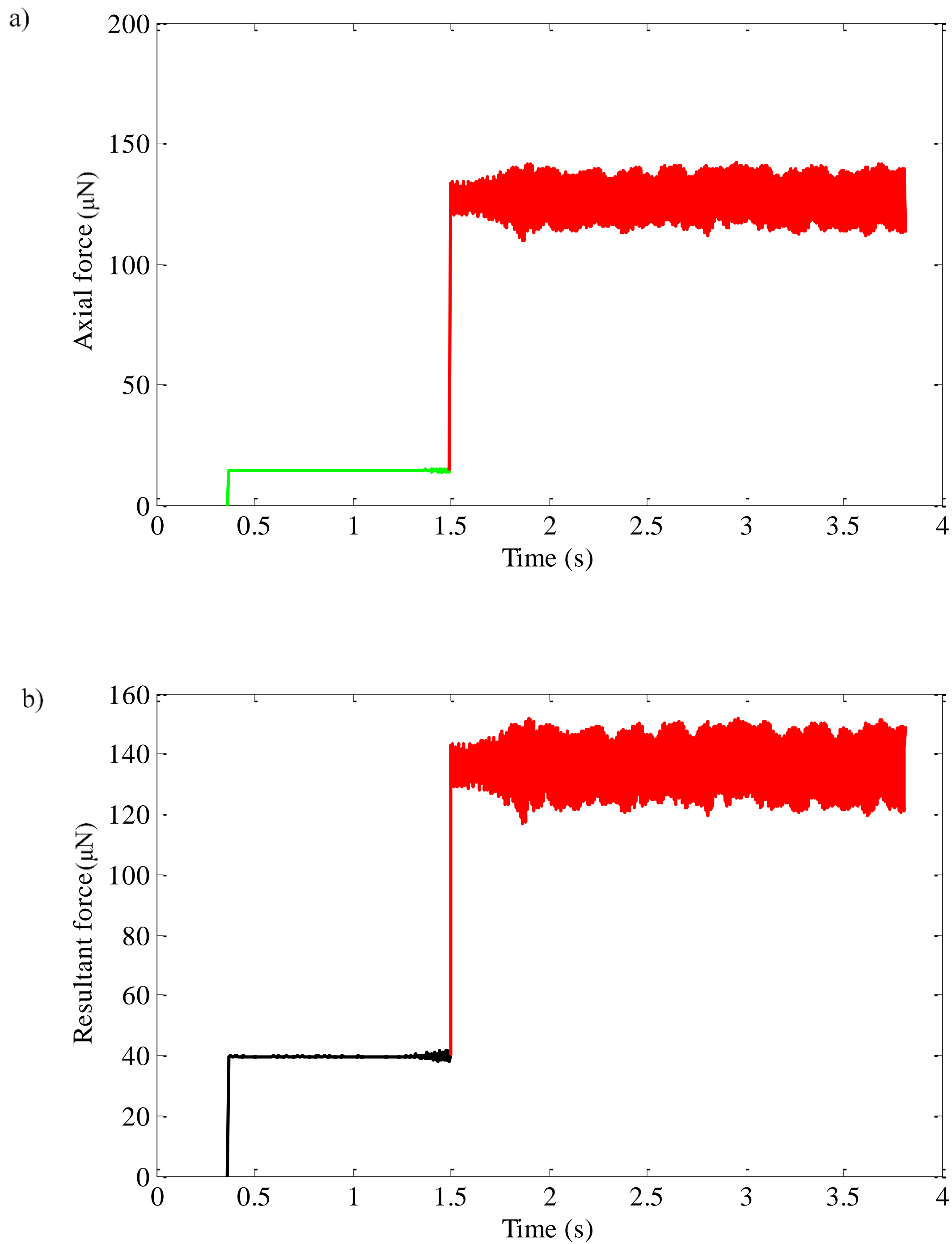

Figure 6.18 a) Axial force and b) resultant force during scratching in the forward direction for a pre-set applied load of 33.5μN

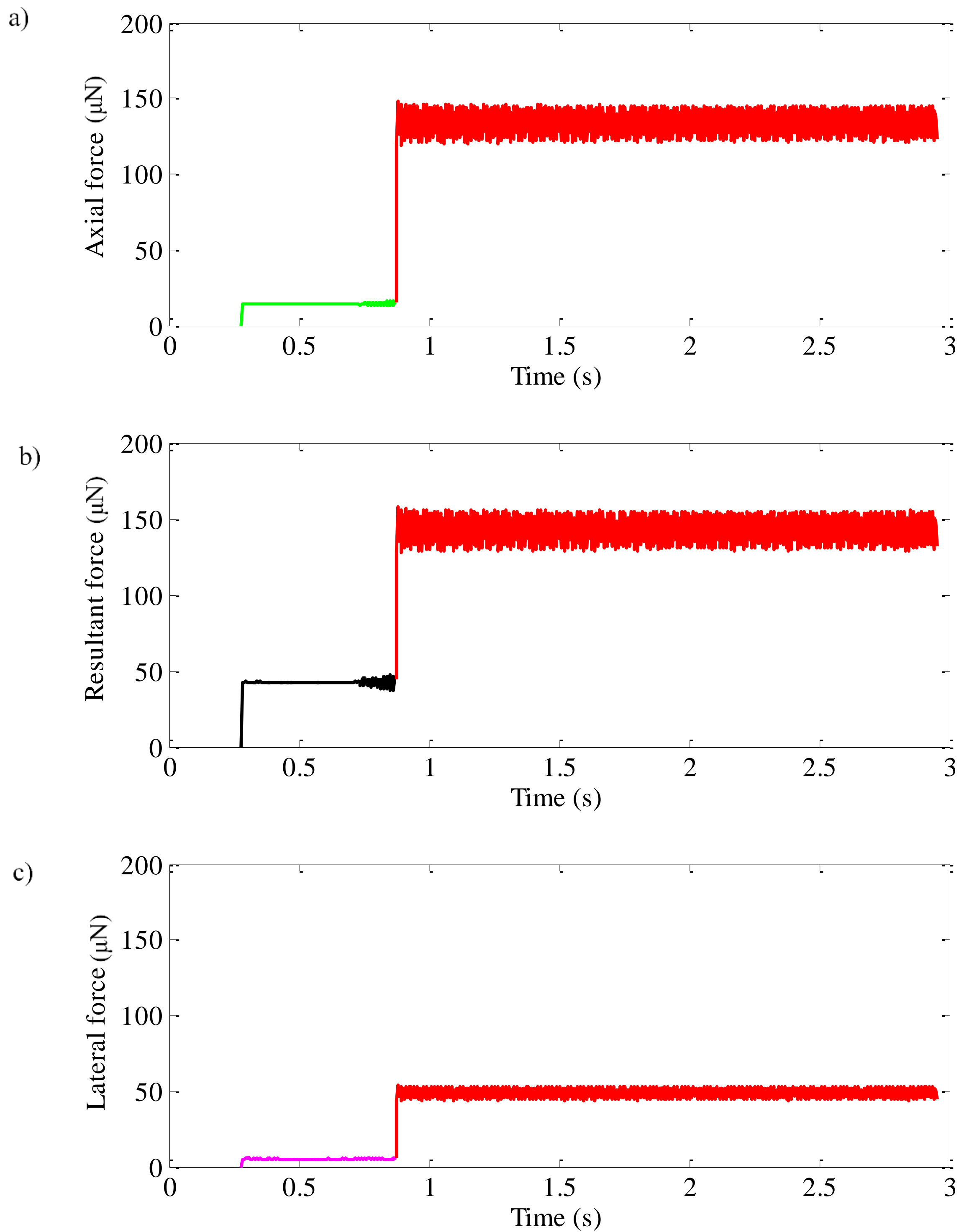

Figure 6.19 (a) Axial, (b) resultant and (c) lateral forces during scratching along the inclined forward direction at a pre-set normal load of 33.4 µN

6.3.2.3 Normal sensitivity, lateral force calibration factor and resultant angle

In the pure forward direction, machining is performed under the influence of two force components, namely the axial and the thrust force. In this respect, the process configuration may be viewed as comparable to orthogonal cutting in traditional machining. On the other hand, three force components are generated when processing in the inclined forward direction, namely, the axial, the lateral and the thrust force. In this case, the cantilever is affected by two elastic deformations: bending and torsion. Consequently, both the normal and lateral sensitivity may be changed. In this experiment, the normal sensitivity as obtained with the common approach where the tip is pressed against a hard sample was found to be 0.0204 μm/V. However, when the tip started the horizontal movement with respect to the sample surface, the quasi-static normal sensitivity, S_{th}, was found to be 0.0195 μm/V for a pre-set applied load of 34.6 μN, while the lateral force calibration factor, α, was found to be 3.9 μN/V. Moreover, as the cantilever deflected shape changed from convex to concave, the quasi-static normal sensitivity was reduced to 0.0077 μm/V. This was accompanied by a reduction in the resultant angle, β, from 70.0º to 20.4º. At the same time, the lateral force calibration factor was calculated to reach 82.3 μN/V.

Finally, the next section aims to provide a comparative summary of the results obtained when applying the percentage method and the fitting method to calculate the thrust force initially, and thus subsequently, to obtain the axial force as well as the resultant angle and the normal sensitivity of the PSPD for a range of pre-set applied loads and for different machining directions.

6.3.3 Comparison between the fitting method and percentage method

Figure 6.20 displays the thrust force values measured by using the fitting and the percentage methods for three machining directions, namely backward, forward and inclined forward and in each case, for different pre-set applied loads. This figure shows that, overall, there is a good agreement between the fitting and the percentage method. Indeed, the average percentage error was found to be approximately 3.7%, 5.3%, and 8.6 % in the backward, forward, and inclined forward direction, respectively. It should also be noticed that when the cantilever deflected shape changes from convex to concave, both methods output a significant variation in the thrust force as it exceeds the pre-set applied load in this case.

The bar chart shown in Figure 6.21 provides a comparison between the fitting and the percentage method when estimating the resultant force for the different cutting conditions considered. It is interesting to observe that the average percentage error between both methods was 0.5% and 0% for the backward and the forward (when the cantilever shape was convex) direction respectively. Moreover, when the cantilever shape changed from convex to concave in the forward direction, this error was still small, approximately 1.8%.

The resultant angle obtained from both the fitting and percentage methods are shown in Figure 6.22. From this data, it can be seen that the resultant angle becomes gradually higher with the increase in the pre-set applied force. However, when the change in the cantilever deflected shape occurs in the forward and inclined forward directions, the resultant angle reduces by approximately 70%. This is due to the comparatively larger increase in axial force than in thrust force when this phenomenon takes place. Furthermore, the best agreement was found between both methods for the backward direction. Indeed, the average percentage error in this case was 4.2%.

Finally, Figure 6.23 provides the results for the calculation of the quasi-static normal sensitivity. It is apparent from this chart that this sensitivity increased gradually as the pre-set applied force was raised. However, in the majority of cases, it remained lower than the value obtained using the conventional approach that estimates the static normal sensitivity. It is also noticeable that, as the cantilever deflected shape changed

from convex to concave, the quasi-static normal sensitivity reduced by more than 50% for the same pre-set applied load.

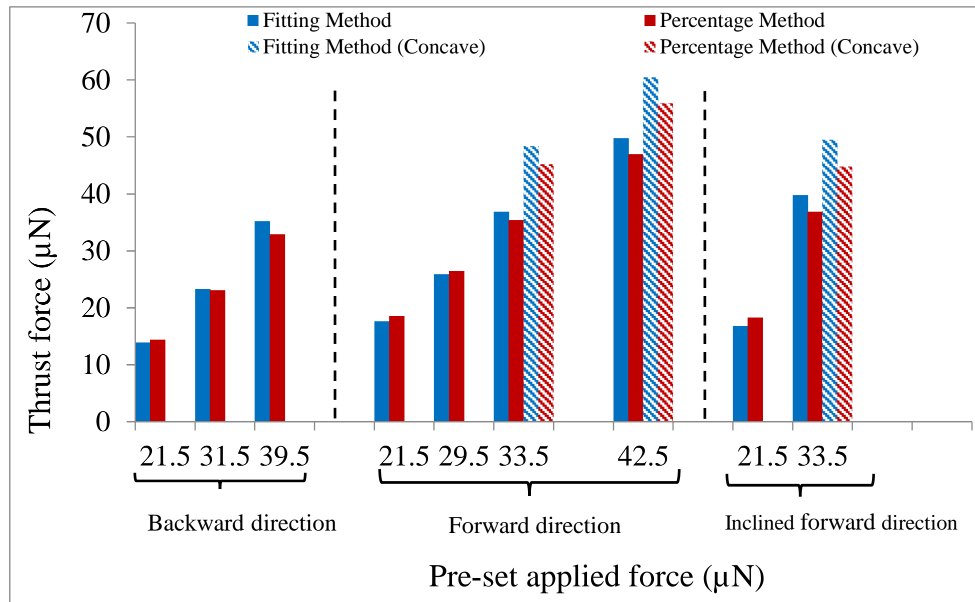

Figure 6.20 Comparison between thrust force values for different pre-set applied loads and machining directions

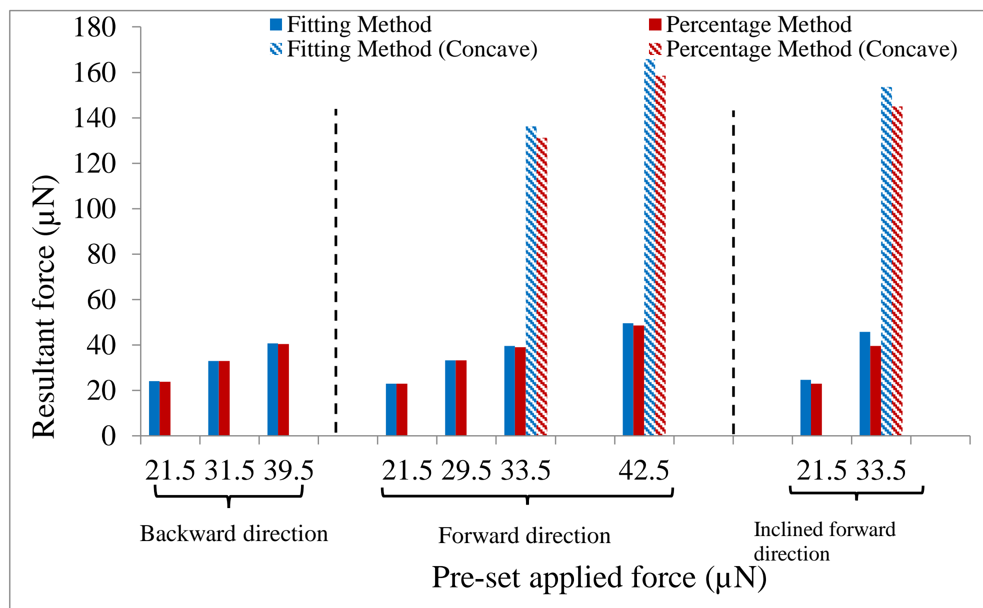

Figure 6.21 Comparison between resultant force values for different pre-set applied loads and machining directions

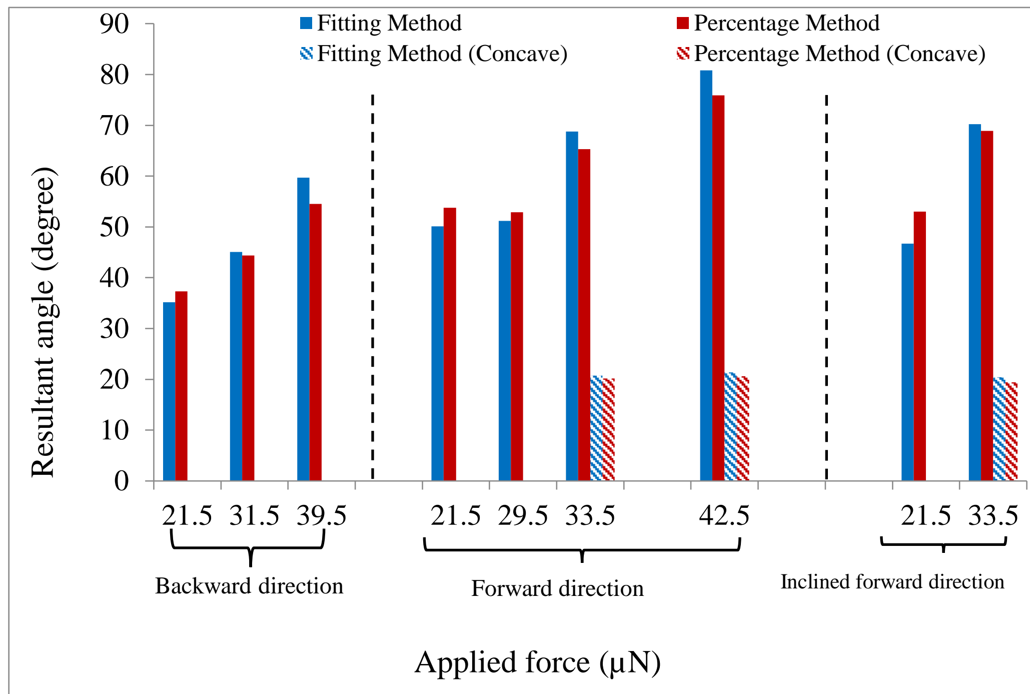

Figure 6.22 Comparison between resultant angle values for different pre-set applied loads and machining directions

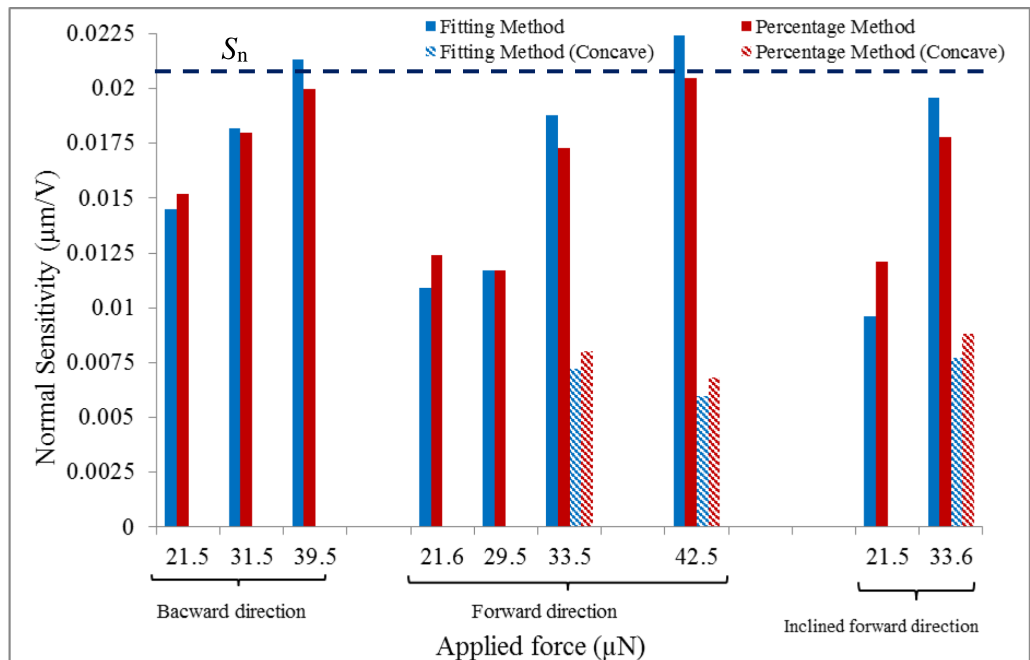

Figure 6.23 Comparison between normal sensitivity values for different pre-set applied loads and machining directions

6.4 Summary

In this chapter, a novel approach was proposed to calibrate and measure the forces acting on the AFM tip during probe-based nanomachining. With this approach, such forces can be measured in any direction of motion. This work was motivated from the theoretical and experimental findings obtained in Chapter 5, which showed that the conventional approaches are not suitable to measure such cutting forces during AFM tip-based nanomachining. The developed procedure was divided in three main steps, as summarised below.

For the first step, the deflection angle of the cantilever was considered constant between the indentation and scratching stages. This relied on the basic principle of optical reflection. Indeed, the fact that $V_{A\text{-}B}$ is kept constant throughout means that the surface of the cantilever where the laser is reflected keeps a fixed orientation in the axial plane. Based on this and by applying a simple theoretical analysis, the axial force, F_a, could be expressed as a function of both the normal force, F_n, when the AFM stage is static and the thrust force, F_{th}, when a relative motion between the tip and the sample occurs. Thus, to estimate F_a, both F_n and F_{th} should be known. To assess F_n, the refined model reported in Chapter 5 can be used. To calculate F_{th}, two new methods were introduced in this chapter. These form part of the implementation of the second step, which is summarised below.

Both of these novel methods rely on the measurement of the Z-detector voltage. They are relatively simple to implement. The first method is referred to as the "fitting method". Its main outcome is that a relationship between the normal force and the Z-detector voltage (hence the vertical movement of the fixed end of the cantilever) can be established. The second method is referred to as the "percentage method". In this case, the percentage variation in the Z-detector voltage output at the start of the horizontal motion between the tip and the sample is recorded. This value is then applied to the calculated normal force at the end of the indentation process to derive the value of the thrust force during scratching.

In the third step, a refined theoretical model was proposed based on classical beam theory to determine the axial force, F_a, during cutting as a function of the cutting direction

and of the cantilever deflected shape (i.e. concave or convex). The model combined the results of first and second steps of the overall approach. Furthermore, the method was also extended to determine the lateral force acting on the tip, F_L, the lateral force calibration factor, α, and normal sensitivity, S_{th}.

In addition, the main conclusions which can be made from the study reported in this chapter are:

- A good agreement was found between the fitting and the percentage methods for the different physical quantities evaluated.
- The change in the cantilever deflected shape from convex to concave was reported in Chapter 4 to be accompanied by a significant variation in the topography of the machined groove. Here, it was shown that following such a shape change, the resultant force became approximately three times higher than that prior to the occurrence of this phenomena.

Chapter 7

Advanced investigations of groove formation mechanisms and machining outcomes

7.1 Introduction

As described in Chapter 1, in order to implement the AFM probe-based machining at nano-scale successfully, one of the main research objectives of this Thesis is to gain further insight into the material removal mechanisms that influence the process. To achieve this, a series of post-machining investigations of the topography of produced grooves is reported in this chapter. In particular, the main aim of this chapter is to report in-depth analyses of a number of processing outcomes based on the experimental observations of machined groves. These investigations were conducted for different applied loads and processing directions, namely in the pure and inclined forward direction and in the pure backward direction. This study also builds on the knowledge established in the previous chapters. In particular, the accurate determination of the cutting forces and the understanding of the deflected shape of the cantilever provide some keys input when analysing the groove formation process.

This chapter is organised as follows. The next section focusses on the observation of different material deformation mechanisms, namely 1) ploughing and 2) cutting through shearing of the workpiece material. The third section reports quantitative data about the width and depth of machined grooves. The fourth section presents a qualitative analysis based on the geometry of the groove cross sections. This includes the analysis of the formation of pile-ups on the edges of the grooves. Section five aims to explain the observations made about the groove geometry and the measured cutting forces based on the analysis of the angles that define the tip geometry. Section six discusses the morphology of the chips resulting from machining in the pure backward and inclined forward directions. The final section provides a summary of the conclusions reached in this chapter about the physical phenomena observed.

7.2 Investigation of material deformation regimes

As presented in Chapter 2, during AFM tip-based nano mechanical machining, there are two types of plastic material deformation mechanisms, namely ploughing and cutting. The ploughing regime results in a portion of the processed material being pushed out on the edges of a machined groove while another portion is compressed under the tip and recovers back after the tip passes. The cutting regime is characterised by the formation of a chip through the shearing of the material. For a given pre-defined normal load, different regimes may occur depending on the particular scratching direction considered.

SEM micrographs were used to examine the grooves generated in the backward direction for two different pre-set forces, F_n, namely 21.5 µN and 36.0 µN (see Figure 7.1). From these images, it is observed that plastic deformation occurred on the sample surface in both cases. Importantly, it can be noticed that a chip was formed for both grooves. Such a chip was connected to the specimen at the end of each grove. Figure 7.2 illustrates the expected flow of material as a function of the geometry of the tip and of the direction of motion. Based on Figure 7.2(a), it can be said that the plane *AOC* of the pyramid tip pushes the material towards the fixed end of the probe. In this case, there is one rake face, which is the backward face of the tip (i.e. defined by (*AOC*) in Figure 7.2). This rake face is flat and its attack angle is oriented at 90º with respect to the cutting direction. Thus, this is a configuration which corresponds to the orthogonal machining mechanism. According to (Koinkar and Bhushan 1997), increasing the attack angle raises the likelihood of generating a chip during the process. Thus, our results are consistent with their findings

Figure 7.3 shows two grooves achieved on the copper sample in the forward direction. These were formed under the pre-set force, F_n, of 36.0 µN and 39.0 µN. It is clear from these SEM micrographs that the grooves are very well defined and that no chip can be observed at the end of the grooves or around them. Thus, these trenches were performed under the ploughing regime only. As shown in Figure 7.2(b), the reason for this results is likely due to the fact that the main cutting edge (*OB*) is parallel to the direction of cutting and that there are two rake faces, one on either side of (*OB*), which are processing the material in an oblique processing configuration. Thus, the material

flow from the channel mainly results in pile-ups, which have been pushed on both sides of the grooves. From the inset micrographs displayed with the higher magnification in Figure 7.3, it is apparent that the grooves exhibit two different geometries because the cantilever deflected shape was changed from convex to concave during processing. Consequently, the cutting forces required for scratching the channel were increased as discussed in Chapter 6. Thus, a larger pile-up was formed to the sides of the groove after the change in the cantilever deflected shape. It is interesting to note that in spite of the increased applied forces following this phenomenon, the scratching process was still conducted under the ploughing regime.

Figures 7.4 and 7.5 show SEM micrographs of grooves obtained in the inclined forward direction for pre-set loads, F_{n}, of 21.5 μN and 33.5 μN. It can be seen clearly, and particularly with Figure 7.5, that an important pile-up is present on one of the sides of the channel. In comparison, a smaller pile-up accumulated on the other side, which also corresponds to the side where a chip formed, as noticed by observing the end of the groove. This indicates that the groove was processed under two mechanisms. The side of the groove with the larger pile-up was scratched under the ploughing mechanism, while chip formation on the other side shows that the cutting regime occurred. This can be explained by analysing the geometry of the tip with respect to the direction of motion. In particular, during inclined forward processing, the plane *BOC* of the pyramid tip acts as a rake face, which tends to become closer to the configuration where orthogonal cutting is taking place (see Figure 7.2(b)). In addition, from the inset micrograph with greater magnification in Figure 7.5, it is apparent that the groove also shows two different geometries because of the cantilever shape change phenomenon during scratching. Furthermore, when this occurred, more material was pushed to the side of the groove.

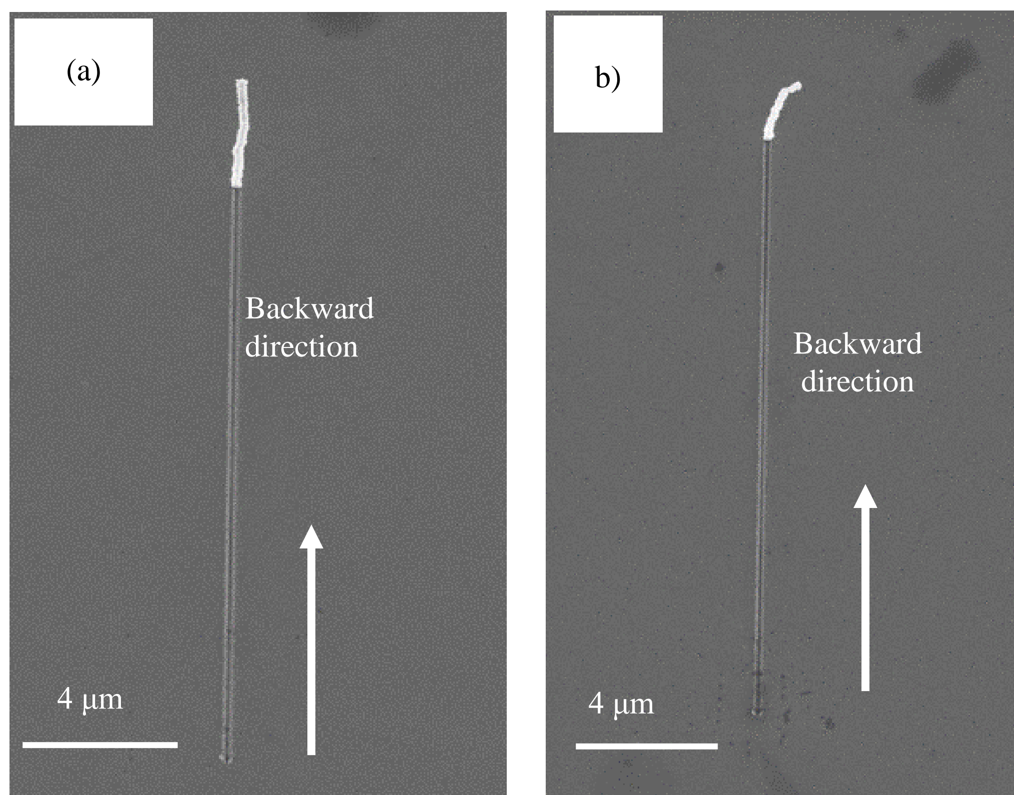

Figure 7.1 SEM micrograph of grooves machined in the backward direction for a pre-defined normal force of a) 21.5 μN and b) 36.0 μN

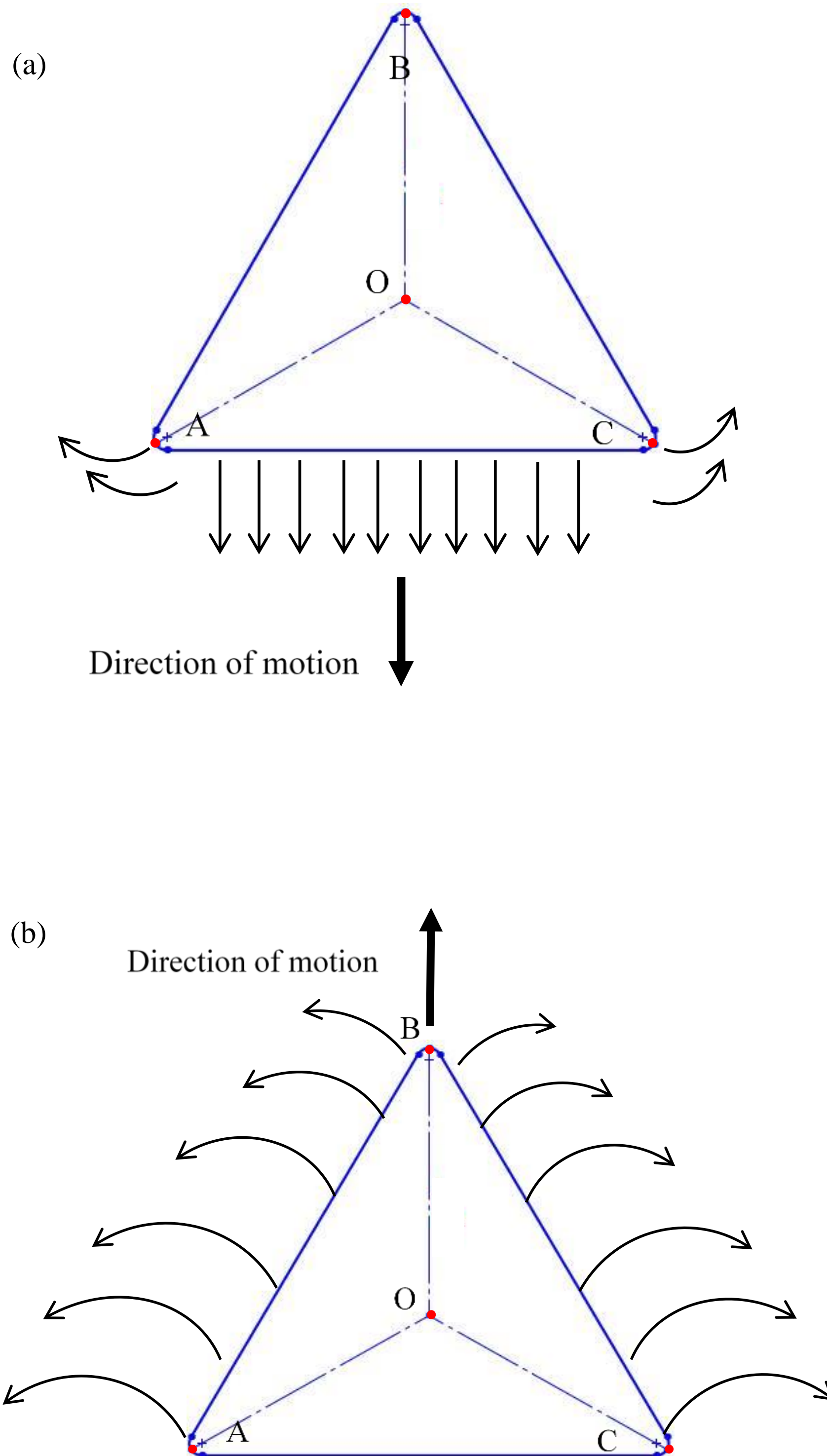

Figure 7.2 Illustration of the flow of material ahead of the tip for (a) the backward direction and (b) the forward direction

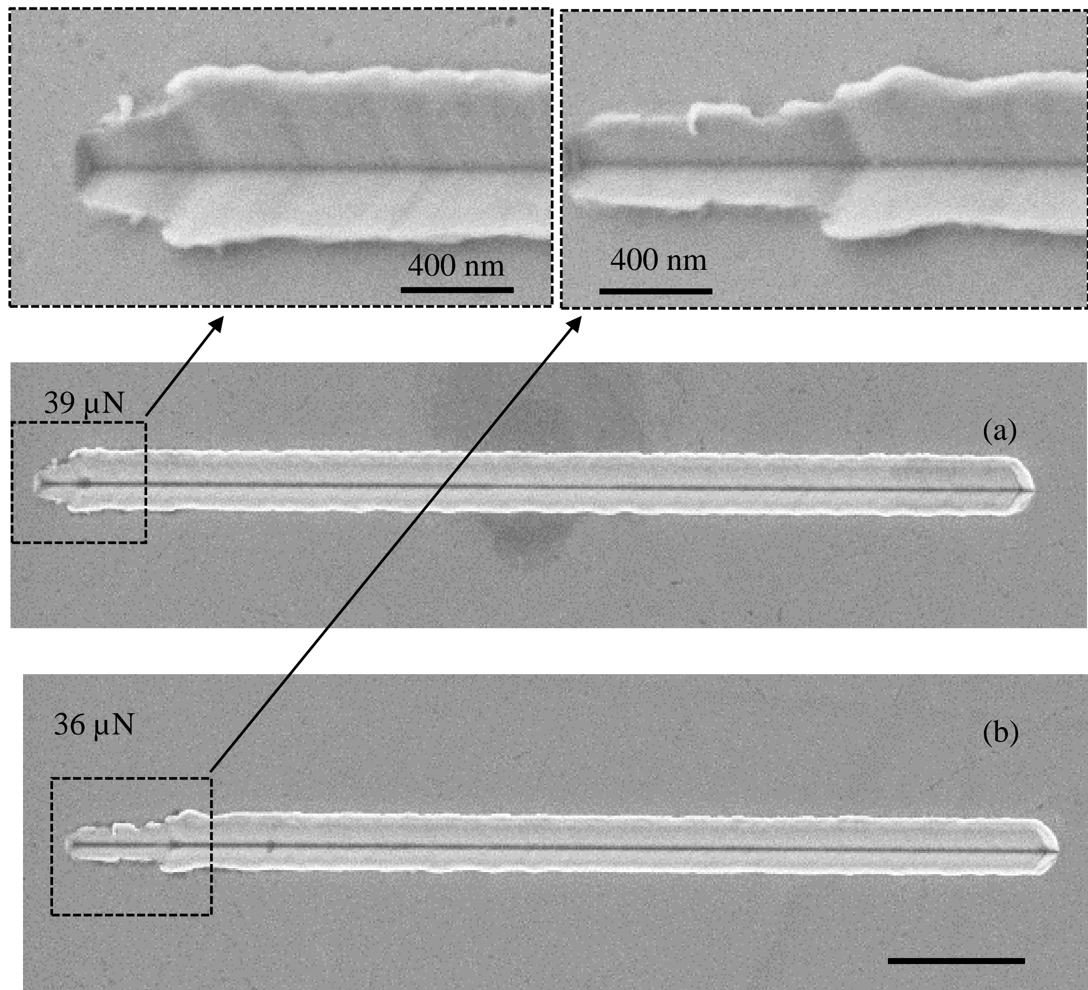

Figure 7.3 SEM micrographs of grooves machined in the forward direction for a pre-defined normal force of (a) 39 μN and (b) 36 μN

The influence of the observed scratching mechanisms on the cutting forces was also studied. The cutting forces were measured and calibrated for each pre-set applied load and direction using the work reported previously in Chapter 5 and Chapter 6. For example, for a pre-set load, F_n , of 21.5 µN, the thrust force, F_{th}, and the axial force, F_a, were found to be 13.9 µN and 19.8 µN, respectively, in the backward direction when the cutting regime was reported. In comparison, for the same pre-set load, the thrust force and the axial force were measured to be 17.6 µN and 14.5 µN, respectively, in the forward direction where ploughing was observed. Thus, the measured axial force was higher in the case where cutting was taking place through the shearing of the material.

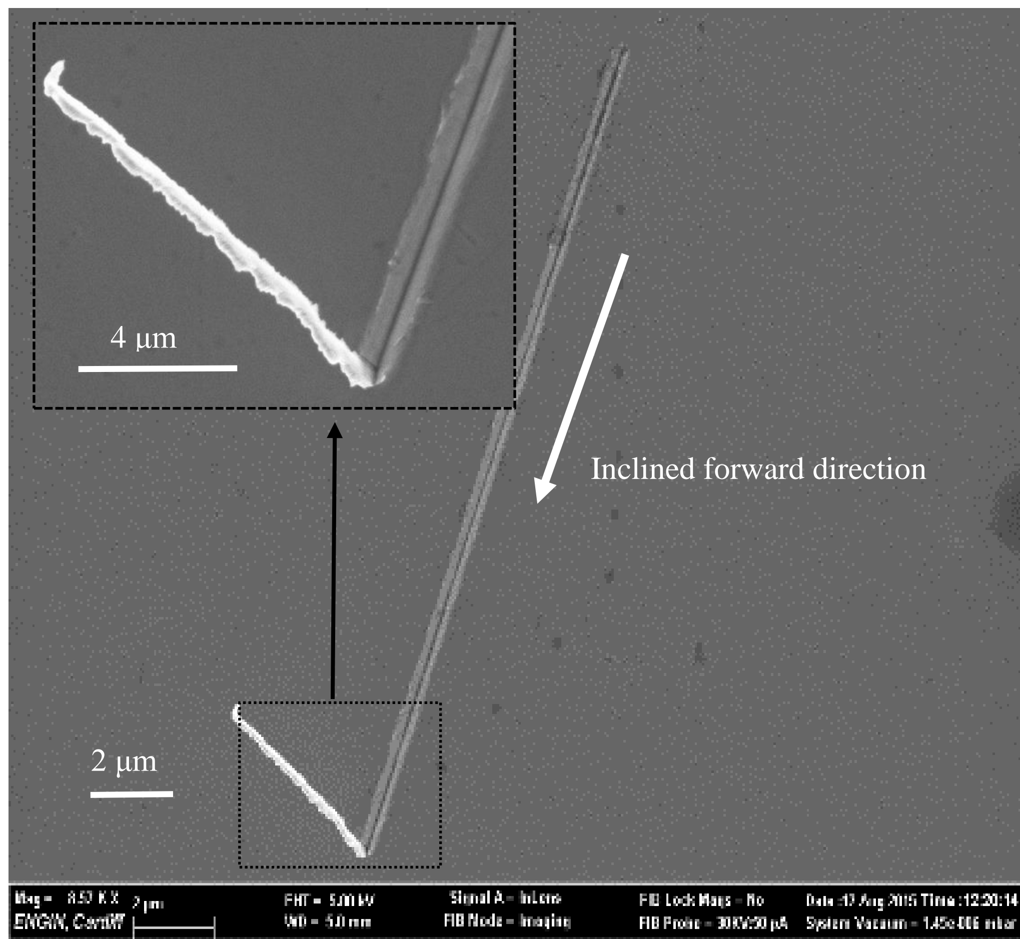

Figure 7.4 SEM micrograph of the groove processed in the inclined forward direction for a pre-defined applied force of 21.5 µN

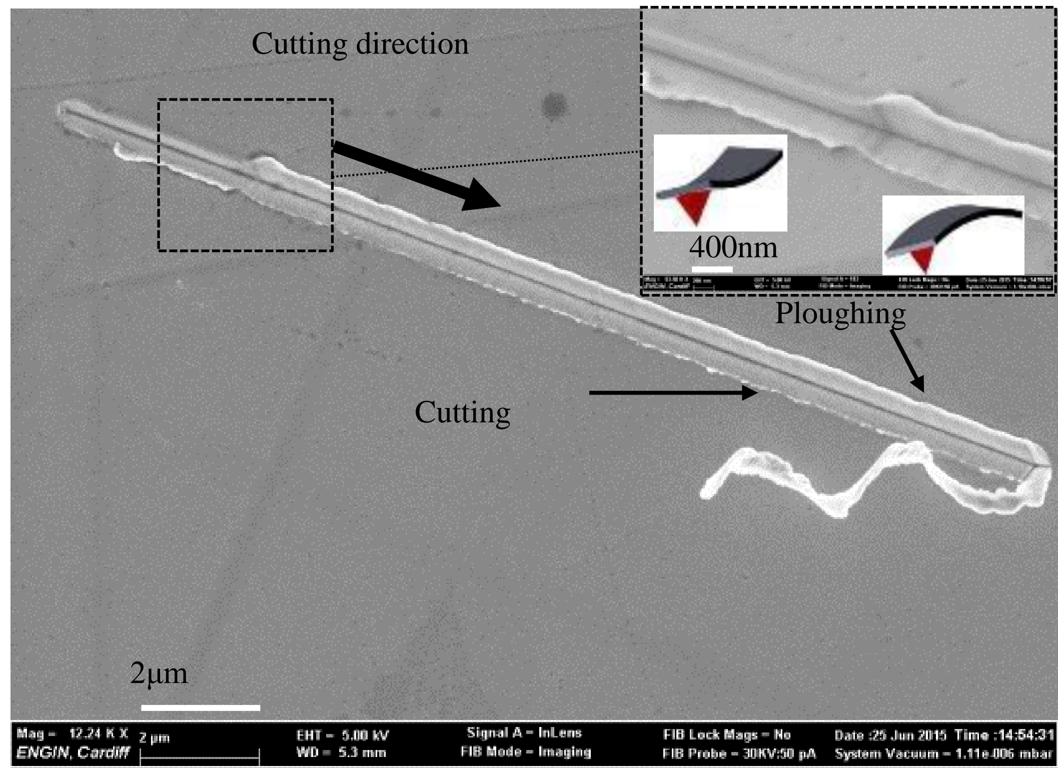

Figure 7.5 SEM micrograph of the groove processed in the inclined forward direction for a pre-defined applied force of 33.5 µN

7.3 Investigation of achieved groove depth and width

As mentioned by Yan *et al* (2015), in order to attain a particular depth for single trenches or even for more complex micro/nano cavities, the pre-set force, F_n, must be defined before the start of the machining operations. Here, the influence of this load and of the cantilever deflected shape on the dimensions of the produced grooves on single crystal copper was investigated. For each groove, AFM scans were completed to obtain their topography data. From these data, eight cross-section profiles were randomly selected at different locations along the groove. The depth and width of cut were calculated for each profile and their average calculated similarly to the procedure followed by (Jiang *et al.* 2011b, Tseng *et al.* 2009b). Figures 7.6 to 7.9 show the depth and width of the grooves plotted as a function of the pre-set load, F_n, for the forward and inclined forward direction of cutting. It can be seen from these figures that a higher pre-set value for F_n obviously produces a larger and deeper groove. However, the increase is

not linear for both the depth and the width due to the possible occurrence of the change in the cantilever deflected shape. In particular, a clear step increase for both dimensions is observed when the cantilever changes from a convex to a concave shape. This result is different from existing reports in the literature (Fonseca Filho *et al.* 2004, Mostofa *et al.* 2013, Tseng *et al.* 2011a). In particular, these previous studies did not report the observed discontinuity in the groove dimensions, which is a consequence of the cantilever behaviour. Thus, the plots indicate that not only the applied load has an effect on the depth and width of the grooves but also the shape of the cantilever deflection has a drastic influence on these dimensions. A result of this phenomenon, in the forward direction, both the depth and width increase by 50% on average. This result is linked to the fact that the thrust force, F_{th}, increases when the cantilever shape changes in comparison with that pre-set by the user. Thus, the contact area increases between the tip and the sample surface. Based on the plotted data in the forward direction, the relation between the pre-set applied load and the depth of the groove can be described as follows depending on the critical load, which is defined as the value of the pre-set load, which results in the cantilever shape change:

$$Depth\ of\ groove = \begin{cases} 0.0232.F_n^2 + 2.16.F_n - 7.1 & if\ F_n \leq Critical\ load \\ -0.088.F_n^2 + 9.62.F_n - 86.06 & if\ F_n \geq Critical\ load \end{cases} \tag{7.1}$$

In Figure 7.10 and 7.11, the scratching depth and width values are plotted as a function of the pre-defined applied load along the backward direction. As expected, the groove size also becomes gradually higher with the increase of the normal load. It is also noted that in comparison with the data obtained for the forward and inclined forward directions, there is not discontinuity in the evaluation of these dimensions because the cantilever shape always stays convex. In this case, the depth of the grove can be expressed as follows:

$$Depth\ of\ groove = -0.086.F_n^2 + 6.7.F_n - 80 \tag{7.2}$$

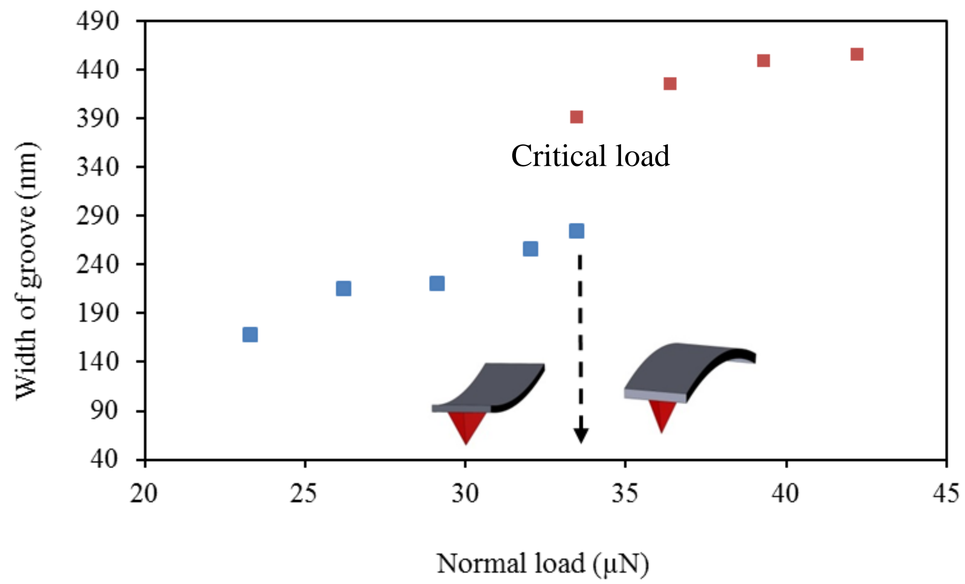

Figure 7.6 Width of scratched grooves as a function of the pre-defined applied normal force in the forward direction

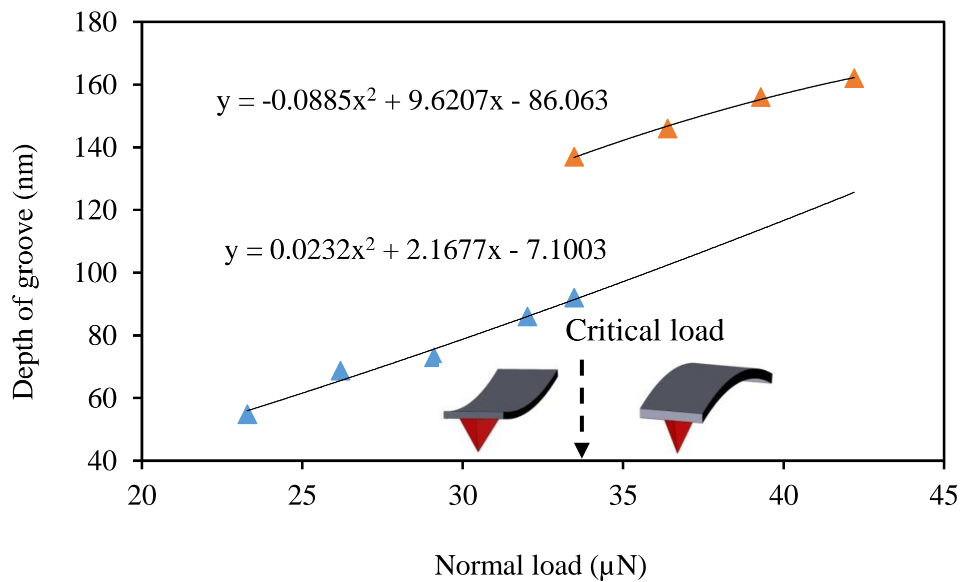

Figure 7.7 Depth of scratched grooves as a function of the pre-defined applied normal force in the forward direction

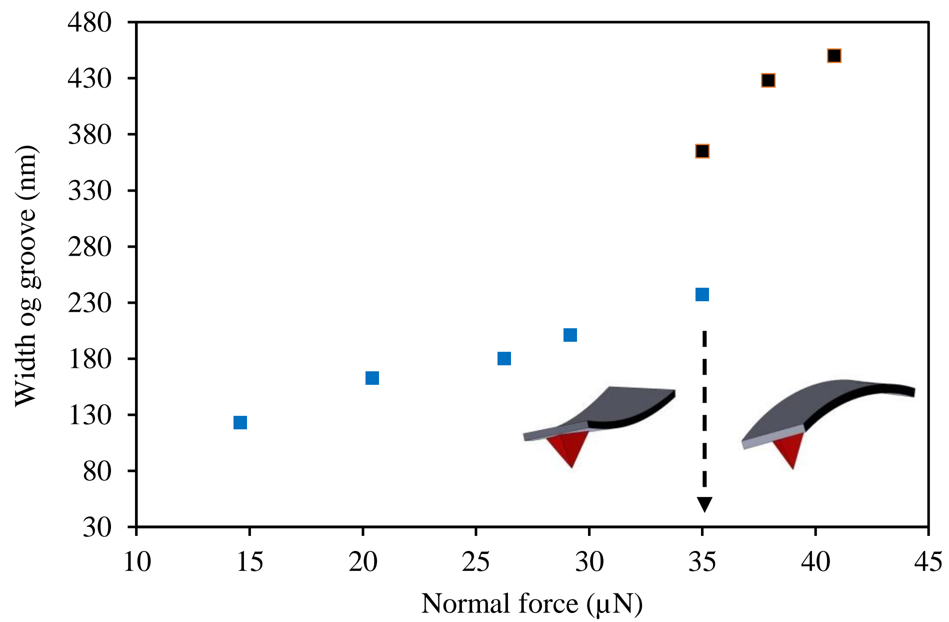

Figure 7.8 Width of scratched grooves as a function of the pre-defined applied normal force in the inclined forward direction

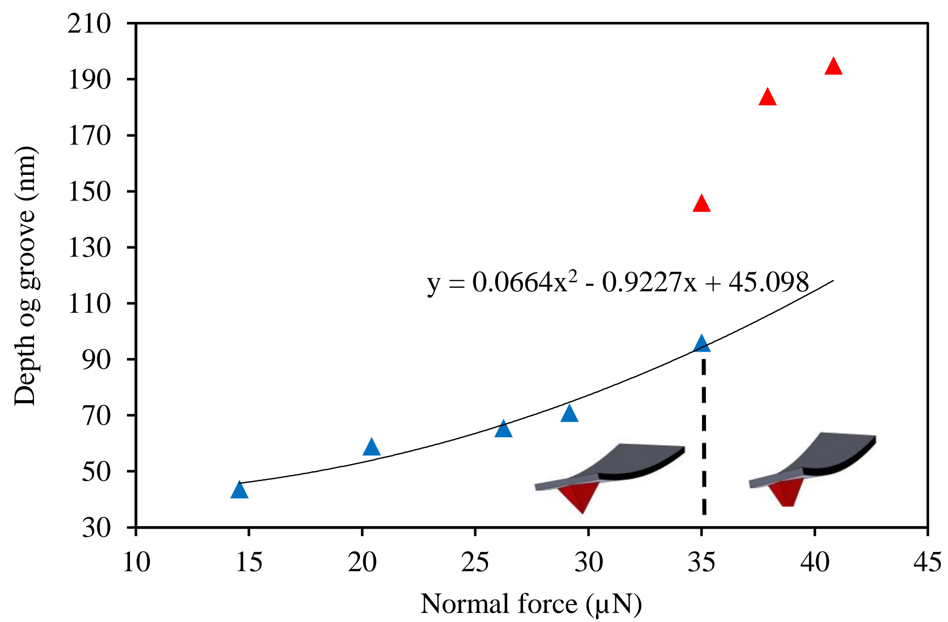

Figure 7.9 Depth of scratched grooves as a function of the pre-defined applied normal force in the inclined forward direction

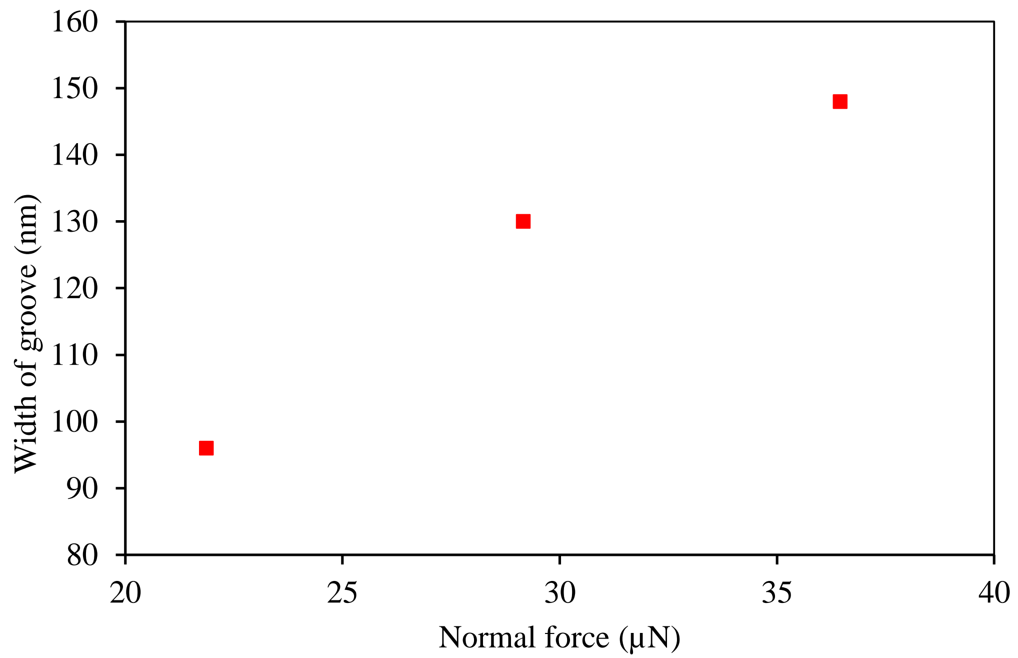

Figure 7.10 Width of scratched grooves as a function of the pre-defined applied normal force in the backward direction

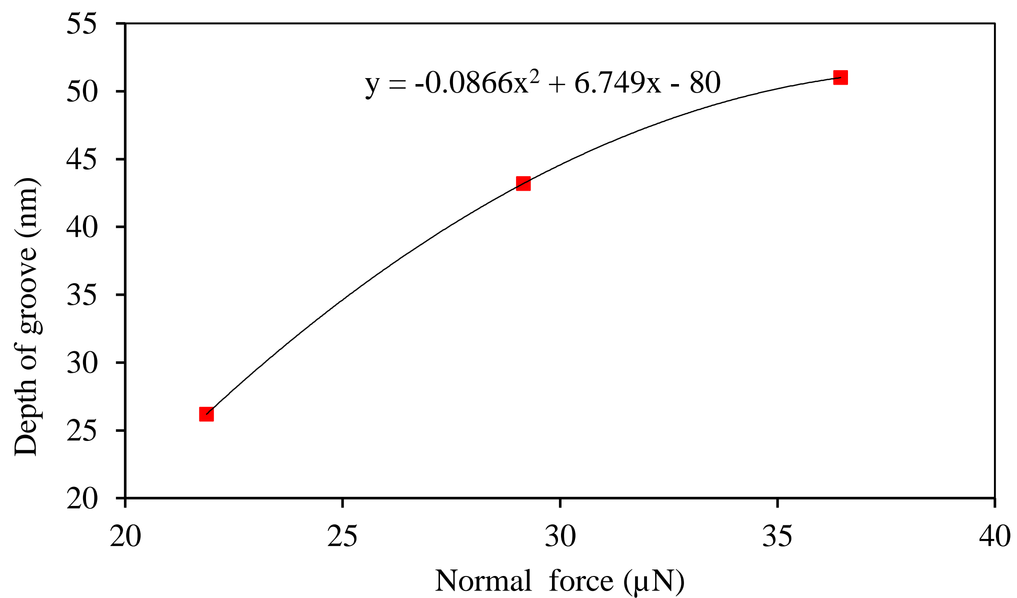

Figure 7.11 Depth of scratched grooves as a function of the pre-defined applied normal force in the backward direction

7.4 Groove geometry and pile-up formation

As reported in the previous sections, the groove dimensions and machining mechanisms are influenced by the tip geometry and direction of scratching for a given pre-set applied load. In this section, the shape of the cross section profiles of produced grooves are examined from a qualitative point of view.

7.4.1 Backward machining

As illustrated with Figure 7.2(a), in the backward direction, the process is conducted in the orthogonal cutting configuration with the normal to the rake face lying in the same plane as the direction of machining, i.e. the axial plane. Figure 7.12 shows typical groove cross section profiles for pre-set loads, F_n, of 16.0 µN, 21.5 µN and 27.0 µN. As expected, the groove cross sections exhibit a V-shape topography. Pile-ups are observed along both sides of the channels. SEM inspections of these grooves confirmed that chips were formed for each of them and thus, that the cutting regime dominated the machining mechanism. It can be observed that the ratio of the sum of the height of the pile-ups to the depth of the grooves decreases when the pre-set normal load is increased. Thus, it is expected that a further reduction of the pre-set normal load would eventually results in ploughing becoming the dominant machining mechanism. This is due to the minimum chip thickness effect, which is a specific size effect in small scale machining as presented in Chapter 2. It is worth noting that Ahn and Lee (2009) suggested that when this ratio become more than one, then ploughing is the main processing regime. Conversely, when this ratio is less than unity, then cutting can be considered the dominant mechanism. It should also be noted from this figure that the V-shaped groove and the pile-up are not symmetrical. This might be due the fact that the normal to the rake face for the particular tip employed did not lie perfectly in the plane of the direction of motion. Previous studies in the literature also reported similar observations of unsymmetrical pile-up accumulated around the sides of the channel (Jiang *et al.* 2012, Tseng *et al.* 2011b, Tseng *et al.* 2010).

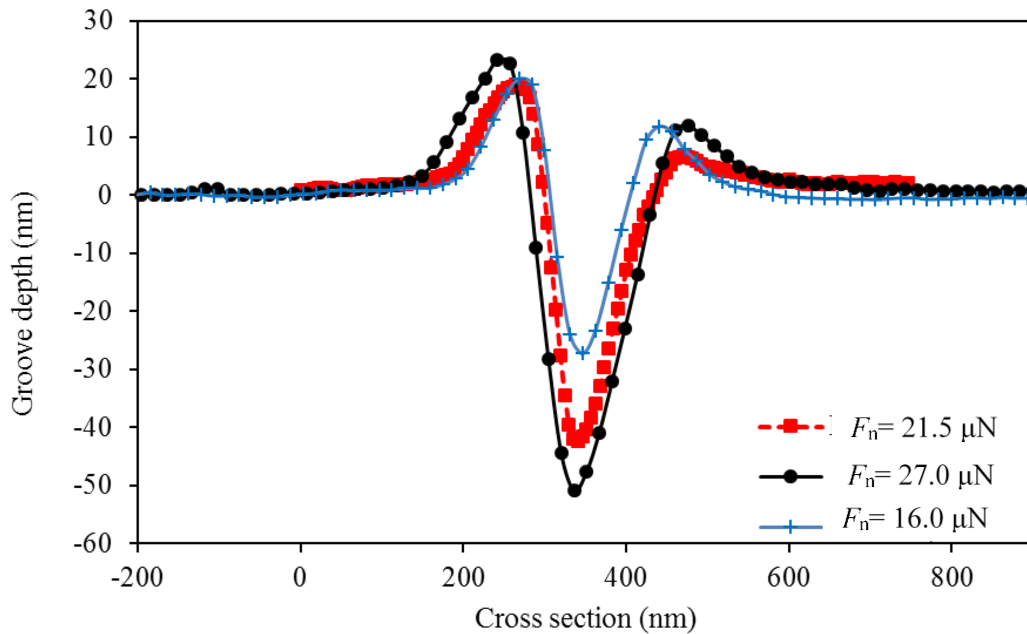

Figure 7.12 Cross-sectional profiles of produced groves for different pre-set applied loads in the backward direction

7.4.2 Forward machining

Figures 7.13 and 7.14 respectively show typical cross-sections and entire AFM scans of machined grooves for several pre-set loads, namely 21.5 µN and 33.5 µN in the forward direction. It is clear from Figure 7.13 that the cross-sectional profiles obtained are also close to a V-shape topography and that pile-ups are formed along both sides of the channel. The ratio of the sum of the height of the pile-ups to the depth of the grooves was found to be always higher than one. According to Ahn and Lee (2009), this is indicative of processing in the ploughing-dominated regime and indeed, this result is consistent with the observations reported in section 7.2 for this set of grooves. For the particular pre-set load of 33.5 µN, the pile-up height was approximately 94.0 nm before the cantilever shape change, while it was 156.3 nm afterwards. This is due to the increase of the thrust force, F_{th}, and axial force, F_a, following this phenomenon.

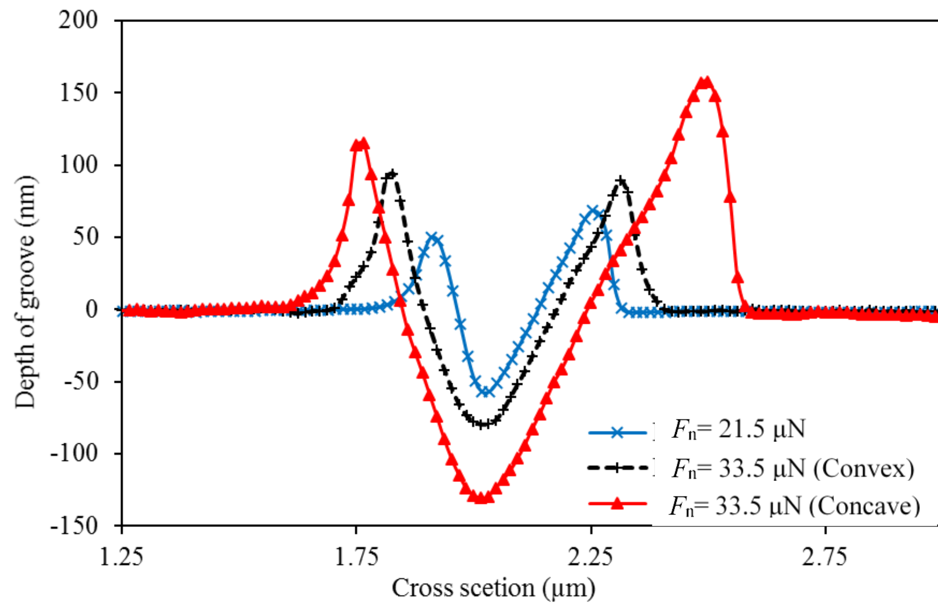

Figure 7.13 Cross-sectional profiles of produced grooves for different pre-set applied loads in the forward direction

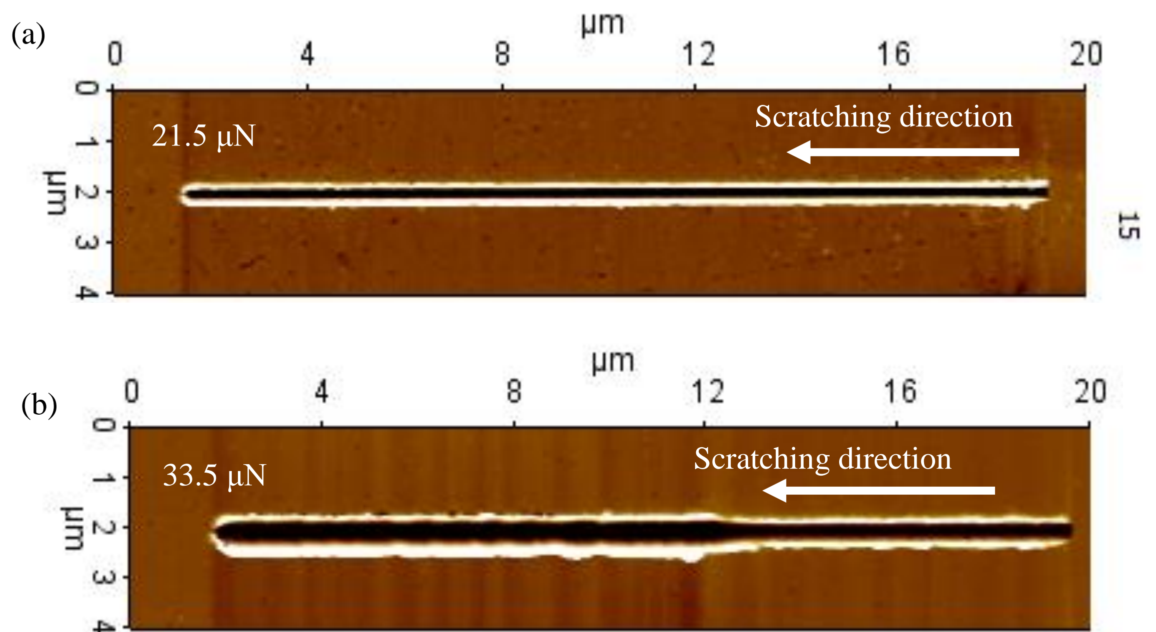

Figure 7.14 AFM image of scratched grooves for pre-set applied forces of (a) 21.5 µN and (b) 33.5 µN in the forward direction

7.4.3 Inclined forward machining

Figures 7.15 and 7.16 illustrate the AFM topography and cross section profiles of machined grooves for two different pre-defined normal loads when processing in the inclined forward direction. It is worth noting that applying the ratio from Ahn and Lee (2009) could be misleading here as it is defined in the context of homogeneous machining on both sides of the grooves. Based on the schematics shown in Figure 7.17, it can be seen that the material was pushed in two regions, A and B. In this case, these regions were scratched under two rake faces namely, *AOB* and part of *AOC* (refer to Figure 7.18).

For the smaller pre-set load, F_n, of 21.5 μN, the groove topography stayed constant throughout the process (see Figure 7.15(a)). In addition, from the inset SEM micrograph already reported in Figure 7.4, one side of this groove was cut though the shearing of the material with chip formation. This is the side referred to as “Region A” in Figure 7.17. In fact, based on the corresponding cross section profile shown in Figure 7.16, this side of the groove appears to exhibit two machining mechanisms, i.e. ploughing to some extend in addition to cutting. In particular, for this smallest value of pre-set load, the height of the pile-up for region A is higher than that for region B. This should be due to the fact that the contact area on the rake face in region B is smaller than that in region A. In addition, it should be noted from Figure 7.17(a) that for region B, the rake face *AOC* has a small attack angle (similar to the forward machining) and pushed the material outside the groove without chip formation.

When the pre-set load was increased to 33.5 μN, the grooves was machined with the cantilever having a convex deflection to start with. However, the topography of this groove displays a sudden change at some point along its length due to the transition in the cantilever deflected shape from convex to concave, as seen in Figure 7.15(b) and Figure 7.16. Prior to the occurrence of this phenomenon, the pile-up height was higher in region A than in region B, similarly to the case where machining was conducted with the smaller pre-set normal load of 21.5 μN. It is interesting to notice that, upon the change in the deflection of the cantilever, it is region B where the pile-up height became higher. This indicates that chip formation through the shearing of the material become more dominant in region A. This should be caused by the increase in the thrust force, F_{th}, and thus, by the further increase of the undeformed chip thickness compared to the minimum chip

thickness as the tip penetrated deeper into the material. In addition, the twisting of cantilever caused the clearance angle to be raised from ψ_1 to ψ_2 (see Figure 7.18(b)). This results from the fact that the value of F_L became approximately 8 times larger after the change in the cantilever deflected shape. Thus, the inclined edge (*OB*) penetrated deeper into the material. Besides, given that the attack angle of the rake face *AOB* was close to 90°, this face removed the majority of material in the region A as a chip. Finally, based on the data shown in Figure 7.16, when the cantilever deflected shape was changed from convex to concave, the pile-up increased by approximately 2.3 times in region B. As mentioned above, this should be a direct result of the increase in applied force and axial force.

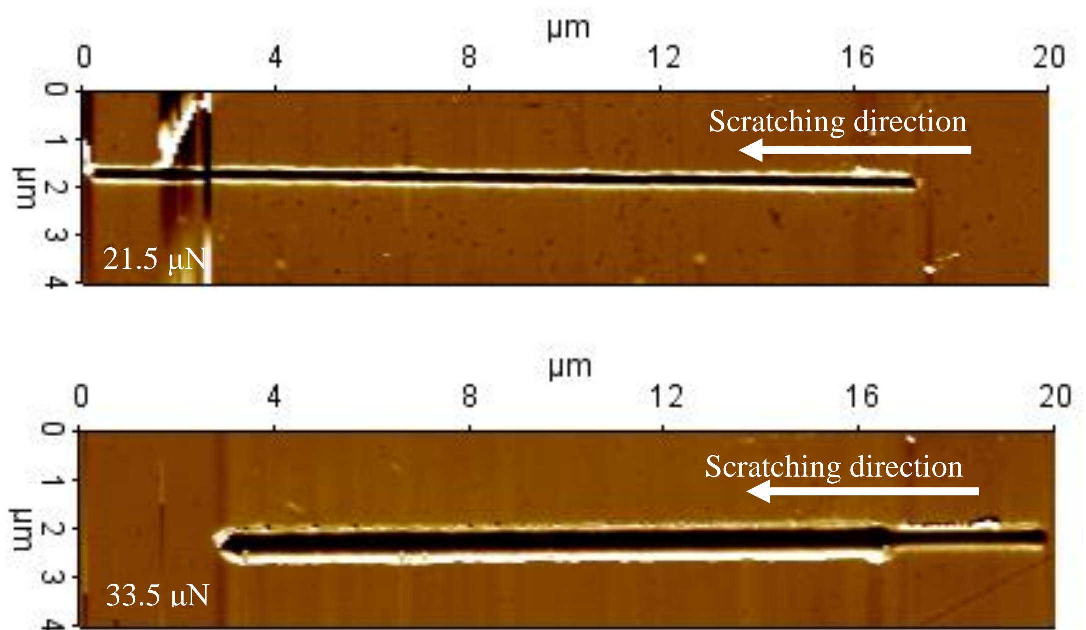

Figure 7.15 AFM image of scratched grooves for pre-set applied forces of (a) 21.5 µN and (b) 33.5 µN in the inclined forward direction

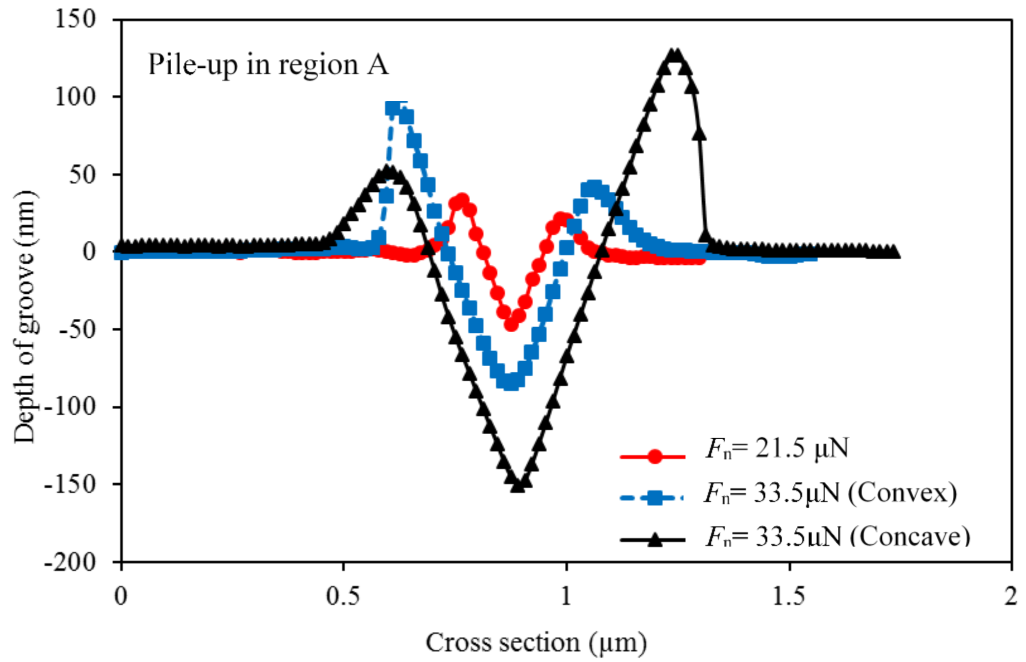

Figure 7.16 Cross-sectional profiles for different pre-set applied loads in the inclined forward direction

(a) Convex deflection shape

F_{th}< critical load

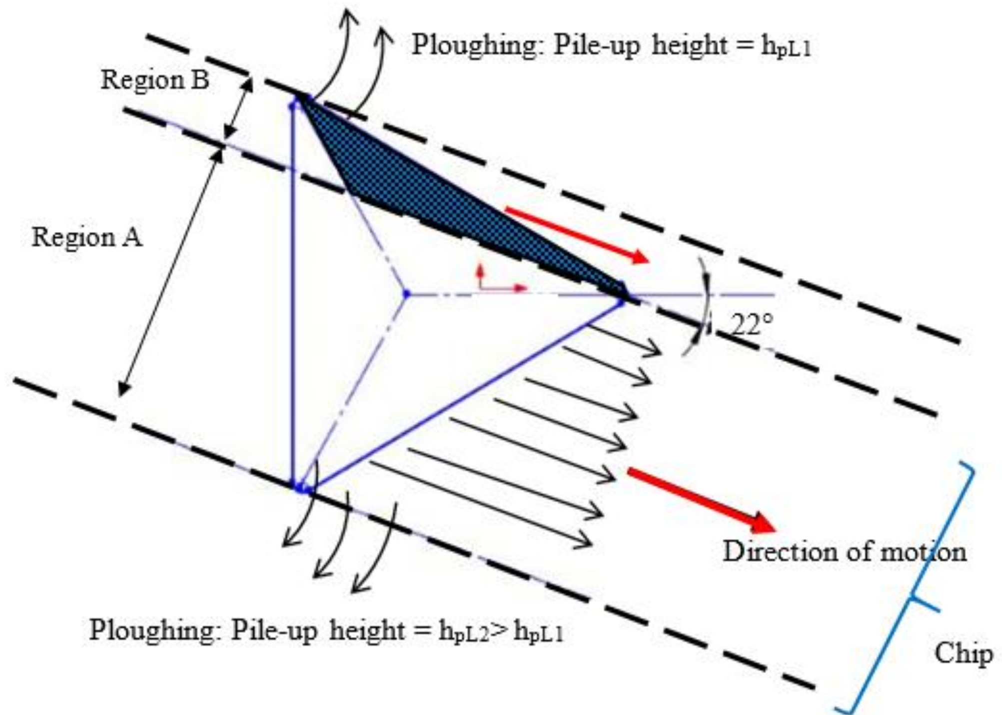

(b) Concave deflection shape

F_{th}> critical load

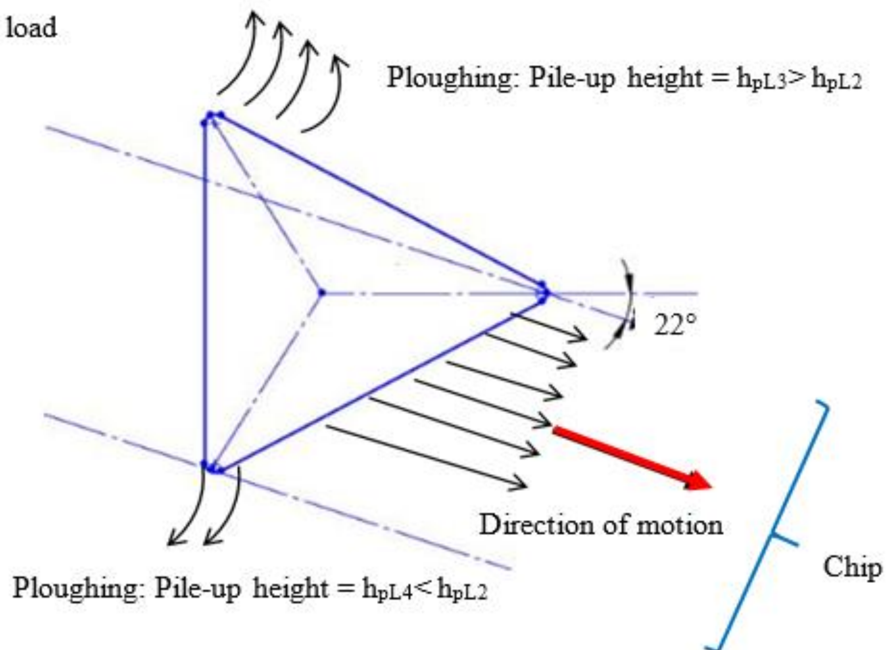

Figure 7.17 Illustration of material flow in inclined forward direction for (a) convex cantilever deflected shape and b) concave cantilever deflected shape

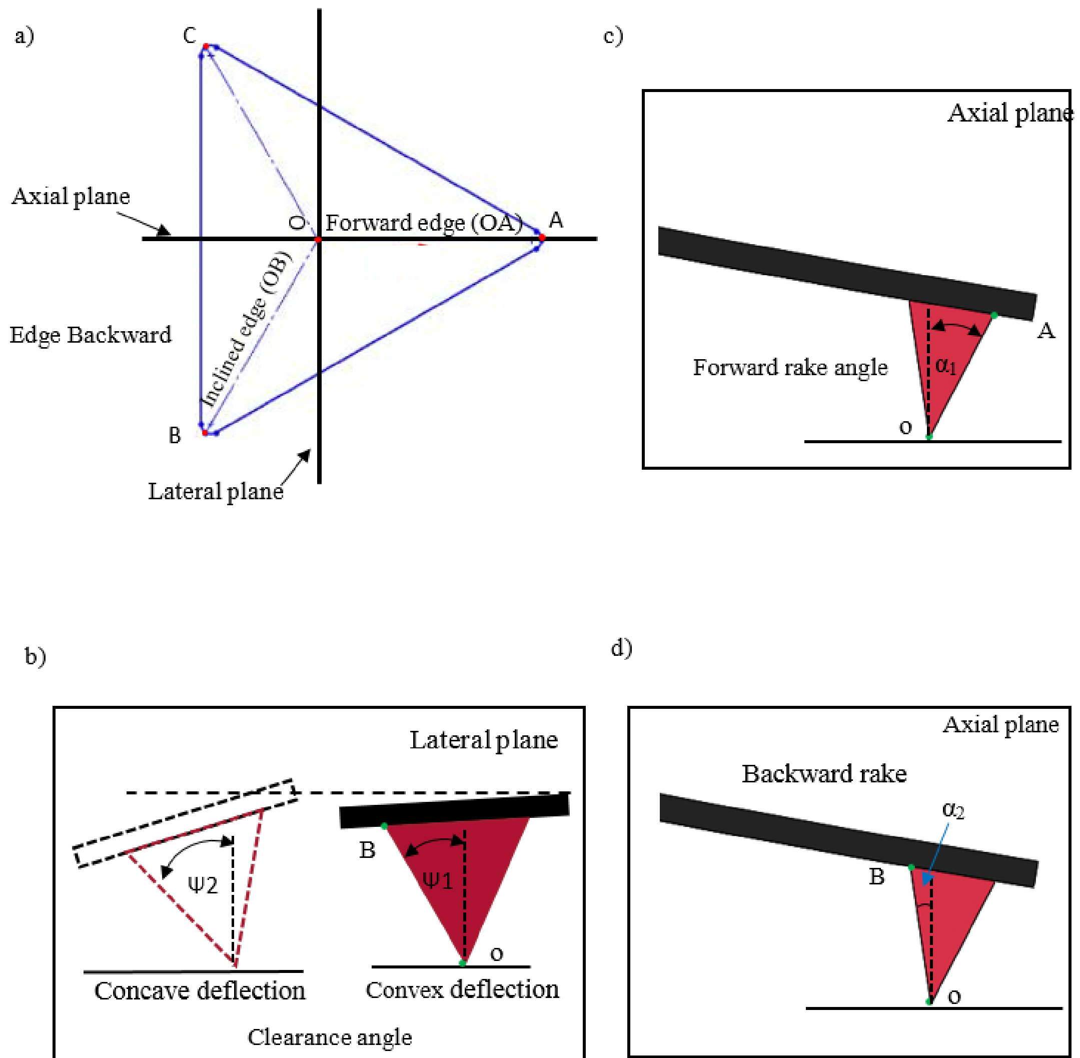

Figure 7.18 Tip planes and angles: (a) top view of the tip; (b) clearance angle; (c) forward rake angle and (d) backward rake angle

7.5 Influence of tool angles and cutting direction during scratching

According to the manufacturer of the DNISP probe utilised in this study, the tip includes a number of angles, which can be defined in different planes. Based on the classification reported in Chapter 2, in the *T-hand-S* case, the forward rake angle, α_1, and the backward rake angle, α_2, for this particular tip are 55±2° and 35±2° respectively. These values are provided by the manufacturer and measured in the axial plane. The clearance angle, ψ, is 51±2° and measured in the lateral plane (refer to Figure 7.18). However, once the probe is placed in the AFM head, the inclination angle of the cantilever, α, as defined in Chapter 4, should be taken into account. Based on the knowledge of this angle, the *T-use-S* case (c.f. the classification defined in Chapter 2) can be established. For the AFM system utilised in this study, the inclination angle is equal to 12°. Therefore, the value of the forward rake angle and backward rake angle become 67±2° and 23±2° respectively as shown in Figure 7.19.

Figures 7.20 and 7.21 show a schematic of the material flow ahead of the tip in both the forward and backward directions. In this figure, the tip is represented with a finite edge radius. In addition, the size of the dead zone is varied depending on the processing direction considered. From these figures, it can be seen that the rake angle is not set by the tool geometry alone. Indeed, it also depends on the direction of scratching. It would be reasonable to expect that the cutting edge radius of the tip in both the forward and the backward directions are the same when the tip in the *T-hand-S* configuration. However, this is not the case. Indeed, during nanomachining, a small dead zone is created as illustrated in Figure 7.20 and 7.21. The size of this area depends on the direction of scratching and the inclination angle, α. The boundary of the dead zone is defined with the vertices A, C and D (see Figures 7.20 and 7.21) and can be obtained when considering the intersection of the tangents to points A and C. Based on this, it can be said that the inclination angle and tip angles have a significant influence on the size of the dead zone. More specifically, the length of the arc (*AC*) in the backward direction is longer than that the forward direction. For the particular tip used, this difference is 14.6 nm. Consequently, the cutting edge in the forward direction can be considered to be sharper than that in the backward direction. Thus, the increased in the arc length of the tip may be an additional

reason behind the increase, observed in Chapter 6, of the cutting force in the backward direction compared with that in the forward direction, for an equal value of pre-set load.

Figure 7.22 presents a comparison between the cross-section profiles of grooves machined for a pre-set load, F_n, of 21.5 μN in the forward and the backward directions. It is interesting to notice that the depth of the machined groove is different in both cases. Indeed, the profile data show that the machined depth in forward scratching is 13.2 nm deeper than that in the backward direction. Moreover, the cross sectional area of the groove and the pile-up formed in the forward direction are both larger than those in the backward direction. Several possible factors should be considered to explain result. First, the plastic flow of material ahead of the probe tip was achieved under ploughing regime in the forward direction, while the shearing regime occurred in backward scratching. At the same time, the axial force generated under ploughing conditions should be lower than that under the shearing regime. Thus, the influence of this force on the bending angle of the cantilever is lower than that which would be generated under shearing with chip formation. Consequently, the magnitude of the variation of the thrust force via the feedback loop of the AFM system is reduced in comparison with the cutting regime. In the case considered here, from a pre-set load of 21.5 μN, the thrust force is reduced by 13.7% in the forward direction, while it is reduced by 32.7% in the backward direction. Second, as mentioned above, the cutting edge in the forward direction can be considered to be sharper. Thus, this should also contribute to reduce the axial force.

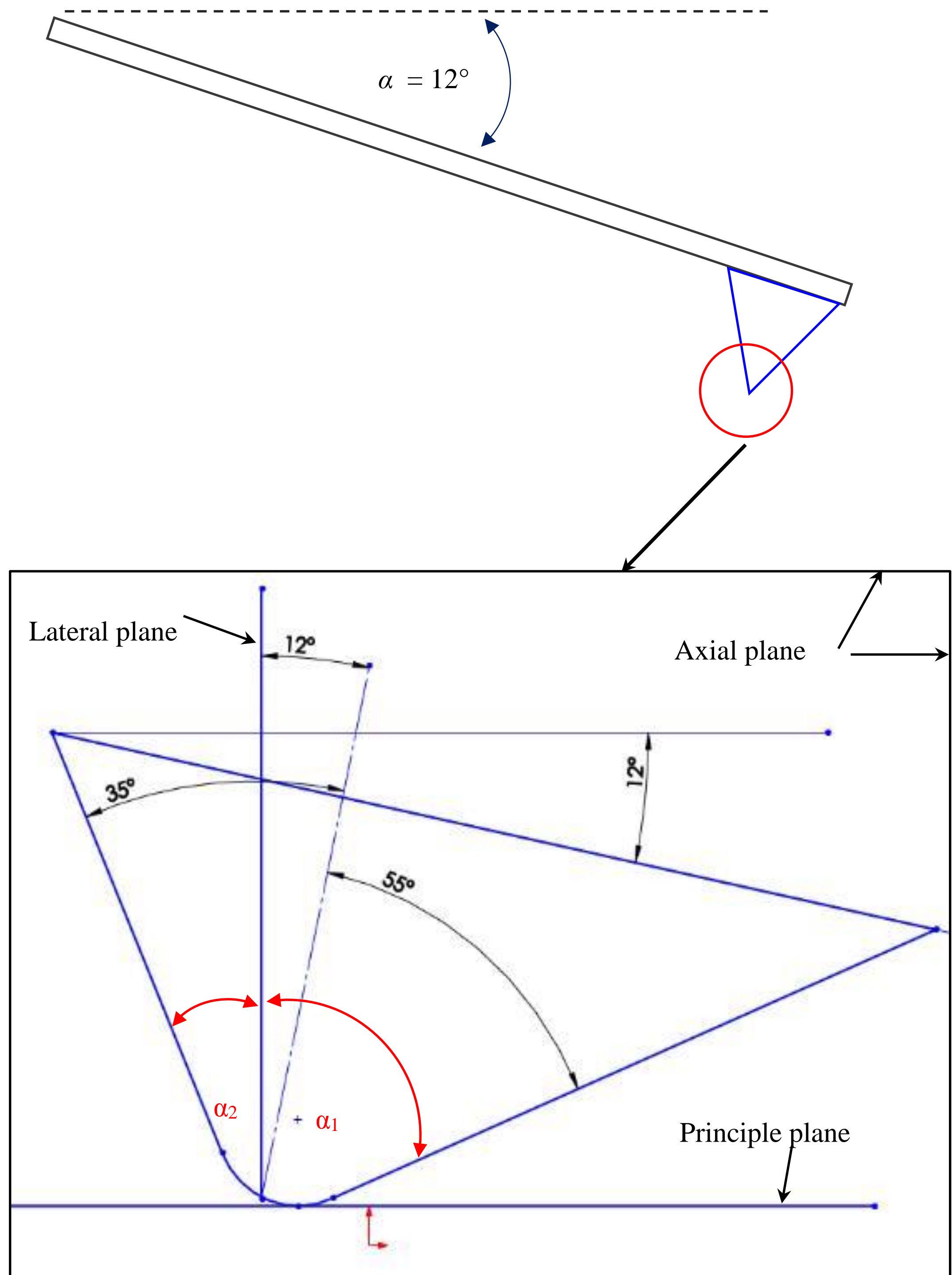

Figure 7.19 Side view of the tip showing the influence of the inclination angle on the cutting tool angles

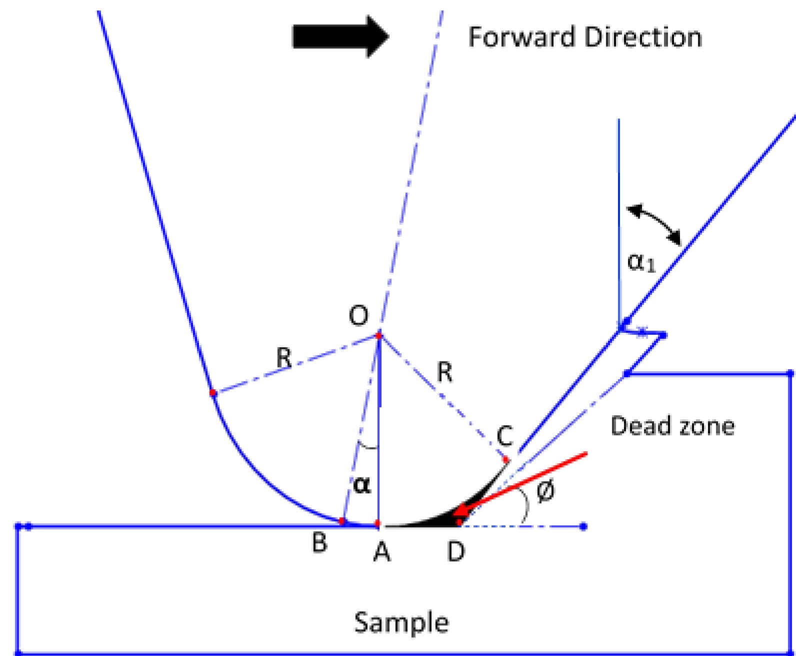

Figure 7.20 A schematic of material flow around a tip in forward direction

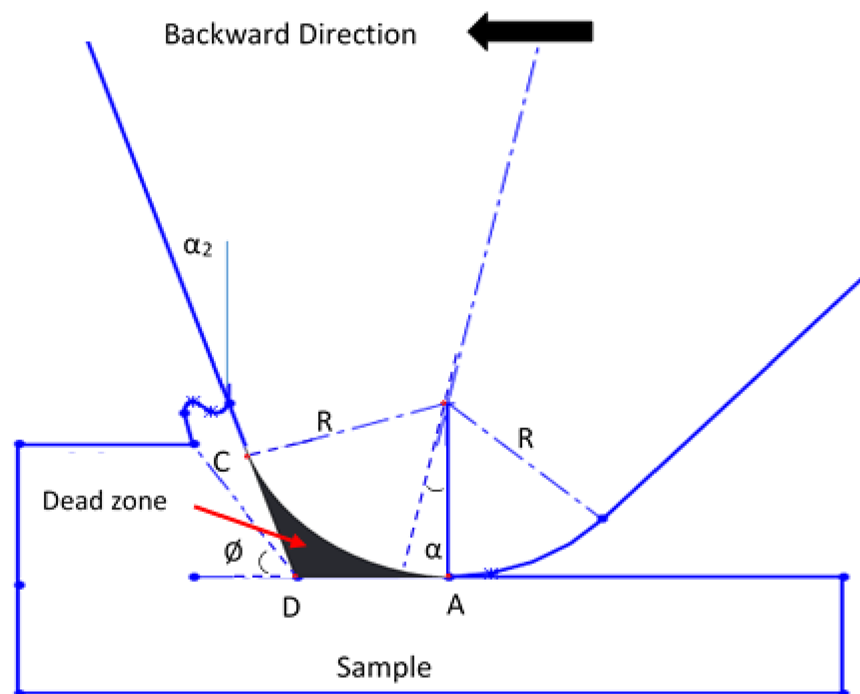

Figure 7.21 A schematic of material flow ahead of the tip in the backward direction

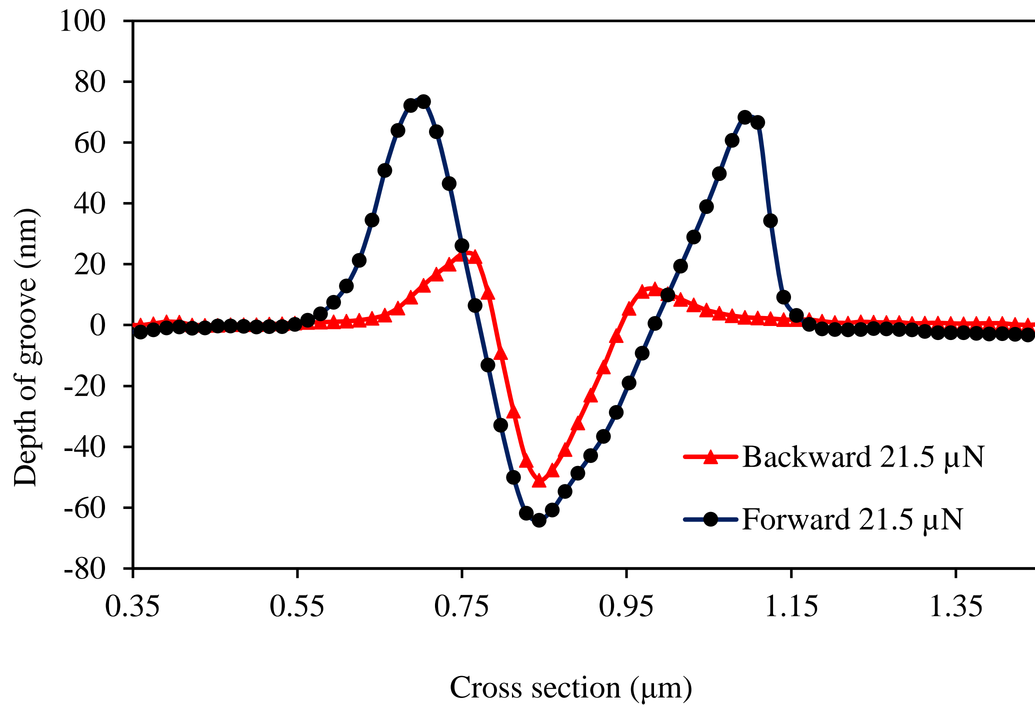

Figure 7.22 Comparison between the groove cross section in the forward and backward directions for an identical pre-set applied load 21.5 µN

7.6 Chip morphology

The understanding of the chip formation process is an important aspect in the field of metal machining. Similarly to conventional cutting, the shape and the dimensions of produced chips could be an effective indicator of phenomena related to the tip-based nanomachining process. Such qualitative and quantitative data could be used to gain further insight into the behaviour of the material under scratching conditions and the interaction forces between the tip and the specimen. Therefore, a better understanding of the chip formation during AFM tip-based nanomachining could also help to control the obtained surface finish and scratching accuracy.

The SEM instrument was used to examine chips, which were present at the end of grooves in the pure backward and inclined forward directions for different pre-set applied loads. The presence of these chips indicated that the process involved the shear-based cutting mechanism. Figures 7.23 and 7.24 show chips produced by scratching along these two directions. From the examination of these SEM micrographs, it was found that all chips shared common features. In particular, the side of each chip which was in contact with the rake face of the tip is always very smooth. In addition, the opposite side of the chips has a rough serrated texture. Interestingly, there are also differences in the shape of the deformed chip between the scenarios when the cantilever deflection was convex or concave. More specifically, when comparing Figure 7.23(a) and Figure 7.23(b) with Figure 7.23(d), it is observed that the chip suffered a higher deformation after the cantilever converted from a convex to a concave shape. This should be due to the higher cutting forces, which were applied on the sample surface following this transition in the shape of the cantilever. Additionally, for the concave deflected shape, it was found that long curly chips were formed and tended to be attached to the specimen at the end of the groove.

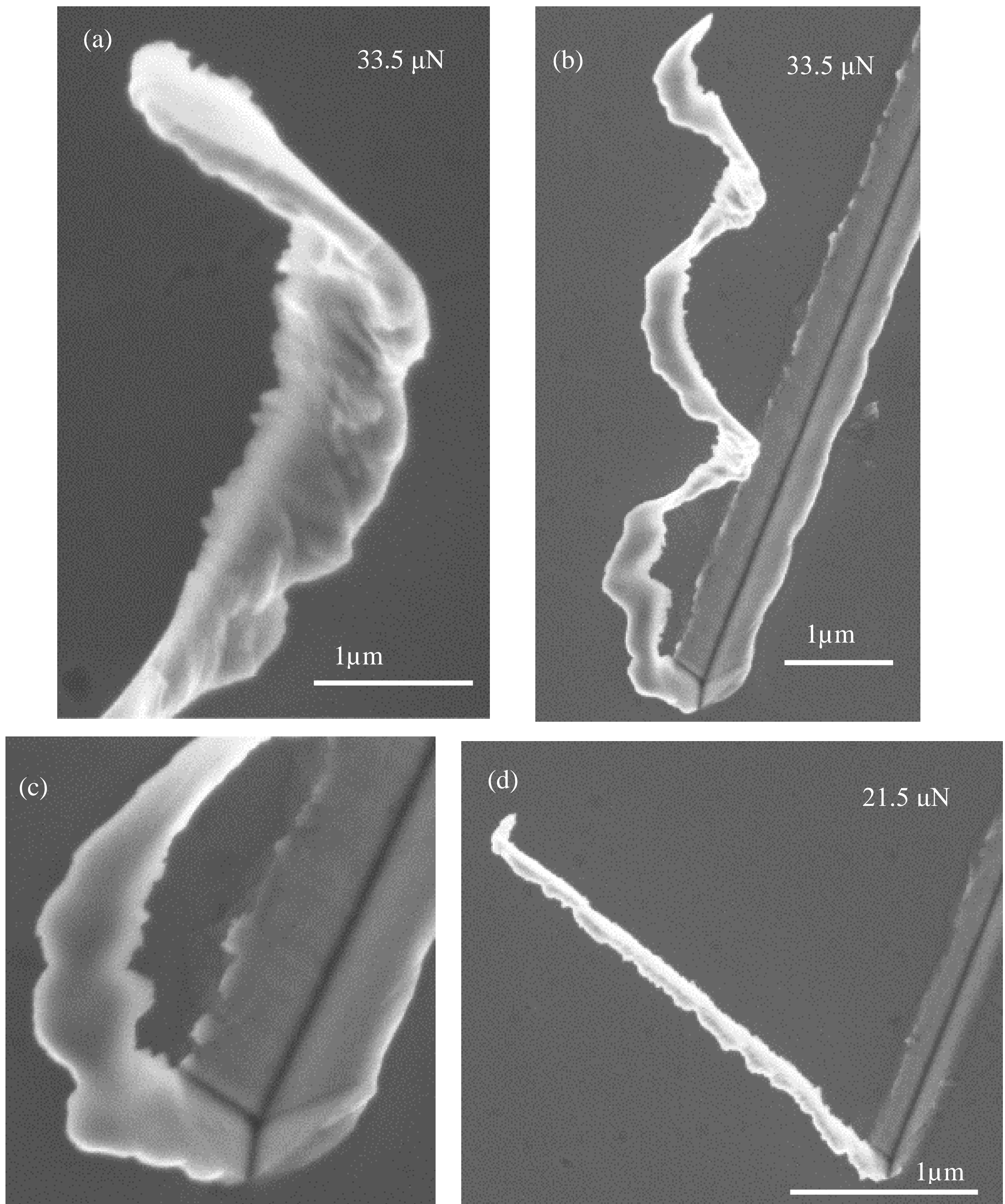

Figure 7.23 Chip formation for the inclined forward direction for two applied loads, namely (a), (b) and (c) 33.5 μN and (d) 21.5 μN

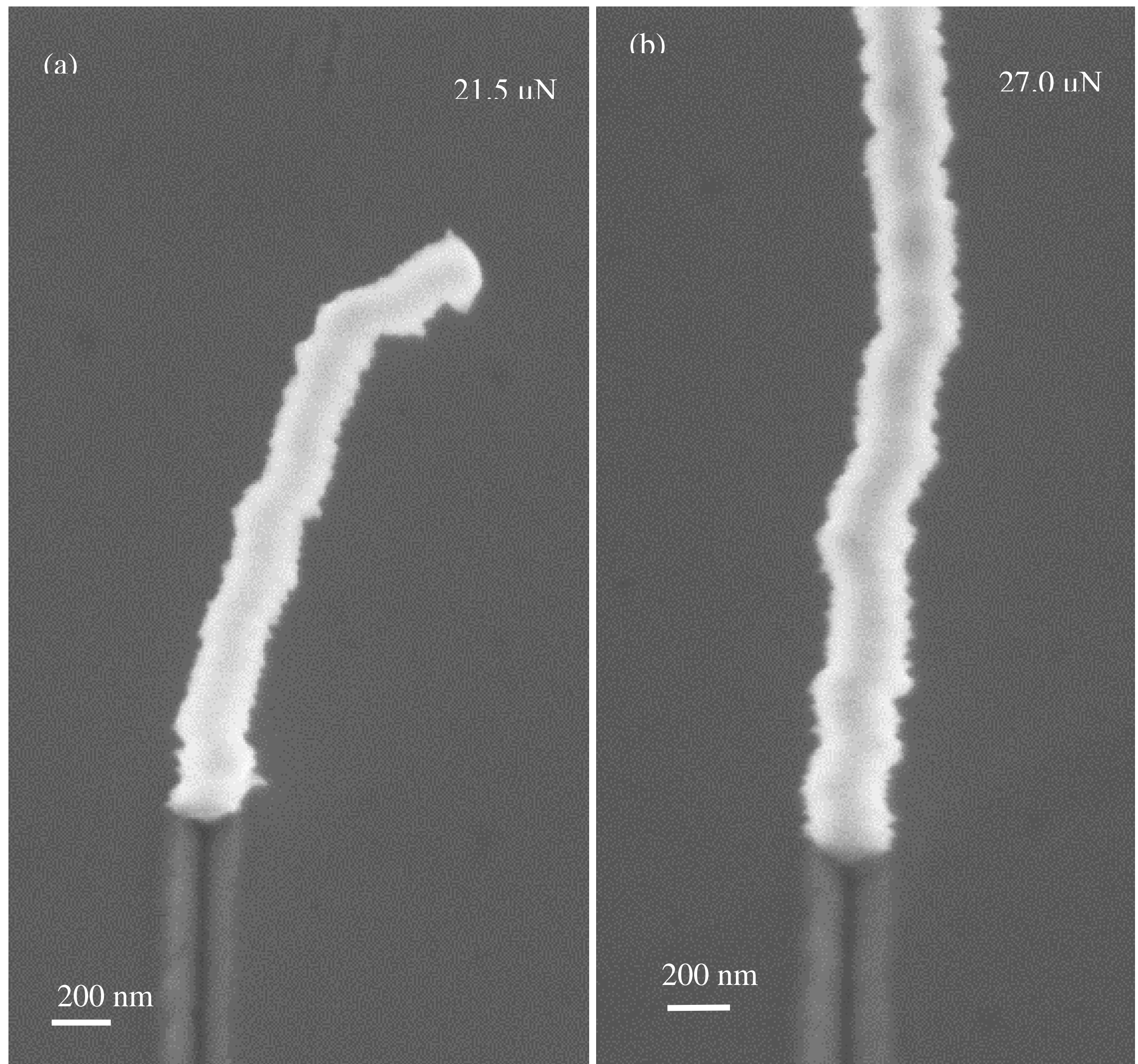

Figure 7.24 Chip formation for the backward direction at the pre-set applied load of (a) 21.6 and (b) 27.0 μN

7.7 Summary

The objective of this chapter was to carry out experimental observations on the topography of grooves produced during the tip-based nanomachining process. In particular, the aim was to provide further insight into the cutting mechanisms at play during the groove formation process based on the new knowledge established in the previous chapters. Based on the reported experimental evidence for the range of loads investigated here, it could be observed that only ploughing took place in the pure forward direction while the shearing regime could occur in the backward direction. In addition, it was also found that both regimes could co-exist along the inclined forward machining direction depending on the side of groove considered.

It was also argued that the inclination angle of the cantilever has a significant influence on the size of the dead zone. This angle leads to the length of the tip arc in contact with the material to be longer in the backward direction than in the forward direction. The smaller arc length in the forward direction makes the tool edge being sharper than in the backward direction. The chips that formed at the end of the machined grooves were also examined. It was reported that the side of each chip in contact with the rake face of the tip was very smooth while the opposite side had a rough serrated texture. Interestingly, differences were also noted in the severity of the chip deformation between the convex and concave cantilever deflected shape. In particular, the chip exhibited higher deformation as the cantilever converted from a convex to a concave shape as a result of the increase in cutting forces associated with this phenomenon.

Chapter 8

Contributions, Conclusions and Future Work

Contributions, Conclusions and Future Work

The main goal of this dissertation was to gain further understanding of the AFM tip-based nano mechanical machining process, particularly when considering the system "cantilever" and "tip" as a flexible cutting tool. This chapter summarises, the main contributions of this research. It also presents the most important conclusions reached. Finally, suggestions for future work are also outlined.

8.1 Contributions

The following original contributions were made in the field of AFM tip-based nanomachining:

1. **A refined model was developed to determine the slope of the deflected cantilever at its free end.** The theoretical development is based on the basic differential equation of the deflection curve of a beam. The aim of this model is to identify loading conditions on the tip that determine the sign of the slope of the deflected cantilever at its free end. With this model, it is possible to critically re-examine the common assumption that the deformed shape of the AFM cantilever is concave along the forward and inclined forward cutting direction.

2. **A new experimental characterisation method was designed to determine the quasi-static bending behaviour of cantilevers during AFM tip-based nanomachining.** This complements the development of the above refined model as it enables the experimental observation of both convex and concave bending of AFM probe cantilevers during real nanomachining operations. This characterisation method relies on 1) an advanced data monitoring set-up and 2) on a novel approach to analyse the vertical motion of the piezoelectric actuator on which the fixed end of the cantilever is mounted.

3. **A refined model was developed to assess the normal force acting on the tip when the AFM stage is static**. The refined theoretical analysis reported is based on the classical beam theory. The distinguishing characteristic of this model is that it takes into account the influence of the cantilever geometry (i.e. length, thickness and tip height) as well as its inclination angle with respect to the surface of a processed specimen. A new correction factor was introduced in this model for determining the normal load in this configuration.

4. **Theoretical and experimental analyses were presented to prove that the conventional method for determining the applied normal load during AFM tip-based nanomachining is wrong**. The experimental analysis consists in comparing the depth of the groove induced as a result of the indentation stage to that resulting from the scratching stage. In addition, the theoretical analysis also put forward to justify this claim rely on the elastic beam theory to calculate the tip deflection for different configurations of loads acting on it.

5. **A new theoretical model was proposed to determine the vertical sensitivity of the PSPD during nanomachining as a function of the machining direction.** The advantage of this model, which also relies on the traditional beam theory, is that it can be applied to cases where the AFM stage is not static.

6. **A novel approach was proposed to estimate all cutting force components acting on the probe during AFM tip-based nanomachining.** This approach is divided into three main steps. First, a relationship between the indentation and the scratching stage is establish based on the deflection angle at the free end of the cantilever. Second, the actual value of normal force is assessed based on two original and alternative methods, which are highlighted below. Third, the axial and lateral force are estimated in practice by combining the result of step one and two. With this approach, all three force components can be measured in any machining direction. Moreover, this model is extended to extract the quasi-static normal sensitivity and lateral force calibration factor of the PSPD.

7. **Two novel methods were proposed to calibrate the actual value of the normal force during nanomachining (i.e. the thrust force).** The first method is referred to as the "fitting method" while the second method one is presented as the "percentage method". Both of these methods rely on the data provided by a strain gauge to assess the vertical motions of the fixed end of the AFM probe. For the "fitting method", the thrust force can be expressed directly as a function of the strain gauge voltage value. For the "percentage method", the percentage change in the strain gauge voltage value is argued to be equal to the percentage change between the pre-set applied load and the actual value of the thrust force. Both method are relatively simple to implement.

8. **Further investigations of the groove formation mechanism and machining outcomes were presented.** A post-machining study of the topography of produced grooves was reported. This experimental study built on the knowledge established throughout the Thesis for the determination of the cutting forces and the understanding of the deflected shape of the cantilever.

8.2 Conclusions

Based on the theoretical and experimental results obtained during this research, the following conclusions can be drawn:

- Using the refined theoretical analysis of the deflection of an AFM cantilever, it was shown that the bending orientation depends on both geometric parameters and machining forces. This model also highlighted that the bending of the cantilever during nanomachining in the forward direction can be convex, especially for small value of the axial force relative to the thrust force.

- The provided experimental evidence showed that both concave and convex bending orientations can take place during AFM tip-based nanomachining. The phenomenon can principally change the depth and width of grooves machined, e.g. the grooves produced on a single crystal copper specimen may increase by 70% on average following such a change in the deformed shape of the cantilever.

- The results of this study indicate that the monitoring of the motion of the piezoelectric actuator, that defines the vertical position of the fixed end of the cantilever, shows that AFM tip-based nanomechanical machining is achieved in a minimum of five stages, namely, approach, indentation, transition, scratching and reset stage.

- This study suggests that following the initial vertical engagement of the tip into the substrate material, the tip may subsequently slide upwards on the face of the created indent when the lateral motion of the AFM stage begins. In this Thesis, this observation was made for the smaller values of pre-set normal loads considered. For increased normal loads, the tip was more likely to stick onto the face of the indent at this specific stage of the process.

- Using the refined theoretical analysis to determine the normal force when the tip is penetrating vertically into a sample material without any horizontal motion between the probe and the sample, it was shown that, for an inclination angle of 12°, the normal force would conventionally be under-estimated by a maximum of 8.6 %. In the case of an inclination angle of 20°, this value was increased to 18.3%.

- The experimental examination of produced grooves together with additional theoretical analyses demonstrated that the value of the thrust force during machining does not correspond to that set by the user prior to the machining trials.

- Using the novel approach to estimate the cutting forces, it was found that even if the deflection angle at free end of probe is constant, this does not mean that the vertical deflection is constant between the nano indentation and the scratching stages.

- The accuracy of the "fitting method" was estimated to be comprised between 1.3% and 4.6%. The maximum discrepancy found between the outcome of the "fitting method" and the "percentage method" was 6.6%, while the minimum percentage error between both methods was almost null.

- During scratching, the variation of the bending angle not only depends on the thrust force but it is also a function of the axial force. For this reason, the normal sensitivity of the PSPD cannot be considered to be a constant quantity.

- The experimental results obtained when processing along the pure and inclined forward directions show that as the pre-set normal load exceeds a critical value, the thrust force is higher than this pre-set load from the start of the machining process. Consequently, at some point during scratching, the cantilever shape change may occur.

- A good agreement was found between the fitting and the percentage methods for different physical quantities evaluated. For example, the average percentage error in the resultant force between the "fitting method" and the "percentage method" was 0.5% and 0% for the backward and forward direction, respectively. This error was still very small, about 1.8%, when the cantilever deflected shape phenomenon occurred in the forward direction.

- From the calculated values for both the resultant angle and the normal sensitivity, it was observed that they increase gradually as the pre-set load is raised. However, when the cantilever changes its deflected shape from convex to concave, the resultant angle and normal sensitivity reduced by more than 70% and 50%, respectively.

- One of the more significant findings to emerge from this study is that not only the applied load has an effect on the depth and width of the grooves but also the shape of the cantilever deflection has a drastic influence on these dimensions. Thus, the depth of the groove produced was not equal to the depth of the initial indent at the beginning of the groove even when the vertical voltage output of the PSPD, which is conventionally refereed to $V_{A\text{-}B}$, was kept constant throughout. The difference in depth was found to be up to 70%.

- The results of this investigation also showed that the depth of a generated groove in the forward direction is clearly deeper than that in the backward direction for the same applied normal force. This supports the idea that the cutting edge in the forward direction can be considered to be sharper than that in the backward direction.

8.3 Future work and recommendations

This research has produced some original contributions and findings in the field AFM tip-based nanomachining process. However, further advances can still be achieved in this area. Examples of direction for future research are as follows:

- **Experimental investigations of the AFM tip wear using the Z-Detector voltage.** Studies focussing on the monitoring of the AFM tip wear normally rely on the inspection of AFM probes via SEM or on the utilisation of specific tip characteriser specimens, which display sharp asperities of nanoscale features. Instead, it is proposed to investigate whether the variation in the Z-Detector voltage may be a suitable indicator of tip wear. Indeed, changes in the Z-Detector voltage occur as a result of the Z-Scanner extending or contracting. A change in the contact area between the tip and the sample due to wear would result in such motions of the Z-Scanner as the contact area also influences the interaction force between the tip and the sample.

- **Study of the effect of the tip wear on the cutting forces during AFM tip-based nano machining.** Using the procedure proposed in Chapter 6 for the on-line evaluation of the cutting forces, the effect of the tip wear on the evolution of such forces during the process could be studied.

- **Further investigations to study the suitability of using the proposed cutting force model to determine the lateral sensitivity factor and the friction coefficient during contact mode AFM scanning rather than during nanomachining**. It is proposed that the procedure developed to assess the cutting forces could also be employed to determine the lateral sensitivity and friction force during the conventional scanning of a specimen surface in contact mode. The results obtained with this model could then be compared with existing methods such as the wedge approach.

References

Ahn, B.W. and Lee, S.H. 2009. Characterization and acoustic emission monitoring of AFM nanomachining. *Journal of Micromechanics and Microengineering* 19 (4), pp. 045028.

Asay, D.B. and Kim, S.H. 2006. Direct force balance method for atomic force microscopy lateral force calibration. *Review of Scientific Instruments* 77 (4), pp. 043903.

Astakhov, V.P. 2010. Basic Definitions and Cutting Tool Geometry, Single Point Cutting Tools. *In* V. P. Astakhov ed. *Geometry of single-point turning tools and drills: fundamentals and practical applications* New York: Springer Science & Business Media, pp. 55-126.

Avouris, P., Hertel, T. and Martel , R. 1997. Atomic force microscope tip-induced local oxidation of silicon: kinetics, mechanism, and nanofabrication. *Applied Physics Letters* 71 (2), pp. 285-287.

Bach, L., Reithmaier, I.P., Forchel, A., Gentner, J.L. and Goldstein, L. 2001. Multiwavelength laterally complex coupled distributed feedback laser arrays with monolithically integrated combiner fabricated by focused-ion-beam lithography. *Applied Physics Letters* 79 (15), pp. 2324-2326.

Backer, W., Marshall, E. and Shaw, M. 1952. The size effect in metal cutting. *Transactions of the ASME* 74 (1), pp. 61.

Baró, A.M. and Reifenberger, R.G. 2012. *Atomic force microscopy in liquid: Biological Applications*. New Jersey, United States: John Wiley & Sons.

Bhushan, B. 2011. *Nanotribology and Nanomechanics I: Measurement Techniques and Nanomechanics*. New York, United States: Springer Science & Business Media.

Bhushan, B. and Kwak, K.J. 2008. Noble metal-coated probes sliding at up to 100 mm s− 1 against PZT films for AFM probe-based ferroelectric recording technology. *Journal of Physics: Condensed Matter* 20 (22), pp. 225013.

Bhushan, B. and Marti, O. 2010. Scanning probe microscopy–principle of operation, instrumentation, and probes. *In* B. Bhushan ed. *Nanotribology and Nanomechanics I*. Berlin and Heidelberg , Germany: Springer, pp. 573-617.

Binnig, G., Gerber, C., Stoll, E., Albrecht, T. and Quate, C. 1987. Atomic resolution with atomic force microscope. *EPL (Europhysics Letters)* 3 (12), pp. 1282-1286.

Binnig, G., Quate, C.F. and Gerber, C. 1986. Atomic force microscope. *Physical Review Letters* 56 (9), 930-934.

Binnig, G., Rohrer, H., Gerber, C. and Weibel, E. 1982. Surface studies by scanning tunneling microscopy. *Physical Review Letters* 49 (1), pp. 57-61.

Borodich, F.M. 2014. The Hertz-type and adhesive contact problems for depth-sensing indentation. *Adv. Appl. Mech* 47, pp. 225-366.

Bowen, W.R. and Hilal, N. 2009. *Atomic Force Microscopy in Process Engineering: An Introduction to AFM for Improved Processes and Products*. Oxford , UK: Butterworth-Heinemann.

Bruker nano system 2012. Fundamentals of Contact Mode and TappingMode Atomic Force Microscopy [online]. Available at: available at: http://www.azonano.com/article.aspx?ArticleID=3010 [Accessed30 August 2016].

Butt, H.-J., Cappella, B. and Kappl, M. 2005. Force measurements with the atomic force microscope: Technique, interpretation and applications. *Surface Science Reports* 59 (1), pp. 1-152.

Chae, J., Park, S. and Freiheit, T. 2006. Investigation of micro-cutting operations. *International Journal of Machine Tools and Manufacture* 46 (3), pp. 313-332.

Christopher, L., F. 2012. *Atomic Force Microscopy Investigations into Biology – From Cell to Protein* Janeza Trdine 9, 51000 Rijeka, Croatia InTech, http://library.umac.mo/ebooks/b28055652.pdf [Accessed7 October 2016].

Cleveland, J., Manne, S., Bocek, D. and Hansma, P. 1993. A nondestructive method for determining the spring constant of cantilevers for scanning force microscopy. *Review of Scientific Instruments* 64 (2), pp. 403-405.

Clifford, C.A. and Seah, M.P. 2005. The determination of atomic force microscope cantilever spring constants via dimensional methods for nanomechanical analysis. *Nanotechnology* 16 (9), pp. 1666-1680.

Cumings, J. and Zettl, A. 2000. Low-friction nanoscale linear bearing realized from multiwall carbon nanotubes. *Science* 289 (5479), pp. 602-604.

Dimov, S., Brousseau, E., Minev, R. and Bigot, S. 2012. Micro-and nano-manufacturing: Challenges and opportunities. *Proceedings of the Institution of Mechanical Engineers, Part C: Journal of Mechanical Engineering Science* 226 (1), pp. 3-15.

Ducker, W.A., Senden, T.J. and Pashley, R.M. 1992. Measurement of forces in liquids using a force microscope. *Langmuir* 8 (7), pp. 1831-1836.

Eaton, P. and West, P. 2010. *Atomic Force Microscopy*. Oxford, United Kingdom: OUP Oxford.

Ee, Y.-K., Li, X.-H., Biser, J., Cao, W., Chan, H.M., Vinci, R.P. and Tansu, N. 2010. Abbreviated MOVPE nucleation of III-nitride light-emitting diodes on nano-patterned sapphire. *Journal of Crystal Growth* 312 (8), pp. 1311-1315.

El-Sayed. and Mostafa, A. 2001. Some interesting properties of metals confined in time and nanometer space of different shapes. *Accounts of Chemical Research* 34 (4), pp. 257-264.

Elings, V.B. 1995. Methods of operating atomic force microscopes to measure friction. Google Patents.

Elkaseer, A. and Brousseau, E. 2013. Modelling the surface generation process during AFM probe-based machining: simulation and experimental validation. *Surface Topography: Metrology and Properties* 2 (2), pp. 025001.

Engstrom, D., Porter, B., Pacios, M. and Bhaskaran, H. 2014. Additive nanomanufacturing–A review. *Journal of Materials Research* 29 (17), pp. 1792-1816.

Facchetti , A. 2010. Π-conjugated polymers for organic electronics and photovoltaic cell applications†. *Chemistry of Materials* 23 (3), pp. 733-758.

Fang, T.-H. and Chang, W.-J. 2003. Effects of AFM-based nanomachining process on aluminum surface. *Journal of Physics and chemistry of Solids* 64 (6), pp. 913-918.

Fang, T.-H., Weng, C.-I. and Chang, J.-G. 2000. Machining characterization of the nano-lithography process using atomic force microscopy. *Nanotechnology* 11 (3), pp. 181-187.

Feiler, A., Attard, P. and Larson, I. 2000. Calibration of the torsional spring constant and the lateral photodiode response of frictional force microscopes. *Review of Scientific Instruments* 71 (7), pp. 2746-2750.

Firtel, M., Henderson, G. and Sokolov, I. 2004. Nanosurgery: observation of peptidoglycan strands in Lactobacillus helveticus cell walls. *Ultramicroscopy* 101 (2), pp. 105-109.

Fonseca Filho, H., Mauricio, M., Ponciano, C. and Prioli, R. 2004. Metal layer mask patterning by force microscopy lithography. *Materials Science and Engineering: B* 112(2), pp. 194-199.

Fujita, J., Ohnishi, Y., Ochiai, Y. and Matsui, S. 1996. Ultrahigh resolution of calixarene negative resist in electron beam lithography. *Applied Physics Letters* 68 (9), pp. 1297-1299.

Garcia, R., Knoll, A.W. and Riedo, E. 2014. Advanced scanning probe lithography. *Nature nanotechnology* 9 (8), pp. 577-587.

Geng, Y., Yan, Y., Xing, Y., Zhang, Q., Zhao, X. and Hu, Z. 2013. Effect of cantilever deformation and tip-sample contact area on AFM nanoscratching. *Journal of Vacuum Science & Technology B* 31(6), 061802.

Geng, Y., Zhao, X., Yan, Y. and Hu, Z. 2014. An AFM-based methodology for measuring axial and radial error motions of spindles. *Measurement Science and Technology* 25 (5), pp. 055007.

Gillibert, R., Sarkar, M., Bryche, J.-F., Yasukuni, R., Moreau, J., Besbes, M., Barbillon, G., Bartenlian, B., Canva, M. and de La Chapelle, M.L. 2016. Directional surface enhanced Raman scattering on gold nano-gratings. *Nanotechnology* 27 (11), pp. 115202.

Gozen, B.A. and Ozdoganlar, O.B. 2010. A rotating-tip-based mechanical nano-manufacturing process: nanomilling. *Nanoscale research letters* 5 (9), pp. 1403-1407.

Gozen, B.A. and Ozdoganlar, O.B. 2014. Wear of ultrananocrystalline diamond AFM tips during mechanical nanomanufacturing by nanomilling. *Wear* 317 (1), pp. 39-55.

Hansma, P., Elings, V., Marti, O. and Bracker, C. 1988. Scanning tunneling microscopy and atomic force microscopy: application to biology and technology. *Science* 242 (4876), pp. 209-216.

Hassani, S.S., Sobat, Z. and Aghabozorg , H.R. 2010. Force nanolithography on various surfaces by atomic force microscope. *International Journal of Nanomanufacturing* 5 (3-4), pp. 217-224.

Hassani, S.S. and Aghabozorg, H. 2011. Nanolithography Study Using Scanning Probe Microscope ,Recent Advances in Nanofabrication Techniques and Applications. *In* P. B. Cui ed. *"Recent Advances in Nanofabrication Techniques and Applications"* http://www.intechopen.com/books/recent-advances-in-nanofabrication-techniques-and-applications/nanolithography-study-using-scanning-probe-microscope: InTech, pp. 614

Haugstad, G. 2012. *Atomic force microscopy: understanding basic modes and advanced applications*. New Jersey, United States: John Wiley & Sons.

Herrera-Granados, G., Ashida, K., Ogura, I., Okazaki, Y., Morita, N., Hidai, H., Matsusaka, S. and Chiba, A. 2014. Effect of cutting angles during the micro-groove fabrication process using a non-rigid cutting mechanism. *9th International Workshop on Microfactories*. Honolulu, USA, pp. 108-115.

Hiroyuki, S. and Nobuyuki, N. 1997. AFM lithography in constant current mode *Nanotechnology* 8(3A), pp. A15-A18.

Hongshun, P.D.Y. 2014. *Atomic Force Microscopy (AFM): Principles, Modes of Operation and Limitations (Chemistry Research and Application)* New York, USA: Nova Science Pub Inc.

Hu, S., Hamidi, A., Altmeyer, S., Köster, T., Spangenberg, B. and Kurz, H. 1998. Fabrication of silicon and metal nanowires and dots using mechanical atomic force lithography. *Journal of Vacuum Science & Technology B* 16 (5), pp. 2822-2824.

Huang, J., Ponce, F., Caldas, P., Prioli, R. and Almeida, C. 2013. The effect of nanoscratching direction on the plastic deformation and surface morphology of InP crystals. *Journal of Applied Physics* 114 (20), p. 203503.

Hyon, C.K., Choi, S.C., Hwang, S.W., Ahn, D., Kim, Y. and Kim, E.K. 1999. Nano-structure fabrication and manipulation by the cantilever oscillation of an atomic force microscope. *Japanese Journal of Applied Physics* 38 (12S), pp. 7257-7259.

Iwanaga, S., Darling, R.B. and Cobden, D.H. 2005. Stable and erasable patterning of vanadium pentoxide thin films by atomic force microscope nanolithography. *Applied Physics Letters* 86 (13), pp. 133113.

Jiang, X., Wu, G., Du, Z., Ma, K.-J., Shirakashi, J.-i. and Tseng, A.A. 2012. Nanoscale scratching of platinum thin films using atomic force microscopy with DLC tips. *Journal of Vacuum Science & Technology B* 30(2), pp. 021605.

Jiang, X., Wu, G., Zhou, J., Wang, S., Tseng, A.A. and Du, Z. 2011. Nanopatterning on silicon surface using atomic force microscopy with diamond-like carbon (DLC)-coated Si probe. *Nanoscale Research Letters* 6 (1), 1-7.

Jin, X. and Unertl, W. 1992. Submicrometer modification of polymer surfaces with a surface force microscope. *Applied Physics Letters* 61 (6), pp. 657-659.

Jung, B., Jo, W., Gwon , M., Lee , E. and Kim, D. 2010. Scanning probe lithography for fabrication of Ti metal nanodot arrays. *Ultramicroscopy* 110, 4.

Jung, T., Moser, A., Hug, H., Brodbeck, D., Hofer, R., Hidber, H. and Schwarz, U. 1992. The atomic force microscope used as a powerful tool for machining surfaces. *Ultramicroscopy* 42-44 (2), pp. 1446-1451.

Kato, Z., Sakairi, M. and Takahashi, H. 2001. Fabrication of grooves on aluminum surface with atomic force microscope probe processing. *Journal of The Electrochemical Society* 148 (12), pp. 790-798.

Keyser, U.F., Schumacher, H.W., Zeitler, U., Haug, R.J. and Eberl, K. 2000. Fabrication of a single-electron transistor by current-controlled local oxidation of a two-dimensional electron system. *Applied Physics Letters* 76 (4), pp. 457-459.

Khurshudov, A.G., Kato, K. and Koide, H. 1996. Nano-wear of the diamond AFM probing tip under scratching of silicon, studied by AFM. *Tribology Letters* 2 (4), pp. 345-354.

Kim, Y. and LIEBER, C. 1992. Machining oxide thin films with an atomic force microscope- Pattern and object formation on the nanometer scale. *Science* 257 (5068), pp. 375-377.

Klinke, C., Hannon, J.B., Afzali, A. and Avouris, P. 2006. Field-effect transistors assembled from functionalized carbon nanotubes. *Nano letters* 6 (5), pp. 906-910.

Koinkar, V.N. and Bhushan, B. 1997. Scanning and transmission electron microscopies of single-crystal silicon microworn/machined using atomic force microscopy. *Journal of Materials Research* 12 (12), pp. 3219-3224.

Krishnan, N., Boyd, S., Somani, A., Raoux, S., Clark, D. and Dornfeld, D. 2008. A hybrid life cycle inventory of nano-scale semiconductor manufacturing. *Environmental Science & Technology* 42 (8), pp. 3069-3075.

Kunze, U. 2002. Invited Review Nanoscale devices fabricated by dynamic ploughing with an atomic force microscope. *Superlattices and Microstructures* 31(1), pp. 3-17.

Lee, G., Jung, H., Son, J., Nam, K., Kwon, T., Lim, G., Kim, Y.H., Seo, J., Lee, S.W. and Yoon, D.S. 2010. Experimental and numerical study of electrochemical nanomachining using an AFM cantilever tip. *Nanotechnology* 21 (18), pp. 185301.

Li, L., Hirtz, M., Wang, W., Du, C., Fuchs, H. and Chi, L. 2010. Patterning of polymer electrodes by nanoscratching. *Advanced Materials* 22 (12), pp. 1374-1378.

Li, X., Wang, X., Xiong, Q. and Eklund, P.C. 2005. Top-down structure and device fabrication using in situ nanomachining. *Applied Physics Letters* 87 (23), pp. 233113.

Link, S. and Mostafa, A.E.-S. 1999. Spectral properties and relaxation dynamics of surface plasmon electronic oscillations in gold and silver nanodots and nanorods. *The Journal of Physical Chemistry B* 103 (40), pp. 8410-8426.

Liu, W., Bonin, K. and Guthold, M. 2007. Easy and direct method for calibrating atomic force microscopy lateral force measurements. *Review of Scientific Instruments* 78 (6), pp. 063707.

Liu, X., DeVor, R.E., Kapoor, S. and Ehmann, K. 2004. The mechanics of machining at the microscale: assessment of the current state of the science. *Journal of Manufacturing Science and Engineering* 126 (4), pp. 666-678.

Lu, G., Zhou, X., Li, H., Yin, Z., Li, B., Huang, L., Boey, F. and Zhang, H. 2010. Nanolithography of single-layer graphene oxide films by atomic force microscopy. *Langmuir* 26 (9), pp. 6164-6166.

Lucas, M., Zhang, X., Palaci, I., Klinke, C., Tosatti, E. and Riedo, E. 2009. Hindered rolling and friction anisotropy in supported carbon nanotubes. *Nature materials* 8 (11), pp. 876-881.

Magno, R. and Bennett, B.R. 1997. Nanostructure patterns written in III–V semiconductors by an atomic force microscope. *Applied Physics Letters* 70 (14), pp. 1855-1857.

Malekian, M., Park, S., Strathearn, D., Mostofa, M.G. and Jun, M. 2010. Atomic force microscope probe-based nanometric scribing. *Journal of Micromechanics and Microengineering* 20 (11), pp. 115016.

Mamin, H.J. 1996. Thermal writing using a heated atomic force microscope tip. *Applied Physics Letters* 69 (3), pp. 433-435.

Manjunathaiah, J. and Endres, W.J. 2000. A new model and analysis of orthogonal machining with an edge-radiused tool. *Journal of Manufacturing Science and Engineering* 122 (3), pp. 384-390.

Martin-Olmos, C., Villanueva, L.G., van der Wal, P.D., Llobera, A., de Rooij, N.F., Brugger, J. and Perez-Murano, F. 2012. Conductivity of SU-8 Thin Films through Atomic Force Microscopy Nano-Patterning. *Advanced Functional Materials* 22 (7), pp. 1482-1488.

Martín, C., Rius, G., Borrisé, X. and Pérez-Murano, F. 2005. Nanolithography on thin layers of PMMA using atomic force microscopy. *Nanotechnology* 16 (8), pp. 1016-1022.

Martin, Y., Williams, C.C. and Wickramasinghe, H.K. 1987. Atomic force microscope–force mapping and profiling on a sub 100-Å scale. *Journal of Applied Physics* 61 (10), pp. 4723-4729.

Massiot, I., Trompoukis, C., Lodewijks, K., Depauw, V. and Dmitriev, A. 2016. Highly conformal fabrication of nanopatterns on non-planar surfaces. *Nanoscale* 8, pp. 11461-11466.

Megson, T.H.G. 1987. *Strength of materials for civil engineers. Second edition*. Edward Arnold (a division of Hodder and Stoughton Ltd), Sevenoaks, United Kingdom: 2nd edition.

Merchant, M.E. 1945. Mechanics of the metal cutting process. I. Orthogonal cutting and a type 2 chip. *Journal of Applied Physics* 16 (5), pp. 267-275.

Meyer, E. 1992. Atomic force microscopy. *Progress in Surface Science* 41 (1), pp. 3-49.

Meyer, G. and Amer, N.M. 1990. Optical-beam-deflection atomic force microscopy: The NaCl (001) surface. *Applied Physics Letters* 56 (21), pp. 2100-2101.

Milekhin, A., Sveshnikova, L., Duda, T., Yeryukov, N., Rodyakina, E., Gutakovskii, A., Batsanov, S., Latyshev, A. and Zahn, D. 2016. Surface-enhanced Raman spectroscopy of semiconductor nanostructures. *Physica E: Low-dimensional Systems and Nanostructures* 75, pp. 210-222.

Mironov, V.L. 2004. *Fundamentals of Scanning Probe Microscopy*. NT-MDT.

Morris, V.J., Kirby, A.R. and Gunning, A.P. 1999. *Atomic force microscopy for biologists*. Imperial College Press, United Kingdom: World Scientific.

Mostofa, M.G. 2014. Nano Mechanical Machining Using AFM Probe. *Department of mechanical and manufacturing engineering*. PhD thesis, University of Calgary, Canada

Mostofa, M.G., Park, C.I. and Park, S.S. 2013. AFM probe based nano mechanical scribing of soda-lime glass. *Journal of Manufacturing Processes* 15 (4), pp. 625-634.

Muir, B.W., Fairbrother, A., Gengenbach, T.R., Rovere, F., Abdo, M.A., McLean, K.M. and Hartley, P.G. 2006. Scanning Probe Nanolithography and Protein Patterning of Low-Fouling Plasma Polymer Multilayer Films. *Advanced Materials* 18 (23), pp. 3079-3082.

Ogino, T., Nishimura, S. and Shirakashi, J.-i. 2008. Scratch nanolithography on Si surface using scanning probe microscopy: influence of scanning parameters on groove size. *Japanese Journal of Applied Physics* 47 (1S), pp. 712-714.

Ogletree, D., Carpick, R.W. and Salmeron, M. 1996. Calibration of frictional forces in atomic force microscopy. *Review of Scientific Instruments* 67 (9), pp. 3298-3306.

Park-systems 2014. Perfectly decoupled XY-Z scanner enables independent movement of Z scanner, which makes True Non-Contact scanning with optimal feedback speed. http://www.parkafm.com/images/applications/semiconductors/note/AN-I04.pdf, Park systems. pp. 2.

Park, J.G., Zhang, C., Liang, R. and Wang, B. 2007. Nano-machining of highly oriented pyrolytic graphite using conductive atomic force microscope tips and carbon nanotubes. *Nanotechnology* 18 (40), pp. 405306.

Perry, J.L. and Kandlikar, S.G. 2005. Review of fabrication of nanochannels for single phase liquid flow. *Microfluidics and Nanofluidics* 2 (3), pp. 185-193.

Piner, R.D. 1999. "Dip-Pen" Nanolithography. *Science* 283 (5402), pp. 661-663.

Rennon, S., Bach, L., Reithmaier, J.P., Forchel, A., Gentner, J.L. and Goldstein, L. 2000. High-frequency properties of 1.55 μm laterally complex coupled distributed feedback lasers fabricated by focused-ion-beam lithography. *Applied Physics Letters* 77 (3), pp. 325-327.

Robinson, A.P.G., Palmer, R.E., Tada, T., Kanayama, T. and Preece, J.A. 1998. A Fullerene derivative as an electron beam resist for nanolithography. *Applied Physics Letters* 72 (11), pp. 1302-1304.

Ruan, J.-A. and Bhushan, B. 1994. Atomic-scale friction measurements using friction force microscopy: part I—general principles and new measurement techniques. *Journal of Tribology* 116 (2), pp. 378-388.

Sadegh Hassani, S., Sobat, Z. and Aghabozorg, H. 2008a. Scanning probe lithography as a tool for studying of various surfaces. *Nano Science and Nano Technology* 2 (2-3), pp. 94-98.

Sadegh Hassani, S., Sobat, Z. and Aghabozorg, H.R. 2008b. Nanometer-Scale Patterning on PMMA Resist by Force Microscopy Lithography. *Iranian Journal of Chemistry and Chemical Engineering (IJCCE)* 27 (4), pp. 29-34.

Sader, J.E., Chon, J.W. and Mulvaney, P. 1999. Calibration of rectangular atomic force microscope cantilevers. *Review of Scientific Instruments* 70(10), 3967-3969.

Santinacci, L., Djenizian, T., Hildebrand, H., Ecoffey, S., Mokdad, H., Campanella, T. and Schmuki, P. 2003. Selective palladium electrochemical deposition onto AFM-scratched silicon surfaces. *Electrochimica Acta* 48 (20), pp. 3123-3130.

Santinacci, L., Djenizian, T. and Schmuki, P. 2001. Atomic force microscopy-induced nanopatterning of Si (100) surfaces. *Journal of The Electrochemical Society* 148 (9), pp. 640-646.

Schulte, C., Rodighiero, S., Cappelluti, M.A., Puricelli, L., Maffioli, E., Borghi, F., Negri, A., Sogne, E., Galluzzi, M. and Piazzoni, C. 2016. Conversion of nanoscale topographical information of cluster-assembled zirconia surfaces into mechanotransductive events promotes neuronal differentiation. *Journal of Nanobiotechnology* 14 (1), pp. 1-24.

Schumacher, H., Keyser, U., Zeitler, U., Haug, R. and Eberl, K. 2000. Controlled mechanical AFM machining of two-dimensional electron systems: fabrication of a single-electron transistor. *Physica E: Low-dimensional Systems and Nanostructures* 6 (1), pp. 860-863.

Schumacher, H., Kracke, B. and Damaschke, B. 1995. Modification of thin gold films with a scanning force microscope. *Thin Solid Films* 264 (2), pp. 268-272.

Snow, E.S. and Campbell, P.M. 1995. AFM Fabrication of sub-10-nanometer metal-oxide devices with in situ control of electrical properties. *Science* 270(5242), pp. 1639-1641.

Sumomogi, T., Endo, T., Kuwahara, K. and Kaneko, R. 1995. Nanoscale layer removal of metal surfaces by scanning probe microscope scratching. *Journal of Vacuum Science & Technology* 13 (3), pp. 1257-1260.

Sumomogi, T., Endo, T., Kuwahara, K., Kaneko, R. and Miyamoto, T. 1994. Micromachining of metal surfaces by scanning probe microscope. *Journal of Vacuum Science & Technology B* 12 (3), pp. 1876-1880.

Sun, L., Qin, G., Seo, J.H., Celler, G.K., Zhou, W. and Ma, Z. 2010. 12-GHz Thin-Film Transistors on Transferrable Silicon Nanomembranes for High-Performance Flexible Electronics. *Small* 6 (22), pp. 2553-2557.

Sun, Y., Yan, Y., Liang, Y., Hu, Z., Zhao, X., Sun, T. and Dong, S. 2013. Effect of the molecular weight on deformation states of the polystyrene film by AFM single scanning. *Scanning* 35 (5), pp. 308-315.

Tao, Z. and Bhushan, B. 2006. Surface modification of AFM silicon probes for adhesion and wear reduction. *Tribology Letters* 21 (1), pp. 1-16.

Teixeira, F., Mansano, R., Salvadori, M., Cattani, M. and Brown, I. 2007. Atomic force microscope nanolithography of polymethylmethacrylate polymer. *Review of Scientific Instruments* 78 (5), pp. 053702.

Thian, S., Tang, Y., Fuh, J., Wong, Y., Lu, L. and Loh, H. 2006. Micro-rapid-prototyping via multi-layered photo-lithography. *The International Journal of Advanced Manufacturing Technology* 29 (9-10), pp. 1026-1032.

Timoshenko, S.P. 1940. *Strength of Materials. Part 1. Elementary Theory and Problems*. D. Van Nostrand Company, Toronto, New York.

Tseng, A.A. 2011. Removing Material Using Atomic Force Microscopy with Single-and Multiple-Tip Sources. *Small* 7 (24), pp. 3409-3427.

Tseng, A.A., Kuo, C.-F.J., Jou, S., Nishimura, S. and Shirakashi, J.-i. 2011. Scratch direction and threshold force in nanoscale scratching using atomic force microscopes. *Applied Surface Science* 257 (22), pp. 9243-9250.

Tseng, A.A., Notargiacomo, A. and Chen, T. 2005. Nanofabrication by scanning probe microscope lithography: A review. *Journal of Vacuum Science & Technology B* 23 (3), pp. 877-894.

Tseng, A.A., Shirakashi, J.-i., Jou, S., Huang, J.-C. and Chen, T. 2010. Scratch properties of nickel thin films using atomic force microscopy. *Journal of Vacuum Science & Technology B* 28(1), 202-210.

Tseng, A.A., Shirakashi, J.-i., Nishimura, S., Miyashita, K. and Notargiacomo, A. 2009. Scratching properties of nickel-iron thin film and silicon using atomic force microscopy. *Journal of Applied Physics* 106 (4), pp. 044314.

Varenberg, M., Etsion, I. and Halperin, G. 2003. An improved wedge calibration method for lateral force in atomic force microscopy. *Review of Scientific Instruments* 74(7), pp. 3362-3367.

Versen, M., Klehn, B., Kunze, U., Reuter, D. and Wieck, A. 2000a. Nanoscale devices fabricated by direct machining of GaAs with an atomic force microscope. *Ultramicroscopy* 82 (1), pp. 159-163.

Vettiger P, Despont M, Drechsler U, Durig U, Haberle W, Lutwyche M I, Rothuizen H E, Stutz R, R, W. and K, B.G. 2000. Millipede—more than thousand tips for future AFM storage. *J. Res. Dev.* 44 (3), pp. 323-331.

Wang, F. and Zhao, X. 2007. Effect of contact stiffness on wedge calibration of lateral force in atomic force microscopy. *Review of Scientific Instruments* 78 (4), pp. 043701.

Wendel, M., Lorenz, H. and Kotthaus, J.P. 1995. Sharpened electron beam deposited tips for high resolution atomic force microscope lithography and imaging. *Applied Physics Letters* 67 (25), pp. 3732-3734.

Wilder, K., Quate, C.F., Adderton, D., Bernstein, R. and Elings, V. 1998. Noncontact nanolithography using the atomic force microscope. *Applied Physics Letters* 73 (17), 2527.

Wu, S., Lin, Q., Yuen, Y. and Tai, Y.-C. 2001. MEMS flow sensors for nano-fluidic applications. *Sensors and Actuators A: Physical* 89 (1), pp. 152-158.

Wu, X., Sun, Z., Meininger, G.A. and Muthuchamy, M. 2012. Application of atomic force microscopy measurements on cardiovascular cells. *In* X. Peng, Antonyak, Marc ed. New York, Unites State Springer Science+Business Media, pp. 229-244.

Xie, X.N., Chung, H.J., Sow, C.H. and Wee, A.T.S. 2006. Nanoscale materials patterning and engineering by atomic force microscopy nanolithography. *Materials Science and Engineering: R: Reports* 54 (1-2), pp. 1-48.

Yabing, Q. 2008. orrelating structural, mechanical, and charge transport properties of molecular monolayers and surfaces. University of California.

Yan, Y. 2016. Review on AFM tip-based mechanical nanomachining: the influence of the input machining parameters on the outcomes. *Current Nanoscience* 12 (6), pp. 666-675.

Yan Y, Hu Z, Zhao X, Sun T, S, D. and X, L. 2010. Top-Down Nanomechanical Machining of Three-Dimensional Nanostructures by Atomic Force Microscopy. *Small* 6(6), pp. 724–728

Yan, Y., Geng, Y. and Hu, Z. 2015. Recent advances in AFM tip-based nanomechanical machining. *International Journal of Machine Tools and Manufacture* 99, pp. 1-18.

Yan, Y., Sun, T., Liang, Y. and Dong, S. 2007. Investigation on AFM-based micro/nano-CNC machining system. *International Journal of Machine Tools and Manufacture* 47(11), pp. 1651-1659.

Yan, Y., Sun, T., Liang, Y. and Dong, S. 2009. Effects of scratching directions on AFM-based abrasive abrasion process. *Tribology International* 42 (1), pp. 66-70.

Yan, Y., Zhao, X., Hu, Z. and Gao, D. 2012. Effects of atomic force microscope silicon tip geometry on large-scale nanomechanical modification of the polymer surface. *Tribology Transactions* 55 (6), pp. 846-853.

Yun, K. and Lieber., C.M. 1992. Machining Oxide Thin Films with an Atomic Force Microscope: Pattern and Object Formation on the Nanometer Scale. *Science* 257(5068), pp. 375-377.

Zhang, L. and Dong, J. 2012. High-rate tunable ultrasonic force regulated nanomachining lithography with an atomic force microscope. *Nanotechnology* 23 (8), pp. 085303.

Zhang, L. and Tanaka, H. 1997. Towards a deeper understanding of wear and friction on the atomic scale—a molecular dynamics analysis. *Wear* 211 (1), pp. 44-53.

Zhao, Q., Sun, T., Liang, Y.-C., Dong, S. and Chen, M. 2001. Atomic force microscope using a diamond tip: a tool for micro/nanomachining on single-crystal silicon surface. *International Symposium on Optoelectonics and Microelectronics*. Nanjing, China International Society for Optics and Photonics. 73-78.

Zhao, X. and Bhushan, B. 1998. Material removal mechanisms of single-crystal silicon on nanoscale and at ultralow loads. *Wear* 223 (1), pp. 66-78.

Zhong, Q., Inniss, D., Kjoller, K. and Elings, V. 1993. Fractured polymer/silica fiber surface studied by tapping mode atomic force microscopy. *Surface Science Letters* 290 (1-2), pp. 688-692.

Zhou, Q. and Kim, T. 2016. Review of microfluidic approaches for surface-enhanced Raman scattering. *Sensors and Actuators B: Chemical* 227, pp. 504-514.

Appendix A

Indenter control window